Massive MIMO From a Terminal Perspective

Bengtsson, Erik L

2019

Document Version:
Publisher's PDF, also known as Version of record

Massive MIMO From a Terminal Perspective

Erik L. Bengtsson

Lund 2019

Department of Electrical and Information Technology
Lund University
Box 118, SE-221 00 LUND
SWEDEN

This thesis is set in Computer Modern 10pt
with the LaTeX Documentation System

Series of licentiate and doctoral theses
ISSN 1654-790X; No. 124
ISBN 978-91-7895-253-3 (print)
ISBN 978-91-7895-254-0 (digital)

Printed in Sweden by *Tryckeriet i E-huset*, Lund.
September 2019.

Whichever way you comb a tennis-ball, there will always be a swirl.
{*Interpretation of the hedgehog theorem by Henri Poincaré*}

Populärvetenskaplig Sammanfattning

Utvecklingen som skett inom trådlös kommunikation de senaste åren saknar motstycke. Den har lett till användningen av överlastade frekvensband och en enorm energiförbrukning. För att bygga system där mångfalt fler användare eller uppkopplade enheter, som kan utgöra allt från ett fordon till en termometer, kan få tillgång till internetanslutning med kapacitet upp mot 10 Gb/s eller mer krävs det ändringar både på nätverkssidan och i terminalerna. Den femte generationens (5G) kommunikationssystem har som målsättning att nå dessa mål. En av många tekniker som studeras inom 5G är s.k. massiv MIMO (MaMi). Idén bakom MaMi bygger på att man ökar antalet antenner i en basstation tills det man når en gräns efter vilken ytterligare antenner inte förbättrar prestandan nämnvärt. Generellt, ger en ökning av antalet antenner en bättre upplösning och möjliggör för en basstation att fokusera energin bättre. På så vis kan den betjäna flera terminaler samtidigt på samma frekvens. Det har visat sig att i storleksordningen 100 antenner i en basstation är tillräckligt för att nå konvergens och att man då uppnår ett 10 gånger bättre frekvensutnyttjande samt en 100 gånger bättre energieffektivitet.

De flesta publikationer inom MaMi-området har fokuserat på basstationssidan eller radiokanalen där man gjort naiva antaganden kring antennlösningen i terminalerna. Min forskning visar tydligt vikten av att använda integrerade antenner när man gör utvärderingar av MaMi system. Vidare visar resultaten att där är mycket prestanda att hämta genom att öka antalet antenner även i terminalerna.

För att utnyttja alla antennerna optimalt behöver basstationen veta hur transmissionskanalen ser ut. Varje terminalantenn måste därför skicka en känd signal (s.k. pilot). Piloten, tas emot med alla antennerna på basstationen och är det som möjliggör för basstationen att simultant fokusera olika signaler till varje individuell terminalantenn i systemet. En etablerad kommunikationskanal är

giltig så länge kanalen inte ändrar sig. Eftersom det handlar om mobila enheter behöver man därför skicka nya pilotsignaler ungefär lika ofta som i dagens avancerade 4G-system system (d.v.s. med millisekundintensitet).

Det faktum att varje terminalantenn i systemet behöver skicka pilotsignal är specifikt för MaMi system och påverkar hur terminalerna måste konstrueras. Till skillnad från dagens terminaler, anpassade för 4G, måste varje antenn i en terminal nu ha tillgång till både sändare och mottagare för att kunna delta i kommunikationen på ett effektivt sätt. Fler antenner i terminalen kommer att öka storleken och antalet sändare/mottagare kommer att öka priset. Det vill man så klart undvika och olika alternativ har därför undersökts i mitt arbete. Eftersom det är terminalen som skickar pilotsignaler får den en viss frihet att bestämma vilken kommunikationskanal basstationen kommer att se. Denna frihetsgrad utgör en stor del av min forskning. Olika algoritmer är undersökta och hur väl de presterar jämfört med optimala lösningar.

För att genomföra undersökningarna har ett simuleringsramverk utvecklats. Ramverket bygger på att uppmätta antenndiagram importeras till simulatorn, vari de belyses med simulerade elektromagnetiska fält som anpassats för att efterlikna det fält en terminal typiskt upplever i ett MaMi system. I korthet kan en ideal MaMi basstation, när den känner kommunikationskanalen, skicka energi utefter alla utbredningsvägar på ett sätt så att alla signalerna vid terminalantennen sammanfaller konstruktivt. Detta innebär att varje utbredningsväg bidrar med en elektromagnetiska våg som ligger i fas med övriga elektromagnetiska vågor samt att varje våg är polarisationsanpassad till terminalantennen i respektive riktning. I simuleringsramverket väljer man: (1) antal utbredningsvägar (s.k. kluster), (2) öppningsvinkel för klustren (hur mycket av terminalen som belyses i respektive riktning) och (3) en klusterstyrkefördelning. Simulatorn slumpar sedan ut belysningsvinkel och klusterstyrka på klustren för att generera olika kanalrealiseringar. Genom att generera ett stort antal kanalrealiseringar kan man få statistiska mått på förväntad prestanda i olika miljöer som bestäms av parameterinställningarna.

Simuleringsramverket kan användas till att optimera prestandan på en terminalantenn avsedd för ett MaMi system genom att välja lämplig algoritm och tillhörande radiolösning. Man kan även jämföra olika antennimplementationer eller studera kanalbeteenden. Dessutom har de olika algoritmerna implementerats i en realtids test basstation, Lund University Massive MIMO (LuMaMi), tillsammans med terminalprototyper med multipla integrerade antenner. Ändamålet med realtidsmätsystemet är för att validera simuleringarna och kalibrera parameterinställningarna för olika miljöer.

Min forskning visar att alla antenner måste vara kapabla att skicka en pilotsignal i ett MaMi system. Detta påverkar såväl systemarkitekturen, där resurser måste finnas för detta, som hårdvarulösningarna i terminalerna. Vi-

dare visar den att klassiska isotropiska antennprestandaparametrar inte ger en rättvis bild på den prestanda man kan vänta sig i ett MaMi system.

För att tillgodose kommande behov för trådlös kommunikation har det visat sig att man måste använda även högre frekvenser. Speciellt millimetervåg band är av intresse på grund av tillgängligheten av stora lediga frekvensområden. För att konstruera kommunikationssystem vid dessa frekvenser, med samma tillförlitlighet och servicekvalitet som dagens system, behövs kunskap om den elektromagnetiska utbredningskanalen. För att mäta dessa egenskaper har en 28 GHz kanalmätutrustning tagits fram. Kanalmätutrustningen kan mäta signaler med extremt hög tids och vinkel noggrannhet. På 326 ms kan 256×128 antennelement mätas, vilket är tio gånger fortare än gängse system.

Tanken är att 28 GHz-kanalmätsystemet ska användas för att göra högupplösta mätningar av utbredningskanaler för millimetervåg frekvenser. Resultaten från mätningarna ska sedan användas som grund för att ta fram kanalmodeller som möjliggör simulering av positionering och mobila situationer som ännu inte är inkluderade eller är baserade på antaganden i de modeller som används i standardiseringsarbete.

Popular Scientific Summary

The immense growth in wireless communications has led both to the overloaded spectrum and growing energy consumption. Predictions suggest that the traffic will continue to increase while, at the same time, the number of connected devices is envisioned to increase. To this end, a paradigm change is necessary, both at the network and at the terminal side, to build systems where each device, which may be anything from a car to a thermometer, attain internet access, potentially with rates of 10 Gb/s or more. Fifth-generation communication systems (a.k.a. 5G) targets those challenges. One of the many techniques that are being investigated to meet the challenges is the so-called massive MIMO (MaMi). The idea behind MaMi is to increase the number of base station (BS) antennas until the system throughput reaches a state where it does not improve even tough more antennas are introduced. More antennas improve the spatial resolution and enable the BS to focus the energy in different directions and serve more terminals at the same time, using the same carrier frequency. Recent literature has shown that in contrast to today's systems, approximately 100 antennas at the BS has the potential to provide an order of magnitude improvement in system capacity and energy consumption.

Almost all of the work on MaMi has been done on the BS side, and naive assumptions are made on the terminal structure, failing to rigorously evaluate the true potential of MaMi. It is important to know that the measured performance gains of MaMi hinge on the optimality of the terminal design at the physical layer. This thesis aims to identify the cautionary tales into the impact of such simple assumptions on the overall MaMi system performance.

To utilize each of its antennas optimally, the BS needs complete knowledge of the electromagnetic propagation conditions. Each terminal needs to transmit a predefined waveform, a.k.a. pilot. The pilot is received by the BS antennas, enabling it to simultaneously focus the desired signals to each terminal. The established communication channels are only valid for as long as the electromagnetic propagation conditions stay constant. To enable mobility, pilot signals, therefore, need to be re-transmitted in a MiMo with approximately

with the same rate as used in today's long term evolution-advance (LTE-A) 4G systems, i.e. millisecond rate.

The above-mentioned aspects naturally impact the way mobile terminals are designed for MaMi systems. Contrary to terminals of today, designed for LTE-A system, each antenna of the terminal needs to be able to both transmit and receive signals modulated at the desired carrier frequency, to utilize the available capacity. Increasing the antenna count in a terminal will naturally impact its size and, increasing the number of transceivers result in higher operational cost. The two conflicting requirements are investigated in the thesis and different solutions have been proposed to identify and achieve the optimal trade-off design for MaMi terminals. As it is the terminal that transmits the pilot signals, it has some degree of freedom to decide what transmission channel the BS sees. This degree of freedom is a large part of my research. Different algorithms have been investigated and how well they perform compared to optimal solutions.

To perform the investigations, a simulation-framework has been developed. The framework uses measured terminal antenna gain-patterns, which, are illuminated by simulated electromagnetic (EM) fields, designed to emulate the fields expected from a real MaMi system. In principle, a MaMi system with full channel knowledge is capable of simultaneously transmitting signals along multiple paths, so that the received signals at the terminal adds up coherently. This means that the signal contributions from different propagation directions are in phase and aligned with the polarization of the terminal antenna, for the respective direction. The advantage of the developed simulation framework is its simplicity while being able to retain a high level of accuracy. To this end, only three parameters are needed: (1) the number of propagation directions (clusters); (2) the angular spread of the clusters (how much of the antenna is illuminated by a cluster); and (3) a cluster strength distribution. Illumination angles and cluster strengths are then randomly set to generate realizations. By generating a large number of such realizations, average performance can be computed for typical settings of the three parameters, that mimic different environments.

The simulation-framework is a tool that can be used for performance optimization of terminals intended for MaMi systems. By selection of appropriate algorithms, the performance of the terminals (antennas and transceivers) can be evaluated. An important conclusion from this study is that classical antenna performance parameters do not give a fair view of how an antenna configuration performs in a MaMi system.

Besides, the various algorithms have been implemented in the real-time Lund Massive MIMO testbed (LuMaMi) together with prototypes with multiple integrated antennas. The main purpose of the real-time test capability is to

validate the simulation tool and calibrate the parameter settings for different environments.

My research shows that a significant part of the achievable performance depends on the terminal antennas and that increasing the antenna count also at the terminal side will improve the figures. My results also show the importance of using realistic, integrated antenna-implementations at the terminal side during the design of MaMi systems.

To meet the future demands in wireless communications also higher frequencies need to be deployed. In particular millimeter-wave (mmWave) bands are proposed due to large chunks of available bandwidths. Nonetheless, to successfully realize cellular systems at such high frequencies with reliability and quality-of-service comparable to today's networks, knowledge of the involved propagation mechanisms is mandatory. To this end, a 28 GHz channel measurement system (a.k.a. channel sounder) is developed to characterize the channel properties. The sounder facilitates temporal and spatial tracking of parameters with extraordinary angular and delay resolutions. Using 256×128 antenna elements a total measurement time of 326 ms is achieved, providing an order of magnitude reduction in the run time.

The idea is that the 28 GHz channel sounder shall be able to perform measurements of dynamic propagation channels at mm-wave frequencies. The results can then be used as a base for the derivation of improved propagation channel models. Mainly for accurate positioning and mobility predictions, which, are areas not covered or are based on assumptions in present simulation models used in the standard.

Abstract

This thesis focuses on the terminal aspects of massive MIMO systems (MaMi). Based on the degree of freedom a terminal has in a MaMi system, different antenna configurations, transceiver topologies with associated transmission schemes, and algorithms are investigated.

The first studied topic concerns multiple-antenna terminals in a MaMi system for sub-6 GHz operated at the center frequency of 3.7 GHz. Terminals designed for today's LTE-A systems can be used in massive MIMO systems. They will, however, not be able to utilize the full potential of the system. The main limitation is that it is not mandatory to have transmitting capability at all antennas in an LTE-A terminal. For a MaMi system, this is a necessity for any diversity or multiplexing scheme. From a terminal-antenna perspective, there is no major difference, while it is of importance to use real integrated antennas in the evaluation of different transmission schemes in a MaMi system. Therefore, multi-antenna terminal prototypes with integrated antennas, based on real Sony Xperia smartphone chassis where designed. The three-dimensional antenna gain-patterns were characterized in an anechoic chamber to ensure that simulations and real-time measurements can be based on the very same antenna properties.

With a zero-forcing precoder at the BS side, classical diversity schemes (i.e., switched diversity, dominant eigenmode transmission, and passive diversity), as well as multiplexed operation (with and without diagonalization precoder at the BS), were investigated.

Simulation environments based on fully-stochastic, as well as geometric-stochastic propagation models, have been developed. The simulated results have been compared to measured results using the Lund University Massive MIMO (LuMaMi) testbed. To enable evaluation of multi-antenna terminals and different transmission schemes, modifications to the LuMaMi framework were necessary. In particular, real-time diversity schemes for dual antenna terminals, as well as a channel capturing feature have been implemented. The latter enables the analysis and post-processing of measured channels from the

multi-antenna terminals.

The second topic in this thesis relates to mm-wave MaMi systems. As a first step toward evaluation of handsets, a 28 GHz channel sounder has been developed for high-resolution measurements of dynamic propagation channels, in both temporal and spatial domains. To facilitate the measurements, a 256×128 antenna-element system was designed together with a control program to handle the switching and the enormous amount of data.

Preface

This thesis completes my work as an industrial Ph.D. student from Sony Mobile Communications (later Sony Research Center, Lund), with the academic collaboration partner Lund University, Department of Electrical and Information Technology (EIT). Besides improving my research capability, the ambition with this Ph.D. was to tighten the link between Sony and the University, to make Sony a part of the research performed at the university, and to ensure the research quality at Sony. In general, I have been responsible for the progress of the research topics. However, most of the work has been carried out in collaboration with supervisors and colleagues at EIT and Sony. The thesis comprises two parts. The first part gives an overview of the field which I have been researching during my Ph.D. studies where I briefly summarize my contributions to it. The second part is a collection of seven papers, listed below, on which I am the lead author that constitute contributions to the area:

Paper I:
E. L. Bengtsson, F. Tufvesson, O. Edfors, "UE Antenna Properties and Their Influence on Massive MIMO System Performance" *in Proc. of the 9:th European Conference on Antennas and Propagation (EuCAP)*, Lisbon, Portugal, Apr. 2015.

Paper II:
E. L. Bengtsson, P. C. Karlsson, F. Tufvesson, J. Vieira, S. Malkowsky, L. Liu, F. Rusek, O. Edfors, "Transmission Schemes for Multiple-Antenna Terminals in Massive MIMO system" *in Proc. of GLOBECOM 2016*, Washington DC, USA, Dec. 2016.

Paper III:
E. L. Bengtsson, F. Rusek, S. Malkowsky, F. Tufvesson, P. C. Karlsson, O. Edfors, "A simulation Framework for Multiple-Antenna Terminals in Massive MIMO Systems" *IEEE Access*, Vol. 5, pp 26819-26831, 2017.

Paper IV:
E. L. Bengtsson, F. Rusek, F. Tufvesson, P. C. Karlsson, O. Edfors, "Analysis of Transmission Schemes for Dual-Antenna Terminals in Massive MIMO Systems" *in Proc. of the 25:th International Conference on Telecommunications (ICT2018)*, Saint Malo, France, Jun. 2018.

Paper V:
E. L. Bengtsson, F. Rusek, P. C. Karlsson, F. Tufvesson, O. Edfors, "Simulation of Multiple-Antenna Terminal Performance in Massive MIMO Systems based on Indoor Measurements" *Accepted for publication with miner revision, in IEEE Transactions on Vehicular Technology (TVT)*, 2019.

Paper VI:
E. L. Bengtsson, J. Flordelis, F. Rusek, P. C. Karlsson, F. Tufvesson, O. Edfors, "A Case Study on the Influence of Multiple Users on the Effective Channel in a Massive MIMO System" *submitted to Wireless Communications Letters (WCL)*, 2019.

Paper VII:
E. L. Bengtsson, H. Tataria, P. C. Karlsson, O. Edfors, F. Tufvesson, "A 28 GHz Channel Sounder for Dynamic Propagation Measurements" *to be submitted to IEEE Transactions on Wireless Communications*, 2019.

Acknowledgements

Taking the challenge of becoming an industrial Ph.D. student is one of the best decision in my career. It has enriched me from a scientific as well as from a social perspective. As much as I like personal challenges, I am aware that the success of them rarely depends on a single person.

I would like to thank my supervisors: main supervisor Professor Ove Edfors, for inspiring me and guiding my research in a captivating direction, and for the review of my numerous text-iterations almost without complaints; my manager at Sony and co-supervisor Dr. Peter Karlsson, for giving me the opportunity to become an industrial Ph.D. student, for being involved in my research, and for ensuring that the outcome of my research has a connection to the real world; co-supervisor Professor Fredrik Tufvesson, for being engaged in my research, reviewing my publications, and for plenty of technical discussions; Associate Professor Fredrik Rusek, neighbor at home, colleague at Sony, and co-supervisor at the University, for increasing the scientific level of my work, for instantaneous tireless feedback on my publications, and for countless technical discussions.

I also want to thank all my colleagues both at EIT and at Sony. I restrict myself to mention those who have been directly involved in my research during my time as an industrial Ph.D. student. Dr. Joao Vieiera, Dr. Steffen Malkowsky, and Sara Gunnarson at EIT, for being there with me in the LabView jungle making LuMaMi great; Dr. Harsh Tataria at EIT, for your dedication in the mm-wave related research and for your contributions to the publications; Erik Jonsson and Martin Nilsson at EIT, for making sure that everything actually works in the end; Thomas Bolin at Sony, for help with prototyping and supplier orchestration; Ying Zhinong, and Dr. Kun Zhao at Sony, for antenna design-work and simulations.

Last but not least, I would like to thank my family. Rebecca, my beloved wife and my lovely children Johanna, Elsa, and Albin, for supporting me with their unconditional TLC on my path becoming Dr. Bengtsson.

List of Acronyms and Abbreviations

2D Two-Dimensional

3D Three-Dimensional

3GPP Third Generation Partnership Project

5G Fifth Generation Wireless Communication

ADC Analog to Digital Converter

AoA Angle of Arrival

AoD Angle of Departure

BD Block Diagonal

BF Beam-Forming

BHHL Beside Head with Hand Left side

BHHR Beside Head with Hand Right side

BS Base Station

CCG Combined Coherent Gain

CDF Cumulative Distribution Function

CNG Combined Non-Coherent Gain

CSI Channel State Information

CSI-RS CSI Reference Signal (i.e. DL pilot)

DAC Digital to Analogue Converter

DEM Dominant Eigenmode

DL Downlink

DPC Dirty Paper Coding

DRAM Dynamic Random Access Memory

EG Effective Gain

EIT Department of Electrical and Information Technology

EM Electro-magnetic

ECC Envelop Correlation Coefficient

FDD Frequency-Division Duplex

FDMA Frequency-Division Multiple Access

FEM Front-End Module

FOM Figure of Merit

FR1 Lower frequency range 450-7125 MHz (sub-6)

FR2 mm-wave frequencies spanning 24250-52600 MHz

FPGA Field-Programmable Gate Array

FS Free-Space

HW Hardware

i.i.d. independent and identically distributed

IL Insertion loss

LH Left Hand

LOS Line-of-Sight

LTE Long Term Evolution

LTE-A LTE-Advanced

LNA Low Noise Amplifier

LuMaMi Lund University Massive MIMO

MaMi Massive MIMO

MEG Mean Effective Gain

MIMO Multiple-Input Multiple-Output

MR Maximum-Ratio

MRC Maximum-Ratio-Combining

MRT Maximum-Ratio-Transmission

MU Multi-User

MUX Multiplexing

NR New Radio

OFDM Orthogonal Frequency-Division Multiplex

PA Power Amplifier

PD Passive Diversity

PCB Printed Circuit Board

PIFA Planar Inverted F-Antenna

PD Passive Diversity / Passive Receive Diversity

RB Resource Block

RH Right Hand

Rx Receive

SC Sub-Carrier

SDMA Space-division Multiple Access

SINR Signal-to-Interference-and-Noise Ratio

SNR Signal-to-Noise Ratio

SP4T Single Pole Four Throw

SA Single Antenna

SRS Sounding Reference Signal (i.e. UL pilot)

SSF Stiftelsen för Strategisk Forskning

SVD Singular Value Decomposition

SW Software

SWD Switched Diversity

TDD Time-Division Duplex

TDMA Time-Division Multiple Access

TE Total Efficiency

TH Tomlinson-Harashima

TLC Tenderness Love and Care

TRP Total Radiated Power

Tx Transmit

USRP Universal Software Radio Platform

UE User Equipment

UL Uplink

UP Unit Power

ZC Zhadoff-Chu

ZF Zero-Forcing

Contents

Part I

Introduction to the Research Topics

Chapter 1

An Overview of Massive MIMO

The purpose of this chapter is to relate our research to a larger context, to make the publications more attainable.

The electromagnetic spectrum is a limited natural resource. It is therefore of interest utilizing it as efficiently as possible. Different approaches to improve spectral efficiency have different pros and cons. Increasing the constellation size of the modulation is an approach that benefits terminals close to a BS as it requires strong signal levels. Densification, where the BS density is increased, can then be used, but it increases the cost of the system and is in many cases not possible from aesthetic or for practical reasons. A different approach is to increase the number of antennas at each base station (BS). The work in this thesis relates to systems targeting large numbers of antennas at the BS with a focus on investigating how this influences the terminal design.

While any system with a large number of antennas at the BS side can be identified as a massive multiple-input-multiple-output (MIMO) system, in the main part of this chapter, we revert to the original definition. massive MIMO (MaMi) was first proposed in 2010 [1], and have ever since been the topic of intensive research, e.g. [2–6], and recently books on the topic have been published, e.g. [7, 8]. More than 50,000 hits, from a search on the term "massive MIMO" on Google scholar, indicates its popularity.

The design and implementation of MaMi precoding at the BS side is a large and well-researched area and not the main topic of this dissertation. We give

an introduction to a MaMi system, the consequences it has on the *effective*[1] propagation channel, and how the terminal can influence the situation. In this chapter, we start our discussions from a generic MIMO perspective before we detail how a sub-6 GHz MaMi system works. We continue with an analysis of the terminal aspects before we motivate why there is a need to also study higher frequencies.

1.1 Acquiring Channel State Information in MIMO Systems

For efficient wireless communication, a system needs to have some knowledge about the wireless propagation channel. Here, we introduce some generic aspects of how this is done in classical MIMO systems before we scale up the number of BS antennas and investigate the consequences it has.

In general, for a communication system with M transmit antennas and N receive antennas the capacity of a wireless channel is in terms of maximum number of spatial streams, limited by $\min(M, N)$. The achievable rate is, in turn, determined by the amount of channel state information (CSI) that can be acquired by either side. CSI, in the context of a narrowband[2] channel, is simply the magnitude and phase of the transfer function, between a transmit and receive antenna pair.

The CSI can be acquired from a pilot signal[3] transmitted from an antenna. The pilot signal is an apriori known signal that without loss of generality can be assumed to be unity. By transmitting independent pilots (in different resource elements in a time-frequency grid) from each of the antennas, at one side of the communication link, and receiving each of them with all antennas at the other side, full CSI can be acquired at the receive side. If full CSI is needed at both sides, pilots may have to be transmitted in both directions[4]. From this, one can understand that for systems with large numbers of antennas, potentially at both sides, it may result in a large number of pilot transmissions.

Most systems of today operate in wide frequency bandwidths and use orthogonal frequency division multiplex (OFDM). OFDM allows the desired frequency band to be divided into independent sub-carriers (SC), where the re-

[1] The effective propagation channel is the part of the available physical propagation channel that is indeed used for transmissions and is a result of the precoding/receive-combining. [2] A narrow-band signal is a reasonable assumption as we assume orthogonal frequency-division multiplexing (OFDM), which is the dominating technique among modern systems. [3] The pilot signal is often implemented using a Zadoff-Chu waveform [9, 10], based on its autocorrelation, flat frequency, and time signature properties. [4] To approach the capacity of a link the eigenmodes of the channel needs to be addressed, this requires CSI at both ends. Note that CSI may also be shared through a control channel.

ceived signal within each SC can be treated as a narrow-band channel. Naturally, the validity of a particular instance of CSI is constrained to a limited bandwidth, i.e., the so-called coherence bandwidth. The total BW is often divided into so-called frequency resource blocks, where each resource block has associated resource-elements for pilot signals. The coherence bandwidth, $\mathrm{BW_c}$, is approximately given by the length of the impulse response, T_m, of the propagation channel, or more precisely the delay spread [11],

$$\mathrm{BW_c} \approx \frac{1}{T_m}. \tag{1.1}$$

Equivalent constraints on CSI validity apply in the temporal domain, where the coherence time governs the duration after which pilot signals need to be re-transmitted. Similarly, the coherence time, T_c , is approximately given by the Doppler spread B_d [11],

$$T_\mathrm{c} \approx \frac{1}{B_d}, \tag{1.2}$$

which, depends on the relative velocity, v, and the frequency of operation, f_0 between the transmit and receive side antennas [11],

$$B_d = \frac{3}{2\pi\sqrt{1-\frac{v^2}{v_{\max}^2}}} \text{ for } |v| < v_{\max}, \tag{1.3}$$

where $v_{\max}$ is the maximum velocity present in the scenario. In the time-frequency domain, the coherence time and coherence BW define a coherence block. Based on assumptions around channels, an upper frequency, and a maximum velocity a maximum size of a coherence block can be defined. In most deployed systems the coherence blocks are statically defined and e.g. in the case of long-term evolution (LTE), a so-called resource block, limited in both time and frequency domains consists of 84 resource-elements, which sets a practical limit on how many pilots that can be transmitted. Assuming that we intend to transmit some payload data, we cannot use all resources for pilot transmissions. To give an example, a typical 2×2 MIMO system with two antennas at each side needs[5] four pilots, two in each direction, to be transmitted to get access to full CSI at both sides. Fig. 1.1 shows a resource-grid where each resource-block have four associated pilot resources. With this in mind, we need a different strategy for CSI acquisition in systems with hundreds of antennas or more.

[5] If reciprocity is assumed the CSI can also be shared over a control channel.

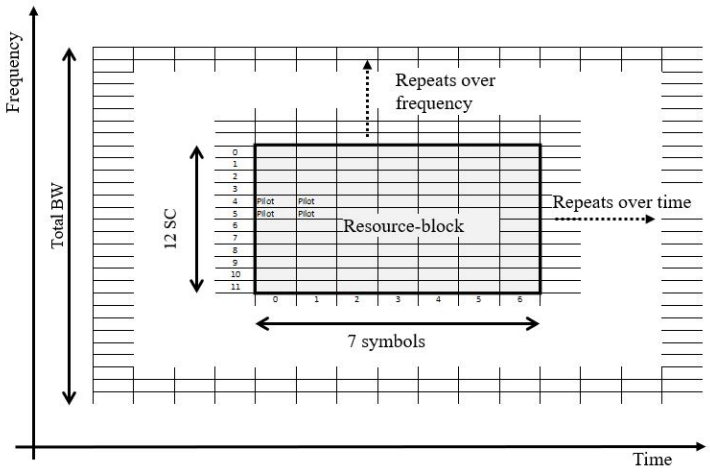

Figure 1.1: Symbolic example of a resource grid with pilot allocation in a resource block.

1.2 Operational Aspects of Large-Scale Antenna Systems

To obtain a consistent definition of our MaMi system, we will first make a few distinctions between alternative technologies. In this section we start with a definition of beam-forming (BF), before we disclose the pilot transmission strategy used by massive MIMO systems. We detail the consequences the pilot transmission strategy has on the effective propagation channel, and how this influences a terminal. We introduce a signaling-model for multi-antenna terminals, in a MaMi context, which lays the ground for the further discussions and relates to our implementations, both for a real-time testbed and in various simulations environments.

1.2.1 Beam-Forming

Beam-forming (BF) relates to the capability multiple antennas have to shape a combined effective gain-pattern. This is achieved by the manipulation of the phase and the amplitude of the signals fed to each antenna. In its most simple form, a.k.a. a phased array, multiple antenna elements with the same antenna gain patterns are fed with signals having constant phase-shifts which are proportional to the distance between the elements. The effective gain-

pattern then takes the shape of a beam with a gain and a width that depend on the number of antenna elements. To this end, with an increasing number of antennas, one can obtain higher gain and consequently a narrower beam-width. Furthermore, a larger phase-shift increases the directive angle from the array.

In the more general case, the effective gain-pattern can take various shapes, limited by the gain patterns of the antenna elements and the shape of the antenna structure. Increasing the number of antenna elements enables a larger degree of freedom to shape the effective-gain-pattern.

Rather interestingly, BF can be implemented in various domains of a cellular communication system. Analog and digital BF are the two variants we discuss here[6]. Operations for transmitting and receiving are the same but to keep it simple, we describe the transmit side only. Analog BF can be achieved through phase shifters and variable gain amplifiers, as shown on the left-hand side in Fig 1.2. The term DAC in the figure denotes digital to analog converter and FEM denotes front-end module, where the latter includes power amplifiers and frequency converters. The limitation with analog BF is that the phase shifters and variable gain amplifiers only can have a single value at the time. This means that only a single beam, corresponding to a single stream of data can be generated for transmission, heavily limiting the system performance and limiting the gains offered by space-division multiple access (SDMA). Besides, the operational bandwidth of the array becomes limited to that of the analog components. The main advantage with the analog BF, compared to the digital case, is the simplicity and the lower cost.

On the other hand, digital BF means that there are a FEM and a DAC associated with each of the antenna elements. This enables each antenna element to transmit independently. It can be shown by the superposition of the wave-fronts principle(e.g. [13]), that a digital BF network can transmit multiple independent signals in different beams, simultaneously. The architecture for a digital transmit BF is shown on the right-hand side in Fig 1.2.

A receiver with digital BF can obtain spatial directive gain by post-processing received signals. This enables the receiver to acquire full CSI from a single received pilot signal transmitted from an antenna, which is not possible with an analog BF.

1.2.2 Massive MIMO

In this subsection, we discuss the strategies related to pilot transmission in a MaMi system for acquiring CSI and specify the requirements that are necessary for a MaMi system to operate.

[6] There is also hybrid BF [12] but in this section, we intend to highlight some fundamental aspects of BF and therefore we leave it out.

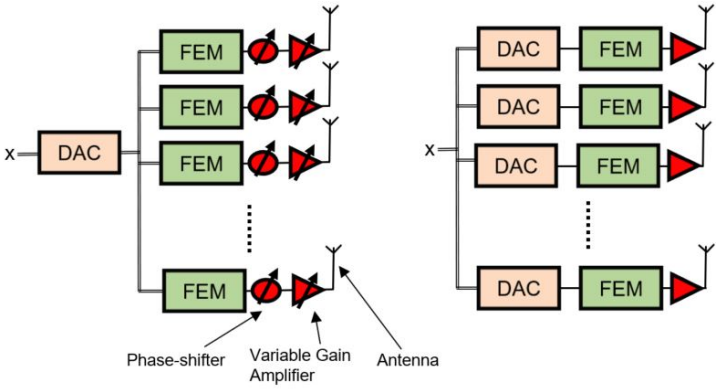

Figure 1.2: Different BF architectures, analog BF to the left and digital BF to the right.

To enable BF in either the analog or digital domains, we need to estimate the CSI, and for this, we need methods to acquire the channel between all receive and transmit antenna-pair combinations. If the CSI between a BS antenna and a terminal antenna is the same at both sides, the channel is said to be reciprocal. With uplink (UL) being signals transmitted by the terminal and received by the BS and downlink (DL) the opposite, reciprocity implies that the CSI attained from UL pilot signals is also valid for DL signaling. This enables a BS, with digital BF, to gain access to full CSI for all of its antennas for both UL and DL transmissions based on a single UL pilot transmission per terminal antenna. As the coherence bandwidth is limited, systems that rely on reciprocity require the UL and DL to share the same frequency band. This is the case in time-division duplex (TDD) and full-duplex systems[7].

From the discussions above, the system that we refer to as a MaMi system can be summarized as:

A TDD system for aggressive spatial multiplexing, where the BS uses fully

[7] Large research efforts has been put on MaMi for frequency-division duplex (FDD) systems, e.g. [14–16], where the UL frequency band is separated from the DL band (a.k.a. paired frequency bands). The approach for acquiring CSI is then different as pilots need to be transmitted in both directions. This is, however, not a topic for this thesis. The achievable performance is worse compared to that of TDD MaMi systems, and the effective channel, seen by the terminals is similar to one obtained from e.g. classical MIMO systems. From our research perspective, it is, therefore, less interesting as it has little impact on the terminal design. The motivations behind FDD based MaMi systems are mainly that they are backward compatible with the conventional FDD MIMO (4G) systems deployed globally where large parts of the spectrum are paired.

digital BF, with at least 100 antennas at the BS side. The BS uses channel reciprocity-based precoding based on UL pilot symbols.

If the terminal antennas can be assumed to radiate isotropically, it will enable the BS to see all available radio frequency channels based on a single pilot transmission. No matter how the terminal is oriented or its mobility, as long as there is a pilot signal transmitted within each coherence block, the BS can acquire full CSI and transmissions of user data can take place.

The assumption of having isotropic radiation patterns at the terminal antennas sets a practical upper limit in frequency to about 6-15 GHz and, often, a distinction between sub-6 GHz systems and mm-wave systems is made (e.g. FR1 and FR2 in [17]). The smaller antenna aperture at higher frequencies increases the path loss and therefore, the total number of antennas in the system needs to be scaled up. To keep the antenna count, complexity, and power consumption reasonable at the BS side, array antennas are introduced also at the terminal side to achieve a strong channel (i.e. reasonable SNR at the receive side and a realistic power level at the transmit side). This causes the antenna gain-patterns at the terminal side to be beam shaped and transmission strategies where combinations of predefined beams from each side, that together give a strong channel, are identified (a.k.a. beam pairs). This is a large part of the new radio (NR) standard defined in [17] but does not apply to the MaMi systems we are discussing in this part of the thesis.

1.2.3 The MaMi Influence on the Effective Channel

We need to understand some important physical mechanisms of a propagation channel to understand the influence the massive number of antennas at the BS side have in combination with the UL pilot based precoding, on the effective channel, as seen by a terminal.

Fading relates to the variation in signal strength and phase a terminal may experience. Fading can be characterized as either small-scale or large-scale, respectively [18]. The small-scale fading originates from signals that arrive and are combined at the antenna with random phases, corresponding to the different multipath detours they take, shown in Fig 1.3. This gives a signal strength variation that depends on whether the signals add constructively or destructively. The small-scale fading depends heavily on the geometry and by changing the position of either side of the link, or a scatterer, by just a fraction of a wavelength, the conditions will change. In contrast, large-scale fading is a much slower process that relates to shadowing and attenuation caused, e.g., by large objects in the environment and user interactions with terminal antennas. The large-scale fading typically behaves the same over a wide frequency range.

With a large number of antennas in a MaMi BS, the spatial resolution en-

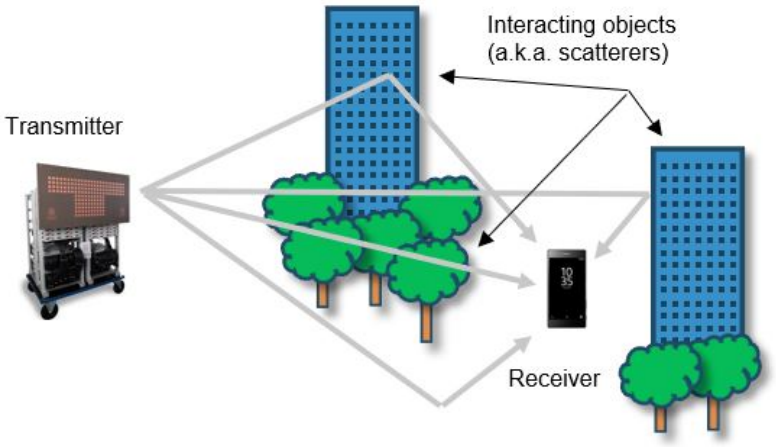

Figure 1.3: Terminal exposed to signals along multiple propagation paths.

ables separation of signals propagating along different propagation paths. The digital BF at the BS will then be able to make sure that signals combine coherently (i.e., constructively). In UL, signals along different propagation paths are coherently combined in the BS. While, in DL, signals along different propagation paths are transmitted with appropriate delays to reach the terminal antennas coherently.

The coherent combination of signals from all antennas results in the following key properties of a MaMi system:

- The small-scale fading, ideally, vanish. Its absence, as the number of antennas at the BS grows larger stabilizes the effective channel. This is known as the *hardening* effect [3] and gives the effective channel deterministic properties rather than the highly random properties typically present in the conventional MIMO systems.
- Full array gain can be obtained also in scattered scenarios which is not the case in systems with codebook based precoder e.g. if analog BF is used.
- The isolation between channels carrying different streams, that are using the same time/frequency resources, increases and we can exploit spatial multiplexing of terminals/antennas to increase the spectral efficiency.

It can be noted that for multiplexed operation in a MaMi system, the BS needs to schedule dedicated pilot resources associated with each data stream. The information carrying resources can then be used by all the multiplexed entities simultaneously.

1.2.4 BS Precoding

Classical MIMO precoding and decoding is a complex matter, where the computational complexity at the baseband grows prohibitively with the number of antennas/multiplexed channels. Non-linear approaches such as dirty paper coding are to be optimal. However, due to the stringent constraints on CSI accuracy, as well as their implementation complexity, such techniques have not been able to be effectively implemented. In stark contrast to this, with the increase in the number of BS antennas, MaMi systems can approach capacity with "linear" precoding after estimating the channel in low mobility scenarios [19]. With linear processing, the complexity scales linearly with the number of antennas and multiplexed channels at the BS.

To exploit all MaMi properties listed in Section 1.2.3 with linear processing, it has empirically been shown that there is a need for five to ten times more antennas at the BS side than the total number of streams that are sharing the same resources [4, 19, 20]. The number of BS antennas needed to approach optimal performance with linear processing is further discussed in e.g. [4, 21], but this is not in the exact scope of this thesis. The BS may use different linear precoders/combiners when it processes the signal, e.g. zero-forcing (ZF), minimum mean squared error (MMSE), maximum ratio combining(MR). One of the more popular techniques is ZF, which have shown promising performance in practical implementations [4, 19, 22, 23]. At high to moderate SNRs, ZF improves the isolation between the terminal antennas and keeps the signal level constant at each of them, also from a large-scale fading perspective. ZF is a linear operation but requires the BS to compute a pseudo-inverse[8] of the full channel matrix. MR is the most straight forward technique and facilitates per-antenna processing and does not require full CSI information from all channels to be co-processed.

The work in this thesis includes both MR and ZF precoder/combiner. The reason is that they give the same effective channel for the single-stream scenario [24] and since the MR technique offers lower complexity in the mathematical derivations, we have used it when possible.

[8] The computation of the pseudo-inverse scales somewhat faster than linear. This, however, has negligible impact for the scales that are relevant for a MaMi system [4].

1.2.5 Terminal Aspects

With all the nice properties offered by the MaMi system it may not be obvious what the terminal can do, or perhaps, needs to do to fully take advantage of them. Despite large research efforts in the MaMi area, only a handful of publications that relate to the terminals in a massive MIMO system are available, e.g. [25, 26]. The main reason for this is that a terminal in a MaMi system is mostly assumed to have a single antenna with omnidirectional (i.e. isotropic) radiation properties. A single pilot transmission will then always enable the BS to acquire full CSI. Full CSI is not needed at the terminal side, and all the MaMi specific properties can be related to the BS side.

Besides the small-scale fading, which ideally vanish in a MaMi system, a wireless communication channel also experiences large-scale fading. Large-scale fading is often compensated for by increasing the power or by transmission redundancy, which are expensive ways of dealing with the problem in particular for battery-powered terminals. Besides, handset antennas are typically integrated into the device which makes it difficult to avoid user interaction. This causes loading, which constitutes a significant part of the large-scale fading.

A more efficient approach to mitigating large-scale fading is to use multiple terminal-antennas. To exploit terminal antenna diversity in conventional MIMO systems a terminal can directly acquire CSI from DL pilot signals[9], and select a diversity scheme based on that. As the small-scale fading is present in conventional MIMO systems the CSI needs to be averaged over time to address the large-scale fading. Consequently, the fundamental performance of terminal antennas at the physical layer is typically specified with the statistical and isotropic figure of merits (e.g. antenna envelope correlation, antenna efficiency, etc.). While this is sufficient for evaluation of conventional MIMO systems where transmission schemes based on statistical approaches are optimal due to the presence of the highly random small-scale fading, they cannot accurately predict the performance of a MaMi. The main reason is the capability of a MaMi BS to manipulate the effective propagation channel in a way so that it behaves deterministically. The statistical assumptions become obsolete and the actual directional properties need to be taken into account.

In a MaMi system, similar diversity schemes as for conventional MIMO systems can be implemented, with the difference that the effective communication channel is defined by the UL pilots. The best diversity scheme for transmissions of data is, therefore, always the same as the one that was used during the pilot transmission. To decide on the best diversity scheme and use it for both the pilot and the further transmissions, a terminal needs a different strategy

[9] DL pilot signals cannot be made available in a MaMi system as it would require far too many resources to send them from all of the BS antennas, as we discussed in Section 1.1.

to acquire relevant CSI.

1.3 Multi-Antenna Terminals in a Massive MIMO system

In this section, we present the necessary system model to understand how the terminal can acquire relevant CSI without requiring the BS to transmit individual pilot signals from all of its antennas. In a real implementation relevant CSI information can be shared by the BS over a control channel. In our work, this would in some cases be inconvenient and by using a unit-power (UP) MR precoder at the BS, the terminal easily get access to the relevant CSI. In the single stream case, UP-MR precoding results in the very same effective channel as if ZF was used[10] [24]. The idea is that the terminal based on DL signals that are associated with UL pilot transmissions, can compute relevant information about the channel. We also introduce different terminal transmission schemes and relate them to different terminal-antenna properties and terminal-hardware architectures.

1.3.1 System Model and Aquisition of Relevant CSI at the Terminal Side

The received signal within a given OFDM SC at a given time can be represented with a narrowband signal model for multiple-antenna, single stream communication [24, 27, 28]. That is,

$$\boldsymbol{y}_{\mathrm{Rx}} = \boldsymbol{H}\boldsymbol{x}_{\mathrm{Tx}} + \boldsymbol{n}_{\mathrm{Rx}}, \tag{1.4}$$

where

$$\boldsymbol{y}_{\mathrm{Rx}} = \left[y_{\mathrm{Rx}0} \;\; y_{\mathrm{Rx}1} \cdots y_{\mathrm{Rx}K-1}\right]^{\mathrm{T}}, \tag{1.5}$$

is the vector of signals at the feed of K receive antennas, and

$$\boldsymbol{x}_{\mathrm{Tx}} = \left[x_{\mathrm{Tx}0} \;\; x_{\mathrm{Tx}1} \cdots x_{\mathrm{Tx}J-1}\right]^{\mathrm{T}}, \tag{1.6}$$

represents the signals fed to J transmit antennas. Note that $\boldsymbol{H}$ is a $K \times J$ matrix representing the radio channel and $\boldsymbol{n}_{\mathrm{Rx}}$ the noise vector at the receiver. In (1.4),

[10] The difference between UP-MR and ZF, for this case, is a constant equal to the normalized magnitude of the channel. Hence, if we use ZF the terminal does not see the variations caused by the large-scale fading. By using a UP-MR precoder the terminal directly get access to the effective channel and therefore we use it here. In the case ZF is used with multiple terminal-antennas the channel may be extracted from the potentially very small signal at the antennas that did not transmit any pilot signal, this is further discussed in Appendix A.

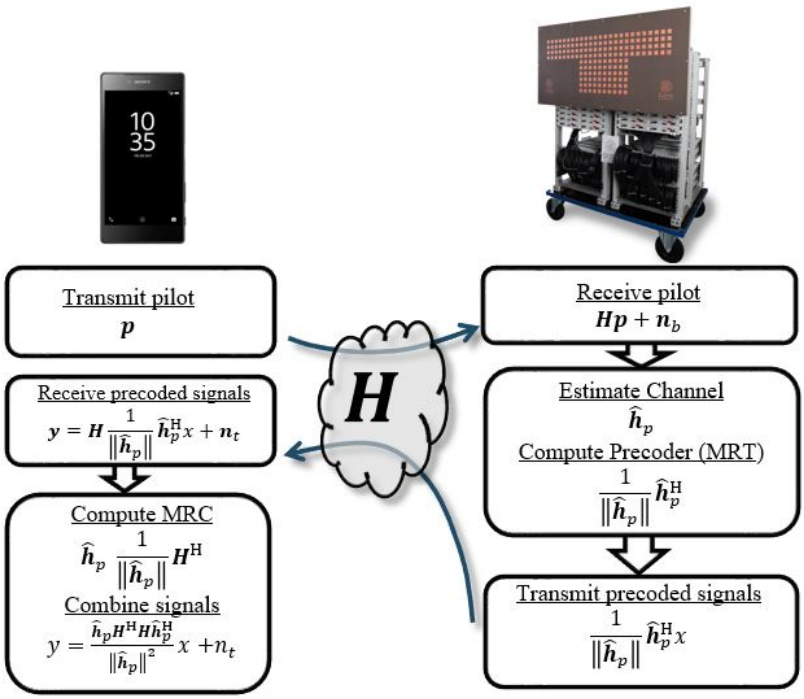

Figure 1.4: Communication model.

each entry h_{kj} in $\boldsymbol{H}$ represents the transfer function from a transmit antenna j to a receive antenna k. These entries include gain and phase properties from the transmit-antenna, the receive-antenna, and the propagation channel, considering all contributions along the different propagation paths. Each entry is represented by a complex number that describes the combined channel gain and phase-delay.

A basic MaMi communication model based on UP-MR processing is shown in Fig. 1.4. The model relates the received DL signals at a multi-antenna terminal to how the pilot signal, $\boldsymbol{p}$, was transmitted. Throughout the thesis, the model has been used mainly in simulations, where the performance of different terminal transmission strategies are evaluated but also in the processing of measured channels.

In the communication model, in Fig. 1.4, the pilot signal $\boldsymbol{p}$ is a weight vector, where the dimensions reflect the number of terminal antennas, K, and

each element defines the complex weight assigned to each of them. As the BS sees the combined pilot signals from all terminal-antennas on each of its receive antennas, transmitted over the channel it can only estimate a one-dimensional sub-space of $\boldsymbol{H}$, which is given by $\hat{\boldsymbol{h}}_{\boldsymbol{p}} = \boldsymbol{H}\boldsymbol{p}$ of size $1\times J$, that depends on the pilot signal.

The optimal way to maximize the received signal at the terminal is to use maximum-ratio-combining (MRC) [27] (a.k.a. matched filtering or conjugate BF). The post-processed received signal at the terminal with a dependency on the UL pilot signal, the BS noise, and the terminal noise is then given by

$$y = \frac{\hat{\boldsymbol{h}}_{\boldsymbol{p}}\boldsymbol{H}^{\mathrm{H}}\boldsymbol{H}\hat{\boldsymbol{h}}_{\boldsymbol{p}}^{\mathrm{H}}}{\|\hat{\boldsymbol{h}}_{\boldsymbol{p}}\|^2}x + n_t, \tag{1.7}$$

where n_t is the processed noise at the terminal side and the BS noise is included as an estimation error in $\hat{\boldsymbol{h}}_{\boldsymbol{p}}$. If we assume perfect channel estimate at the BS side, $\hat{\boldsymbol{h}}_{\boldsymbol{p}} = \boldsymbol{h}_{\boldsymbol{p}}$, we can express the signal-to-noise-ratio (SNR) at the terminal as

$$\mathrm{SNR} = \frac{\boldsymbol{h}_{\boldsymbol{p}}\boldsymbol{H}^{\mathrm{H}}\boldsymbol{H}\boldsymbol{h}_{\boldsymbol{p}}^{\mathrm{H}}}{\|\boldsymbol{h}_{\boldsymbol{p}}\|^2}\frac{1}{\sigma_t^2}, \tag{1.8}$$

where σ_t^2 is the variance of the processed noise at the terminal side.

The terminal has a certain freedom to determine which channel the BS sees based on how it transmits the pilots. More importantly, if the precoder at the BS side is known by the terminal, it can, based on the DL signals associated with pilot transmissions from the individual antennas, estimate the channel inner product, a.k.a. the Gramian. For the two antenna case, the Gramian is given by

$$\boldsymbol{G} = \boldsymbol{H}^{\mathrm{H}}\boldsymbol{H} = \begin{bmatrix} \boldsymbol{h}_0\boldsymbol{h}_0^{\mathrm{H}} & \boldsymbol{h}_0\boldsymbol{h}_1^{\mathrm{H}} \\ \boldsymbol{h}_1\boldsymbol{h}_0^{\mathrm{H}} & \boldsymbol{h}_1\boldsymbol{h}_1^{\mathrm{H}} \end{bmatrix}, \tag{1.9}$$

where $\boldsymbol{h}_k$ is the $1 \times J$ channel vector from terminal antenna k to the J BS antennas. Below, we show how this can be done for an UP-MR precoder at the BS. It is possible to do this for other BS precoders, which we show in Appendix A. The Gramian of a transmission channel carries enough information for the terminal to compute an optimal pilot vector.

For notational simplicity, we limit the number of terminal antennas to two in the following derivation. The principles are the same also for a larger number of antennas. By transmitting pilots $\boldsymbol{p}_0 = [1\ \ 0]$ and $\boldsymbol{p}_1 = [0\ \ 1]$ in different time/frequency resources, the associated received signals are given by the expression

$$\boldsymbol{y} = \frac{\boldsymbol{H}\hat{\boldsymbol{h}}_p^{\mathrm{H}}}{\|\hat{\boldsymbol{h}}_p\|}x, \tag{1.10}$$

i.e. "Received precoded signals" at terminal side in Fig. 1.4. This leads to

$$\begin{cases} \boldsymbol{p}_0 = [1 \;\; 0] \Rightarrow \boldsymbol{y}_0 = \dfrac{\boldsymbol{H}\hat{\boldsymbol{h}}_0^{\mathrm{H}}}{\|\hat{\boldsymbol{h}}_0\|}x = \dfrac{1}{\|\hat{\boldsymbol{h}}_0\|}[\boldsymbol{h}_0\hat{\boldsymbol{h}}_0^{\mathrm{H}} \;\; \boldsymbol{h}_1\hat{\boldsymbol{h}}_0^{\mathrm{H}}]^{\mathrm{T}}x \\ \boldsymbol{p}_1 = [0 \;\; 1] \Rightarrow \boldsymbol{y}_1 = \dfrac{\boldsymbol{H}\hat{\boldsymbol{h}}_1^{\mathrm{H}}}{\|\hat{\boldsymbol{h}}_1\|}x = \dfrac{1}{\|\hat{\boldsymbol{h}}_1\|}[\boldsymbol{h}_0\hat{\boldsymbol{h}}_1^{\mathrm{H}} \;\; \boldsymbol{h}_1\hat{\boldsymbol{h}}_1^{\mathrm{H}}]^{\mathrm{T}}x \end{cases}, \tag{1.11}$$

and if x is known (e.g. being a DL pilot signal or estimated from DL data signals), the terms in the Gramian of the channel matrix can be identified. Further details are given in Appendix A.

1.3.2 Terminal Transmissions Schemes

Different transceiver architectures will also in some cases limit the terminals' ability to freely select a pilot vector. Furthermore, there is a relation between the terminal transceiver architectures, the envelope correlation between its antennas, and the effective channel.

To obtain gain from multiple-antennas at the terminal side the Gramian needs to be known. Large correlation between the signals at different terminal antennas means that they see the same transmission channel. Hence, it is enough to sound the channel from one of the terminal antennas in this case. Uncorrelated signals at the antennas, on the other hand, means that the antennas see different transmission channels and individual pilot transmissions from the antennas are necessary. The relation between the gain-pattern correlation between terminal antennas, the effective channel, and the gain potential in a MaMi system was studied in Paper I. It was shown that for a poorly scattered channel (i.e. few alternative propagation paths) the average envelope correlation is large and as the channel is getting richer it converges toward the envelope correlation coefficient [29].

The influence form terminal transceiver architecture is studied in all of papers II-V. Five transceiver architectures, associated with different transmission schemes, their SNR expressions, and by architecture restricted complex-valued pilot-vectors are shown in Fig. 1.5, where the blue triangles indicate receive capability and the red triangles transmit capability.

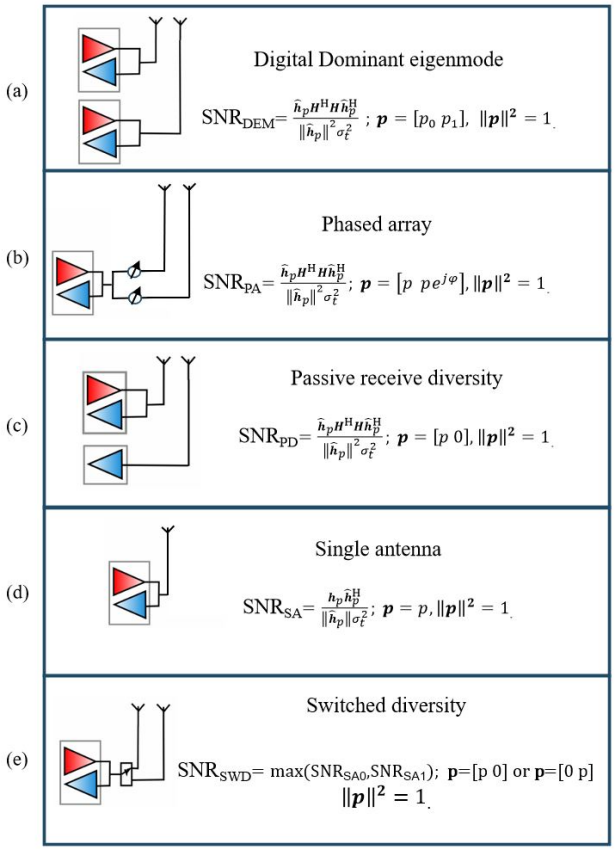

Figure 1.5: Transceiver architectures and their associated SNR expressions. In (b), $\varphi \in [-\pi, \pi]$. In (e), index SA0 and SA1 refer to the SNR expression in (d) for the antennas 0 and 1 respective.

The dual transceiver, in Fig. 1.5(a), offers the most flexibility as it has unrestricted access to both antennas. It is the only topology that enables dual streams (i.e. multiplexed operation) in both UL and DL. From a gain perspective, it can choose any pilot vector and therefore achieve the strongest effective channel, which is when the pilot is aligned with the dominant eigenvector of the Gramian, $\boldsymbol{G}$. The dominant eigenvector is the eigenvector associated with the largest eigenvalue of $\boldsymbol{G}$. It can be obtained from an eigenvalue-value-decomposition, $\boldsymbol{G} = \boldsymbol{Q}\boldsymbol{\Lambda}\boldsymbol{Q}^H$, where $\boldsymbol{\Lambda}$ is a diagonal matrix with the sorted eigenvalues along the diagonal and $\boldsymbol{Q}$ is a unitary matrix defining the eigen-

vectors. By using the first row of $\boldsymbol{Q}$, $\boldsymbol{q}_1$ where the index refer to the row, as pilot vector the power of the pilot signal reaching the BS is maximized.

For multiplexed operation, the terminal needs to transmit independent pilots for each stream. Maximized rate is achieved by precoding the pilots from the terminal antennas along different eigenvectors, as they, per definition, are orthogonal[11]. So far, we have used MRT as the precoder at the BS. We motivated it with that it simplifies the expressions, and that it addresses the same effective channel as the ZF precoder for the single-stream case. However, for the multiplexed operation we have more than one stream and therefore, we assume ZF[12] at the BS. Based on the Moore-Penrose pseudoinverse of the channel estimate $\hat{\boldsymbol{H}}$, the BS computes a precoder

$$\boldsymbol{W}_{\mathrm{ZF}} = \hat{\boldsymbol{H}}^{\mathrm{H}}(\hat{\boldsymbol{H}}\hat{\boldsymbol{H}}^{\mathrm{H}})^{-1}. \tag{1.12}$$

Depending on the correlation between the signals at the terminal-antennas, the effective channel, based on ZF, cannot be assumed equal to that of MRT but, converges to it if the correlation between the channels seen by the different terminal antennas is small. The SNR, however, for each antenna converges to that of a single antenna (Fig. 1.5(d)) as the number of BS antennas grows large. This is due to a property of ZF, where the power level at each terminal-antenna is kept constant at the cost of required power at the BS side. It has the drawback that if the correlation between the signals at the terminal-antennas is large, the power level at the BS may become very large, at some point limited by the transceiver implementation at the BS. For the terminal, the drawback with the dual transceiver architecture is that it is also the most expensive and power-consuming, as it requires two front-ends and up/down conversion chains to be simultaneously active. This motivates the alternative solutions.

The architecture in Fig. 1.5(b), is known as a phased array. Under the assumption that all antennas have the same gain pattern it can be seen as an analog implementation of a dominant eigenmode architecture. The weakness of this architecture is that it is limited to single-stream operation but, under the assumption that all antennas have the same gain patterns it, per definition, addresses the dominant eigenmode and therefore is optimal. The performance will in the end be limited by the antenna gain patterns.

Passive receive diversity, in Fig. 1.5(c), operates only in the DL and is an opportunistic approach where the diversity antenna *cannot* transmit any pilot. The received signal at the diversity antenna depend strongly on the correlation between the channels from the terminal antennas to the BS. The SNR expression is the same as that of the dual transceiver and the phased array. The limitation comes from the restriction on the pilot vector $\boldsymbol{p}$.

[11] All eigenvectors in $\boldsymbol{Q}$ associated with eigenvalues $\neq 0$ from an eigenvalue-decomposition of a Hermitian matrix are by definition orthogonal [30]. [12] Other precoders are possible.

Finally, switched diversity, in Fig. 1.5(e), is a low-cost solution where a single transceiver has access to all antennas via a switch. This solution can only obtain gain if the correlation between the signals at the antennas is low because only one antenna can be active at the time. A drawback with switched solutions is the insertion loss from the switch, which scales with the number of terminal antennas and more switch states need to be introduced.

In papers II-V we investigate various aspects of all the presented transmissions schemes and variants of them[13], based on simulated and measured channels with up to four antennas.

The selection of antenna and transceiver architecture in terminals is not only determined by cost and flexibility, but it also depends on the frequency of operation. In general, it is good to have terminal antennas with low envelope correlation. This both increases the potential diversity gain, and/or the multiplexing efficiency. Fortunately, the physical size of the antennas compared to the size of a typical handset in the 2-6 GHz frequency band makes it easy to obtain antennas with on the average low envelope correlation. The level of envelope correlation for antennas in this frequency domain[14], in the end depend on the wireless transmission channel, which was studied in Paper I. The, on the average, low envelope correlation between the terminal antennas in the frequency span 2-6 GHz limits the potential benefit of passive diversity and phased array. For the same reason, the switched diversity scheme reach close to optimal (i.e., the performance of the dominant eigenmode scheme) under the same conditions, which was concluded in Paper V.

Multiplexed operation in LTE-A is only supported in the DL, motivated by the in general higher traffic-load in that direction. Based on the availability of DL pilot signals in LTE-A the terminal can detect and separate the streams and the transceiver architecture Fig. 1.5(c) is therefore sufficient. For a MaMi system, the channel to each antenna is determined by the UL pilot signals and to enable DL multiplexed operation, UL pilots associated with each stream needs to be transmitted. Therefore UL transmit-capability on all antennas is a prerequisite for multiplexed operation in MaMi systems. The transceiver architecture Fig. 1.5(a) is, therefore, the only transceiver that supports DL multiplexed operation in Fig. 1.5. A hybrid solution between the transceiver architectures Fig. 1.5(c) and Fig. 1.5(d), transmit switch diversity, is shown in Fig. 1.6. With transmit switch diversity, transmit capability is enabled to both antennas by a switch, while there are individual receivers to each antenna.

[13] Various combinations can be obtained e.g. two transmission chains switched to four antennas or implementations with an asymmetric number of UL/DL chains. [14] For frequencies below 1 GHz the envelope correlation tend to increase in handset sized terminals, and low envelope correlation is typically achieved in the polarization domain and, therefore, limited to two streams. This has with the radiating modes in the handset chassis to do but, is not the topic of this work.

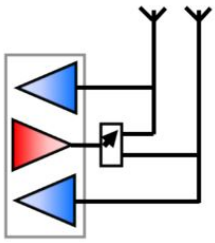

Figure 1.6: Teansmit Switch Diversity Architecture.

The transmit switch diversity architecture would enable DL MIMO in a MaMi system, avoiding the need for two transmitters, with the restriction that the pilot signals can not be transmitted simultaneously.

Multiplexed operation is related to having multiple user (MU) in a MaMi system. There are some fundamental differences between the two scenarios. One is that in the MU case, the signals at different terminals cannot be co-processed. All optimization, therefore, relates to the BS implementation. Another difference is that the antennas in different terminals move relative to each other which gives different channel distributions compared to those when the antennas are fixed relative to each other in a terminal. In Paper VI we investigate the channel properties for a terminal under the influence of other terminals.

1.4 mm-wave channels

The major part of wireless communication systems of today operates at frequencies below 6 GHz. To meet the traffic demands predicted by the industry, it will not be enough to increase the spectral efficiency to the realms of what is possible. This has motivated both the industry and academia to look at higher frequencies. Some 5G systems at 28 GHz have are already been deployed, e.g. by Verizon in the USA [31]. BF at the terminal side, discussed in 1.3.2, is utilized to reach a reasonable compromise between performance, cost, and complexity for both the BS and the terminals.

The mm-wave frequency band 24-52.6 GHz is a significant part of the 5G NR, by [32]. This frequency range needs further attention as today's models, used by the third generation partnership project (3GPP), are based on a limited set of channel measurements and, therefore, cover a limited set of mainly static scenarios. Extensions to the present models require further measurements of propagation channels with higher resolution, in particular where

dynamic aspects are considered. New use cases, e.g., accurate indoor positioning, or vehicular communications, are currently not supported by the 3GPP channel models and there is, therefore, room for improvement. The improvements need to be based on measured propagation channel statistics commonly generated by channel sounders capable of addressing such scenarios.

In this thesis, we present a mm-wave channel sounder, which can be seen as the first step toward the evaluation of terminals at mm-wave frequencies.

Chapter 2

Channel Models

This Chapter discusses different channel modeling approaches, their advantages and disadvantages, and how they can be used to evaluate multiple-antenna terminals in a MaMi system.

2.1 Abstractions

As we discussed in Chapter 1, a MaMi BS acquires the full CSI for both UL and DL transmissions based on the UL pilots. Giving the terminal access to full CSI (i.e., $\boldsymbol{H}$ a J$\times K$ matrix, where J is in the order 100 and K 2-8.), would require far too much overhead. Since the terminal only has few antennas, limited spatial degrees of freedom are present when it selects the pilot signal. Hence, there is no need to share the full CSI. The $K \times K$ channel inner product matrix, a.k.a. the Gramian, given by

$$\boldsymbol{G} = \boldsymbol{H}^{\mathrm{H}}\boldsymbol{H}, \tag{2.1}$$

carries all necessary channel properties for a realization [24,33] of $\boldsymbol{H}$, and being a Hermitian matrix, the Gramian can be represented by only $K(K+1)/2$ complex terms[1]. From the Gramian, the terminal can compute the singular

[1] It is to be noted that under certain conditions the Gramian matrix collapses to a so-called "Wishardt" matrix. That is, each entry of $\boldsymbol{H}^{\mathrm{H}}\boldsymbol{H}$ then follows a Wishart distribution. The underlying theory of Wishart matrices have been substantially developed over the last decades by multivariate statistical techniques (see e.g. [34]), and applied to MIMO systems (see e.g. [35–37]). The specific conditions for the translation of a more general Gramian matrix into a Wishart matrix can be found in [36–40]. We omit detailed discussion on Wishart theory, as it is not within the scope of the thesis. Interested readers are referred to the above-mentioned works.

values of the channel[2] and further derive an optimal pilot vector as we showed in 1.3.2.

There are different methods for a terminal to acquire the Gramian from the received signals and they depend on the precoding used at the BS. In Appendix A we show how this can be implemented for three different precoders. Besides, the Gramian can be shared by the BS over a control channel.

Terminal diversity schemes, in general, are often addressing only large-scale fading, which is a slow process with a weak frequency dependency. In conventional MIMO systems, a terminal can use the average of the Gramian to address the large-scale fading, a.k.a. the covariance matrix, $\boldsymbol{V} = \mathbb{E}\{\boldsymbol{G}\}$, where the expectation is performed over the ensemble of all values in $\boldsymbol{H}$, i.e., individual element to element correlations. In Paper IV we showed that when the number of BS antennas grow large in a MaMi system, the Gramian converges towards the covariance matrix, as a result of the hardening. This means that a terminal can get instant access to an estimate of the covariance matrix based on a precoded DL signal. Practically speaking, the coherence time for the limited CSI needed by the terminal (i.e., the covariance matrix) in a MaMi system is in the order of 2-3 magnitudes longer than the full CSI needed by the BS (i.e., the required UL pilot rate). Therefore, the overhead needed by the terminal to gain access to the covariance matrix is negligible in a MaMi system. To this end, in simulations we can be assume that the terminal has access to CSI.

In our measurements, the normalized covariance matrix is used, since it represents the effective channel without the absolute power, which we are not interested in[3]. Similarly, in the simulations, the normalized Gramian for each realization is derived. From the Gramian (or covariance matrix), it is straight forward to derive the SNR-gain or rate improvement that can be expected from different transmission schemes. The detailed derivations are presented in the papers III and V. Furthermore, the use of the normalized Gramians allows us to compare and match the statistical distributions of the effective channels derived from simulations to those measured.

To sum up, for simulations we can assume that a terminal can get access to CSI, that the needed CSI is limited in size, and that it has a long coherence time. When we evaluate a terminal in a MaMi system we do not need to include the small-scale fading due to the hardening effect, nor the frequent pilot transmissions to the BS. Just as long as we capture the large-scale fading

[2] This is based on that all eigenvalues $\neq 0$ are the same for the inner and outer product, $\text{eig}(\boldsymbol{H}\boldsymbol{H}^{\text{H}})=\text{eig}(\boldsymbol{H}^{\text{H}}\boldsymbol{H})$ and $\boldsymbol{H}\boldsymbol{H}^{\text{H}}$ is a $J \times J$ matrix while $\boldsymbol{H}^{\text{H}}\boldsymbol{H}$ is $K \times K$ matrix. [3] The absolute power relates to the distance between the BS and the terminal and to the attenuation in the total channel. For a given system, the only ways to compensate for a weak channel is to increase the transmit power or to increase the transmission redundancy, which does not add to the scientific value. The normalized channel, on the other hand, still contain all channel properties that can be exploited by both the terminal and the BS.

variations of the effective channel.

Different channel models focus on different properties of a channel and can be divided into fully-stochastic, stochastic-geometric, and deterministic models [41]. The latter, which includes ray-tracing and Maxwell equation-based, are not treated in this thesis. The fully stochastic models are more general and do not consider spatial properties, while, the stochastic-geometric models (e.g. [42]), are derived from a geometric description or a spatial behavior. There are also various hybrid models where some of the geometric properties are modeled by stochastic properties e.g. [17]. In the next sections, we present the two models that have been used in our research.

2.2 The Kronecker-Model

The Kronecker-model is a fully-stochastic channel model and is based on the assumption that the correlation matrix $\boldsymbol{R}$ is separable, i.e. $\boldsymbol{R} = \boldsymbol{R}_{\mathrm{b}} \otimes \boldsymbol{R}_{\mathrm{t}}$, where $\boldsymbol{R}_{\mathrm{t}}$ and $\boldsymbol{R}_{\mathrm{b}}$ are the correlations at the terminal and BS side, respectively. The separability implies that the antennas at the terminal are uncorrelated to the antennas at the BS side [27], which allows the channel matrix $\boldsymbol{H}$ to be generated as a product

$$\boldsymbol{H} = \boldsymbol{R}_{\mathrm{b}}^{1/2} \boldsymbol{H}_{\mathrm{W}} \boldsymbol{R}_{\mathrm{t}}^{1/2}, \tag{2.2}$$

(i.e., is separable) where the $\boldsymbol{R}_{\mathrm{b}}$ and $\boldsymbol{R}_{\mathrm{t}}$ covariance matrices define large-scale fading properties and $\boldsymbol{H}_{\mathrm{W}}$, is a white, independent and identically distributed (i.i.d.), complex Gaussian matrix, representing small-scale fading. In our simulations only terminal antenna properties are investigated under the assumption that the BS antennas are uncorrelated[4], hence $\mathbb{E}\{\boldsymbol{R}_{\mathrm{b}}\} = I$. The channel is then given by

$$\boldsymbol{H} = \boldsymbol{H}_{\mathrm{W}} \boldsymbol{R}_{\mathrm{t}}^{1/2}. \tag{2.3}$$

Based on this model, terminal antenna properties can be introduced based on their statistical measures (e.g. radiation efficiency and correlation coefficient). This inherently assumes isotropic behavior with limited[5] possibilities to include directional properties. The model, however, is easy to use and makes it possible to evaluate different terminal transmission strategies as a function of gain imbalance or correlation between the signals at the terminal antennas. This is not possible in simulators where the gain imbalance and correlation are deterministically defined by measured antenna-patterns e.g. the simulator we present

[4] the assumption means that the channel is rich enough, and the BS antennas separated enough to see independent channels. [5] With detailed modeling of the antenna spacing, angular spread, and number of contributing MPCs geometrical properties can to some extent be included.

in Section 2.3. The model is suitable for evaluations of intrinsic behaviors, like different levels of noise or number of antennas at either side.

Simulations are performed based on the Monte-Carlo method where a large number of realizations of $\boldsymbol{H}_{\mathrm{W}}$ are randomly generated. The resulting channel $\boldsymbol{H}$ from each realization can be used to compute distributions of the received signals in (1.4). Also the various transmission schemes presented in Section 1.3, Fig. 1.5 can be studied.

The Kronecker approach enables a convenient way to arbitrarily control imbalance and correlation between the signals from the terminal antennas. It can show that a channel realization will have a great impact on performance but not how realistic or likely it is across various changes in the system parameters. The Kronecker approach cannot include directional properties. Neither from the antennas or the channel.

Nevertheless, based on the following facts:

1. When increasing the number of BS antennas, the spatial resolution increases and the spatial properties become more prominent [19, 20, 43, 44]. MaMi has the capability to control phase, amplitude, and polarization of multiple signal contributions that illuminate the terminal antennas and thus enable a coherent combination of them.

2. Gain, polarization and correlation between handset antenna gain patterns vary dependent on how they are illuminated, as shown in Paper I.

3. Handset antennas are influenced by the user in many scenarios, this influences the directive properties of the antennas, as shown in Paper II.

4. Terminal transmission strategies often utilize the directional properties.. This is even more important at higher frequencies, anticipated in [32, 45, 46], when the smaller apertures motivate multiple antenna elements with the same gain pattern.

The lack of directional properties in combination with the properties listed above are the reasons why simulations based on the Kronecker model fails to accurately predict the performance of a MaMi system. This is the motivation behind the development of the simulation framework presented in Paper III and introduced in the next section.

2.3 Stochastic-Geometric Models

Different stochastic-geometric models are available, e.g. [42], [47], most of them include both the BS, multiple terminals, and an environment to model the behavior of propagation channels. The propagation models are either defined as

propagation paths in the angular-delay domain or as three-dimensional (3D) structures with positions and absolute distances between nodes and relative to scattering objects (e.g. ray tracing). The statistical behavior is introduced either by assigning the angles and delays to distribution functions or in the latter case by randomly dropping the terminals at different positions. Due to the ability to model a more insightful propagation channel with amplitudes, delays, and polarizations, such approach would be preferred in 3GPP standardization for both sub-6 GHz and above (TS 38.901 in [17]). It is noteworthy that the models in [42, 48] take the more geometric approach of defining the relevant area around the BS and terminal, and model the visibility regions across which the terminal moves for characterizing the propagation channel.

In our research, the focus is on terminal-antenna configurations and transmission schemes with limited focus on the BS implementation. To isolate the influence of the terminal antenna pattern on each entry, h_{kj}, in the channel matrix $\boldsymbol{H}$, modeling the channel as propagation paths in the angular-delay domain is most suitable. With this approach the relative distance or position of the BS becomes irrelevant and it can be substituted with a behavioral model of the effective channel.

However, to assign relevant properties to the parameters that define the effective channel in the angular-delay domain, we need to understand the mechanisms that control them. In Section 1.2.3, we listed inherent properties of the effective MaMi channel, namely: *hardening, full array gain in scattered scenarios, and improved isolation between terminal antennas.*

To convert these properties, of the effective MaMi channel to properties in the angular delay domain we start from a geometric channel description. Fig. 1.3 shows a scenario where we have a BS, a propagation channel and a terminal. Seen from the terminal, we have signal contributions from various angles. Based on observations, e.g. [49–51], contributions of signals propagating along various paths, a.k.a. multipath components (MPCs), tend to be clustered. This can be explained by the reflections caused by various objects in the environment. The surface of a reflection point dictates the properties of a cluster, in terms of physical size (i.e., angular spread (AS)) and signal strength. The environment will also determine the number of clusters, a.k.a. scattering richness.

Due to limited operational bandwidth, in particulare in the sub-6 GHz frequency band, even an ideal MaMi BS, with infinitely many antennas, will not be able to resolve individual MPCs from each other. This has the effect that also in the MaMi case we can generalize a cluster to have a power density, polarization and phase delay, which are all constant over the angles defined by the cluster. This is in line with how clusters are typically defined, also for conventional MIMO models [41, 47, 52, 53].

The precoding, causes the phase from different *clusters* to be coherent. The power seen from each cluster is optimized by the BS to maximize the SNR under a power constraint. This means that the MaMi BS allocates power to the different clusters according to a maximum-ratio-transmission (MRT) algorithm[6][7]. With MRT distributed power among the clusters, we achieve the property of full array gain also in the angular domain, i.e. the same gain as with a single beam in line of sight conditions. Furthermore, as the MaMi BS addresses both polarizations, based on the MRT the polarization of a cluster, therefore, aligns to that of the terminal antenna in the angular delay domain.

The cluster-based simulation framework that we developed, is based on the above-mentioned assumptions around the MaMi BSs capability to achieve coherent combination, individual gain-control, and polarization alignment, of signals from multiple clusters. The simulation framework is in its entirety is presented in Paper III, where motivate all our assumptions around the channel and the MaMi BS capability to control it. The simulation framework also lays the foundation to the results in papers I and V. An overview of the framework and its capabilities is further described in Section 3.2.

[6] We discussed in 1.3.1, that for a single terminal antenna also ZF allocates power according to the MRT precoder and, that the difference relates to the normalization. [7] In Paper III we show that when power is MR distributed at the BS antennas, it results in MR distribution also at the clusters.

Chapter 3

Technical Tools and Systems

This chapter presents the tools and the systems we have developed for evaluation of multi-antenna terminals. Terminal prototypes, simulation tools, functionalities for the Lund University MaMi real-time testbed (LuMaMi), and a mm-wave channel sounder. In general, this chapter gives an overview of the different tools with the intention to fill out the gaps of what did not fit in the papers. We have therefore tried to not duplicate what is already present in the papers. Table 3.1 lists the different tools that have been developed for the research and how they are related to the different publications included in this thesis. Besides, several MATLAB scripts for data processing and plot generation have been developed.

Table 3.1: Tools developed and their relation to the publications

Tool:	Paper I	Paper II	Paper III	Paper IV	Paper V	Paper VI	Paper VII
Terminal prototype	X		X	X	X	X	
Cluster based simulation framework	X		X		X		
Kronecker-model based simulation framework		X		X			
Real time diversity implementation for LuMaMi		X	X				
Real time channel capturing for LuMaMi				X	X	X	
Multi terminal simulation framework						X	
28 GHz channel sounder implementation							X

3.1 3.7 GHz Terminal Prototypes

In this section, we motivate why it is important to use prototypes with realistic shape, with integrated antennas, and present the 3.7 GHz prototypes that were used throughout the research.

3.1.1 The Importance of Realistic Prototypes

Most of the published measured channels from MaMi systems, so far, are performed using dipole antennas or similar at the terminal side [19,20,26,43,54–57]. The performance of any wireless communication system depends heavily on the terminal-antenna properties and dipole antennas are close to ideal in their radiation properties. A dipole antenna is based on a straight metal structure with a length of a wavelength of the frequency of operation. The far-field antenna gain-pattern of a dipole-antenna is donut-shaped [58] and linearly polarized along the antenna axis. The polarization does therefore not change if the antenna is rotated along that axis. Also, the gain and phase variation of the dipole-antenna gain-pattern shows small variation except for at the angles toward the edges. This is far from what can be expected in any realistic hand-held product, such as a smart-phone with integrated antennas. Besides, a transmission channel behaves differently when two or more antennas are physically fixed relative to each other, as the orientation of the terminal is changed, as compared to random placement of antennas in a limited volume. Furthermore, user interaction is hard to mimic realistically with a dipole antenna.

The reason why integrated antennas behave differently compared to dipole antennas relates to the physical properties of the device. The shape and size of an integrated antenna depend on the industrial product-design and thus the available volume. Integrated antennas for frequencies below 6 GHz are therefore typically 3D structures rather than the single-dimensional structure of dipole antennas. Antennas are resonant structures; the orientation of the current flow determines the properties of the electrical field [58]. When a current flows in a multi-dimensional structure, the far-field properties is given by the sum of the contributions (i.e., the superposition of wave-fronts principle e.g., [13]) from currents that flow in different parts of the structure. This gives an angular dependency and both the complex gain and the polarization will, therefore, depend on the angle from which it is observed. The principle is shown in Fig. 3.1 where the red arrows illustrate the current-flows in two structures. The left figure shows a current flow in a one-dimensional antenna structure and the associated electric field. In the right figure, we show a 3D antenna structure, the resulting polarization of the electric field is derived by superposition from three contributions.

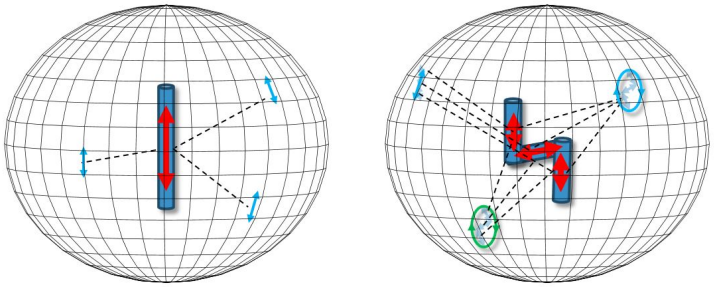

Figure 3.1: Antenna far-field relation to current distributions. The left figure illustrates a dipole antenna where the current is limited to flow along a single dimension and the right figure shows a three-dimensional structure where the current can be allowed to flow in all three dimensions.

When an object is introduced in the near-field of an antenna, the current distribution will be affected. For a one-dimensional structure this mainly causes a reduction in signal strength, while, in a 3D structure, also, the relative contribution from the different currents may change. This may, therefore, cause a change in both the complex gain and polarization distributions.

Figure 3.2: Phantom head with hand left (BHHL) and phantom hand left (LH) fixtures.

To capture large-scale effects realistically, from a user-antenna interaction perspective, a realistic prototype with well defined, repeatable load scenarios is of importance. There are standardized load cases in the industry, used for the type approval and generally during the product development. Besides free-space (FS) characterization, tests that involve loading scenarios where a phantom head and phantom hands are used, e.g. beside-head-with-hand-left-side (BHHL) load case and left-hand (LH) load case, which are both shown in Fig. 3.2. It is clear that BHHL is not a typical 5G use case, but its use in our research is motivated by being well-defined, repeatable, and that it represents a moderate loading scenario.

Multiple antennas in a terminal can be characterized in a common coordinate system with the same center of origin. This is crucial for the stochastic-geometric simulation models and allows measurements and simulations to be based on the very same terminal-antenna gain-patterns and relative antenna positions, which is essential for matching simulations to measurements.

Figure 3.3: Five prototypes based on Sony Xperia-ZL and -SP chassis. The top picture shows the fronts and the bottom picture the rear of the same prototypes. The two prototypes to the left are the based on the Xperia ZL and have four antennas integrated. The three prototypes to the right are based on Xperia SP and have two antennas each.

3.1.2 Integration and Evaluation of Terminal Antennas for 3.7 GHz

For the research, two sets of prototypes have been designed. Fig. 3.3 shows all prototypes. The Prototypes are based on two different Sony Xperia models. They are equipped with integrated antennas tuned to the 3.7 GHz used by the LuMaMi testbed. Two of the prototypes, based on the Sony Xperia ZL smart-phone, have four antennas integrated and switch circuitry to enable any two antennas to be connected to the coaxial feeds. The other three prototypes are based on Sony Xperia SP smart-phones and have two antennas integrated.

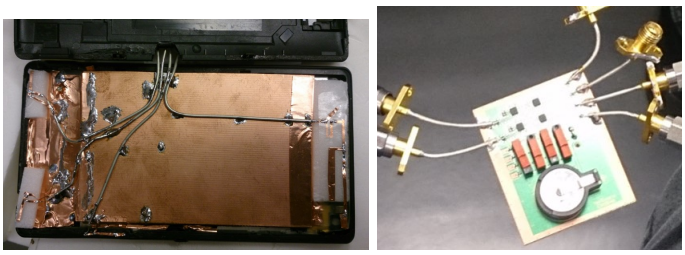

Figure 3.4: Integrated antennas in the Sony Xperia-ZL prototype and switch circuitry.

Fig. 3.4 shows the integrated antennas in one of the ZL prototypes. The top two antennas and the side antenna are planar inverted F-antennas (PIFA) while the bottom antenna is an off-ground branched monopole antenna. The bottom antenna is designed to have additional resonances at both 900 MHz and 2 GHz in order to increase the realism of the implementation. Both the antenna and switch circuitry were designed for this project. The SP prototypes have a similar approach with a multi resonant antenna in the bottom and a PIFA in the top.

All antennas have been characterized in an anechoic measurement-chamber (Satimo stargate 64) and the far-field antenna gain patterns have been computed. The antenna gain patterns for the different antennas in each prototype are measured with the same geometrical center and coordinate system.

There is no specific requirement on antenna gain patterns or directional properties for LTE. It is assumed to be in the interest of a phone manufacturer to achieve a good performance. An antenna gain pattern depends heavily on how it is loaded and this is complicated to consider during the design. Therefore, the total radiated power (TRP) for free-space condition is specified [59], which is the integrated power over all angles and reflect the equivalent power from an isotropic radiator. Often operators put additional requirements on loaded scenarios, e.g. how much the TRP is allowed to drop under a condition such as BHHL.

In Section 2.3 we discussed the importance of including the directional properties of the propagation-channels and antenna gain patterns in simulation models of MaMi systems. Therefore, we present a selection of antenna gain patterns. We also present the total isotropic radiation efficiency, which relates to the TRP, but is the isolated antenna performance metric, without the radio front-end. The patterns in the figures 3.5-3.8 are plotted in polar coordinates. The ellipses in the figures indicate the polarization properties, different color

for different rotational direction. The polarization shows large variations as a function of the direction. Note that the polarization is plotted along the Θ (elevation) and Φ (azimuth) coordinates why they tend to rotate as a function of the azimuth angle.

Fig. 3.5 shows the FS patterns for one of the ZL prototype antennas. In general, the gain is omnidirectional, except for the bottom antenna, which show some directivity downwards. The total isotropic radiation efficiency of all antennas in the ZL prototypes is about -5 dB for all antennas. This includes insertion loss from the switch circuitry, which is about 2 dB. In general, the polarization depends heavily on the direction. The four patterns were used for the generation of Fig 3.9.

Fig. 3.6 shows antenna-gain-patterns based on the BHHL scenario. The directive gains are larger for all antennas and the average absolute gain is, as expected, lower. Cumulative distributions functions (CDF) for mixed load cases are presented in Paper V. Similar behavior can be observed for the SP-prototypes antennas. They are all similar and the patterns from one of them are shown in the figures Fig. 3.7 and Fig. 3.8. The SP prototypes show a gain imbalance of about 1.5 dB between the antennas. This is implementation loss related to the industrial design, where a transparent gap was present. It can be mentioned that there is some effect from the cabling in the plots. Although the cables are also present in the real-time measurements performed together with the LuMaMi test-bed, they will likely have some influence on the repeatability. This aspect has not been investigated. Note also that the FS and HHHL patterns cannot be directly compared to each other as the prototypes, for practical reasons were not oriented the same way in the chamber during the characterization.

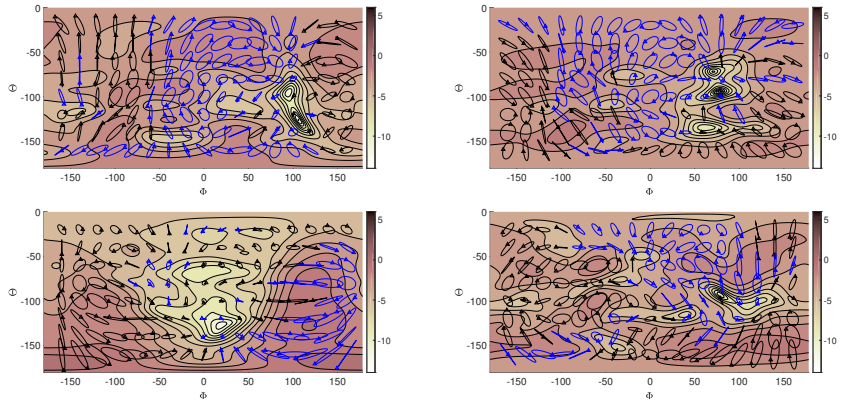

Figure 3.5: Antenna Gain patterns and total isotropic radiation efficiency for the Xperia ZL prototype Free-space. In order top-left antenna (-5.4 dB), top-right antenna (-5.0 dB), side antenna (-5.4 dB) and bottom antenna (-5.2 dB).

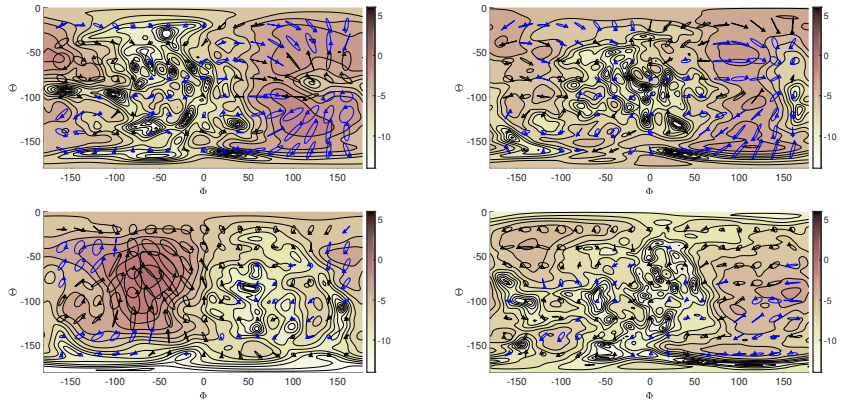

Figure 3.6: Antenna Gain patterns and total isotropic radiation efficiency for the Xperia ZL prototype Loaded beside phantom head with hand left. In order top-left antenna (-8.7 dB), top-right antenna (-10.0 dB), side antenna (-13.0 dB) and bottom antenna (-7.9 dB).

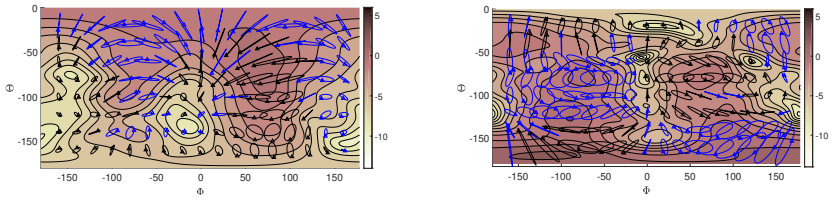

Figure 3.7: Antenna Gain patterns and total isotropic radiation efficiency for the Xperia SP prototype Free-space. In order, top-antenna (-4.6 dB) and bottom antenna (-3.0 dB).

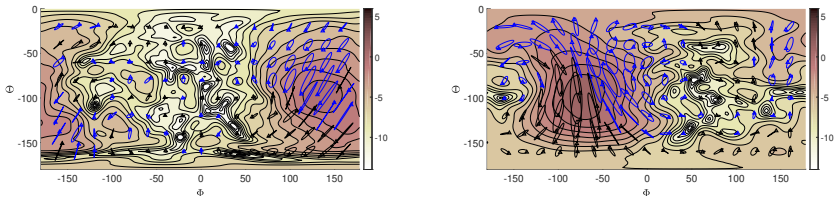

Figure 3.8: Antenna Gain patterns and total isotropic radiation efficiency for the Xperia SP prototype Loaded beside phantom head with hand left. In order, top-antenna (-7.5 dB) and bottom antenna (-5.1 dB).

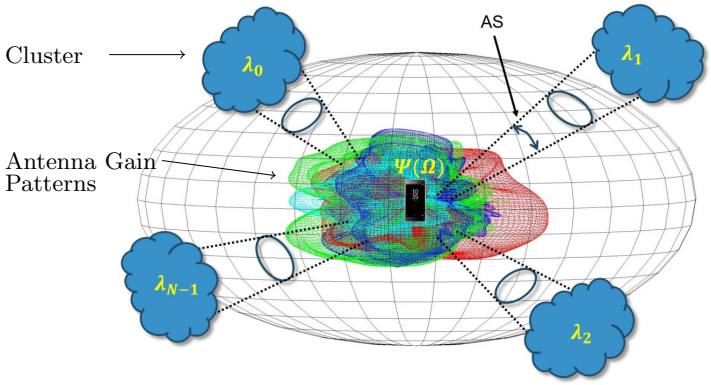

Figure 3.9: Terminal with four antennas exposed to signals from multiple clusters.

3.2 Cluster-based simulator

The stochastic-geometric modeling approach that we discussed in Section 2.3 enables major simplifications when evaluating terminal properties in a MaMi system. The model avoids the complexity of a BS with all its antennas and related signal processing and can be used for performance evaluation of terminal-antenna implementations, terminal transmission schemes, and terminal hardware implementations.

Fig. 3.9 illustrates a setup. In the center, there is a terminal with four antennas. The measured[1] antenna gain patterns, $\boldsymbol{\Psi}(\boldsymbol{\Omega})$, are shown colored cyan, blue, green, and red. In Fig. 3.9, the terminal is illuminated by N clusters of MPCs, each with a power strength Λ_n, that together defines the effective transmission channel. All clusters have the same angular spread, AS, defined in both azimuth and elevation that defines the physical size of the clusters as seen from the terminal. The simulator uses the MaMi communication protocol we presented in Fig 1.4. The BS precoder assumption, however, is MR normalized to the channel power. If the terminal sends individual pilots from its antennas the MR precoder yields received signals at the terminal side that directly reflects the entries of the Gramian. This is in detail described in Appendix A.

It is assumed that a pilot vector is transmitted from the terminals one or more antennas and that the BS from it acquire perfect (i.e., noise-free) CSI. Based on the MR precoder, the massive number of BS antennas, and perfect

[1] Also simulated antenna gain patterns can be used.

channel knowledge it is further assumed that the BS is capable of addressing each cluster individually. The precoder distributes the power to the different clusters in an MR sense, make sure that the signals from each cluster arrive coherently to that of the pilot vector, and also have a polarization aligned according to that of the pilot vector.

The simulator generates random illumination angles (AoA) in azimuth and elevation, uniformly distributed over the sphere, for the N clusters. To this end, only three parameters are used to define the clusters, and thus the effective channel: the cluster count, N; the cluster angular spread, AS; and the standard deviation of the cluster strength, Λ_n. By selecting the parameters and generating a large number of cluster realizations, the distribution of the received signals can be matched to distributions obtained from measurements in various environments. All details of the derivations, as well as motivations to all our assumptions, are presented in Paper III.

During development, mapping simulations to measured channels showed to be a challenging task and additional settings that relate to physical properties a real propagation channel may have were implemented. Additional control features to the simulator are:

- The alignment of the polarization of the cluster to that of the terminal antenna can be randomized, to investigate cross-polarization distortion.
- Arbitrarily fixed clusters can be used to evaluate the contribution from changes caused only by altering terminal orientation.
- Arbitrarily fixed clusters in combination with limited terminal orientations, i.e. rotation along one, two, or three axes to enable mapping to measurement conditions.
- Clusters restricted in elevation, for evaluation of horizontally distributed clusters.
- Clusters restricted in azimuth and elevation, for evaluation of dense clusters.
- An arbitrary level of randomness can be added to the clusters power, phase and polarization to emulate reduced channel knowledge at the BS side.
- A secondary set of clusters with smaller AS and lower power can be activated to emulate an environment with diffuse multipath components.

The output from the simulator can be set to be in the form of distributions of the complex Gramian for an arbitrary count of randomly generated channel

realizations. A separate script is used to post-process the results, e.g. to derive statistics of e.g. different transmission schemes as we described in 1.3.2.

The simulator can generate generic channel distributions for typical environments. It is possible to match those distributions to measured distributions, but this has turned out to require extensive measurement campaigns, with random locations and orientations of the terminal. Matching the simulation set-up to the measurement approach showed to be necessary. A good matching was obtained by limiting the simulator to rotate the terminal along a single axis with a fixed set of clusters.

An early version of the simulation framework was used in the study presented in Paper I. Furthermore, the cluster noise parameter was used to emulate a system with only two, orthogonally polarized, BS antennas. Results from simulations based on this have been used in a project investigating the directional properties of a non-MaMi channel [60].

3.3 Simulator Based on the Kronecker-Model

A simulator based on the Kronecker-model was developed for evaluation of terminal transmission strategies applied on an independent identically distributed (i.i.d.) complex Gaussian channel. The simulator was used to derive performance for different transmission schemes and to study the covariance matrix and how it depends on noise at both the BS and the terminal side. The Kronecker simulation framework was used for the evaluations presented in Paper II and Paper IV.

3.4 Post-Processing of Channel Distributions

Various evaluation scripts have been developed to derive performance metrics and to generate figures. Different versions of the same basic script were used to derive figures from measured Gramians, measured channel matrices as well as from simulated Gramians. Furthermore, the results in Paper VI are based on a simulation framework, where we compute eigenvalues based on measured channel vectors from terminals located in a limited space and relate them to the clusters in the cluster-based based model.

Figure 3.10: The Lund University Massive MIMO testbed.

3.5 Lund University Massive MIMO Testbed

The LuMaMi testbed [61,62] is a MaMi system designed for real-time measurements at 3.7 GHz. The testbed was designed as a large collaboration between Lund University and National Instruments Inc. later University of Bristol also joined the team.

The LuMaMi system, shown in Fig. 3.10, is the first of its kind and is mainly based on hardware from National Instruments. It uses 50 dual transceivers, a.k.a. universal software radio peripheral (USRPs), to feed 100 antennas. Besides, five dedicated FPGA units are used to perform real-time signal processing. The system is programmed in the graphical programming language LabVIEW and is controlled by an integrated computer, the host computer. The terminals comprise USRPs similar to those at the BS and are also con-

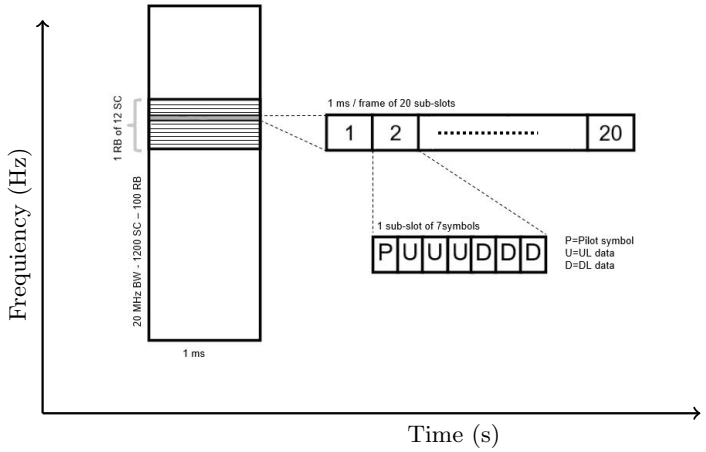

Figure 3.11: Numerology of the LuMaMi communication framework.

trolled by software programmed in LabVIEW. Each USRP can control two terminal-antennas.

The transmission protocol is based on OFDM with a similar numerology as in LTE, shown in Fig. 3.11. With a total bandwidth of 20 MHz, the system processes 1200 sub-carriers (SC) divided into resource blocks (RB) of 12 SC. Each RB consists of 12×7 resource-units (shown in Fig. 1.1) and carries a dedicated pilot resource for each data stream. The system per default uses the first symbol in each RB for pilot transmission, which allows for up to 12 simultaneous transmission streams, and the remaining part of the RB is used as a data carrier, configurable for either uplink or downlink transmissions. The first sub-slot in each frame is dedicated for DL broadcast of synchronization signals.

As we discussed in Section1.3.1, a MaMi system relies on reciprocity, i.e. the UL pilots define the precoding for the DL signals. Therefore, compensation for differences in the phase delay between the transmit and receive paths in the USRPs, at the BS side, is needed and so-called reciprocity calibration is implemented [62].

3.5.1 Modifications to Enable Multi-Antenna Terminals

The LuMaMi testbed is designed as a real-time MU-MaMi system with up to 12 multiplexed streams of data. The initial goal with LuMaMi was to show

that all the advantageous properties associated with the MaMi concept could also be harvested in reality with real hardware. Besides, the system is designed to be flexible enough for further development, optimization, and evaluation of ideas related to the MaMi concept.

In the default implementation of the LuMaMi framework, each terminal is limited to have a single antenna. Consequently, each USRP acts as two independent terminals. In this version of the LuMaMi system, power control loop was not integrated. Aligning the power levels from the terminals, that reach the BS, at the same frequency band, is critical for the overall system throughput and requires terminal power control.

For the evaluation of multi-antenna terminals, there are two approaches. The first approach is to simply capture the complex UL pilot signals received at the BS side (i.e., full CSI) and further post-process them in a different environment. This, however, does not enable real-time demonstration capability of different transmission schemes. The second approach is to implement a control channel[2] between the BS and the terminals, and functions in the terminals to co-process the signals from multiple antennas. This would enable the BS to feedback the CSI needed by the terminal. As we discussed in Section 2.1, the terminal can from the Gramian compute a pilot vector according to any of the transmission schemes and communicate accordingly.

Initially, we selected the second approach but limited it to dual-antenna terminals, as this could be integrated into a single USRP. A downlink control channel over which CSI can be shared by the BS was implemented. The CSI is represented only by the power of the received UL pilot signals for each stream, averaged over all SCs and over an adjustable amount of time. The averaging was implemented to limit the overhead and to reduce fluctuations[3] in the signal. At the terminal side, all transmission schemes presented in Section 1.3.2 were implemented as real-time algorithms. Performance, in terms of power gain obtained by the different transmission schemes, was captured for each measurement scenario. Results from measurement campaigns and further details based on this implementation are included in Paper II and Paper III.

At some point, the LuMaMi system framework was migrated to a new ver-

[2] Based on that the BS uses a ZF precoder it is hard to acquire CSI based on the received signals. This is further discussed in Appendix A. [3] Note that the small-scale fading is still present in the pilot signals received by the BS. The BS uses the pilots to derive the precoder which is responsible for the hardening of the associated communication channel. We are only interested in the covariance matrix (i.e. large-scale fading), which is addressed by the diversity schemes at the terminal side, and gain access to it by the averaging. The underlying assumption is that each measurement is performed on a channel which is static from a large-scale fading perspective. The lack of phase information in the fed back CSI is motivated by the fact that we use only two terminal antennas. The eigenvalues of the Gramian do then not depend on the phase and the terminal can compute the optimal pilot vector without this information.

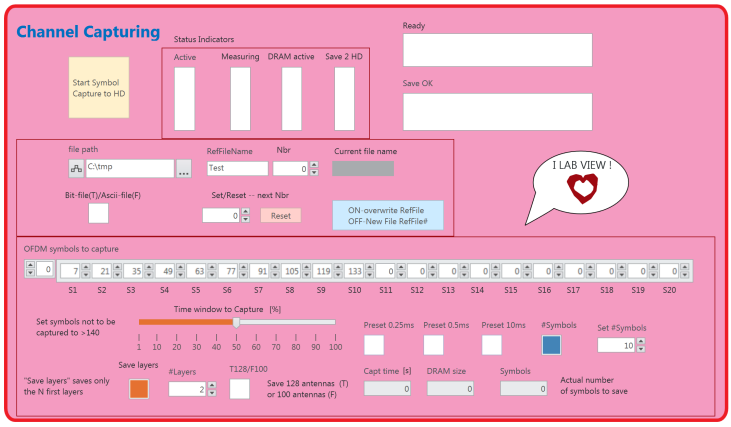

Figure 3.12: Control-interface for channel capturing in LuMaMi.

sion that involved major SW as well as hardware (HW) modifications, and all implemented features became obsolete. The general need, also from other researchers, motivated an implementation of channel capturing at the BS side. From our perspective, this corresponds to approach 1 and has the further advantage that we can evaluate terminals with more than two antennas. Besides, access to the full channel-matrix enables investigations related to e.g. different BS precoders, hardening effects, and positioning. The real-time channel capturing is implemented at the FPGA and enables up to 13 000 symbols to be streamed into a local DRAM (i.e. fast memory) and, with some delay, be passed on to the local hard drive for further post-processing. The control interface is shown in Fig. 3.12.

The channel-capturing feature is dynamic, and it is possible to select which symbols in each frame to capture. Up to 20 arbitrary defined symbol-positions per frame enable filtering of e.g. pilots. It is possible to select which SCs to save, e.g. if CSI of only selected terminals is of interest. Each resource element generates 40 kB of data. This can be derived from the ADC resolution of the complex CSI, multiplied by the 100 BS-antennas, and again multiplied by the 100 of RBs. With a total DRAM size of 2 GB, about 10 s of data can be captured if all pilots and all SCs are selected. On the other end, with a single SC and a single pilot per frame, several minutes of channel data can be captured. The channel-capturing feature was used to generate the measurement results presented in the papers IV-VI.

3.6 28 GHz Channel Sounder System

To evaluate terminal antennas at mm-wave frequencies a prerequisite is to know the channel properties. As of now, there is limited knowledge about channel behavior in dynamic environments at mm-wave frequencies. The dynamic properties may originate either from that the terminal that is moving or from moving scatterers in the environment. Low dispersion and high reflection loss will have a large influence on the mm-wave channels and will likely make them very different from the micro-wave channels that we have studied so far in this thesis. As we discussed in Section 1.4, also the terminal antennas are different. Improved channel knowledge and new models can then be used to migrate the cluster-based simulation framework to the mm-wave case and enable further studies of different terminal strategies also at these frequencies. In this thesis, we present a mm-wave channel sounder, which can be seen as the first step toward the evaluation of terminals at mm-wave frequencies. The antennas of the sounder are shown in Fig.3.13. In the following sections, we first give some background to our approach and describes prior achievements that have made it possible, and then continue with further details on our implementation. In Paper VII we present the channel sounder. The paper is under preparation as the results from a measurement campaign is still pending. Before high resolution processing can be made, there is a need for third party 3D characterization of the antennas as well as calibration of the power level at the transmit side.

Antenna characterization needs to be performed in an anechoic chamber. It is a tedious process where a mechanical positioner rotates the antenna in small steps, and for each position, the gain pattern for a particular direction is measured. The process typically takes a few hours for an antenna, mainly limited by the mechanical positioner and the angular resolution. In our case, with $256 + 128$ gain patterns to be measured, we cannot use a standard chamber SW implementation. Instead, all antenna elements, on one of the antennas, need to be measured for each position. This sounds like a minor modification to a chamber but has shown to be a large challenge. The needed control signals to switch the antennas, the association of the measured patterns to the different elements, etc. all needs to be taken care of.

To reach a reasonable coverage with the sounder system, external amplifiers are necessary to boost the signal levels. In particular, at the transmit side a PA is needed. To protect the sensitive switches at the antennas the power needs to be accurately calibrated to not exceed what they can handle. This calibration is complicated as we are using a modulated wave form and it is the peak power of the signal that needs to be characterized, which requires a synchronized and ultra-fast power-meter to be integrated to the sounder system. A part of this

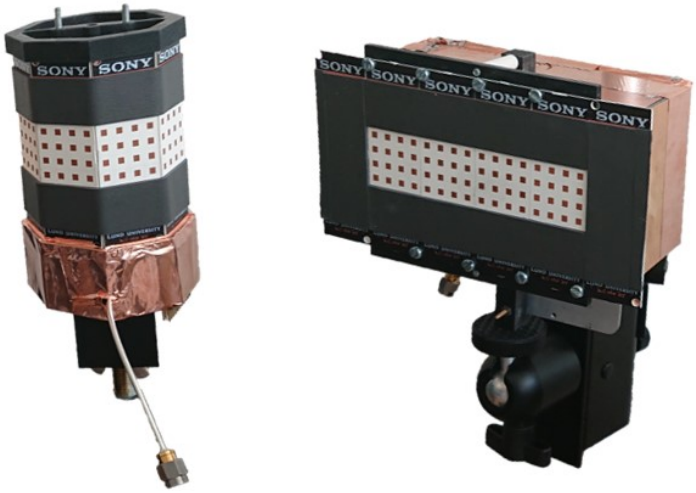

Figure 3.13: Antennas for the 28 GHz channel-sounder. Left, cylindrical array with 8 antenna panels, 265 dual-polarized patch antenna elements. Right, the flat antenna array with 4 panels and 128 dual-polarized patch antenna elements.

calibration includes verification of the phase stability of the external PA, a.k.a. load pull, from possible impedance variations over the antenna switch states. Both the antenna characterization and the power calibration was still pending during the printing of this thesis and our target is to have measured results during the fall of 2019. The rest of this section focus on the implementation part of the channel sounder and some of the challenges we faced when designing it.

3.6.1 Motivation and Enables Behind the Lund University 28 GHz Channel Sounder

Most reported mm-wave channel sounders published [63–71] are limited in at least one of the following aspects: the omnidirectional coverage, the spatial resolution, the temporal resolution, and single polarized antennas. In particular, there are no publications of mm-wave sounders capable of characterization of the dynamic properties of the transmission channel and at the same time offer a high spatial resolution and coverage. The limitations in the prior art originate from compromises. There is a strong connection between the number

of antennas to the angular resolution, the spherical coverage, the sensitivity, and the measurement duration of a channel sounder. Recent advances in semiconductor technology have enabled fast switching with lower insertion-loss at mm-wave frequencies than was possible before. This enables a far larger number of antenna elements. Furthermore, for any channel sounder, a snapshot[4] needs to be performed within the coherence time of the channel. With a switching time of less than 100 ns the duration of each switch state is mainly defined by the duration of the impulse response of the channel. This poses a compromise between the number of antenna pairs and the velocities that can be captured, which is entirely defined by the physical properties of the channel rather than the sounder implementation. Furthermore, randomized switching order removes the ambiguity in the simultaneous estimation of Doppler and spatial angles otherwise present [72]. The randomization of the switch order suppress the aliasing distortion caused by systematic switching order, however, conditioned to that the dynamic properties of the channel do not change, i.e., no acceleration present during the snapshots.

It should be noted that different sounder implementations are designed to investigate different aspects of the channel properties. In our case, the cell edge coverage is not the main interest and we can therefore compromise some of the sensitivity to the advantage of higher spatial resolution and coverage at both ends of the link.

3.6.2 mm-wave Channel Sounder System Aspects

The capability of a channel sounder is to a large extent defined by its antennas. We have designed a state of the art channel sounder with 256×128 antenna-elements, shown in Fig. 3.13. It has the following characteristics:

- High resolution in the spatial domain at both sides.
- Close to full azimuthal coverage at the receive side.
- Close to half-azimuthal coverage at the transmit side.
- Wide bandwidth enables a temporal resolution of < 1 ns.
- Dual polarization at both the transmit and the receive sides.
- Fast randomized switching, enabling estimation of dynamic channel properties.

[4] A snapshot comprises all the channels between the different antenna pairs.

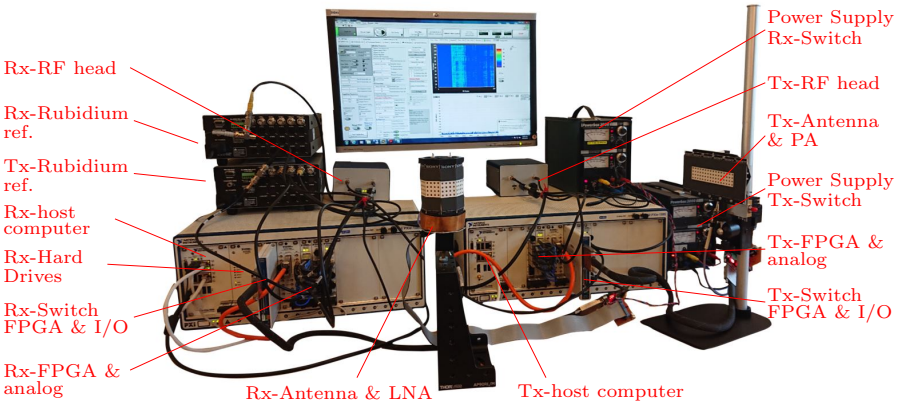

Figure 3.14: Sounder measurement system with sub-units indicated.

The channel sounder involves antenna arrangements where dual-polarized patch antennas are used to sound the channels. The sounding process is as follows: A pilot signal is transmitted between each transmit to receive antenna-pair where after the received signal at the receive side is correlated with the original waveform, and the channel impulse response (CIR) is estimates. The CIR for an antenna-pair shows the delay profile for all resolvable propagation paths between the two antennas, where the temporal resolution relates to the bandwidth of the pilot. In the post-processing stages, by combining the signals from all antenna pairs, high resolution directional and delay properties of the channel can be estimated. Larger antenna counts results in a better spatial resolution, and the directivity of different elements relates to the spherical coverage. Multiple consecutive snapshots are then used to capture the dynamics of the channel. The gain pattern of the individual antenna elements will have a large influence on the measured signals. Therefore, in the post-processing this influence needs to be calibrated and accurate characterization of the pattern from each patch antenna is a prerequisite. The entire sounder is shown in Fig. 3.14, where the different subunits are marked out. The controller program, as well as the FPGA programs, are all developed in LabVIEW environment.

3.6.3 Waveform Design and Data Processing

Based on the basic sounding procedure described above, here we share details of the waveform design (i.e., the pilot), the consequences it has on the data quantities, and the related HW implementation. The pilot waveform is based on a Zadoff-Chu (ZC) [9, 10] sequence motivated by that it has a close to flat profile in both time and frequency domains, as well as good auto-correlation properties. Our ZC sequence has a duration of 2.6 us and this sets the maximum delay spread that can be characterized. The waveform is quantified by 2048 samples in the time domain, resolved by a 12-bits. For all the 32,768 antenna-pairs this generates about 1 GB of data for every snapshot. To improve the sensitivity, the system further supports retransmissions of the pilots that then are averaged. A snapshot can be measured in 326 ms but this time extends with the level of averaging. In the end, the snapshot duration needs to be shorter than one second, as this is the trigger rate from the rubidium clocks. At the receive side, averaging and correlation are both performed in real-time in an FPGA. The CIRs are then streamed to an array of hard-discs that manage the massive data quantities in real-time. After that a measurement campaign is completed, the CIRs from all snapshots are calibrated with delay and gain profiles relevant for that measurement set-up (e.g. based on the distance between the antennas and system losses). Further post-processing of the measured CIRs is performed in MATLAB environment, where angular properties, delay profiles, dynamic properties, and clustering can be estimated.

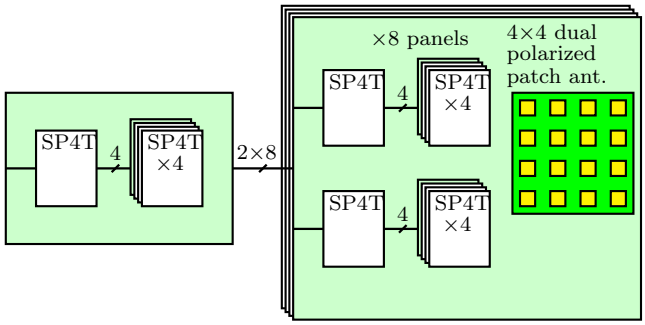

Figure 3.15: The cascaded switch topology divided into a switchboard feeding up to 8 antenna panels with 16 dual-polarized antennas each.

3.6.4 The mm-wave Sounder Antenna Integration

The switch circuitry needed to support all our antennas is based on single-pole-four-throw (SP4T) switches developed by Sony, arranged as a four-level cascade. The structure enables up to 256 antennas. Half of the switching circuitry is located on a dedicated switchboard and the other half at the antenna panels, this is shown in Fig. 3.15. The switchboard has 16 ports that can feed up to 8 antenna panels, each with two ports.

Figure 3.16: To the left, antenna panels before assembly. To the right, antenna panels assembled into the octagonal shape.

All boards are designed in a six-layer printed-circuit-board (PCB) technology based on Rogers material (Ro4450B). The process support stacked vias[5] through all layers. This enables a more compact layout with low insertion loss and made it possible to put half of the switch circuitry at the back of the panels next to the feed of the patch antennas. Each antenna is assembled from the antenna panels, shown in Fig. 3.16, each with 4×4 dual-polarized patch antennas. A corrugation structure (i.e., the horizontal stripes on the panels in Fig. 3.16) was introduced to prevent surface currents from distorting the antenna gain patterns. Due to processing limitations, the required grounding of the corrugation structure could not be supported, and a layer of an absorbing material was later added instead. The panels are further assembled into an eight faced cylinder shown to the right in Fig. 3.16 and to the left in Fig. 3.13, and the flat array shown to the right in Fig. 3.13.

[5] Stacked vias enable signal-paths to go through arbitrary layers of a PCB without introducing sidewise offsets.

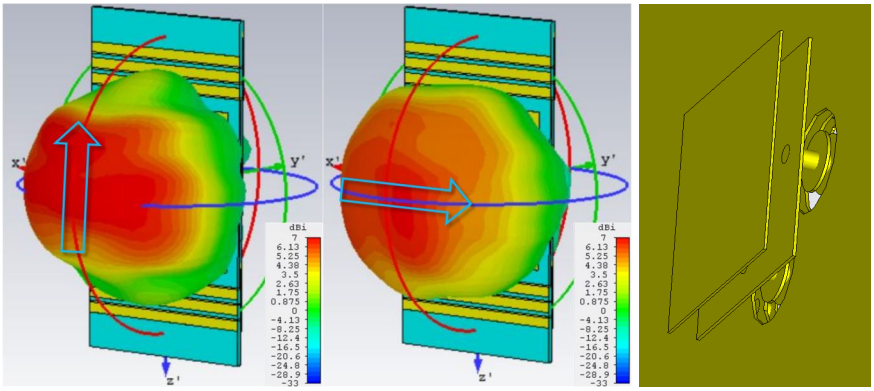

Figure 3.17: To the left, simulated gain patterns for vertical and horizontal polarization. To the right, the structure of a dual-polarized patch antenna element.

The antenna elements, shown to the right in Fig. 3.17, are capacitively coupled patch elements designed in a three-layered structure. The lowest layer in the patch design is the ground plane; the second layer elevated 100 μm, is a dual feed coupling element; and the top layer elevated 300 μm, is the radiating patch. The coupling element in combination with the patch generate two closely spaced resonances that are tuned to achieve a bandwidth that covers the desired frequencies. The simulated radiation patterns for both the vertical and horizontal modes from a patch element is shown in Fig. 3.17, with a peak gain of about 6 dB. The -3 dB beamwidth is about 85° in azimuth and 50° in elevation for both modes. The simulated total -10 dB return-loss BW is about 4 GHz, and this matches the measured radiation BW. The simulated isolation between antenna elements is about 20 dB, but does not include the switch circuitry. The peak radiated power from the antenna panel including the switch circuitry was measured and compared to that of a reference patch antenna. The insertion loss (IL) from the switch circuitry was then estimated to about 5 dB, which is close to the expectation. The total IL from cabling and switch circuitry, including the switchboard, is about 15 dB for the fully assembled antenna.

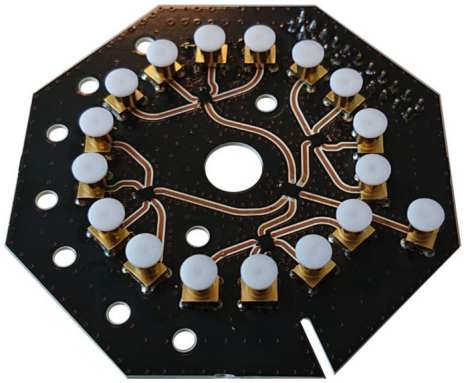

Figure 3.18: The switchboard with two layers of cascaded SP4T switches, coaxial connectors for input and 16 outputs and a control interface.

Each switchboard include the first two layers of the switch cascade and is equipped with a coaxial connector for the feeding and 16 coaxial connectors that distribute the signal to the panels. The switchboard is shown in Fig 3.18. Amplifiers are attached to the feeds at both the receive and transmit antennas. This ensures that we can maximize the link budget by having an as high power as the switches can tolerate at the transmit side, despite a long feed cable. Similar at the receive side, a low-noise amplifier (LNA) is used to minimize degradation of the SNR from cable-related loss.

3.6.5 Sounder features

The sounder design is flexible from the aspect that the number of antenna pairs can easily be changed by downloading a different codebook. This enables a shorter snapshot duration, which in turn enables estimation of higher Doppler, i.e., higher velocity of antennas or scatterers. For example, if the snapshot duration needs to be shortened a codebook limited in: polarization, bi-directionality, omnidirectional coverage, or spatial resolution can be used. With all antennas included in a snapshot, the snapshot rate is limited to a single snapshot per second due to the large quantity of data. By reducing the set of antennas, the snapshot rate can be increased. This will increase the ability to estimate the second order statistics of the dynamic channel properties.

Chapter 4

Contributions

The thesis is built on seven manuscripts of which four are peer-reviewed, one is accepted for publication with minor revision, one is submitted, and one is still being drafted and is pending measured results. All seven manuscripts are included in the second part of this dissertation. In general, the planning of each investigation and the strategies for evaluating results have been discussed with the relevant co-authors. I am lead author on all papers included in the thesis and have also contributed a majority of the text in them. Based on all papers I have created presentation material and in some cases posters, which have been presented at various conferences.

Furthermore, I have written all simulation code and performed the simulation studies on which the publications are based. I have also performed essentially all sub-6 GHz measurements, designed and built hardware prototypes specific to the terminal measurements. In this process, I have used the available experimental equipment in the department lab, such as the LuMaMi massive MIMO testbed and channel sounders. Below follow the contributions from each paper where I have defined my part beyond what was specified above:

Paper I
E. L. Bengtsson, F. Tufvesson, O. Edfors, "UE Antenna Properties and Their Influence on Massive MIMO System Performance" *in Proc. of the 9:th European Conference on Antennas and Propagation (EuCAP)*, Lisbon, Portugal, Apr. 2015.
Contributions: This publication introduces simulation results from an early implementation of a stochastic-geometric simulation framework. The results reveal the advantage of using a more realistic stochastic-geometric approach rather than a Kronecker based. We investigate the correlation and gain prop-

erties of a dual-antenna terminal under different conditions related to a MaMi channel. Channel properties, in terms of number clusters of coherent signals from different illumination angles and the angular spread, are investigated. The coherently received signals are compared to non-coherently received to give an idea of the array gain and its dependency on the environment. Multiplexed performance and how it relates to channel richness are presented, in this publication, using multiplexing-gains. This measure has the advantage that it does not depend on absolute SNR. The results presented in the paper contribute to the understanding of how the terminal is influenced by the effective channel in a MaMi system. In particular, how the number of clusters in a channel influence the correlation and gain properties at the terminal antennas.
My part: This is mainly a self-contained investigation with contributions as above. In addition, I gave the presentation at the conference in Lisbon, Portugal.

Paper II:
E. L. Bengtsson, P. C. Karlsson, F. Tufvesson, J. Vieira, S. Malkowsky, L. Liu, F. Rusek, O. Edfors, "Transmission Schemes for Multiple-Antenna Terminals in Massive MIMO system" *in Proc. of GLOBECOM 2016*, Washington DC, USA, Dec. 2016. **Paper II:**

Contributions: Here we introduce the multiple-antenna communication protocol and derive SNR-gains, which we use in our comparisons. Different transmission schemes for two-antenna terminals are introduced. Likely, based on the first-ever measured channels with two-antenna terminals with integrated antennas in a MaMi system, we derive performance for switched-diversity, dominant-eigenmode, passive-receive-diversity, and multiplexed-operation. For the latter, we compare capacities at a selected SNR level. The main conclusion is that we show the importance of having pilot transmit capability on all antennas in the terminal.
My part: This investigation needed some input about, and assistance on, the LuMaMi testbed. This was contributed by co-authors. The remaining work was all performed by me. I gave the presentation at the conference in Washington DC, USA.

Paper III:
E. L. Bengtsson, F. Rusek, S. Malkowsky, F. Tufvesson, P. C. Karlsson, O. Edfors, "A simulation Framework for Multiple-Antenna Terminals in Massive MIMO Systems" *IEEE Access*, Vol. 5, pp 26819-26831, 2017.
Contributions: In this publication, the complete stochastic-geometric simulation framework is presented. From a list of assumptions, we derive a simplified channel model where only three parameters are needed to define the

environment. We use the method of maximum likely-hood to match the distribution of the Gramian generated by the framework to that of measurements. Measured and simulated SNR-gains are compared for the different diversity schemes. The main contributions is that we show that the simulator can generate realistic channel distributions, we confirm the importance of having pilot transmit capability at all terminal antennas.
My part: This publication contains one of the mathematical frameworks for the simulations, which was discussed with co-authors. The main work in developing the simulation framework was done by me.

Paper IV:
E. L. Bengtsson, F. Rusek, F. Tufvesson, P. C. Karlsson, O. Edfors, "Analysis of Transmission Schemes for Dual-Antenna Terminals in Massive MIMO Systems" *in Proc. of the 25:th International Conference on Telecommunications (ICT2018)*, Saint Malo, France, Jun. 2018.
Contributions: In this publication, we use a fully-stochastic simulation approach. Based on the Kronecker assumption we study different diversity schemes under different noise conditions. We conclude that the UL pilot is crucial and defines the performance. Via closed-form expressions we analyze the behavior of what we call dominant-eigenmode and passive-receive-diversity schemes. The areas in which the different transmission schemes are most effective is compared to scatter plots from measured channels, and the associated distributions are presented. The main contribution of this paper is that we show that the Gramian converge toward the covariance matrix as the number of MS antennas grow large. Thus, the terminal can get instant access to an estimate of the covariance matrix.
My part: This publication contains another (simplified) mathematical framework of the simulations, which was also discussed with co-authors. The main work in developing the simulation framework was done by me. I gave the presentation at the conference in Saint-Malo, France.

Paper V:
E. L. Bengtsson, F. Rusek, P. C. Karlsson, F. Tufvesson, O. Edfors, "Simulation of Multiple-Antenna Terminal Performance in Massive MIMO Systems based on Indoor Measurements" *Accepted for publication with minor revision, in IEEE Transactions on Vehicular Technology (TVT)*, 2019.
Contributions: This work is a continuation of Paper III, where we use the stochastic-geometric simulation framework to evaluate different transmission schemes based on a four-antenna terminal. We show that the simulation framework is capable of generating a distribution that matches a specific measurement scenario. We conclude that the distribution changes dramatically for

a generic cluster distribution. From simulations of a four-antenna terminal, we conclude that switched solutions reach the rank-conditioned capacity. Thus, terminal-antenna count is more important than the number of transceivers.
My part: A paper in which the framework derived in Paper III is further investigated and tuned to/compared with measurements. The investigation was discussed with co-authors. I performed all measurements and evaluations.

Paper VI:
E. L. Bengtsson, J. Flordelis, F. Rusek, P. C. Karlsson, F. Tufvesson, O. Edfors, "A Case Study on the Influence of Multiple Users on the Effective Channel in a Massive MIMO System" *submitted to Wireless Communications Letters (WCL)*, 2019.
Contributions: We make a deeper investigation in how the effective channel behave from a terminal perspective, with a zero-forcing (ZF) precoder at the BS, under the influence of multiple terminals. We explain the low cluster-count seen by a terminal. Supported by the measurement results, we confirm that with > 40 BS antennas, MaMi properties apply and that it is possible to resolve 20 streams with a reduction only in channel strength. We demonstrate that two terminals with a distance of only 5 m, share essentially no clusters. We study empirically the advantage BDZF have over classical ZF in MaMi systems and relate it to the terminal antenna correlation.
My part: A comparative measurement study, based on a large set of measurements all performed by me. Evaluations and comparisons discussed with co-authors.

Paper VII:
E. L. Bengtsson, H. Tataria, P. C. Karlsson, O. Edfors, F. Tufvesson, "A 28 GHz Channel Sounder for Dynamic Propagation Measurements" *to be submitted to IEEE Transactions on Wireless Communications*, 2019.
Contributions: This paper presents the design and implementation of a massive-antenna based channel sounder. The sounder is capable of measuring dynamic propagation-channels at 28 GHz with dual-polarization, bi-directionality, highly resolved in spatial as well as in temporal domains. We present the implementation of the 256×128 dual-polarized antenna arrays and the associated switch circuitry. We detail both the hardware and software implementation of the entire sounder system as well as the waveform design. Furthermore, the result of a measurement campaign will be included in the paper.
My part: For this paper there was a broader collaboration between co-authors. I am still the lead author, but there have been more contributions from co-authors here than in the other publications. I have been heavily

involved in both the antenna design, re-programming, and evaluation of the designed channel sounder.

In addition, I have contributed to two additional publications where I am not the main author:

Paper VIII: K. Zhao and E. Bengtsson and Z. Ying and S. He, "Multiplexing efficiency of high order MIMO in mobile terminal in different propagation scenarios", *Proceedings of the 10th European Conference on Antennas and Propagation (EUCAP)*, Apr. 2016.
My Contribuions: The study is partly based on my simulation framework, from which parts where shared, i.e., for illumination of antenna gain patterns.

Paper IX: P. Harris, S. Malkowsky, J. Vieira, E. L. Bengtsson, F. Tufvesson, W. B. Hasan, L, Liu, M. Beach, S. Armour, O. Edfors, "Performance Characterization of a Real-Time Massive MIMO System with LOS Mobile Channels", *IEEE Journal on Selected Areas in Communications*, pp.1244-1253, Apr. 2017.
My Contributions: My contribution to this paper is limited to support during measurements and review of the paper.

Chapter 5

General Conclusions and Future Work

The vision of this research was based on the capability of a MaMi system: to investigate the propagation channel behavior at the terminal side; to develop simulation tools that reflect these properties; and to derive terminal algorithms that utilize the properties of the effective channel. The target was to start at sub-6 GHz and then extend it to mm-wave frequencies.

The work in the MaMi sub-6 GHz area most importantly has brought up the importance for each terminal-antenna to have pilot transmission capability. All results show that today's opportunistic diversity and multiplexing approaches do not work well in a MaMi system and that different algorithms are needed. Like in conventional MIMO systems, the asymmetric traffic-load, with less uplink-traffic than downlink-traffic makes it attractive for cost reasons to have fewer transmit chains than receive chains. We have shown that switched architectures reach close to the rank-conditioned capacity. This suggests that, from a power/cost optimization perspective, it is advantageous to increase the terminal-antenna count but not necessary to have a transceiver associated with each antenna. uplink switched diversity is an option that enables all antennas to transmit pilots, and at the same time allows for downlink multiplexed operation. Additionally, switched antennas need to be considered also at the system side as uplink pilots, in this case, cannot be transmitted simultaneously from the multiple terminal antennas. An interesting observation is that the terminal in a massive MIMO system, based on the channel hardening, can get instantaneous access to an estimate of the covariance matrix. This enables the terminal to compute optimal pilot vectors with a minimal effort. The results

further confirm the importance of taking spatial properties into account both in channel modeling and for the evaluation of MaMi systems. They suggest that typical isotropic antenna characterization parameters, (e.g. total radiated power, envelope correlation coefficient, mean effective gain, etc.) will not give accurate predictions of what performance to expect in a MaMi system. To this end, the importance of using integrated antennas with spatial properties that can be expected from real products with multiple antennas has also been shown. One of the largest challenges was to match simulated channel distributions to those measured. During this process the importance of accurately reflecting the measurement conditions in the simulation environment become clear. This also showed that in order to obtain simulation parameters that reflect an environment, massive measurement campaigns are needed. Furthermore, we found that the effective channel depend only dominant clusters. This has the effect that the number of active terminals in the system will influence the effective channel and to enable an accurate channel model the raw propagation channel data shall be used, this is possible with the LuMaMi channel capturing feature. Further research on sub-6 GHz MaMi systems should address the relation between eigenmodes and clusters. Such investigation would be greatly simplified with a calibrated BS antenna, as it would allow for a geometrical interpretation of the clusters which is essential for the simulation framework.

When it comes to mm-wave systems, our vision was also here to study terminal aspects. How different antenna configurations best can utilize an available channel. The vision was to adapt the cluster-based simulation framework to the mm-wave case and further study different terminal strategies. However, time runs fast, and my work as a Ph.D. student in the mm-wave area focused on the design and implementation of a state of the art 28 GHz channel sounder. The sounder is presented in Paper VII and can be considered the first step towards the vision. In short, technology advancements relating to insertion loss in semi-conductor switches, and switching strategies, enable a massive number of fast switched antenna elements. This, in turn, enables measurement of dynamic properties of the propagation channel with a never before published resolution and coverage. The sounder is presented in Paper VII.

Further measurements with the mm-wave sounder will be performed. A potential influence on channel models for mobile scenarios and accurate positioning for mm-wave frequencies are among the target areas. Related to this, a frequency up-conversion of the LuMaMi testbed to 28 GHz, for real-time evaluation of precoded massive MIMO channels, is implemented. With realistic handset implementations measured in the same environment as was measured with the sounder, further steps towards our vision can be made.

References

[1] T. L. Marzetta, "Noncooperative Cellular Wireless with Unlimited Numbers of Base Station Antennas OFDM," *IEEE Trans. Wireless Commun.*, vol. 9, no. 11, pp. 3590–3600, Nov. 2010, doi: http://dx.doi.org/10.1109/TWC.2010.092810.091092.

[2] F. Rusek, D. Persson, B. K. Lau, E. G. Larsson, T. L. Marzetta, O. Edfors, and F. Tufvesson, "Scaling Up MIMO: Opportunities and Challenges with Very Large Arrays," *IEEE Signal Processing Magazine*, vol. 30, no. 1, pp. 40–60, Dec. 2012, doi: http://dx.doi.org/10.1109/MSP.2011.2178495.

[3] B. M. Hochwald, T. L. Marzetta, and V. Tarokh, "Multiple-Antenna Channel Hardening and its Implications for Rate Feedback and Scheduling," *IEEE Trans. Inf. Theory*, vol. 50, no. 9, pp. 1893–1909, Sep. 2004, doi: http://dx.doi.org/10.1109/TIT.2004.833345.

[4] E. Björnson, E. G. Larsson, and T. L. Marzetta, "Massive MIMO: 10 Myths and One Critical Question," *IEEE Communications Magazine*, pp. 114–123, Feb. 2016, doi: http://10.1109/MCOM.2016.7402270.

[5] E. G. Larsson, F. Tufvesson, O. Edfors, and T. L. Marzetta, "Massive MIMO for Next Generation Wireless Systems," *IEEE Communications Magazine*, vol. 52, no. 2, pp. 186–195, Feb. 2014, doi: http://dx.doi.org/10.1109/MCOM.2014.6736761.

[6] H. Q. Ngo, E. G. Larsson, and T. L. Marzetta, "Energy and Spectral Efficiency of Very Large Multiuser MIMO Systems," *IEEE Transactions on Communications*, vol. 61, no. 4, pp. 1436–1449, Apr. 2013, doi: http://dx.doi.org/10.1109/TCOMM.2013.020413.110848.

[7] E. G. Larsson, T. L. Marzetta, H. Yang, and H. Q. Ngo, *Fundamentals of Massive MIMO*, 1st ed. CAMBRIDGE UNIVERSITY PRESS, 2016.

[8] E. Björnson, J. Hoydis, and L. Sanguinetti, *Massive MIMO Networks: Spectral, Energy, and Hardware Efficiency*, 1st ed. now Publishers Inc., 2017.

[9] D. Chu, "Polyphase codes with good periodic correlation properties (Corresp.)," *IEEE Transactions on Information Theory*, vol. 18, no. 4, pp. 531–532, July 1972, url: http://10.1109/TIT.1972.1054840.

[10] R. Frank, "Comments on "Polyphase codes with good periodic correlation properties" by Chu, David C." *IEEE Transactions on Information Theory*, vol. 19, no. 2, pp. 244–244, March 1973, url: http://10.1109/TIT.1973.1054970.

[11] J. Proakis and M. Salehi, *Digital Communications*, 5th ed. Mc Graw Hill, 2014.

[12] A. F. Molisch, V. V. Ratnam, S. Han, Z. Li, S. L. H. Nguyen, L. Li, and K. Haneda, "Hybrid Beamforming for Massive MIMO: A Survey," *IEEE Communications Magazine*, vol. 55, no. 9, pp. 134–141, Sep. 2017, doi: http://dx.doi.org/10.1109/MCOM.2017.1600400.

[13] H. D. Young, *Physics*, 8th ed. Addison-Wesley Publishing Company, 1992.

[14] M. Alleven, "Samsung conducting Massive MIMO demo with Sprint at MWCA," https://www.fiercewireless.com/wireless/samsung-conducting-massive-mimo-demo-sprint-at-mwca, Sep. 2017.

[15] Z. Jiang, A. F. Molisch, G. Caire, and Z. Niu, "Achievable Rates of FDD Massive MIMO Systems With Spatial Channel Correlation," *IEEE Transactions on Wireless Communications*, vol. 14, no. 5, pp. 2868–2882, May 2015, doi: http://dx.doi.org/10.1109/TWC.2015.2396058.

[16] J. Flordelis, F. Rusek, F. Tufvesson, E. G. Larsson, and O. Edfors, "Massive MIMO Performance - TDD Versus FDD: What Do Measurements Say?" *CoRR*, vol. abs/1704.00623, 2017. [Online]. Available: http://arxiv.org/abs/1704.00623

[17] *Technical Specification Group Services and System Aspects for Release 15*, 15th ed., ETSI, 3GPP TR 21.95 v1.1.0, Mar. 2019.

[18] A. F. Molisch, *Wireless Communications*, 2nd ed. Wiley, 2012.

[19] X. Gao, O. Edfors, F. Rusek, and F. Tufvesson, "Linear Pre-Coding Performance in Measured Very-Large MIMO Channels," *Proc. of the 74th IEEE Vehicular Technology Conference*, 2011.

[20] ——, "Massive MIMO Performance Evaluation Based on Measured Propagation Data," *IEEE Transactions on Wireless Communications*, vol. 14, no. 7, pp. 3899–3911, Jul. 2015, doi: http://dx.doi.org/10.1109/TWC.2015.2414413.

[21] E. Björnson, E. G. Larsson, and M. Debbah, "Massive MIMO for Maximal Spectral Efficiency: How Many Users and Pilots Should Be Allocated?" *IEEE Transactions on Wireless Communications*, vol. 15, no. 2, pp. 1293–1308, Feb 2016, doi: http://dx.doi.org/10.1109/TWC.2015.2488634.

[22] Q. H. Spencer, A. L. Swindlehurst, and M. Haardt, "Zero-Forcing Methods for Downlink Spatial Multiplexing in Multiuser MIMO Channels," *IEEE Transactions on Signal Processing*, vol. 52, no. 2, pp. 461–471, Feb. 2004.

[23] J. Vieira, "Doctoral Thesis: Algorithms and Proofs of Concept for Massive MIMO Systems," *Series of Licentiate and Doctoral Theses*, 2017.

[24] A. Paulraj, R. Nabar, and D. Gore, *Introduction to Space-Time Wireless Communications*, 1st ed. Cambridge University Press, 2003.

[25] E. Björnson, J. Hoydis, M. Kountouris, and M. Debbah, "Massive MIMO Systems with Non-Ideal Hardware: Energy Efficiency, Estimation, and Capacity Limits," *IEEE Transactions on Information Theory*, vol. 60, no. 11, pp. 7112–7139, Nov. 2014, doi: http://dx.doi.org/10.1109/TIT.2014.2354403.

[26] À. O. Martínez, P. Popovski, J. Ø. Nielsen, and E. D. Carvalho, "Experimental Study of the Benefits of a Second Antenna at the User Side in a Massive MIMO System," *IEEE Access*, vol. PP, no. 99, pp. 1–1, 2017, doi: http://dx.doi.org/10.1109/ACCESS.2017.2785860.

[27] B. Clerckx and C. Oestges, *MIMO Wireless Networks*, 2nd ed. Academic Press, 2013.

[28] G. Foschini and M. Gans, "On Limits of Wireless Communications in Fading Environment when Using Muntiple Antennas," *Wireless Personal Communications*, vol. 6, no. 3, pp. 311–335, Mar. 1998, doi: https://doi.org/10.1023/A:1008889222784.

[29] R. G. Vaughan and J. B. Andersen, "Antenna Diversity in Mobile Communications," *IEEE Transactions on Vehicular Technology*, vol. 36, no. 4, pp. 149–172, Nov. 1987, doi: http://dx.doi.org/10.1109/T-VT.1987.24115.

[30] A. Holst and V. Ufnarovski, *Matrix Theory*, 1st ed. Studentlitteratur, 2014.

[31] B. Fletcher, "Verizon hits 10 5G cities with Phoenix launch," https://www.fiercewireless.com/5g/verizon-hits-10-5g-cities-phoenix-launch, Aug. 2019.

[32] *Study on New Radio (NR) Access Technology*, 14th ed., ETSI, 3GPP TR 38.912, 2017.

[33] X. Gao, F. Tufvesson, O. Edfors, and F. Rusek, "Measured Propagation Characteristics for Very-Large MIMO at 2.6 GHz," in *Proc. of Asilomar Conference on Signals, Systems and Computers (ASILOMAR)*, Nov. 2012, pp. 295–299, doi: http://dx.doi.org/10.1109/ACSSC.2012.6489010.

[34] A. T. James, "Distributions of Matrix Variates and Latent Roots Derived from Normal Samples," *The Annals of Mathematical Statistics*, vol. 35, no. 2, pp. 475–501, 1964, doi: http://www.jstor.org/stable/2238504.

[35] P. J. Smith, S. Roy, and M. Shafi, "Capacity of MIMO systems with semi-correlated flat fading," *IEEE Trans. Information Theory*, vol. 49, no. 10, pp. 2781–2788, 2003, doi: http://dx.doi.org/10.1109/TIT.2003.817472.

[36] A. M. Tulino, A. Lozano, and S. Verdu, "Impact of Antenna Correlation on the Capacity of Multiantenna Channels," *IEEE Transactions on Information Theory*, vol. 51, no. 7, pp. 2491–2509, July 2005, doi: http://dx.doi.org/10.1109/TIT.2005.850094.

[37] H. Tataria, P. J. Smith, and P. A. Dmochowski, "On the General Analysis of Coordinated Regularized Zero-Forcing Precoding: An Application to Two-Tier Small-Cell Networks," *IEEE Transactions on Communications*, vol. 65, no. 7, pp. 3133–3150, July 2017, doi: http://dx.doi.org/10.1109/TCOMM.2017.2695199.

[38] M. Matthaiou, M. R. McKay, P. J. Smith, and J. A. Nossek, "On the condition number distribution of complex wishart matrices," *IEEE Trans. Communications*, vol. 58, no. 6, pp. 1705–1717, 2010, doi: http://dx.doi.org/10.1109/TCOMM.2010.06.090328.

[39] H. Tataria, P. J. Smith, L. J. Greenstein, P. A. Dmochowski, and M. Shafi, "Performance and Analysis of Downlink Multiuser MIMO Systems with Regularized Zero-Forcing Precoding in Ricean Fading Channels," in *2016 IEEE International Conference on Communications (ICC)*, May 2016, pp. 1–7, doi: http://dx.doi.org/10.1109/ICC.2016.7510850.

[40] A. Zanella, M. Chiani, and M. Z. Win, "On the Marginal Distribution of the Eigenvalues of Wishart Matrices," *IEEE Transactions on*

Communications, vol. 57, no. 4, pp. 1050–1060, April 2009, doi: http://dx.doi.org/10.1109/TCOMM.2009.04.070143.

[41] P. Almers, E. Bonek, A. Burr, N. Czink, M. Debbah, V. Degli-Esposti, H. Hofstetter, P. Kyösti, D. Laurenson, G. Matz, A. Molisch, C. Oestges, and H. Özcelik, "Survey of Channel and Radio Propagation Models for Wireless MIMO Systems," *EURASIP Journal on Wireless Communications and Networking*, pp. 1–19, 2007, doi: http://10.1155/2007/19070.

[42] *Digital Mobile Radio Towards Future Generation Systems*, Final ed., COST, 231.

[43] J. Flordelis, X. Gao, G. Dahman, F. Rusek, O. Edfors, and F. Tufvesson, "Spatial Separation of Closely-Spaced users in Measured Massive Multi-User MIMO Channels," in *Proc. IEEE International Conference on Communications (ICC)*. IEEE, Jun. 2015, pp. 1441–1446, doi: http://dx.doi.org/10.1109/ICC.2015.7248526.

[44] X. Gao, J. Flordelis, G. Dahman, F. Tufvesson, and O. Edfors, "Massive MIMO Channel Modeling - Extension of the COST 2100 Model," 2015.

[45] *Study on Scenarios and Requirements for Next Generation Access Technologies*, 14th ed., ETSI, 3GPP TR 38.913, 2017.

[46] M. Shafi, J. Zhang, H. Tataria, A. F. Molisch, S. Sun, T. S. Rappaport, F. Tufvesson, S. Wu, and K. Kitao, "Microwave vs. Millimeter-Wave Propagation Channels: Key Differences and Impact on 5G Cellular Systems," *IEEE Communications Magazine*, vol. 56, no. 12, pp. 14–20, December 2018, doi: http://dx.doi.org/10.1109/MCOM.2018.1800255.

[47] *Universal Mobile Telecommunications System UMTS Spatial channel model for Multiple Input Multiple Output MIMO simulations*, 12th ed., ETSI, 3GPP TR 25.996, 2014.

[48] R. Verdone and A. Zanella, *Pervasive Mobile and Ambient Wireless Communications*, final ed., COST 2100, 2012.

[49] Q. H. Spencer, B. D. Jeffs, M. A. Jensen, and A. L. Swindlehurst, "Modeling the statistical time and angle of arrival characteristics of an indoor multipath channel," *IEEE Journal on Selected Areas in Communications*, vol. 18, no. 3, pp. 347–360, March 2000, doi: http://10.1109/49.840194.

[50] Y. Li, J. Zhang, and Z. Ma, "Clustering in Wireless Propagation Channel With a Statistics-Based Framework," in *2018 IEEE Wireless Communications and Networking Conference (WCNC)*, April 2018, pp. 1–6, doi: http://10.1109/WCNC.2018.8377218.

[51] K. Yu, Q. Li, D. Cheung, and C. Pretie, "On the Tap and Cluster Angular Spreads of Indoor WLAN Channels," *Proceedings IEEE Vehicular Technology Conference*, 2004.

[52] J. Poutanen, J. Salmi, K. Haneda, V. Kolmonen, F. Tufvesson, and P. Vainikainen, "Propagation Characteristics of Dense Multipath Components," *IEEE Antennas and Wireless Propagation Letters*, vol. 9, pp. 791–794, 2010, doi: http://10.1109/LAWP.2010.2064751.

[53] A. F. Molisch, "A Generic Model for MIMO Wireless Propagation Channels in Macro- and Microcells," *IEEE Transactions on Signal Processing*, vol. 52, no. 1, pp. 61–71, Jan 2004, doi: http://dx.doi.org/10.1109/TSP.2003.820144.

[54] P. Harris, S. Malkowsky, J. Vieira, E. Bengtsson, F. Tufvesson, W. Hasan, L. Liu, M. Beach, S. Armour, and O. Edfors, "Performance Characterization of a Real-Time Massive MIMO System with LOS Mobile Channels," *IEEE Journal on Selected Areas in Communications*, pp. 1244–1253, Apr. 2017.

[55] "New World Record in 5G Wireless Spectrum Efficiency," https://www.sciencedaily.com/releases/2016/03/160323115500.htm, 2016.

[56] "Introducing Facebook's new Terrestrial Connectivity Systems, Terragraph and Project ARIES," https://code.facebook.com/posts/1072680049445290/introducing-facebook-s-new-terrestrial-connectivity-systems-terragraph-and-project-aries, 2016.

[57] A. Nordrum, "5G Researchers Set New World Record For Spectrum Efficiency," *IEEE Spectrum*, May 2016.

[58] D. K. Chengi, *Field and Wave Electromagnetics*, 2nd ed. Addison-Wesley Publishing Company, 1989.

[59] *Technical Specification Group Services and System Aspects for Release 14*, 11th ed., ETSI, 3GPP TR 37.902, Jan. 2014.

[60] K. Zhao, E. Bengtsson, Z. Ying, and S. He, "Multiplexing Efficiency of High Order MIMO in Mobile Terminal in Different Propagation Scenarios," in *Proceedings of the 10th European Conference on Antennas and Propagation (EUCAP)*, Apr. 2016, pp. 1–4.

[61] J. Vieira, S. Malkowsky, K. Nieman, Z. Miers, N. Kundargi, L. Liu, I. Wong, V. Öwall, O. Edfors, and F. Tufvesson, "A Flexible 100-Antenna

Testbed for Massive MIMO," in *Globecom Workshops (GC Wkshps)*, 2014, pp. 287–293.

[62] S. Malkowsky, J. Vieira, L. Liu, K. Nieman, N. Kundargi, I. Wong, F. Tufvesson, V. Öwall, and O. Edfors, "The Worlds First Real-Time Testbed for Massive MIMO: Design, Implementation, and Validation," *IEEE Access*, vol. 5, pp. 9073 – 9088, May. 2017, doi: http://dx.doi.org/10.1109/ACCESS.2017.2705561.

[63] R. Sun, C. A. Gentile, J. Senic, P. Vouras, P. B. Papazian, N. T. Golmie, and K. A. Remley, "Millimeter-Wave Radio Channels vs. Synthetic Beamwidth," *IEEE Communications Magazine*, vol. 56, no. 12, pp. 53–59, December 2018, doi: http://10.1109/MCOM.2018.1800177.

[64] C. Gentile, P. B. Papazian, N. Golmie, K. A. Remley, P. Vouras, J. Senic, J. Wang, D. Caudill, C. Lai, R. Sun, and J. Chuang, "Millimeter-Wave Channel Measurement and Modeling: A NIST Perspective," *IEEE Communications Magazine*, vol. 56, no. 12, pp. 30–37, December 2018, doi: http://10.1109/MCOM.2018.1800222.

[65] C. U. Bas, R. Wang, D. Psychoudakis, T. Henige, R. Monroe, J. Park, J. Zhang, and A. F. Molisch, "A Real-Time Millimeter-Wave Phased Array MIMO Channel Sounder," in *2017 IEEE 86th Vehicular Technology Conference (VTC-Fall)*, Sep. 2017, pp. 1–6, doi: http://10.1109/VTCFall.2017.8287875.

[66] J. Ko, Y. Cho, S. Hur, T. Kim, J. Park, A. F. Molisch, K. Haneda, M. Peter, D. Park, and D. Cho, "Millimeter-Wave Channel Measurements and Analysis for Statistical Spatial Channel Model in In-Building and Urban Environments at 28 GHz," *IEEE Transactions on Wireless Communications*, vol. 16, no. 9, pp. 5853–5868, Sep. 2017, doi: http://10.1109/TWC.2017.2716924.

[67] S. Salous, "Multi-band multi-antenna chirp channel sounder for frequencies above 6 GHz," in *2016 10th European Conference on Antennas and Propagation (EuCAP)*, April 2016, pp. 1–4, doi: http://10.1109/EuCAP.2016.7481753.

[68] S. Salous, S. M. Feeney, X. Raimundo, and A. A. Cheema, "Wideband MIMO Channel Sounder for Radio Measurements in the 60 GHz Band," *IEEE Transactions on Wireless Communications*, vol. 15, no. 4, pp. 2825–2832, April 2016, doi: http://10.1109/TWC.2015.2511006.

[69] "5G Channel Sounding, Reference Solution. [Online]." available: https://
/literature.cdn.keysight.com/litweb/pdf/5992-0983EN.pdf?id=2630865.

[70] Z. Wen, H. Kong, Q. Wang, S. Li, X. Zhao, M. Wang, and S. Sun, "mmWave channel sounder based on COTS instruments for 5G and indoor channel measurement," in *2016 IEEE Wireless Communications and Networking Conference*, April 2016, pp. 1–7, doi: http://10.1109/WCNC.2016.7564643.

[71] J. Ala-Laurinaho, J. Aurinsalo, A. Karttunen, M. Kaunisto, A. Lamminen, J. Nurmiharju, A. V. Räisänen, J. Säily, and P. Wainio, "2-D Beam-Steerable Integrated Lens Antenna System for 5G*E*-Band Access and Backhaul," *IEEE Transactions on Microwave Theory and Techniques*, vol. 64, no. 7, pp. 2244–2255, July 2016, doi: http://10.1109/TMTT.2016.2574317.

[72] R. Wang, O. Renaudin, C. U. Bas, S. Sangodyin, and A. F. Molisch, "Antenna Switching Sequence Design for Channel Sounding in a Fast Time-Varying Channel," in *2018 IEEE International Conference on Communications (ICC)*, May 2018, pp. 1–6, doi: http://10.1109/ICC.2018.8422542.

Appendix A

In this appendix, we have collected derivations of formulas used for extraction of the Gramian based on received signal properties for different BS precoders.

Throughout the work, different precoders have been used at the BS side. Common for them all is that they, for the single terminal case, all obtain the same effective channel to the UE. The normalization of the transmitted signal at the BS heavily depends on the precoder. Here we use the term precoding, both for the multiplexing related operations and the normalization that defines the power allocation. For the communication scheme shown in Fig. 1.4 we used UP-MR precoding, motivated by the fact that the equations become less involved compared to e.g. ZF. When there is only a single stream in the system, the effective channel becomes the same as that of ZF. This means that the relative power allocation and phase offset between the BS antennas is the same. Therefore, also relative power, phase, and polarization between the signals along different propagation paths is the same. The difference is the normalization factor. The ZF strives to keep the power level at the terminal constant while the UP-MR feeds a constant power of one to the channel. For the Kronecker based simulations and in some cases where we post process measured channels, UP-MR is used while the LuMaMi testbed uses ZF. In the cluster-based simulator, we use a third approach, namely, MR precoder without any power normalization at the BS. This approach has the advantage, in a simulation context, that the magnitude of the received signal at the terminal antennas directly reflects the Gramian.

To derive the correlation, α, and imbalance, β, used for comparison of the effective channels based on received signals from measurements or various simulations, we need to take different approaches depending on the precoder. In Table 1 our precoders and the influence they have on the signal received by a terminal are listed. In the derivations below, the terminal noise is set to zero. The equations reflect a two antenna terminal to keep it simple. Similar derivations can be made for a higher number of terminal antennas.

Table 1: BS precoder impact

Method	Precoder	Influence on the signal at the terminal
ZF	$\boldsymbol{W} = \frac{\boldsymbol{h}_p}{\|\boldsymbol{h}_p\|^2}$	$\boldsymbol{P}_{\mathrm{UE}} \sim$ C (where C is a constant)
UP-MR	$\boldsymbol{W} = \frac{\boldsymbol{h}_p}{\|\boldsymbol{h}_p\|}$	$\boldsymbol{P}_{\mathrm{UE}} \sim \|\boldsymbol{h}\|^{-1}$
$\mathrm{MR}_{\text{channel norm}}$	$\boldsymbol{W} = \boldsymbol{h}_p$	$\boldsymbol{P}_{\mathrm{UE}} \sim \|\boldsymbol{h}\|^{-2} \Rightarrow \boldsymbol{Y}_{\mathrm{UE}} \sim \boldsymbol{H}^{\mathrm{H}}\boldsymbol{H}$

Method 1, UP-MR

Equation (1.8) defines the downlink SNR given UP-MR precoding. The UP-MR precoder is used in the Kronecker based simulations and for the post processing of measured channel data from LuMaMi and is used in papers II-VI. The approach for deriving the correlation, α, and imbalance, β, is as follows. The precoding matrix is given by

$$\boldsymbol{W} = \frac{\boldsymbol{h}_p}{\|\boldsymbol{h}_p\|}. \tag{1}$$

The denominator normalizes the transmitted power to unity. From this, the terminal DL SNR directly reflects the channel gain, $\|\boldsymbol{h}_p\|$. The effective precoding vectors at the BS given a pilot is transmitted from each terminal antenna independently are given by:

$$\begin{cases} \boldsymbol{p}_0 = [1 \;\; 0] \rightarrow \text{precoding } \boldsymbol{w}_0 = \dfrac{\hat{\boldsymbol{h}}_0}{\|\hat{\boldsymbol{h}}_0\|} \\ \boldsymbol{p}_1 = [0 \;\; 1] \rightarrow \text{precoding } \boldsymbol{w}_1 = \dfrac{\hat{\boldsymbol{h}}_1}{\|\hat{\boldsymbol{h}}_1\|} \end{cases}, \tag{2}$$

where $\hat{\boldsymbol{h}}_k$ is the estimated channel at the BS side. For the respective pilot vector, there is an associated receive vector at the terminal side. In matrix form this becomes

$$\boldsymbol{Y} = \begin{bmatrix} \boldsymbol{y}_{p_0} \\ \boldsymbol{y}_{p_1} \end{bmatrix} = \begin{bmatrix} \dfrac{\hat{\boldsymbol{h}}_0\boldsymbol{h}_0^{\mathrm{H}}}{\|\hat{\boldsymbol{h}}_0\|} \approx \|\boldsymbol{h}_0\| & \dfrac{\hat{\boldsymbol{h}}_0\boldsymbol{h}_1^{\mathrm{H}}}{\|\hat{\boldsymbol{h}}_0\|} \\ \dfrac{\hat{\boldsymbol{h}}_1\boldsymbol{h}_0^{\mathrm{H}}}{\|\hat{\boldsymbol{h}}_1\|} & \dfrac{\hat{\boldsymbol{h}}_1\boldsymbol{h}_1^{\mathrm{H}}}{\|\hat{\boldsymbol{h}}_1\|} \approx \|\boldsymbol{h}_1\| \end{bmatrix}. \tag{3}$$

By multiplying (3) with its diagonal, we arrive at the channel inner product, (i.e the Gramian), which is given by

$$\boldsymbol{G} = \boldsymbol{H}^{\mathrm{H}}\boldsymbol{H} = \begin{bmatrix} \|\boldsymbol{h}_0\|^2 & \boldsymbol{h}_0\boldsymbol{h}_1^{\mathrm{H}} \\ \boldsymbol{h}_1\boldsymbol{h}_0^{\mathrm{H}} & \|\boldsymbol{h}_1\|^2 \end{bmatrix}, \tag{4}$$

as the noise at the BS gets small. From the normalized Gramian

$$\boldsymbol{G}_{\mathrm{N}} = \frac{2}{\mathrm{tr}(\boldsymbol{G})}\boldsymbol{G} = \begin{bmatrix} 1+\beta & \alpha \\ \alpha^* & 1-\beta \end{bmatrix}, \tag{5}$$

we can identify

$$\begin{cases} \alpha = \boldsymbol{G}_{\mathrm{N}}(1,2) \\ \beta = \boldsymbol{G}_{\mathrm{N}}(1,1) - 1 \end{cases}. \tag{6}$$

Method 2, ZF

In the LuMaMi testbed, we used a ZF precoder for the measurements. The main reason was to keep the SNR at the terminal reasonably the same for the different scenarios. Therefore, we need to take the following approach to extract the correlation, α, and imbalance, β. The precoder is given by

$$\boldsymbol{W} = \frac{\boldsymbol{h}_p}{\|\boldsymbol{h}_p\|^2}. \tag{7}$$

In the BS there is an additional (unknown) normalization factor. The transmitted power from the BS is multiplied with the gain factor, C_k, related to the hardware implementation. The effective precoding vectors at the BS given a pilot is transmitted from each terminal antenna independently are given by

$$\begin{aligned} \boldsymbol{p}_0 = [1 \;\; 0] \rightarrow \hat{\boldsymbol{h}}_0 \rightarrow \text{precoding } \boldsymbol{w} = C_0 \frac{\hat{\boldsymbol{h}}_0}{\|\hat{\boldsymbol{h}}_0\|^2} \\ \boldsymbol{p}_1 = [0 \;\; 1] \rightarrow \hat{\boldsymbol{h}}_1 \rightarrow \text{precoding } \boldsymbol{w} = C_1 \frac{\hat{\boldsymbol{h}}_1}{\|\hat{\boldsymbol{h}}_1\|^2}, \end{aligned} \tag{8}$$

from which the received signal at the terminal-antennas becomes

$$\boldsymbol{Y} = \begin{bmatrix} C_0 \dfrac{\hat{\boldsymbol{h}}_0 \boldsymbol{h}_0^H}{\|\hat{\boldsymbol{h}}_0\|^2} \approx C_0 & C_0 \dfrac{\hat{\boldsymbol{h}}_0 \boldsymbol{h}_1^H}{\|\hat{\boldsymbol{h}}_0\|^2} \\ C_1 \dfrac{\hat{\boldsymbol{h}}_1 \boldsymbol{h}_0^H}{\|\hat{\boldsymbol{h}}_1\|^2} & C_1 \dfrac{\hat{\boldsymbol{h}}_1 \boldsymbol{h}_1^H}{\|\hat{\boldsymbol{h}}_1\|^2} \approx C_1 \end{bmatrix}. \tag{9}$$

With the diagonal elements representing the power constants C_k we can simplify,

$$\boldsymbol{Y}_2 = \begin{bmatrix} 1 & \dfrac{\hat{\boldsymbol{h}}_0 \boldsymbol{h}_1^H}{\|\hat{\boldsymbol{h}}_0\|^2} \\ \dfrac{\hat{\boldsymbol{h}}_1 \boldsymbol{h}_0^H}{\|\hat{\boldsymbol{h}}_1\|^2} & 1 \end{bmatrix}, \tag{10}$$

which is normalized, i.e. $2/\mathrm{tr}(\boldsymbol{Y}_2)$=1.

From equations (4) and (5) we can identify

$$\boldsymbol{Y}_2 = \begin{bmatrix} 1 & \dfrac{\alpha}{1+\beta} \\ \dfrac{\alpha^*}{1-\beta} & 1 \end{bmatrix}. \tag{11}$$

This gives

$$\begin{cases} \alpha = \dfrac{2\boldsymbol{Y}_2(1,2)\boldsymbol{Y}(2,1)}{\boldsymbol{Y}_2(1,2)+\boldsymbol{Y}(2,1)} \\ \beta = \dfrac{\boldsymbol{Y}_2(1,2)-\boldsymbol{Y}(2,1)}{\boldsymbol{Y}_2(1,2)+\boldsymbol{Y}(2,1)}. \end{cases} \tag{12}$$

Note that due to the C_k we can not simply multiply with the square of the diagonal similar to what we did in the UP-MR case. Also, note that with the off-diagonal elements typically being very small the SNR needs to be large. This makes this approach hard to use in real implementations where the need for a good estimate of the inner product is increasingly important as the SNR decrease.

Method 3, Channel Normalized MR

For the case of the cluster-based simulator, we use an MR precoder that does normalize its transmitted power to that of the channel norm, the BS simply perform a MR (i.e., conjugate beam-forming or matched filtering). The precoder then equals

$$\boldsymbol{W} = \boldsymbol{h}_p. \tag{13}$$

With cluster n illuminating the angles $\mathcal{A}_n$, the gain of antenna k is given by

$$\overline{\boldsymbol{\Psi}}_{k,n} = \int_{\mathcal{A}_n} \boldsymbol{\Psi}_k(\boldsymbol{\Omega})\mathrm{d}\boldsymbol{\Omega}. \tag{14}$$

When a pilot is transmitted from terminal antenna k, the contribution from a cluster n, with gain λ_n, show up at the BS as $\lambda_n \overline{\boldsymbol{\Psi}}^{\mathrm{H}}_{k,n}$. Based on MR precoding, the BS transmits the Hermitian transpose of the received signal. As the signal goes through the same cluster, the electrical field at the terminal become $\lambda_n^2 \overline{\boldsymbol{\Psi}}_{k,n}$, where a square influence from the cluster gain is obtained. The received signal contribution, from the cluster n, at the terminal antenna l, become $y_l = \lambda_n^2 \overline{\boldsymbol{\Psi}}^{\mathrm{H}}_{l,n} \overline{\boldsymbol{\Psi}}_{k,n}$.

When the contribution from all N clusters are summed, the terminal can get direct access to the channel inner products, by transmitting a pilot from each antenna and receiving the associated downlink signals at all antennas. For the two antenna case, we get

$$\boldsymbol{G} = \sum_{n=0}^{N-1} \lambda_n^2 \begin{bmatrix} \overline{\boldsymbol{\Psi}}^{\mathrm{H}}_{0,n} \\ \overline{\boldsymbol{\Psi}}^{\mathrm{H}}_{1,n} \end{bmatrix} \begin{bmatrix} \overline{\boldsymbol{\Psi}}_{0,n} & \overline{\boldsymbol{\Psi}}_{1,n} \end{bmatrix}. \tag{15}$$

Normalization by the average of the diagonal elements, gives

$$\boldsymbol{G}_{\mathrm{N}} = \frac{2}{\sum_{n=0}^{N-1} \lambda_n^2 \left(\left\| \overline{\boldsymbol{\Psi}}_{0,n} \right\|^2 + \left\| \overline{\boldsymbol{\Psi}}_{1,n} \right\|^2 \right)} \sum_{n=0}^{N-1} \lambda_n^2 \begin{bmatrix} \left\| \overline{\boldsymbol{\Psi}}_{0,n} \right\|^2 & \overline{\boldsymbol{\Psi}}_{0,n}^{\mathrm{H}} \overline{\boldsymbol{\Psi}}_{1,n} \\ \overline{\boldsymbol{\Psi}}_{1,n}^{\mathrm{H}} \overline{\boldsymbol{\Psi}}_{0,n} & \left\| \overline{\boldsymbol{\Psi}}_{1,n} \right\|^2 \end{bmatrix}, \quad (16)$$

were we directly can identify

$$\boldsymbol{G}_{\mathrm{N}} = \begin{bmatrix} 1+\beta & \alpha \\ \alpha^* & 1-\beta \end{bmatrix}. \quad (17)$$

In Paper V this method is presented for the case of more than 2 terminal antennas.

Appendix B

This appendix present formulas used for conversion from two dimensional (2D) spherical coordinates to three dimensional (3D) Cartesian coordinate system and back. The conversion simplifies the generation of 3D uniformly distributed center AoA distributions and aid the derivation of the integration area, $\mathbb{A}_n$, for circular clusters defined in 3D to the spherical coordinate system. The equations are used to compute antenna gain in different illumination scenarios in the cluster based simulation framework.

The measured antenna gain patterns are represented by 2D matrices in spherical coordinates. Spherical coordinates describes the directional angle in three dimensions by $\boldsymbol{\Omega} = [\Theta \ \Phi]^{\mathrm{T}}$, where $\Theta, \in [0 \ \pi]$, defines the elevation angle and $\Phi, \in [0 \ 2\pi]$, the azimuth angle. Generation of uniform random angles is easiest done in Cartesian coordinate system where each element in $[x \ y \ z]^{\mathrm{T}}$ is drawn from a uniform distribution, U[-1,1]. The relations between the spherical coordinates and the Cartesian are given by

$$\begin{cases} x = r\sin(\Theta)\cos(\Phi) \\ y = r\sin(\Theta)\sin(\Phi) \\ z = r\cos(\Theta) \end{cases} \Leftrightarrow \begin{cases} r = \frac{1}{\sqrt{x^2+y^2+z^2}} \\ \Theta = \arccos\left(\frac{z}{\sqrt{x^2+y^2+z^2}}\right) \\ \Phi = \arctan\left(\frac{y}{x}\right) \end{cases}, \tag{18}$$

where r is the length of the 3D vector and can be used for normalization of the length.

The measured antenna gain patterns are given as 90×180 large complex valued matrices in spherical coordinates. Each entry do therefore not define an equal angular area and before the integration we need to convert the antenna gains to gain densities. The average complex gain for an illuminated area is then given by the integral of the gain-densities, multiplied by the total illuminated area. In the simulations we compute the sum of the illuminated matrix entries, where each entry is scaled as a function of the elevation. Furthermore, we needed to determine the area to integrate over, i.e. which matrix entries to sum. The shapes a circular cluster takes when represented in spherical coordinates, for various elevation angles, are shown in Fig. 1.

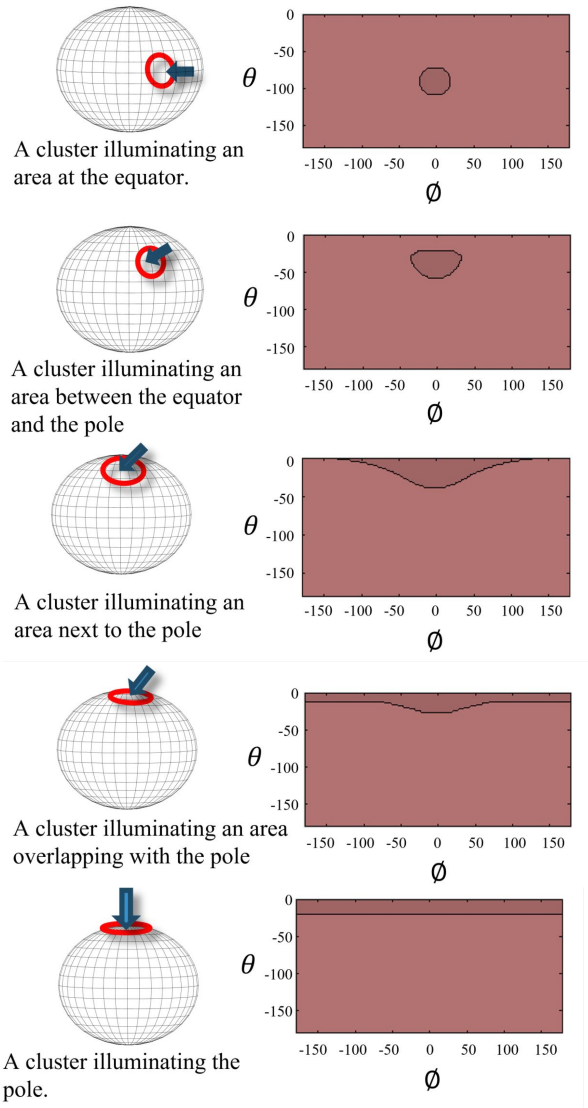

Figure 1: Different elevation angles of a circular cluster and the corresponding areas in spherical coordinates.

Part II

Included Papers

Paper I

UE Antenna Properties and Their Influence on Massive MIMO System Performance

The use of large-scale antenna arrays can bring substantial improvements both in energy and spectral efficiencies. This paper presents an initial study of user equipment (UE) antenna performance based on prototypes for a massive MIMO test bed. Most publications in the massive MIMO area have assumed isotropic or dipole antenna characteristics at the UE side. It is, however, of greatest interest to evaluate the impact of realistic antenna implementations and user loading on such systems. In this study antennas are integrated into realistic UE form factors. Simulations are carried out to evaluate system performance using the UE antenna characteristics measured in a Satimo StarGate 64. Comparisons are made with ideal isotropic un-correlated antennas. The presented UEs are designed for the 3.7 GHz band used by the LuMaMi massive MIMO test bed at Lund University.

1 Introduction

Massive MIMO (MaMi) technology [1] is emerging as one of the major candidates for increasing capacity and efficiency of future wireless communications systems [2]. Recent predictions show that energy efficiency can be increased by several orders of magnitude and spectral efficiency by at least one order of magnitude, under reasonable assumptions on channel behavior and system configurations [3]. Predictions like these have opened up a frenetic research activity in the field. Despite great efforts spent on investigating how efficient MaMi systems should be designed, the terminal perspective has been almost entirely neglected. One reason for this is that most of the new concepts relate directly to the base station and only indirectly to the terminal devices. The terminal designs will, however, to a large extent influence the overall performance of MaMi systems, including how well different MaMi transmission techniques perform under real conditions and how transmission protocols are designed. A notable exception to the base station (BS) focus is [4] where the impact of non-linearities in the UE implementation are studied. The study concludes that HW impairments of the UE limit the achievable capacity as the number of BS antennas grows large.

In contrast to most published studies in the MaMi area, where ideal or omni-directional UE antenna behavior is assumed, we address real UE antenna designs, integrated into commercially available smart phone chassis. The antennas are tuned for operation in the 3.7 GHz band used by the Lund University MaMi (LuMaMi) testbed [5]. The unavoidable user interaction with the integrated antennas in the current and future consumer devices influences performance of the antenna systems as well as of the overall communication system. User loading of the antennas cannot be avoided and it is a challenge to minimize its negative effects on the performance. When channel variations that originate from user-loading of the antenna occur, they are commonly compensated for by means of higher power, which is an inefficient method. From the UE perspective, introducing diversity antennas in the terminals was initially a way to combat performance degradation caused by fading. Higher diversity gains, however, often originate from overlooked loading generated antenna losses. Due to the channel hardening effect antenna diversity should not be necessary in MaMi terminals, but we expect that it can not be avoided in devices where the antennas may be exposed to loading.

2 Approach

While the impact of UE antennas in MaMi systems is a large and complex topic, we start our investigations by performing simulation studies along the lines of multiplexing efficiency as defined in [6]. Multiplexing efficiency is a figure of merit for the combined UE antennas in a MIMO system, under the assumption of isotropic propagation conditions. In [7] the authors developed the concept further to take arbitrary distributions of incoming power into account. In this paper we use this concept and extend it to a full MaMi system with multiple UEs, each having an arbitrary number

of antennas. Following [7], and for reasons of tractability, we adopt the Kronecker channel model

$$\boldsymbol{H} = \boldsymbol{R}^{1/2}\boldsymbol{H}_W, \tag{1}$$

where $\boldsymbol{R}$ denotes the UE antenna correlation matrix and $\boldsymbol{H}_W$ is a white, independent and identically distributed (i.i.d.), complex Gaussian channel. It is also, in this first study, assumed that the large BS array has zero antenna correlation. If we in the MaMi context incorporate all UE antennas from different terminals into $\boldsymbol{R}$ and assume zero correlation between antennas on different terminals we get an $N \times N$ correlation matrix

$$\boldsymbol{R} = \begin{pmatrix} \boldsymbol{R}_1 & 0 & \cdots & 0 \\ 0 & \boldsymbol{R}_2 & \cdots & 0 \\ \vdots & \vdots & \ddots & \vdots \\ 0 & 0 & \cdots & \boldsymbol{R}_K \end{pmatrix}, \tag{2}$$

where $\boldsymbol{R}_k$ is the $N_k \times N_k$ correlation matrix for the N_k antennas on UE k and

$$N = \sum_{k=1}^{K} N_k. \tag{3}$$

Here we limit ourselves to one or two antennas per UE, i.e. $N_k = 1$ or 2. For an M antenna BS, $\boldsymbol{H}_W$ is an $N \times M$ matrix. The eigenvalue distribution of $\boldsymbol{H}\boldsymbol{H}^H$ gives an indication of the system performance and we are able to analyze how the system capacity is affected by the individual UE antenna performances. The correlation matrices $\boldsymbol{R}_k$ are calculated by combining measured antenna characteristics with different angular distributions on incoming clusters of multipath components (MPCs). For the ideal case, where there is no correlation between any of the UE antennas, $\boldsymbol{R}$ becomes a diagonal matrix. As an illustration of what happens for other correlation values, we present expected values of the sorted eigenvalues of $\boldsymbol{H}\boldsymbol{H}^H$, for a set-up with a 50-antenna BS and four two-antenna UEs (see Fig. 1). For low antenna correlation, the eigenvalue spread is small and we can expect high system capacity, and the opposite as the antenna correlation grows. Antenna correlation is, as we will show, affected by angular spread (AS), distribution of clusters and channel richness.

The exact relation between eigenvalues of $\boldsymbol{H}\boldsymbol{H}^H$ and system performance is non-trivial and can be measured in several ways, which is beyond the scope of this paper. In short, the proposed approach is simplifying the analysis to:

1. concentrating information about UE antenna properties (patterns) and angular distribution of incoming clusters to a single antenna correlation matrix $\boldsymbol{R}_k$ per UE, and
2. that $\boldsymbol{R}_k$ be used in the model (1) to evaluate performance of an entire MaMi system with realistic UE properties. The assumptions enable us to quickly analyze how degraded antenna performance of a single UE, or a number of UEs, influence the entire system. We can also compare different operational modes (diversity vs. spatial multiplexing) for individual UEs.

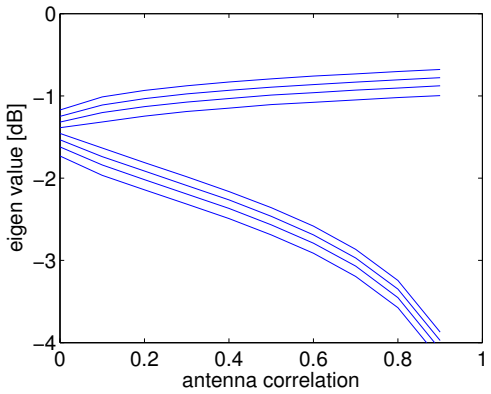

Figure 1: Impact of pairwise increase of correlation between UE antennas on eigen values.

In the paper we focus on the analysis of UE antenna pairs and spatial multiplexing properties. We concentrate on the limitations seen for the individual antenna configurations, hence $\boldsymbol{R}_k$, and how the antenna performance may impact the performance in a MaMi context. The underlying mechanisms approximated by the model (1) include directional properties of both environment and antennas. In order to more clearly separate antenna and environment influences we use directional descriptions below. To illustrate the difference between MaMi and conventional systems we need to introduce some new measures. To make the investigation manageable we also make some simplifying assumptions that may upper bound the results.

The first assumption is that the MaMi BS is capable of providing phase coherent signals from different clusters of MPCs with individually controlled amplitude to each antenna, here set to unity. The effective gain (EG) and mean effective gain (MEG) of an antenna, for a specific scenario, are both normalized to the performance of an isotropic ideal radiator, for the same scenario. This, however, hides the additional gain available in a MaMi system. Traditionally, diversity or multiplexing gain offered by a channel is obtained in the receiver, as seen in e.g. RAKE and MIMO, and there is no need to include this in the antenna characteristics. In our investigation, however, it is of interest to visualize the additional gain obtained within the channel in order to be able to compare the performance improvements offered by different diversity schemes and antenna configurations. Therefore, we introduce two new measures, the combined coherent gain (CCG) and combined non-coherent gain (CNG). If we assume a cluster of MPCs with an angular spread (AS) illuminating the antenna from an arbitrary angle of arrival (AoA), we can describe the MEG for such a cluster as

$$\rho(\Theta, \Phi, \eta(\Theta, \Phi), \mathrm{A}) = \frac{\int_{\mathrm{A}} (\eta(\Theta, \Phi)) \mathrm{dA}}{\mathrm{A}} \tag{4}$$

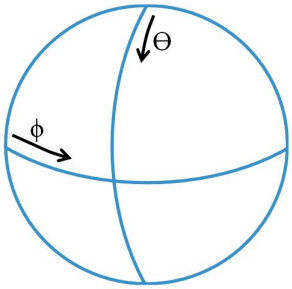

Figure 2: Orientation of Φ and Θ.

where Θ and Φ are elevation and azimuth AoA, respectively, $\eta(\Theta, \Phi)$ is antenna gain at this AoA, and A is an integration area around Θ and Φ defined by the AS. We assume uniform distribution of incoming power over this area. The polar coordinates are defined for $\Phi \in (-\pi, \pi)$ and $\Theta \in (0, \pi)$ with orientation according to Fig. 2. Polarization direction is also defined accordingly, with components along Θ and Φ.

We define CCG as an expectation

$$\mathrm{CCG}(n, \mathrm{A}) = \mathrm{E}_{\boldsymbol{\Theta}, \boldsymbol{\Phi}} \left\{ \sum_{i=1}^{n} \rho_i(\Theta_i, \Phi_i, \eta(\Theta_i, \Phi_i), \mathrm{A}) \right\} \tag{5}$$

for n clusters with randomly distributed AoAs, all with the same AS. Expectation is over $\boldsymbol{\Theta}, \boldsymbol{\Phi}$, which are vectors collecting the n random AoAs and $\rho_i(\Theta_i, \Phi_i, \eta(\Theta_i, \Phi_i), \mathrm{A})$ is defined in (4). If the AoAs are uniformly distributed over the sphere this equals

$$\mathrm{CCG}(n) = \sum_{i=1}^{n} \rho_{\mathrm{iso}} = n\rho_{\mathrm{iso}}, \tag{6}$$

where ρ_{iso} is the total isotropic efficiency ($\mathrm{TE}_{\mathrm{iso}}$) of the antenna. The contribution from each cluster is added in amplitude as we assume coherent contributions from all clusters after massive MIMO pre-coding. For the non coherent case we correspondingly define

$$\mathrm{CNG}(n, \mathrm{A}) = \mathrm{E}_{\boldsymbol{\Theta}, \boldsymbol{\Phi}} \left\{ \sqrt{\sum_{i=1}^{n} \rho_i^2(\Theta_i, \Phi_i, \eta(\Theta_i, \Phi_i), \mathrm{A})} \right\} \tag{7}$$

which, for uniformly distributed AoAs becomes

$$\mathrm{CNG}(n) = \sqrt{\sum_{i=1}^{n} \rho_{\mathrm{iso}}^2} = \sqrt{n}\rho_{\mathrm{iso}}, \tag{8}$$

where we add the power contribution from each cluster, assuming the phase of each contribution to be independent and uniformly distributed over the sphere. The last simplification in both (6) and (8) are possible as the expectation on ρ_{iso} is independent on n. From a simulation perspective we can calculate the expected CCG by means Monte Carlo (MC) simulation and

$$\text{CCG}(n, \text{A}) \approx \frac{\sum_{k=1}^{K} \sum_{i=1}^{n} \rho_i(\Theta_i, \Phi_i, \eta(\Theta_i, \Phi_i), \text{A})}{K}, \tag{9}$$

where n is the number of clusters, K is the number of random realizations of the AoA, and for each k new $\boldsymbol{\Theta}, \boldsymbol{\Phi}$ are generated. As we know that ρ_{iso} has no dependency on n we can make the same simplification as in (6) and (8) also in our simulation, and

$$\text{CCG}(n, \text{A}) \approx \frac{\sum_{k=1}^{K} \left(n \frac{\int_{\text{A}_{\text{tot}}} \eta(\boldsymbol{\Theta}, \boldsymbol{\Phi}) \text{dA}}{\text{A}_{\text{tot}}} \right)}{K} \tag{10}$$

yield the same result as (9) for large K. In (10) we integrate over the combined area, $\text{A}_{\text{tot}} = \cup_{m=1}^{n} \text{A}_m$, of all clusters instead of each individual area, A_m, as in (9). Equations (9) and (10) approach (5) for large K. In our MC simulations we found $K = 2000$ to be sufficient. Expression (10) is useful later in the calculation of multiplexed CCG and multiplexed CNG. The CNG can be estimated as

$$\text{CNG}(n, \text{A}) \approx \frac{\sum_{k=1}^{K} \sqrt{\sum_n \rho_i^2(\Theta_i, \Phi_i, \eta(\Theta_i, \Phi_i), \text{A})}}{K}, \tag{11}$$

and similarly

$$\text{CNG}(n, \text{A}) \approx \frac{\sum_{k=1}^{K} \left(\sqrt{n} \frac{\int_{\text{A}_{\text{tot}}} \eta(\boldsymbol{\Theta}, \boldsymbol{\Phi}) \text{dA}}{\text{A}_{\text{tot}}} \right)}{K}. \tag{12}$$

As cluster powers are added in (11), the MEG for the combined area in (12) needs to be multiplied by $\sqrt{n}$. Again (11) and (12) approach (7) as K grows large.

Fig. 3 shows CCG and CNG for an ideal isotropic radiator. For CCG the slope is 3 dB each time the clusters are doubled and for the CNG case it is 1.5 dB. It is noted that CCG and CNG for a single cluster are the same and equals the isotropic total efficiency (TE_{iso}) of the radiator. Looking into combined antenna performance metrics, we assume that the transmission channel determines the AoA and that the small spacing between the UE antennas cause the AoA for each cluster to be the same for all the antennas in a UE. Here we introduce an error in directions where antenna pattern correlation is large and gain imbalance is moderate. The results can therefore be seen as upper bounds on what to expect from a real system. A deeper analysis of the magnitude of the deviation is not included as we assume it to be small. For a real system the problem can be solved with zero forcing or other methods to ensure orthogonality. For the squared correlation,

$$\text{ECC}_{\text{A}_{\text{tot}}} = \left| \frac{\int_{\text{A}_{\text{tot}}} (\boldsymbol{E}_1 \cdot \boldsymbol{E}_2') \text{dA}}{\sqrt{\int_{\text{A}_{\text{tot}}} \|\boldsymbol{E}_1\| \text{dA} \int_{\text{A}_{\text{tot}}} \|\boldsymbol{E}_2\| \text{dA}}} \right|^2, \tag{13}$$

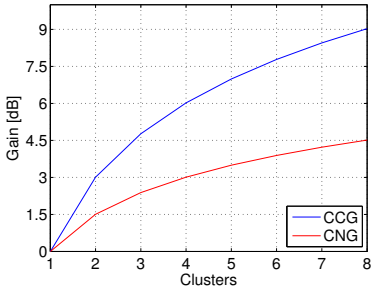

Figure 3: CCG and CNG for ideal isotropic radiator vs. number of clusters.

where the vector $\boldsymbol{E}_a = [E_{\Theta_a}, E_{\Phi_a}]^T$ contains the complex E-fields for each polarization for antenna a. Integration is performed for the combined area of the multiple clusters, $\mathrm{A_{tot}}$ as defined in (10). The $\mathrm{ECC_{A_{tot}}}$ can be interpreted as the squared local correlation and we can use it to calculate

$$\mathrm{CCG_{MPE}} \approx \frac{\sum_{k=1}^{K} n\sqrt{\frac{\int_{\mathrm{A_{tot}}}(\eta_1)\mathrm{dA}}{\mathrm{A_{tot}}}\frac{\int_{\mathrm{A_{tot}}}(\eta_2)\mathrm{dA}}{\mathrm{A_{tot}}}(1-\mathrm{ECC_{A_{tot}}})}}{K} \tag{14}$$

for high SNRs [6]. This approximation becomes more accurate as K grows. We need to integrate over $\mathrm{A_{tot}}$ as the effect of reduced gain imbalance otherwise will be lost when the number of clusters grows larger. Like in (10) we need to multiply each antenna MEG by n, in order to include the effect of coherent amplitude addition of the multiple clusters. For the $\mathrm{CNG_{MPE}}$ the corresponding expression becomes

$$\mathrm{CNG_{MPE}} \approx \frac{\sum_{k=1}^{K} \sqrt{n\frac{\int_{\mathrm{A_{tot}}}(\eta_1)\mathrm{dA}}{\mathrm{A_{tot}}}\frac{\int_{\mathrm{A_{tot}}}(\eta_2)\mathrm{dA}}{\mathrm{A_{tot}}}(1-\mathrm{ECC_{A_{tot}}})}}{K}, \tag{15}$$

and, like in (12), we multiply each antenna MEG by $\sqrt{n}$, since the power from each cluster is added. All expressions are defined for linear units while the results are primarily presented in dB. The expected performance of $\mathrm{CCG_{MPE}}$ and $\mathrm{CNG_{MPE}}$ for two uncorrelated ideal isotropic antennas would equal CCG and CNG shown in Fig. 3.

3 Antenna evaluation results

For the investigation, five Sony Xperia ZL and Xperia SP chassis have been modified with different antenna configurations. Either with four antennas and circuitry for switching between any antenna pair combination or with two antennas, located at the top and bottom. For the four-antenna prototypes two antennas are located at the top corners, one at the side and one at the bottom. The $\mathrm{TE_{iso}}$ for free space

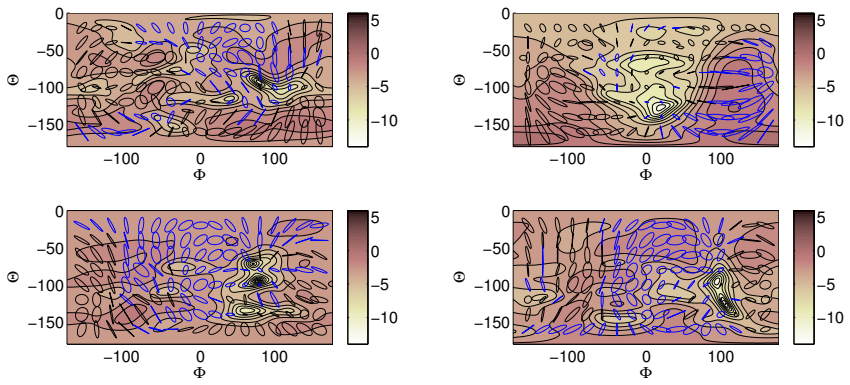

Figure 4: FS performance for four antenna prototype, upper right, upper left, bottom and side antennas in order. Blue ellipses indicate left hand polarization and black right hand polarization.

(FS) is similar, about -5 dBi for all 4 antennas, including the loss from the switch circuitry. All antenna configurations have been characterized in a Satimo StarGate 64 measurement facility. 3D patterns for FS, left and right hand (LH/RH), beside head with hand left and right (BHHL/R) have also been measured. The TE_{iso} range over levels from -5 dB down to -14 dB dependent on load scenario. Fig. 4 shows the measured FS antenna E-field patterns for the four-antenna prototype, with ellipses indicating polarization. It can be noted that the patterns for the two top and the side antennas are rather omni-directional, while the bottom antenna shows a directivity downwards. For the two-antenna prototype, the patterns for both antennas in FS show directivity in different directions and their efficiencies are also quite different. The bottom antenna has a TE_{iso} of -3 dB and the top antenna -4.6 dB.

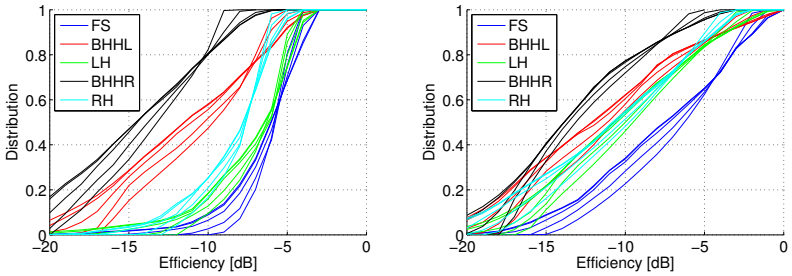

Figure 5: CDFs of antenna E-field patterns for two of the antennas

Fig. 5 shows cumulative distribution functions (CDFs) for E-field patterns for two of the antennas, with different colors for different load scenarios. For each scenario the impact of AS, ranging from 4°to 90°is included as curves with the same color. The load not only decreases the average power by moving the curve to the left but usually also decreases the slope, i.e. directivity which translates to larger variation for different AoA. AS tend to have larger impact when the antennas are loaded and increases the variation even more, i.e. higher probability of low efficiency that may lead to drop outs. The directivity increase is caused by a combination of the hand and head absorption and impact on the current distributions on the radiators. It can also be noted that the slope of the bottom antenna CDF (right) for FS (blue) is less steep compared to the top L antenna (left) already for FS condition.

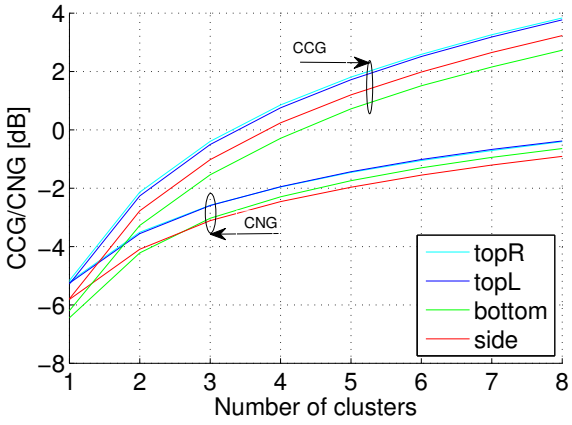

Figure 6: CCG and CNG vs. number of clusters with AS=4°, for the four antenna prototype in FS.

In Fig. 6 we see CCG and CNG vs. number of clusters, which is the same as Fig. 3 but based on the measured FS patterns from the four-antenna prototype. Performance is plotted with different colors for different antennas. CCG grows almost ideally with about 3 dB per doubling of clusters and CNG with about 1.5 dB. The MaMi gain is obvious but may also translate to faster roll-off when the channel becomes poor. Despite the faster roll-off, the CCG never gets worse than the CNG.

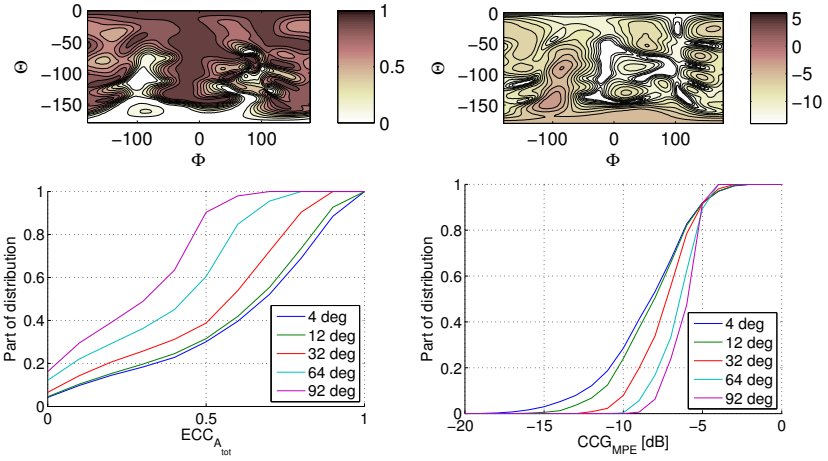

Figure 7: FS performance for the combination of the top antennas, in terms of $\mathrm{ECC}_{\mathrm{A_{tot}}}$(n=1) and $\mathrm{CCG}_{\mathrm{MPE}}$(n=1) patterns for an AS=4°. Below the corresponding CDFs for a wider range of ASs. The $\mathrm{ECC}_{\mathrm{iso}}$=0 and the $\mathrm{CCG}_{\mathrm{MPE_{iso}}}$=-5.2 dB.

The local antenna correlation pattern for a single cluster (n=1), $\mathrm{ECC}_{\mathrm{A_{tot}}}$, and multiplexed efficiency pattern, $\mathrm{CCG}_{\mathrm{MPE}}$, for an AS=4°for the two top antennas on one of the prototypes are shown in the upper part of Fig. 7. Below, the corresponding CDFs for a wider range of AS are shown. Even if the antenna correlation is low in an isotropic environment, the dependency on AS of incoming clusters is substantial and the correlation degrades for a more narrow AS (lower left). The AS also influences the $\mathrm{CCG}_{\mathrm{MPE}}$, which is seen as less steep slopes when the AS decreases (lower right). This translates to larger variations and a worse minimum.

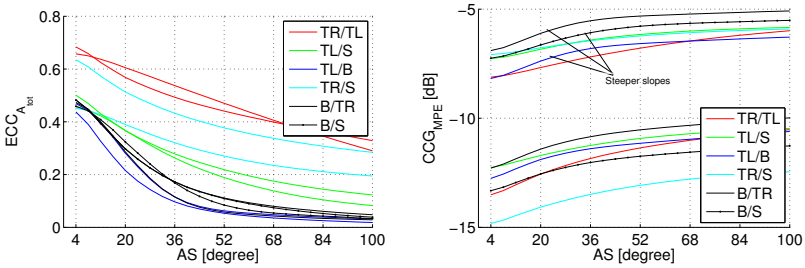

Figure 8: Average $\mathrm{ECC}_{\mathrm{MPE}}$ and average $\mathrm{CCG}_{\mathrm{MPE}}$ for FS and BHHL vs. AS for single cluster.

Fig. 8 shows average $\mathrm{ECC}_{\mathrm{A_{tot}}}$ and average $\mathrm{CCG}_{\mathrm{MPE}}$, as defined in (13) and (9), vs. the AS for a single cluster. The figures for FS and BHHL conditions are included for all 6 antenna combinations for the four-antenna prototype. We see low load dependency on $\mathrm{ECC}_{\mathrm{A_{tot}}}$, except for the combination of top-right and side antenna (indexed TR/S) where the hand probably was close to touching the radiator and obviously affected the current distribution. Larger load dependency on $\mathrm{ECC}_{\mathrm{A_{tot}}}$ is expected for lower frequencies as the wavelength approaches the size of the prototype and the hand to a larger extent interacts with the current distributions as they to a larger extent are located in the actual grounding structure. For the $\mathrm{CCG}_{\mathrm{MPE}}$, there is an offset based on the efficiency drop. For FS (upper curves), combinations with the bottom antenna (indexed B) have steeper slope due to the higher directivity and this yields larger probability for AoA dependent gain imbalance as the AS gets small.

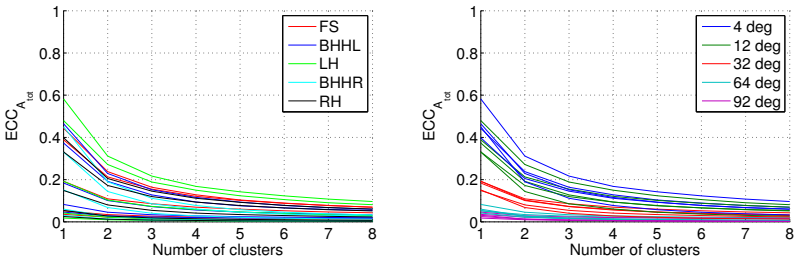

Figure 9: $\mathrm{ECC}_{\mathrm{A_{tot}}}$ for one antenna combination of the 4 antennas in the four antenna prototype, vs. clusters, colored vs. load and AS.

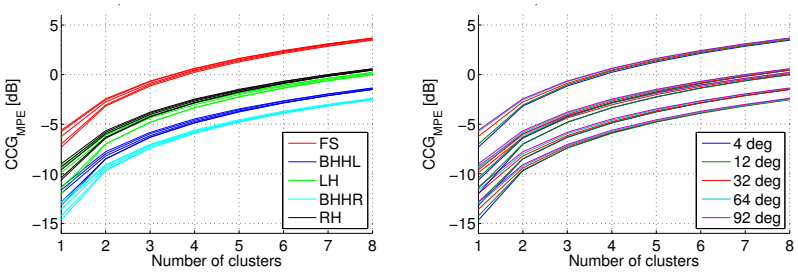

Figure 10: Typical $\mathrm{CCG}_{\mathrm{MPE}}$ for an antenna pair vs. number of clusters, coloured vs. AS and vs. load.

In order to evaluate what happens to the average $\mathrm{ECC}_{\mathrm{A_{tot}}}$ and average $\mathrm{CCG}_{\mathrm{MPE}}$ in the different load scenarios, MC simulations of (14) and (15) have been performed where the number of clusters increases from one to eight, with random AoA and all with same AS. Fig. 9 shows the average $\mathrm{ECC}_{\mathrm{A_{tot}}}$ vs. number of clusters for an antenna pair in the four-antenna prototype. The curves are colored according to load in the left sub-figure and according to AS in the right sub-figure. While for a single antenna combination, the presented $\mathrm{ECC}_{\mathrm{A_{tot}}}$ are quite representative for any of the antenna combinations and point towards a low load dependency and a strong AS dependency. It can be noted that the $\mathrm{ECC}_{\mathrm{A_{tot}}}$ converges towards isotropic performance as the number of clusters grows large.

The corresponding $\mathrm{CCG}_{\mathrm{MPE}}$ curves are shown in Fig. 10, colored according to loading in the left sub-figure and according to AS in the right sub-figure. The coloring shows that the dependency on loading is strong, while the dependency on AS is much weaker. The AS dependency is the strongest the fewer the clusters are, seen as a larger spread for few clusters. As $\mathrm{CCG}_{\mathrm{MPE}}$ is dependent on AS, number of clusters, and antenna directivity, the slope reaches up to 6 dB going from 1 to 2 clusters for

some loading conditions and antenna combinations. This is to be compared with the expected 3 dB discussed earlier and depicted in Fig. 3. The result may be interpreted as 3 dB comes from doubling the energy and 3 dB from the fact that two clusters are needed[1] for multiplexed operation (rank 2).

[1] This statement is not fully correct as there are two polarizations available in each cluster. The 3 dB do originate from decreased correlation as the number of clusters increase but rank 2 is still possible with a single cluster. The correlation for the single narrow cluster is defined by the antennas polarization property in the direction of that cluster.

4 Summary and Conclusions

Simulations show that the channel in combination with the antenna directional properties have a substantial impact on the performance of a MaMi pre-coded system. Going from a single cluster to two clusters improves $\mathrm{CCG}_{\mathrm{MPE}}$ significantly more than increasing AS area by a factor of 2 (3 dB vs. 0.1 dB) due to the impact of the gain imbalance and the fact that the two clusters come in from different AoAs. This tells us that even if the BS may be able to improve phase coherence within a narrow cluster of MPCs the impact of gain imbalance at UE side can not be compensated for. The results indicate between 2 and 5 dB of additional drop for single cluster as compared to the isotropic multiplexed efficiency. However, $\mathrm{CCG}_{\mathrm{MPE}}$ is a rank-two performance indicator and the results simply indicate that we need to switch to rank one, i.e., diversity mode. It can also be mentioned that a design with cross polarized UE antennas would be less sensitive to the channel richness.

For the $\mathrm{ECC}_{\mathrm{A_{tot}}}$ there is no or very little dependency on load for most antenna combinations while smaller AS and fewer clusters degrade it significantly from the isotropic value (which is zero for all our antenna combinations). What happens with the local correlation, $\mathrm{ECC}_{\mathrm{A_{tot}}}$, when we go down in frequency is an interesting topic. In this situation the $\mathrm{ECC}_{\mathrm{iso}}$ is known to vary as current distributions are more affected by user interaction, but the average local correlation may behave differently.

5 Acknowledgement

The authors would like to thank Peter Karlsson and Ying Zhinong at Sony Mobile in Lund for their help with the manuscript

References

[1] T.L. Marzetta, *"Noncooperative cellular wireless with unlimited numbers of base station antennas*, Wireless Communications, IEEE Transactions on, vol. 9 no.11 pp. 3590-3600, 2010.

[2] E.G. Larsson, F. Tufvesson, O. Edfors, and T.L. Marzetta, *Massive MIMO for Next Generation Wireless Systems*, IEEE Commun. Mag., vol. 52, no. 2, pp. 186-195, Feb. 2014.

[3] H.Q. Ngo, E.G. Larsson, and T.L. Marzetta, *Energy and Spectral Efficiency of Very Large Multiuser MIMO Systems*, IEEE Trans. Commun., vol. 61, no. 4, pp. 1436-1449, Apr. 2013.

[4] E. Björnsson, J. Hoydis, M. Kontouris, M. Debbah, *"Massive MIMO Systems with Non-Ideal Hardware: Energy Efficiency, Estimation, and capacity Limts"* Reviced for resubmission to IEEE Transaction on Information Theory, (available online arxiv.org/abs/1307.2584)

[5] J. Vieira, et al., *A flexible 100-antenna testbed for Massive MIMO*, IEEE International Workshop on Massive MIMO: From theory to practice. Austin, TX, USA, Dec. 2014 (to appear)

[6] R. Tian, B.K. Lau and Z. Ying, *"Multiplexing efficiency of MIMO antennas"* IEEE Antennas Wireless Propagat. Lett., vol. 10, pp. 183-186, 2011.

[7] R. Tian, B.K. Lau and Z. Ying, *"Multiplexing efficiency of MIMO antennas in Arbitrary Propagation scenarios"* 6th European Conference on Antennas and Propagation, (EUCAP), Prague, Czech Republic, Mar. 2012.

Paper II

Transmission Schemes for Multiple Antenna Terminals in real Massive MIMO systems

In massive MIMO performance evaluations it is often assumed that the terminal has a single antenna. The combination of multiple antennas in a terminal and massive MIMO precoding at the base station side can further improve overall system performance. We present measurement results for multi antenna terminals operating in different transmission schemes and how they perform under varying loading conditions. Gain expressions are derived that enable easy comparison between the transmission schemes. The evaluation is performed on realistic antennas integrated into Sony Xperia handsets tuned to 3.7 GHz and operated together with the Lund University massive MIMO (LuMaMi) test bed. It is concluded that the approach used in today's mobile systems, where up link and down link are addressed independently, will not provide the best performance. The performance can be improved by the selection of transmission schemes optimized for massive MIMO.

Erik L. Bengtsson, Peter C Karlsson, Fredrik Tufvesson, Joao Vieira,
Steffen Malkowsky, Liang Liu, Fredrik Rusek, Ove Edfors,
"Transmission Schemes for Multiple Antenna Terminals in real Massive MIMO systems,"
in *Proc. of GlobeCom 2016, Washington DC, USA, Dec. 2016.*

1 Introduction

Massive MIMO technology is emerging as one of the major candidates for increasing capacity, coverage and efficiency of future wireless communications systems [1]. Massive MIMO differs from traditional multi-user (MU) MIMO approaches by employing a large number of BS antennas - typically in the order of hundreds - to serve a relatively small number of user equipments (UE) [2]. It has been shown that energy efficiency can be increased by several orders of magnitude in Massive MIMO systems and spectral efficiency by at least an order of magnitude compared to single-antenna systems [3]. Promising results from initial studies have spurred a frenetic research activity in the field and also made massive MIMO a topic in the "new radio access technology for 5G" item in the 3GPP standardization forum.

Despite great efforts in massive MIMO systems design, the UE side of the link has not been in the main focus of attention. The design of UEs and their operating modes, will however influence overall performance of realistic massive MIMO systems and should be designed accordingly. Antenna-user interaction is often an unwanted practical effect that is hard to avoid in realistic handset form factor UEs, and challenging to overcome [4]. It is often compensated by means of increased transmit power, which is a straightforward but inefficient approach. UEs having multiple antennas can be an option to mitigate such problems, where different transmission/receiving processing schemes can be used not only to inhibit the user influence, but also to harvest further channel gains, e.g. diversity or spatial multiplexing. Understanding the possibilities of such a multitude of schemes, and their interplay with the UE antenna design, is thus important for the overall system design.

We provide a few examples on the literature regarding the impact of UE designs and their operating schemes in a massive MIMO set-up follows. In [5] the impact of UE hardware (HW) non-linearities was studied. It was verified that HW impairments of the UE limit the achievable capacity as the number of BS antennas grows large. In [6] the performance of the multiplexed operation of a handset UE with dual antennas in a massive MIMO setting was investigated, by means of numerical simulations. The focus of that paper was the property of phase coherent cluster combination and the impact of local correlation between handset antennas. It also provided initial insights into the range of the gains that can be obtained with multi-antenna handsets, for different receiver schemes. Thus, it is of interest to quantify the performance that can be achieved when a multi-antenna UE operates with different processing schemes in a realistic Massive MIMO set-up.

In this paper we study the influence of real handset antenna designs on the system performance of a massive MIMO system. We use a commercially available smart phone chassis tuned for operation in a 3.7 GHz band at the UE side, and a massive MIMO software-defined radio test-bed to emulate a massive MIMO BS [7].We have investigated how the quality of the down-link communication is influenced by different pilot transmission strategies from the UE for different channel realizations. A brief overview of massive MIMO follows here.

Massive MIMO in short: The Massive MIMO precoding we are using sort under MU-MIMO where we use orthogonal up-link (UL) pilots to determine the precod-

ing matrix for down-link (DL) payload. Hence, we utilize time division duplex and rely on channel reciprocity for the DL and spatially multiplex the UEs. Reciprocity calibration is implemented to compensate for non ideal hardware. This also means that the pilots contained in the header of each frame become a scarce resource. In the LuMaMi testbed there are 100 RF chains feeding 100 antennas at the base station side and it is capable of serving up to 12 different UEs simultaneously. Zero forcing (ZF) precoding is used in order to separate the different UEs and also, in some cases, streams to multiple antennas in the same handset. The Massive MIMO precoding impacts on how we may utilize different transmission schemes for operation of multiple antennas within a single UE. As the channels are estimated from the UL pilots, we need to transmit a pilot signal from all of the UE antennas in order for the BS to be aware of them. Consequently the difference between the received signals at an antenna that has transmitted a pilot and an antenna that has not becomes substantial and we talk about Massive MIMO antenna isolation. The channel hardening, where small scale fading is eliminated, is only valid for the antennas that transmitted the pilot signal. With two UE antennas, the BS can serve the UE with spatial multiplexing. However, in a crowded system with many users, it may not be possible to accommodate for this (due to the limitation of time-frequency resources allocated to pilot transmission). It is therefore of operational interest to research transceiver strategies for a multi antenna UE, served via a single stream from the BS. The performance of such strategies should then be evaluated and compared with the performance reached by single-antenna operation and spatial multiplexing performance using multiple antennas.

2 System description

The system setup is that we have a UE with two antennas and a BS with M antennas. What we want to study is how the quality of the DL communication is influenced by different pilot transmission strategies from the UE. For this purpose we model the UL transmission of pilots and the DL transmission of data to the UE, as shown in Fig. 1.

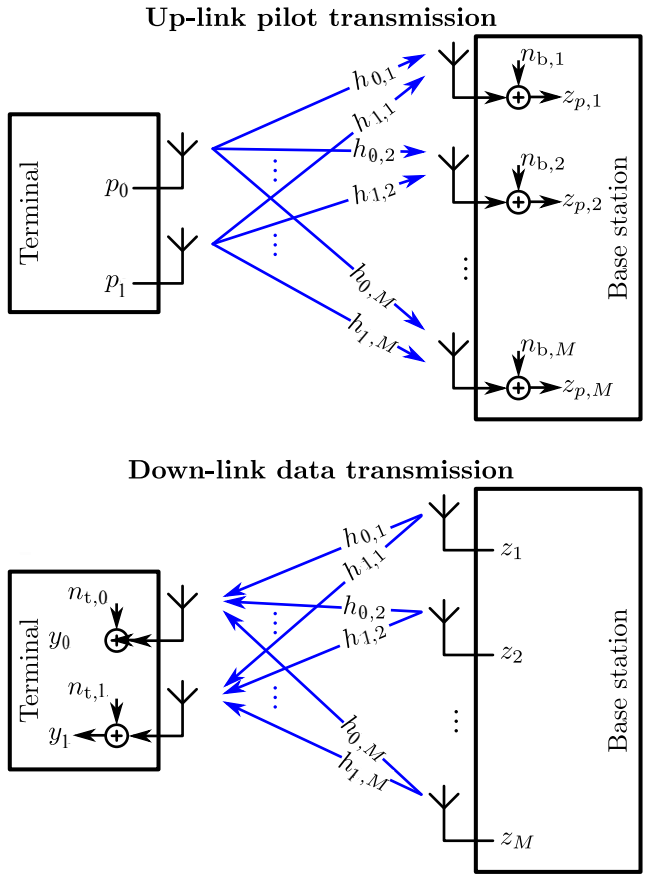

Figure 1: Up-link transmission of pilots for channel estimation and down-link data transmission on reciprocal channel.

The received signal at the BS for a pilot transmission $\boldsymbol{p} = [p_0 \;\; p_1]^{\mathrm{T}}$ becomes

$$\boldsymbol{z}_{\mathrm{p}} = [z_{\mathrm{p},1} \;\; \ldots \;\; z_{\mathrm{p},M}]^{\mathrm{T}} = \boldsymbol{H}^{\mathrm{T}}\boldsymbol{p} + \boldsymbol{n}_{\mathrm{b}}. \tag{1}$$

DL transmission of (pre-coded) data $\boldsymbol{z} = [z_1 \;\; \ldots \;\; z_M]^{\mathrm{T}}$

$$\boldsymbol{y} = [y_0 \;\; y_1]^{\mathrm{T}} = \boldsymbol{H}\boldsymbol{z} + \boldsymbol{n}_{\mathrm{t}}, \tag{2}$$

where the DL reciprocal radio channel is

$$\boldsymbol{H} = \begin{bmatrix} h_{0,1} & h_{0,2} & \ldots & h_{0,M} \\ h_{1,1} & h_{1,2} & \ldots & h_{1,M} \end{bmatrix}, \tag{3}$$

base-station side noise $\boldsymbol{n}_\mathrm{b} \in \mathcal{CN}(\boldsymbol{0}, \sigma_\mathrm{b}^2 \boldsymbol{I}_{M\times M})$ and UE side noise $\boldsymbol{n}_\mathrm{t} \in \mathcal{CN}(\boldsymbol{0}, \sigma_\mathrm{t}^2 \boldsymbol{I}_{2\times 2})$.

With two antennas, the UE may be seen as one single antenna UE or two single-antenna UEs, depending on the particular pilot configuration used. To be able to handle spatial multiplexing of two streams with linear processing and closely spaced UE antennas, ZF precoding is assumed in the down-link data transmission. For the single antenna case, this is equivalent to maximum-ratio transmission (MRT), since we assume that no other UEs are present.

2.1 UE acting as a single antenna UE

When the BS assumes a single antenna UE, its model of the pilot transmission is

$$\boldsymbol{z}_\mathrm{p} = [z_{\mathrm{p},1} \quad \dots \quad z_{\mathrm{p},M}]^\mathrm{T} = \boldsymbol{h}^\mathrm{T} p + \boldsymbol{n}_\mathrm{b}, \tag{4}$$

where p is a known pilot, which without loss of generality is a positive real number, and the channel $\boldsymbol{h} = [h_1 \quad \dots \quad h_M]$ a row vector. Assuming independent and identically distributed (i.i.d.) DL channel coefficients, the channel is estimated accordingly as

$$\hat{\boldsymbol{h}}_\mathrm{p} = \frac{1}{p}\boldsymbol{z}_\mathrm{p}^\mathrm{T}. \tag{5}$$

Considering that the UE has two antennas and can transmit pilots from both, the equivalent single antenna channel $\boldsymbol{h}_\mathrm{p} = \boldsymbol{p}^\mathrm{T}\boldsymbol{H}$ depends on the transmitted pilots in $\boldsymbol{p}$, making it possible to change what channel the BS sees in the up-link and thereby influence how it transmits data in the down link. Substituting (1) in (5) we obtain

$$\hat{\boldsymbol{h}}_\mathrm{p} = \frac{1}{p}\left(\boldsymbol{p}^\mathrm{T}\boldsymbol{H} + \boldsymbol{n}_\mathrm{b}^\mathrm{T}\right). \tag{6}$$

For a fair comparison, we restrict the combined pilot to have the same energy as the single pilot p assumed by the BS, i.e., $||\boldsymbol{p}||^2 = p^2$. In general, all pilots fulfilling the requirement can be expressed as $\boldsymbol{p} = p\boldsymbol{u}$, where $||\boldsymbol{u}|| = 1$. Based on this, down-link precoding is done as

$$\boldsymbol{z} = \boldsymbol{w}_\mathrm{s} x = \frac{1}{||\hat{\boldsymbol{h}}_\mathrm{p}||}\hat{\boldsymbol{h}}_\mathrm{p}^\mathrm{H} x \tag{7}$$

where $\boldsymbol{w}_\mathrm{s} = \hat{\boldsymbol{h}}_\mathrm{p}^\mathrm{H}/||\hat{\boldsymbol{h}_\mathrm{p}}||$ is the ZF/MRT precoding vector and x is data in the form of a complex-valued signal constellation point. Without loss of generality, we assume that $E\{|x|^2\} = 1$ below. The resulting received data signals, on the two UE antennas,

$$\boldsymbol{y} = \boldsymbol{H}\frac{1}{||\hat{\boldsymbol{h}}_\mathrm{p}||}\hat{\boldsymbol{h}}_\mathrm{p}^\mathrm{H} x + \boldsymbol{n}_\mathrm{t}, \tag{8}$$

are given by (2), with $\boldsymbol{z}$ from (7). Optimal reception for the sampling is achieved by maximum ratio combining (MRC) of the signals in $\boldsymbol{y}$, hence,

$$r = \frac{\hat{\boldsymbol{h}}_\mathrm{p}\boldsymbol{H}^\mathrm{H}}{||\hat{\boldsymbol{h}}_\mathrm{p}||}\boldsymbol{y}, \tag{9}$$

where r is the scalar output of the MRC and, the SNR becomes

$$\mathrm{SNR} = \frac{\hat{\boldsymbol{h}}_{\mathrm{p}} \boldsymbol{H}^{\mathrm{H}} \boldsymbol{H} \hat{\boldsymbol{h}}_{\mathrm{p}}^{\mathrm{H}}}{||\hat{\boldsymbol{h}}_{\mathrm{p}}||^2} \frac{1}{\sigma_t^2}. \tag{10}$$

It should be noted that this SNR depends on the transmitted pilot $\boldsymbol{p}$, making it generic and useful in several of the schemes detailed below. The UE can control how the BS transmits data in the DL by selecting the transmitted pilots in $\boldsymbol{p}$.

In order to simplify our notation we define $\boldsymbol{p}_0 = p[1\ \ 0]^{\mathrm{T}}$ and $\boldsymbol{p}_1 = p[0\ \ 1]^{\mathrm{T}}$ for the special cases when the pilot has been transmitted from antenna 0 and 1, respectively.

We investigate the use of four different strategies in the UE for transmitting pilots in the UL and using signals received on the antennas in the DL:

A single antenna UE (SA)

This is a benchmark case, used only for reference purposes. In this strategy, the UE has a single antenna only. Depending on the antenna used both for UL pilot transmission and DL reception, the pilot vector is either $\boldsymbol{p}_0$ or $\boldsymbol{p}_1$, as defined above and the received signal from the same antenna is obtained by selecting the corresponding (first or second) element of $\boldsymbol{y}$ in (8), which gives

$$y = \boldsymbol{h}_{\mathrm{p}} \frac{1}{||\hat{\boldsymbol{h}}_{\mathrm{p}}||} \hat{\boldsymbol{h}}_{\mathrm{p}}^{\mathrm{H}} x + \boldsymbol{n}_{\mathrm{t}}, \tag{11}$$

and from (10), the SNR becomes

$$\mathrm{SNR}_{\mathrm{SA},k} = \frac{||\boldsymbol{h}_{\mathrm{p}} \hat{\boldsymbol{h}}_{\mathrm{p}}||^2}{||\hat{\boldsymbol{h}}_{\mathrm{p}}||^2} \frac{1}{\sigma_t^2}. \tag{12}$$

Here, the same antenna is used, independent of channel realization and , we indicate if it is antenna 0 or antenna 1 with the k.

Switched diversity (SWD)

In SWD the UE has two antennas but only a single transceiver chain, thus, it can only transmit and receive from a single antenna. In view of (1), the pilot vector is either $\boldsymbol{p}_0$ or $\boldsymbol{p}_1$, depending on which channel is strongest. The expression for the SNR becomes the same as for $\mathrm{SNR}_{\mathrm{SA}}$ in (12), but with the fundamental difference that the best antenna of the two is selected for each channel realization.

Passive diversity (PD)

In PD the UE has two antennas and two receive chains, but only a single transmit chain. The second antenna is used only for receive diversity. In view of (1), the pilot vector is either $\boldsymbol{p}_0$ or $\boldsymbol{p}_1$, depending on which antenna is the transmitting one. With this transmission scheme the UE utilizes the MRC (9) and its associated SNR is given

by (10). The difference in signal power level at the antennas, what we call massive MIMO antenna isolation, can be derived as the ratio

$$\Delta\mathrm{SNR}_0 = \frac{||\boldsymbol{h}_{\boldsymbol{p}_0}\hat{\boldsymbol{h}}_{\boldsymbol{p}_0}||^2}{||\boldsymbol{h}_{\boldsymbol{p}_1}\hat{\boldsymbol{h}}_{\boldsymbol{p}_0}||^2} \tag{13}$$

of SNRs at the two antennas, for the case the pilot was transmitted on antenna 0. By exchanging $\boldsymbol{p}_0$ and $\boldsymbol{p}_1$, $\Delta\mathrm{SNR}_1$ is obtained for the case when the pilot transmission is done from antenna 1 instead.

Dominant Eigenmode Scheme (DEM)

For DEM the UE has two antennas and two transceiver chains simultaneously active. The pilot vector[2] is chosen as $\boldsymbol{p} = p\boldsymbol{u}_0$, where $\boldsymbol{u}_0$ is the eigenvector corresponding to the largest eigenvalue of $\boldsymbol{H}^*\boldsymbol{H}^{\mathrm{T}}$. This to is to maximize the received pilot signal power $||\boldsymbol{z}_{\mathrm{p}}||^2$ at the BS and allow the BS to see and estimate the strongest one-dimensional subspace of the two-dimensional channel $\boldsymbol{H}$. As for PD, in this transmission scheme the UE utilizes MRC from (9) and its associated SNR is also given by (10).

2.2 UE acting as two single antenna UEs

Multiplexed operation (MUX) is when the UE is acting as two single-antenna UEs, an UL pilot p is transmitted from each antenna in an orthogonal fashion (e.g. in one time or frequency slot each). This allows the BS to estimate the full channel as

$$\hat{\boldsymbol{H}} = \boldsymbol{H} + \frac{1}{p}\boldsymbol{N}_{\mathrm{b}}, \tag{14}$$

where the noise matrix $\boldsymbol{N}_{\mathrm{b}}$ is of size $2 \times M$ with i.i.d. rows originating from the noise term in (6). The corresponding down-link precoding is done as

$$\boldsymbol{z} = \boldsymbol{W}_{\mathrm{ZF}}\boldsymbol{x} = \frac{1}{\sqrt{\mathrm{Tr}\left((\hat{\boldsymbol{H}}\hat{\boldsymbol{H}}^{\mathrm{H}})^{-1}\right)}}\hat{\boldsymbol{H}}^{\mathrm{H}}\left(\hat{\boldsymbol{H}}\hat{\boldsymbol{H}}^{\mathrm{H}}\right)^{-1}\boldsymbol{x}, \tag{15}$$

where $\mathrm{Tr}(\cdot)$ is the trace operator, $\boldsymbol{W}_{\mathrm{ZF}}$ the pseudo-inverse of the estimated channel, normalized to unit energy, and $\boldsymbol{x} = [x_0 \;\; x_1]^{\mathrm{T}}$ data in the form of complex-valued signal constellation points.

The resulting received data signals, on the two UE antennas,

$$\boldsymbol{y} = \frac{1}{\sqrt{\mathrm{Tr}\left((\hat{\boldsymbol{H}}\hat{\boldsymbol{H}}^{\mathrm{H}})^{-1}\right)}}\boldsymbol{H}\hat{\boldsymbol{H}}^{\mathrm{H}}\left(\hat{\boldsymbol{H}}\hat{\boldsymbol{H}}^{\mathrm{H}}\right)^{-1}\boldsymbol{x} + \boldsymbol{n}_{\mathrm{t}}, \tag{16}$$

are given by (2), with (15) substituted. For large M on the BS side the SNR for the individual antennas will converge to (12), assuming the same pilot power used at each antenna.

[2] In practice the UE does not have access to the full channel. The result can, however, be seen as an indication of what is possible in an ideal situation.

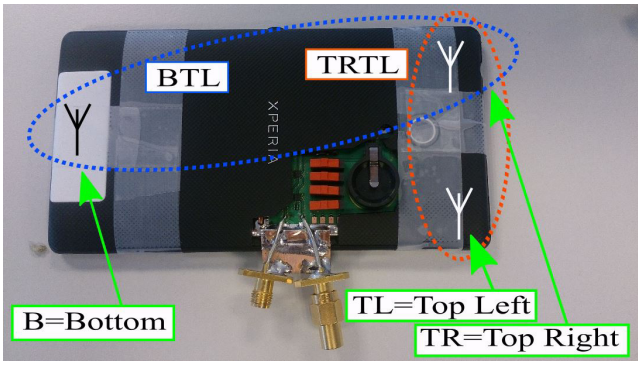

Figure 2: Sony Xperia ZL handset with antennas and investigated antenna combinations marked.

Table 1: Isotropic efficiency figures

Mode	Top-R	Top-L	Bottom
free space	-5.0	-5.4	-5.4
BHHR	-9.1	-12.0	-9.7

3 Prototypes and test setup

For our measurements, a prototype based on a Sony Xperia ZL handset, shown in Fig. 2, has been designed and characterized. Two different antenna combinations as indicated in the figure are investigated. Fig. 3 shows the 3D antenna patterns in spherical coordinates for the three antennas used in this campaign under free space condition and, when loaded beside head with hand right side (BHHR). BHHR is shown in the left of Fig. 4 where the UE is positioned in right side talk position beside a phantom head held by a phantom hand. The ellipses in Fig. 3 show the polarization and blue and black colors indicate right and left hand circular polarization, respectively. Fig. 3 shows that in free space the upper antenna pair has a close to omni-directional radiation pattern while the directivity is larger on the bottom antenna or when loaded. Hence, the power is concentrated to a limited area. The total isotropic efficiency is indicated in Table 1 for all the patterns. The reason for evaluating BHHR is not that we believe that this is a typical use case for a high rate data connection but, as it is a bad loading condition that is well defined and that we are able repeat both in the anechoic chamber and in our live measurements.

This initial evaluation is based on measurements inside a lab. Two different scenarios were considered, one with a direct path between the antenna array and the UE and one where we tried to avoid the line of sight component by measuring

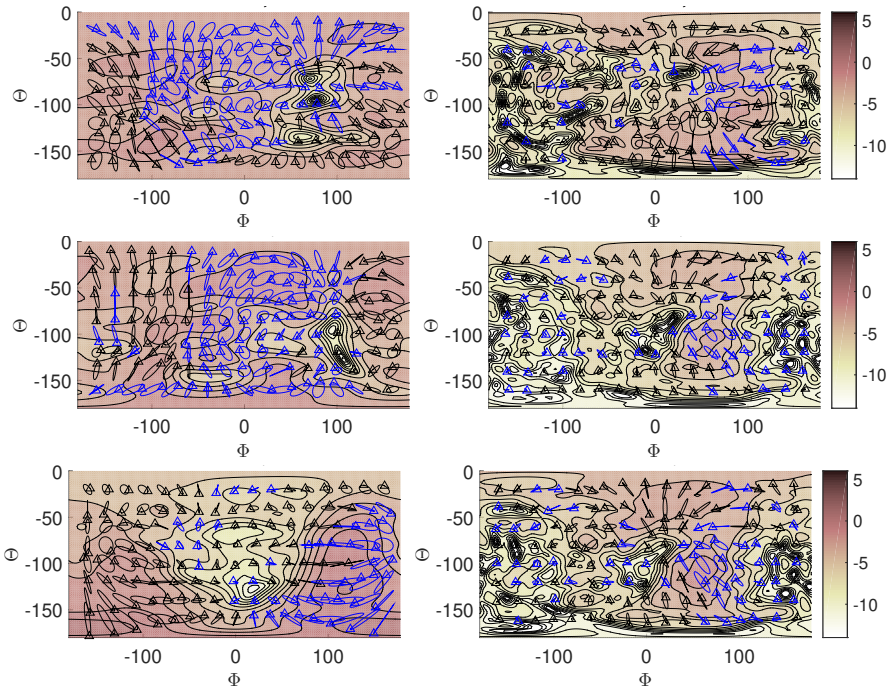

Figure 3: Prototype antenna far-field patterns for free space and BHHR. From the top, the TL, TR and the B antennas in order

slightly behind and beside the BS antenna array. For the first case the handset was simply placed some 3 m right in front of the BS antenna array and for the second case slightly behind, 3 m to the side of the array antenna.

Figure 4: Set up for the direct path BHHR measurements to the left and free space non direct path to the right.

The set ups are shown in Fig. 4. The main reason for our scenario selection was to generate as realistic channel variations as possible, given the limitations associated with our lab environment.

Measurements were performed for eight scenarios generated by the permutations of UE antenna loading, position relative to the BS and antenna combination. For the latter, Bottom/Top-Left antennas (BTL) vs. Top-Right-Top-Left (TRTL) antenna combinations. For each scenario four measurements were performed where the phone setup was rotated by about 90°in the horizontal plane between each measurement.

4 Results

The gain figures in the plots are derived as the ratio of the measured SNR for the different transmission schemes and the $\mathrm{SNR}_{\mathrm{SA},k}$ of the selected reference antenna, as defined in (10) and (12). For the different transmission schemes this becomes

- $\mathrm{Gain}_{\mathrm{DEM},k} = \mathrm{SNR}_{\mathrm{DEM}}/\mathrm{SNR}_{\mathrm{SA},k}$,
- $\mathrm{Gain}_{\mathrm{PD},k} = \mathrm{SNR}_{\mathrm{PD}}/\mathrm{SNR}_{\mathrm{SA},k}$, and
- $\mathrm{Gain}_{\mathrm{SWD},k} = \mathrm{SNR}_{\mathrm{SWD}}/\mathrm{SNR}_{\mathrm{SA},k}$.

Were the k, indicate what antenna was used as reference for the gain figures. The measured gains both for $k = 0$ and $k = 1$ are plotted in the same figures, against relative single-antenna performance for the two antennas. For the case $k = 0$ the gains are plotted against Offset_0=$\mathrm{SNR}_{\mathrm{SA},1}$/ $\mathrm{SNR}_{\mathrm{SA},0}$ and when $k = 1$ against Offset_1=$\mathrm{SNR}_{\mathrm{SA},0}$/ $\mathrm{SNR}_{\mathrm{SA},1}$. With this set up we can compare the different transmission schemes and how they depend on the relative antenna performance.

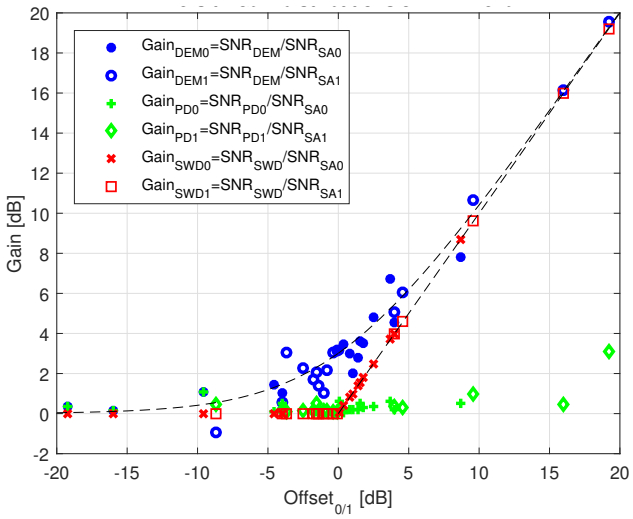

Figure 5: TRTL antenna combination scatter plot of the diversity gain for the different transmission schemes and channel realizations.

In Fig. 5 we present the results for the TRTL antenna combination. We separate the figures for the transmission schemes as we use different reference antennas and can see that the distributions are similar.

When the relative performance of the added diversity antenna is negative (negative numbers on the x-axis), it should be interpreted as adding an inferior antenna to using a particular scheme, while positive numbers means that we add a better antenna. When adding a lower performing antenna, there are no gains from SWD, while both DEM and PD generate some improvements. An upper bound for the DEM performance is obtained when ideal constructive addition of the antenna signals takes place. This idealized DEM asymptotically converges to the SWD performance, when the relative performance of the added antenna $\text{Offset}_{0/1}$ grows large. This is shown as dashed lines in the graph.

For PD, as we add a better performing antenna we still transmit the UL pilot signal from the bad antenna and the scheme does therefor not have the capability to improve a badly loaded antenna with increased outage as a risk. The PD performance may also be understood as a consequence of the of Massive MIMO isolation, (13) that reduce the signal to the non pilot transmitting antenna. The median of the Massive MIMO isolation for the channel realizations in this measurement campaign was 12 dB.

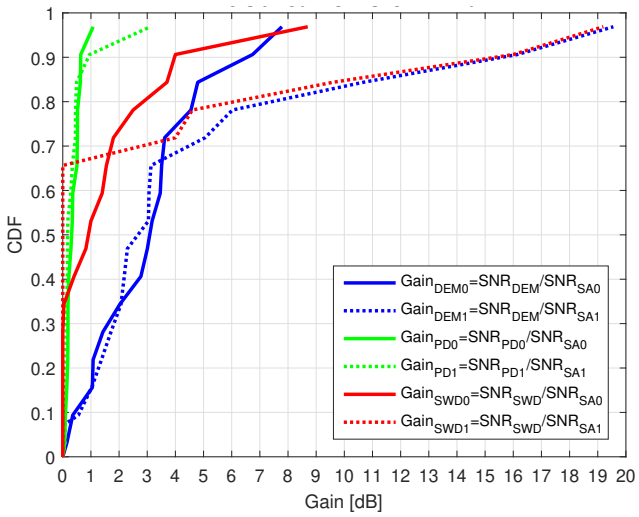

Figure 6: TRTL antenna combination CDF of the gain distributions for the different transmission schemes and channel realizations.

Fig. 6 shows the CDFs of the diversity gain shown in Fig. 5. Based on the gains shown in Fig. 6 the medians can be determined for all transmission schemes with respect to the reference antenna, those medians are shown in Table 2 for both the TRTL and the BTL antenna combinations. The median for SWD is low for any antenna combination and any reference and the strength from this scheme lays rather in its ability to reduce outage indicated by the tail in Fig. 6.

Table 2: Median performance for the transmission schemes

Antenna pair/ref	PD	DEM	SWD
TRTL/TR	0.3 dB	3.0 dB	0.9 dB
TRTL/TL	0.2 dB	2.7 dB	0 dB
BTL/TL	0.4 dB	2.7 dB	0 dB
BTL/B	0.5 dB	3.3 dB	0.5 dB
Median all	0.3 dB	3 dB	0 dB

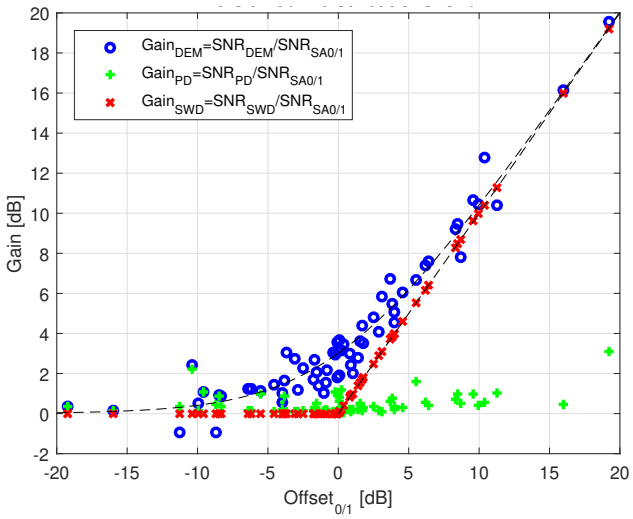

Figure 7: Scatter plots for all measurements combined in a single plot.

From the results, even tough the statistical base is small, we do see clear trends of what to expect from the different transmission schemes. In Fig. 7 all measurements from the TRTL and BTL antenna combinations with the different references are combined into a single plot. Only the different schemes are separated and the reason for combining the results is to increase the measurement base.

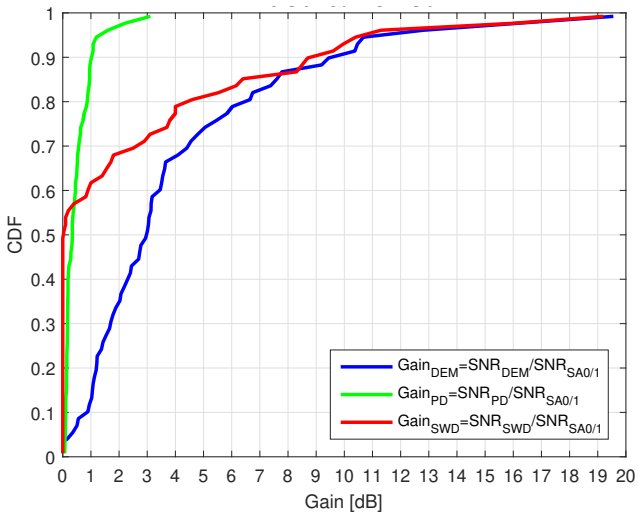

Figure 8: CDF of the gains for all measurements combined.

In Fig. 8 we show the CDFs for the gains presented in Fig. 7, the medians are also included in Table 2. The results show that the medians are about the same for the different antenna combinations, for the different references, and not far from the common median.

The variations in the measurement results are dominated by the fact that the channel was not static over the time of the measurement for each realization.

In order to compare MUX to the diversity schemes we convert the diversity gain into capacity by the expression $R = \log_2(1 + \text{SNR})$. Also here we use one of our antennas as the reference and plot against the $\text{Offset}_{1/0}$, which is the same as for the gain plots. As the performance is dependent on the absolute SNR, here we extracted results where the SNR of the reference antenna was set to 1. This is a low value but enable us to differentiate between the different schemes.

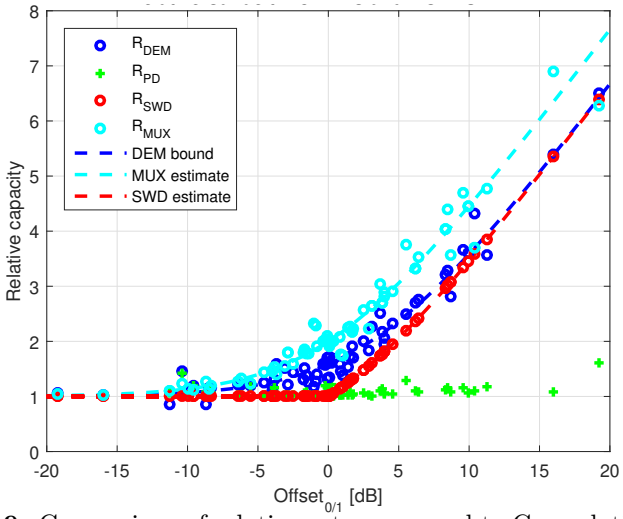

Figure 9: Comparison of relative rate compared to C_{SA} relative performance of the second antenna for MUX, coherent combined and DEM/PD measurements.

Fig. 9 shows the relative rates for DEM, SWD and PD transmission schemes plotted together with the relative rate potential from the MUX mode. The DEM bound and the expectations for the schemes are also included as dashed lines. The MUX performance seems better in the comparison but as discussed earlier to the average cost of twice the power in both UL and DL and twice the pilot resources. The MUX performance has the same slope as SWD and DEM as the relative performance increases but with an offset. The result indicate very small difference between DEM and SWD from a rate perspective and only PD stand out as a bad option with insignificant potential.

5 Summary and conclusion

From a diversity perspective, the DEM scheme gives the largest gains. The phase offset and amplitude balance of the signals to the antennas needs to be optimized for each individual scenario, both for UL pilots as well as for combination of DL signal streams. The measurement based results show that it is possible to reach close to the theoretical 3 dB gain for antennas with equal channel gain. When the difference in channel gain is large, all power is directed to the better antenna and performance converges to that of SWD, where only the antenna with the strongest channel is used.

It has also been shown that the massive MIMO antenna isolation degrades what can be achieved with the PD scheme. Measurements show only a 0.3 dB median gain. The massive MIMO antenna isolation was measured at about 12 dB and PD is perhaps only interesting for its backwards compatibility with today's LTE UEs.

The less compex SWD scheme shows low median gains, but a significant outage reduction potential. For cases when the difference in channel gain between the antennas is large, in the order of 10 dB, SWD performs as well as the DEM. Hence, from the perspective of mitigating outage, SWD could be as good as DEM.

The measurements did not indicate any degradation in channel gain to the antennas when operating the handset in MUX mode, in any of the scenarios. This, in combination with the large massive MIMO induced antenna isolation, indicate that MUX operation with two spatial channels to a single UE can be fully utilized, at the cost of an additional UL pilot resource and twice the power.

It can be noted that the approach in 4G LTE systems, as specified until Rel-13, where UL and DL is addressed independently, will not provide the best performance and, that performance can be improved by the selection of transmission schemes optimized for massive MIMO.

Finally, it is worth highlighting that for the small amount of data, 32 scenarios, about 25% of the measurements had antenna channel gain imbalance of 10 dB or more, evenly distributed over the different scenarios. This is significant and again stresses the need for UE diversity schemes also in a Massive MIMO systems. However, more measurements in realistic environments may be needed before any final conclusions can be drawn. It shall also be noted that the presented gain figures are valid for situations where the SNR is large enough to obtain good channel estimates.

6 Acknowledgment

The authors would like to thank Ying Zhinong at Sony Mobile in Lund for help during the review process of this document. We also like to thank SSF and Sony mobile Communications for funding the work.

References

[1] E. G. Larsson, F. Tufvesson, O. Edfors, and T. L. Marzetta, "Massive MIMO for Next Generation Wireless Systems," *IEEE Communications Magazine*, vol. 52, no. 2, pp. 186–195, Feb. 2014, doi: http://dx.doi.org/10.1109/MCOM.2014.6736761.

[2] T. L. Marzetta, "Noncooperative Cellular Wireless with Unlimited Numbers of Base Station Antennas OFDM," *IEEE Trans. Wireless Commun.*, vol. 9, no. 11, pp. 3590–3600, Nov. 2010, doi: http://dx.doi.org/10.1109/TWC.2010.092810.091092.

[3] H. Q. Ngo, E. G. Larsson, and T. L. Marzetta, "Energy and Spectral Efficiency of Very Large Multiuser MIMO Systems," *IEEE Transactions on Communications*, vol. 61, no. 4, pp. 1436–1449, Apr. 2013, doi: http://dx.doi.org/10.1109/TCOMM.2013.020413.110848.

[4] H. Li and B. K. Lau, "MIMO systems and antennas for terminals," 2015, doi: http://dx.doi.org/10.1007/978-981-4560-75-7.

[5] E. Björnson, J. Hoydis, M. Kountouris, and M. Debbah, "Massive MIMO Systems with Non-Ideal Hardware: Energy Efficiency, Estimation, and Capacity Limits," *IEEE Transactions on Information Theory*, vol. 60, no. 11, pp. 7112–7139, Nov. 2014, doi: http://dx.doi.org/10.1109/TIT.2014.2354403.

[6] E. L. Bengtsson, F. Tufvesson, and O. Edfors, "UE Antenna Properties and Their Influence on Massive MIMO Performance," in *Proceedings of the 9th European Conference on Antennas and Propagation, (EUCAP)*, Lisbon, Portugal, Apr. 2015.

[7] J. Vieira, S. Malkowsky, K. Nieman, Z. Miers, N. Kundargi, L. Liu, I. Wong, V. Öwall, O. Edfors, and F. Tufvesson, "A Flexible 100-Antenna Testbed for Massive MIMO," in *Globecom Workshops (GC Wkshps)*, 2014, pp. 287–293.

Paper III

A Simulation Framework for Multiple-Antenna Terminals in 5G Massive MIMO Systems

The recent interest in massive MIMO has spurred intensive work on massive MIMO channel modeling in contemporary literature. However, current models fail to take the characteristics of terminal antennas into account. There is no massive MIMO channel model available that can be used for evaluation of the influence of different antenna characteristics at the terminal side. In this paper, we provide a simulation framework that fills this gap. We evaluate the framework with antennas integrated into Sony Xperia handsets operating at 3.7 GHz as this spectrum is identified for the 5G new radio standard by 3GPP. The simulation results are compared with measured terminal performance when communicating with the Lund University's massive MIMO testbed under the same loading conditions. Expressions are derived for comparison of the gain obtained from different diversity schemes computed from measured far-field antenna patterns. We conclude that the simulation framework yields results close to the measured ones and that the framework can be used for antenna evaluation for terminals in a practical precoded massive MIMO system.

1 Introduction

Massive MIMO (MaMi) technology [1] is emerging as one of the major candidates for increasing capacity and efficiency of future wireless communications systems [2]. Recent predictions show that MaMi can increase energy efficiency by several orders of magnitude and spectral efficiency by at least one order of magnitude, under reasonable assumptions on channel and system configurations [3]. Lately, world records in measured spectral efficiency have been reported [4]. The current one (145.6 bits/s/Hz) is more than 20 times what can be achieved with LTE Rel-10. The large gains have spurred various companies to promote MaMi as a component in the 3GPP new radio (NR) standard for the fifth generation wireless communication [5], [6]. Despite a frenetic research activity on MaMi, terminal antenna and RF configuration perspectives have been almost entirely neglected. One reason for the base station (BS) focus is that most new concepts relate to it and only indirectly to terminal devices. Terminal modems with baseband algorithms and antenna designs, however, influence overall performance to a large extent.

Notable exceptions to the BS focus are [7–9]. In [7] the impact of terminal hardware impairments on the achievable capacity, as the number of BS antennas grows large, is studied. [8] deals with simulation of measured terminal far-field antenna patterns in MaMi multi-stream operation, and can be seen as a starting point of our work in this area. In [9] we conducted an initial measurement campaign and formulated a number of transceiver strategies for MaMi systems with multi-antenna terminals.

In this paper, we propose a simulation framework based on [8], including the transceiver strategies from [9], designed for evaluation of multi-antenna terminals. The framework avoids the complexity of a MaMi BS with its hundreds of antennas and a full geometric channel description, but still takes effects of terminal antenna patterns and BS precoding into account. We demonstrate the simulation framework performance under different terminal antenna loading conditions in combination with different transceiver strategies. Ideally MaMi can coherently combine signals associated with different propagation paths, thereby remove the small-scale fading. Therefore, the diversity schemes studied here target large-scale fading caused by shadowing and antenna loading at the terminal side. Antennas have been integrated into commercially available smartphone chassis and tuned for operation in the 3.7 GHz band used by the Lund University MaMi (LuMaMi) testbed [10], [11]. Results provided by the simulation framework are compared to measurements obtained by using the same terminal in the LuMaMi testbed.

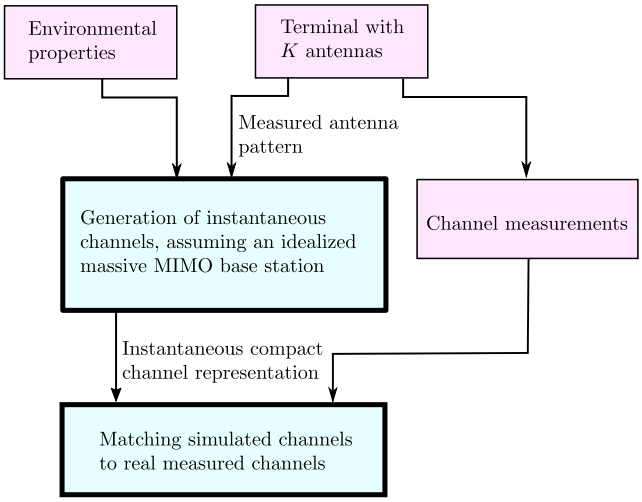

Figure 1: Approach for the derivation of environmental properties. The environmental parameters and antenna patterns are inputs to the simulation framework, and the same antennas are measured in a real massive MIMO channel. The environmental parameters are changed so that the distribution of the compact channel representation match the measured ones.

1.1 Paper Contributions

The main contributions of this paper are that we

- derive a simulation framework for the evaluation of measured far-field antenna patterns from multi-antenna terminals, in a precoded MaMi system.
- match simulated and measured MaMi channel matrices by tuning only three environmental parameters.
- show that for a multi-antenna terminal, the chosen uplink pilot transmission strategy can give substantial SNR gains in the precoded downlink.
- evaluate the generality of the environmental parameters by the testing of a second terminal with a different antenna implementation. Antenna patterns from the second terminal are used in the simulation framework, with environmental settings derived for the first prototype. Finally, the simulated SNR gains and powers are compared to measured values.

Fig. 1 outlines our simulation approach and its inputs: a few environmental parameters and measured antenna patterns.

1.2 Paper organization

In Section 2 we briefly discuss channel models and motivate a cluster-based approach for the simulation framework. Section 3 presents the main contribution of this work, the simulation framework. In Section 4 we tune environmental properties so that statistical properties of simulations match those of measured channels. In Section 5 we incorporate the different transceiver schemes from [9] to illustrate how the framework can be used. We derive expressions for received signal power where the transceiver schemes are reflected. Section 6 presents the simulated power gains and compares to testbed measurements. A summary is provided in Section 7.

2 Channel Models

The most common narrowband signal model for wireless transmission in general, and for MaMi in particular, is

$$\boldsymbol{y} = \boldsymbol{H}\boldsymbol{x} + \boldsymbol{n}, \tag{1}$$

where $\boldsymbol{y} = [y_0 \;\; y_1 \cdots y_{K-1}]^{\mathrm{T}}$ is the vector of signals at the feed of K terminal receive antennas, and $\boldsymbol{x} = [x_0 \;\; x_1 \cdots x_{2J-1}]^{\mathrm{T}}$ represents the signals fed to J dual orthogonal polarized antenna elements (henceforth referred to as antenna elements) with 2 ports each, giving $2J$ antenna ports at the BS. $\boldsymbol{H}$ is a $K \times 2J$ matrix representing the radio channel and $\boldsymbol{n}$ the noise vector. In (1), each entry h_{kj} in $\boldsymbol{H}$ represents the transfer function from a BS transmit antenna port j to a terminal receive antenna k. These entries include antenna gains from the transmit and receive antennas, as well as the propagation channel gain considering all contributions along the different propagation paths, respectively. To evaluate the impact of different antenna configurations, we need to isolate the influence of the terminal antenna pattern on h_{kj}.

In [8], we used a Kronecker assumption [12] for evaluating different transceiver schemes. A shortcoming of the Kronecker model is the limited possibility to include directional properties of the antennas; handset antennas are influenced by the user in many scenarios, which changes directive properties of the antennas. The directional gain will also increase as multi-antenna terminals become more important to compensate for smaller apertures at higher frequencies, anticipated in [5], [6]. Similarly, classic models assuming independent identically distributed (i.i.d.) signal contributions at the terminal side do not model the MaMi channel in a realistic manner and ignores directional properties [13–16]. Equivalently, the mean effective gain (MEG) [17] [18], a commonly used figure of merit for antennas, does not apply for MaMi. As the name implies, a mean of independent contributions is then considered. MaMi, on the other hand, has the capability to control phase, amplitude, and polarization of multiple signal contributions, that illuminate the terminal antennas and thus enable a coherent combination of them. This, in combination with channel hardening [19], makes the effective channel more deterministic. This points towards a need for new performance evaluation strategies.

To evaluate the impact of different antenna configurations and their directional properties, we must know the directional properties of the propagation channel. We

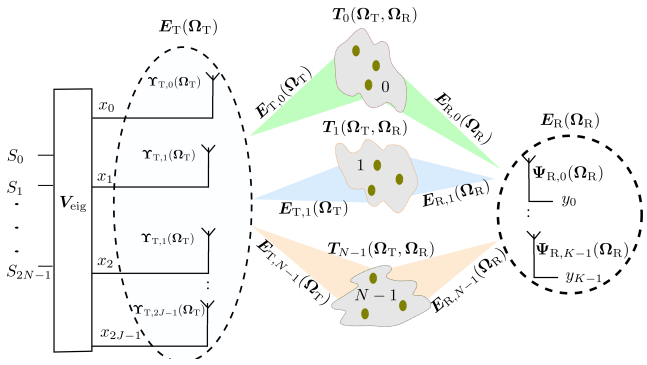

Figure 2: Transmission from J BS transmit antennas to K closely spaced terminal receive antennas over N spatially separated clusters. Note that the variables in the figure are defined later in the text.

use a cluster-based channel model in our simulation framework, thereby including directional properties naturally. Each entry h_{kj} in $\boldsymbol{H}$ is a sum of contributions from N clusters, as described in the channel model in Fig. 2. This enables us to include real measured antenna patterns and characterize the effective precoded MaMi channel with a few environment dependent cluster parameters.

3 Derivation of the simulation framework

3.1 A Cluster Based Propagation Model

A typical MaMi BS uses received uplink pilot signals (SRS in [6]) to obtain channel estimates, from which it determines terminal specific precoding vectors. For a detailed analysis of a given deterministic channel, one may evaluate different antenna configurations with full wave analysis. However, defining the complex E-field at the terminal side by linear combinations of transmitted signals from the BS side may limit the intuitiveness, and some simplifications can hence be convenient. Here we, with the help of well-motivated assumptions, model the propagation channel with only a few input parameters, still capturing the dominant propagation effects. The assumptions we make are the following:

1. All clusters are in the far field as seen from the antennas. By defining the antennas at the receiver side to have the same center points and similar for the transmit antennas, equations are greatly simplified as all antennas at each side will be exposed to the same electrical field. (Note that as a consequence, near field effects are not captured).

2. A cluster is defined by a center angle and an angular spread. The cluster gain function, and thus also the signal strength, of a cluster is constant within angles defined by the cluster.
3. The BS can individually control power level, phase, and polarization of the signal to each cluster seen by the BS.
4. The cluster gain does not depend on polarization as it does not favor any polarization direction.
5. The center angles of clusters are uniformly distributed, as seen by the terminal antennas.

We discuss the assumptions in greater detail and their consequences as we derive our framework next. We also refer back to these assumptions when we derive our expressions.

The angular resolution of an antenna array depends on the number of antennas. However, even with hundreds of antennas, we cannot assume that it is possible for a MaMi BS to resolve every individual multipath component (MPC) in the channel. Motivated by [20, 21], we use N clusters to represent signals from multiple propagation paths with similar illumination angles and propagation delays. Directional angles are represented by $\boldsymbol{\Omega} = [\Theta\ \Phi]^{\mathrm{T}}$ where Θ and Φ are elevation and azimuth angles, respectively, see Fig. 2. We use subscript R in $\boldsymbol{\Omega}_{\mathrm{R}}$ to define the AOA of the received signals at the terminal side and subscript T in $\boldsymbol{\Omega}_{\mathrm{T}}$ to define the AOD of the transmitted signals from the BS side.

The E-field $\boldsymbol{E}_{\mathrm{R}}(\boldsymbol{\Omega}_{\mathrm{R}})$, illuminating the terminal antennas, is a sum of N contributions from the clusters, $\boldsymbol{E}_{\mathrm{R}}(\boldsymbol{\Omega}_{\mathrm{R}}) = \sum_{n=0}^{N-1} \boldsymbol{E}_{\mathrm{R}n}(\boldsymbol{\Omega}_{\mathrm{R}})$. The E-field generated by each cluster $\boldsymbol{E}_{\mathrm{R}n}(\boldsymbol{\Omega}_{\mathrm{R}}) = 0$ for $\boldsymbol{\Omega}_{\mathrm{R}} \notin \mathcal{A}_n$, where $\mathcal{A}_n$ is the set of AOAs illuminated by cluster n. Based on Assumption 1), all terminal antennas see the same E-field, and for terminal antenna k this gives an output signal

$$y_k = \sum_{n=0}^{N-1} \int_{4\pi} \boldsymbol{\Psi}_k^{\mathrm{H}}(\boldsymbol{\Omega}_{\mathrm{R}}) \boldsymbol{E}_{\mathrm{R}n}(\boldsymbol{\Omega}_{\mathrm{R}}) \mathrm{d}\boldsymbol{\Omega}_{\mathrm{R}}, \tag{2}$$

where $\boldsymbol{\Psi}_k(\boldsymbol{\Omega}_{\mathrm{R}})$ is the gain function of terminal antenna k. Both $\boldsymbol{E}_{\mathrm{R}n}(\boldsymbol{\Omega}_{\mathrm{R}})$ and $\boldsymbol{\Psi}_k(\boldsymbol{\Omega}_{\mathrm{R}})$ are 2×1 vectors of functions where the entries represent the different polarizations along the respective angles, i.e., $\boldsymbol{\Psi}_k(\boldsymbol{\Omega}_{\mathrm{R}}) = [\Psi_k^{\Theta}(\boldsymbol{\Omega}_{\mathrm{R}})\ \ \Psi_k^{\Phi}(\boldsymbol{\Omega}_{\mathrm{R}})]^{\mathrm{T}}$.

To model the properties of cluster n we use a cluster transfer function $\boldsymbol{T}_n(\boldsymbol{\Omega}_{\mathrm{R}}, \boldsymbol{\Omega}_{\mathrm{T}})$, a 2×2 matrix, with entries for each polarization on the diagonal and cross polarization terms at the off-diagonals. The cluster transfer function couples the AOD at the BS transmit antennas to AOA at the terminal receive antennas and defines the cluster gain and phase properties.

Each BS antenna element has two orthogonal linearly polarized ports. The antenna patterns for both ports of the j^{th} antenna element are assembled into the 2×2 diagonal matrix,

$$\boldsymbol{\Upsilon}_j(\boldsymbol{\Omega}_{\mathrm{T}}) = \begin{bmatrix} \Upsilon_j^{\Theta}(\boldsymbol{\Omega}_{\mathrm{T}}) & 0 \\ 0 & \Upsilon_j^{\Phi}(\boldsymbol{\Omega}_{\mathrm{T}}) \end{bmatrix}. \tag{3}$$

As we assume far field conditions also at the BS side, all BS antennas see the same clusters. Like the terminal antennas, the BS antenna patterns are defined with a common center point. Hence, assuming that all elements have equal gain patterns, the physical distance between the antennas yields an AOD dependent phase offset in the signal.

We can express each element in the channel matrix $\boldsymbol{H}$ in (1) as a sum of contributions from the different clusters,

$$h_{kj}=\sum_{n=0}^{N-1}\int_{4\pi}\int_{4\pi}\boldsymbol{\Psi}_k^{\mathrm{H}}(\boldsymbol{\Omega}_{\mathrm{R}})\boldsymbol{T}_n(\boldsymbol{\Omega}_{\mathrm{R}},\boldsymbol{\Omega}_{\mathrm{T}})\boldsymbol{\Upsilon}_j(\boldsymbol{\Omega}_{\mathrm{T}})\mathrm{d}\boldsymbol{\Omega}_{\mathrm{R}}\mathrm{d}\boldsymbol{\Omega}_{\mathrm{T}}. \tag{4}$$

Cluster gains are often defined with a profile (the so-called transition region) where power diminishes at the cluster edges. According to Assumption 2), however, we simplify and assume phase, amplitude gain, and polarization rotation over the opening angles of a cluster to be constant. The error is assumed negligible for small angular spreads (ASs). Thus, $\boldsymbol{T}_n(\boldsymbol{\Omega}_{\mathrm{R}},\boldsymbol{\Omega}_{\mathrm{T}})$ is constant within the transmit AS,

$$\boldsymbol{T}_n(\boldsymbol{\Omega}_{\mathrm{R}},\boldsymbol{\Omega}_{\mathrm{T}})=\begin{cases}\boldsymbol{F}_n(\boldsymbol{\Omega}_{\mathrm{R}}) & \boldsymbol{\Omega}_{\mathrm{T}}\in\mathcal{D}_n\\ 0 & \boldsymbol{\Omega}_{\mathrm{T}}\notin\mathcal{D}_n,\end{cases} \tag{5}$$

where $\mathcal{D}_n$ defines the AODs of cluster n. Inserting (5) into (4) we get

$$h_{kj}=\sum_{n=0}^{N-1}\int_{4\pi}\boldsymbol{\Psi}_k^{\mathrm{H}}(\boldsymbol{\Omega}_{\mathrm{R}})\boldsymbol{F}_n(\boldsymbol{\Omega}_{\mathrm{R}})\Big(\int_{\mathcal{D}_n}\boldsymbol{\Upsilon}_j(\boldsymbol{\Omega}_{\mathrm{T}})\mathrm{d}\boldsymbol{\Omega}_{\mathrm{T}}\Big)\mathrm{d}\boldsymbol{\Omega}_{\mathrm{R}}. \tag{6}$$

Defining $\overline{\boldsymbol{\Upsilon}}'_{nj}$ as the contribution from BS antenna element j to cluster n, we have

$$\begin{aligned}\overline{\boldsymbol{\Upsilon}}'_{nj} &= \int_{\mathcal{D}_n}\boldsymbol{\Upsilon}_j(\boldsymbol{\Omega}_{\mathrm{T}})\mathrm{d}\boldsymbol{\Omega}_{\mathrm{T}}\\ &= \begin{bmatrix}\overline{\boldsymbol{\Upsilon}}^{\Theta}_{nj}e^{j\varphi_{nj}} & 0\\ 0 & \overline{\boldsymbol{\Upsilon}}^{\Phi}_{nj}e^{j\varphi_{nj}}\end{bmatrix},\end{aligned} \tag{7}$$

where φ_{nj} is the phase offset determined by the antenna geometry in relation to cluster n. In (5) we have

$$\boldsymbol{F}_n(\boldsymbol{\Omega}_{\mathrm{R}})=\begin{bmatrix}F_n^{\Theta\Theta}(\boldsymbol{\Omega}_{\mathrm{R}}) & F_n^{\Theta\Phi}(\boldsymbol{\Omega}_{\mathrm{R}})\\ F_n^{\Phi\Theta}(\boldsymbol{\Omega}_{\mathrm{R}}) & F_n^{\Phi\Phi}(\boldsymbol{\Omega}_{\mathrm{R}})\end{bmatrix}, \tag{8}$$

which defines the gain, phase, polarization, and the AOAs seen from the terminal receive antennas for cluster n. Simplifying the notation, we collect $\boldsymbol{F}_n(\boldsymbol{\Omega}_{\mathrm{R}}),\forall\, n$, in a $2\times 2N$ matrix, $\boldsymbol{F}(\boldsymbol{\Omega}_{\mathrm{R}})=[\boldsymbol{F}_0(\boldsymbol{\Omega}_{\mathrm{R}})\ \boldsymbol{F}_1(\boldsymbol{\Omega}_{\mathrm{R}})\cdots\boldsymbol{F}_{N-1}(\boldsymbol{\Omega}_{\mathrm{R}})]$. We also define $\overline{\boldsymbol{\Upsilon}}$, a $2N\times 2J$ matrix constructed from matrices $\overline{\boldsymbol{\Upsilon}}'_{nj}$, as

$$\overline{\boldsymbol{\Upsilon}}=\begin{bmatrix}\overline{\boldsymbol{\Upsilon}}'_{00} & \cdots & \overline{\boldsymbol{\Upsilon}}'_{0(J-1)}\\ \vdots & \ddots & \vdots\\ \overline{\boldsymbol{\Upsilon}}'_{(N-1)0} & \cdots & \overline{\boldsymbol{\Upsilon}}'_{(N-1)(J-1)}\end{bmatrix}. \tag{9}$$

In matrix notation we now express (6) as,

$$h_{kj} = \Big(\int_{4\pi} \boldsymbol{\Psi}_k^{\mathrm{H}}(\boldsymbol{\Omega}_{\mathrm{R}}) \boldsymbol{F}(\boldsymbol{\Omega}_{\mathrm{R}}) \mathrm{d}\boldsymbol{\Omega}_{\mathrm{R}} \Big) \overline{\boldsymbol{\Upsilon}}_j, \tag{10}$$

where $\overline{\boldsymbol{\Upsilon}}_j$ denotes one of the $2J$ columns in $\overline{\boldsymbol{\Upsilon}}$.

According to Assumption 3) we consider orthogonal clusters as seen from the BS, i.e., the signal transmitted towards cluster i does not leak to the terminal via any other cluster $j \neq i$. By assuming that clusters, and therefore also E-fields, are non-overlapping as seen from the BS side, $\boldsymbol{E}_{\mathrm{T},i}^{\mathrm{H}}(\boldsymbol{\Omega}_{\mathrm{T}}) \boldsymbol{E}_{\mathrm{T},j}(\boldsymbol{\Omega}_{\mathrm{T}}) = 0$, $i \neq j$ holds and orthogonality is trivially satisfied. Consequences of this assumption are that we neglect energy leakage between clusters and dispersion induced weak signal contributions outside the defined clusters. As the number of BS transmit antenna elements J increases, the angular resolution increases, and the AOD dependency on the phases in the entries of $\overline{\boldsymbol{\Upsilon}}$ makes the different rows asymptotically orthogonal, i.e.

$$\lim_{J \to \infty} \overline{\boldsymbol{\Upsilon}} \overline{\boldsymbol{\Upsilon}}^{\mathrm{H}} = I. \tag{11}$$

Further simplifying notation, we collect our K terminal antennas in a $K \times 2$ matrix, $\boldsymbol{\Psi}(\boldsymbol{\Omega}) = [\boldsymbol{\Psi}_0(\boldsymbol{\Omega}) \ \boldsymbol{\Psi}_1(\boldsymbol{\Omega}) \cdots \boldsymbol{\Psi}_{K-1}(\boldsymbol{\Omega})]^{\mathrm{T}}$ where all $\boldsymbol{\Psi}_k(\boldsymbol{\Omega})$ are defined with a common center point. Finally, we express the $K \times 2J$ channel transfer function matrix in (1) as

$$\boldsymbol{H} = \Big(\int_{4\pi} \boldsymbol{\Psi}^{\mathrm{H}}(\boldsymbol{\Omega}) \boldsymbol{F}(\boldsymbol{\Omega}) \mathrm{d}\boldsymbol{\Omega} \Big) \overline{\boldsymbol{\Upsilon}}, \tag{12}$$

where we have removed the subscript R from $\boldsymbol{\Omega}$, as we now only need to consider angles at the terminal side. Note that (12) is valid for any K, as long as all antennas are exposed to the same electrical field.

3.2 Further Simplification of the Channel Transfer Function and derivation of an expression for the Gramian

The Gramian, $\boldsymbol{G} = \boldsymbol{H}\boldsymbol{H}^{\mathrm{H}}$, of a channel transfer function $\boldsymbol{H}$ defines the inner product space for a channel realization. It is well known that system performance depends only on $\boldsymbol{G}$ and not on $\boldsymbol{H}$ itself. Since the Gramian is Hermitian it can be represented by $K(K+1)/2$ numbers. This is much less compared to the full channel matrix which requires $K \times 2J$ numbers. For the special case $K = 2$, a normalized version of the Gramian is reflecting the correlation, α, and the power imbalance, β, between the two terminal receive antennas for a given realization [22],

$$\boldsymbol{G}_{\mathrm{N}} = \begin{bmatrix} 1+\beta & \alpha \\ \alpha^* & 1-\beta \end{bmatrix}. \tag{13}$$

Invoking our assumptions on the channel properties, we can express α and β entirely based on terminal antenna patterns $\boldsymbol{\Psi}(\boldsymbol{\Omega})$ and a limited set of cluster properties.

Inserting (12) in (1) we have

$$\boldsymbol{y} = \Big(\int\limits_{4\pi} \boldsymbol{\Psi}^{\mathrm{H}}(\boldsymbol{\Omega}) \boldsymbol{F}(\boldsymbol{\Omega}) \mathrm{d}\boldsymbol{\Omega} \Big) \overline{\boldsymbol{\Upsilon}} \boldsymbol{x} + \boldsymbol{n}. \tag{14}$$

Provided that $J \geq N$, where each antenna element is represented by two orthogonal polarized antenna ports, we may control phase, amplitude and polarization of the E-field $\boldsymbol{E}_{\mathrm{R}n}(\boldsymbol{\Omega})$ in the direction of each cluster individually (11). By a few manipulations, we can substitute the $2J$ transmit signals with $2N$ signals addressing the respective polarization of the different clusters. To do so, we perform the singular value decomposition (SVD) $\overline{\boldsymbol{\Upsilon}} = \boldsymbol{U}\boldsymbol{S}\boldsymbol{V}^{\mathrm{H}}$. Multiplying $\overline{\boldsymbol{\Upsilon}}$ with a truncated version of $\boldsymbol{V}$ corresponds to addressing the dominant eigenmodes; the signals $\boldsymbol{x}$ also need to be transformed accordingly. We assign $\boldsymbol{s} = \boldsymbol{V}_{\mathrm{eig}}^{\mathrm{H}} \boldsymbol{x}$ and $\boldsymbol{Q} = \overline{\boldsymbol{\Upsilon}} \boldsymbol{V}_{\mathrm{eig}}$ where $\boldsymbol{V}_{\mathrm{eig}}$ is the first $2N$ columns of $\boldsymbol{V}$. This gives $\overline{\boldsymbol{\Upsilon}} \boldsymbol{x} = \boldsymbol{U}\boldsymbol{S}\boldsymbol{V}^{\mathrm{H}} \boldsymbol{x} = \boldsymbol{U}\boldsymbol{S}\boldsymbol{V}^{\mathrm{H}} \boldsymbol{V}_{\mathrm{eig}} \boldsymbol{V}_{\mathrm{eig}}^{\mathrm{H}} \boldsymbol{x} = \boldsymbol{Q}\boldsymbol{s}$. The input signal $\boldsymbol{s}$ is a $2N \times 1$ vector and $\boldsymbol{V}_{\mathrm{eig}}$ the precoding matrix generating corresponding signals (i.e. $\boldsymbol{x}$) for the $2J$ antennas, shown to the left in Fig. 2. The matrix $\boldsymbol{Q}$ has a block diagonal structure where each block of size 2×2 is associated with a cluster. Equation (14) now becomes

$$\boldsymbol{y} = \Big(\int\limits_{4\pi} \boldsymbol{\Psi}^{\mathrm{H}}(\boldsymbol{\Omega}) \boldsymbol{F}(\boldsymbol{\Omega}) \mathrm{d}\boldsymbol{\Omega} \Big) \boldsymbol{Q}\boldsymbol{s} + \boldsymbol{n}, \tag{15}$$

and the Gramian can be expressed as

$$\boldsymbol{G} = \int\limits_{4\pi} \int\limits_{4\pi} \boldsymbol{\Psi}^{\mathrm{H}}(\boldsymbol{\Omega}_1) \boldsymbol{F}(\boldsymbol{\Omega}_1) \boldsymbol{Q}\boldsymbol{Q}^{\mathrm{H}} \boldsymbol{F}^{\mathrm{H}}(\boldsymbol{\Omega}_2) \boldsymbol{\Psi}(\boldsymbol{\Omega}_2) \mathrm{d}\boldsymbol{\Omega}_1 \mathrm{d}\boldsymbol{\Omega}_2. \tag{16}$$

Orthogonality among rows in $\overline{\boldsymbol{\Upsilon}}$ is maintained also in $\boldsymbol{Q}$, i.e.,

$$\lim_{J \to \infty} \boldsymbol{Q}\boldsymbol{Q}^{\mathrm{H}} = \boldsymbol{I}. \tag{17}$$

With a few more assumptions we are able to simplify (16). Following [20], [23], and Assumption 4), cluster functions $\boldsymbol{F}_n(\boldsymbol{\Omega})$ are represented by a scalar gain factor multiplied with a unitary matrix, $\boldsymbol{F}_n(\boldsymbol{\Omega}) = \lambda_n \boldsymbol{U}_n(\boldsymbol{\Omega})$. We assume the error caused by this assumption to be small and that it can be assigned to λ_n, the cluster gain. Here we are interested in how environmental variations impact the number of clusters, their relative power distribution, and the AS (defined as 2 times the angle from the center AOA to the periphery of a circular cluster). We constrain the total power of all clusters for a realization to N, hence $\sum_{n=0}^{N-1} \lambda_n^2 = N$. The Gramian can now be expressed

$$\boldsymbol{G} = \sum_{n=0}^{N-1} \lambda_n^2 \int\limits_{4\pi} \int\limits_{4\pi} \boldsymbol{\Psi}^{\mathrm{H}}(\boldsymbol{\Omega}_1) \boldsymbol{U}_n(\boldsymbol{\Omega}_1) \boldsymbol{U}_n^{\mathrm{H}}(\boldsymbol{\Omega}_2) \boldsymbol{\Psi}(\boldsymbol{\Omega}_2) \mathrm{d}\boldsymbol{\Omega}_1 \mathrm{d}\boldsymbol{\Omega}_2. \tag{18}$$

According to Assumption 2) the BS can only resolve a scalar property for each cluster and polarization, $\boldsymbol{U}_n(\boldsymbol{\Omega}_1) \boldsymbol{U}_n^{\mathrm{H}}(\boldsymbol{\Omega}_2) = \boldsymbol{I}$, for the AOA illuminated by each cluster

($\boldsymbol{\Omega}_1, \boldsymbol{\Omega}_2 \in \mathcal{A}_n$), and $\mathbf{0}$ otherwise. Thus, each cluster only impacts the amplitude and angular properties at the terminal receive side and the Gramian becomes

$$\boldsymbol{G} = \sum_{n=0}^{N-1} \lambda_n^2 \int_{\mathcal{A}_n} \Big(\int_{\mathcal{A}_n} \boldsymbol{\Psi}^{\mathrm{H}}(\boldsymbol{\Omega}_1) \mathrm{d}\boldsymbol{\Omega}_1 \Big) \boldsymbol{\Psi}(\boldsymbol{\Omega}_2) \mathrm{d}\boldsymbol{\Omega}_2. \tag{19}$$

Simplifying notation further, we define

$$\overline{\boldsymbol{\Psi}}_{k,n} = \int_{\mathcal{A}_n} \boldsymbol{\Psi}_k(\boldsymbol{\Omega}) \mathrm{d}\boldsymbol{\Omega}. \tag{20}$$

and arrive at

$$\boldsymbol{G} = \sum_{n=0}^{N-1} \lambda_n^2 \begin{bmatrix} \overline{\boldsymbol{\Psi}}_{0,n}^{\mathrm{H}} \\ \overline{\boldsymbol{\Psi}}_{1,n}^{\mathrm{H}} \end{bmatrix} \begin{bmatrix} \overline{\boldsymbol{\Psi}}_{0,n} & \overline{\boldsymbol{\Psi}}_{1,n} \end{bmatrix}, \tag{21}$$

which, with normalization by the average of diagonal elements, is cast in the form of (13) as

$$\boldsymbol{G}_{\mathrm{N}} = \frac{1}{B} \begin{bmatrix} \sum_{n=0}^{N-1} \lambda_n^2 \left\| \overline{\boldsymbol{\Psi}}_{0,n} \right\|^2 & \sum_{n=0}^{N-1} \lambda_n^2 \overline{\boldsymbol{\Psi}}_{0,n}^{\mathrm{H}} \overline{\boldsymbol{\Psi}}_{1,n} \\ \sum_{n=0}^{N-1} \lambda_n^2 \overline{\boldsymbol{\Psi}}_{1,n}^{\mathrm{H}} \overline{\boldsymbol{\Psi}}_{0,n} & \sum_{n=0}^{N-1} \lambda_n^2 \left\| \overline{\boldsymbol{\Psi}}_{1,n} \right\|^2 \end{bmatrix}, \tag{22}$$

where

$$B = \frac{1}{2} \sum_{n=0}^{N-1} \lambda_n^2 \left(\left\| \overline{\boldsymbol{\Psi}}_{0,n} \right\|^2 + \left\| \overline{\boldsymbol{\Psi}}_{1,n} \right\|^2 \right). \tag{23}$$

We have now reached a point where our communication link is characterized by only a few environment parameters, namely the number of clusters N, the cluster gains λ_n and their ASs as defined by $\mathcal{A}_n$. Beside those, the simulation framework also uses terminal antenna gain patterns $\boldsymbol{\Psi}_k(\boldsymbol{\Omega})$, see Fig. 1.

3.3 Assigning Model Parameters

In our simulations, we assume circular clusters uniformly distributed over angle (Assumption 5) with a fixed AS. This assumption is motivated by matching our channel to indoor measurements similar to observations from [24].

However, the measurements in [24] were performed for a limited set of environments, therefore there are no statistical distributions for the propagation delay for the different clusters, and the proposed cluster gain standard deviation, therefore, include effects of both delay and cluster gain. In our simulations, we use the approach in [23], where

$$\lambda_n^2 = N \frac{10^{-D_n/10}}{\sum_{i=0}^{N-1} 10^{-D_i/10}}, \tag{24}$$

Figure 3: Phantom head with hand left.

and $D_n \sim \mathcal{N}(0, C^2)$ has a Gaussian distribution with mean 0 and standard deviation C.

Monte Carlo (MC) simulations are used to calculate empirical distributions of correlation α and power imbalance β for the Gramian (22), for various N, AS and C.

4 Comparison between simulated and measured performance

We compare free-space (FS) performance with that of beside-head-with-hand-left side (BHHL) in order to analyze in different channel conditions the same environment. The terminal antenna gain patterns are measured patterns of the two top antennas of the Xperia ZL prototype that was used in [9]. The antenna patterns were measured and characterized in an anechoic chamber where a phantom head and a phantom hand were used for the BHHL case, see Fig. 3. Although antenna gain patterns are continuous 2D functions, the measured patterns have 2° resolution in both azimuth and elevation dimensions. We are aware that BHHL is not a typical 5G use case, but its use here is motivated by being well-defined, repeatable, and representing a moderate loading scenario with increased antenna directivity.

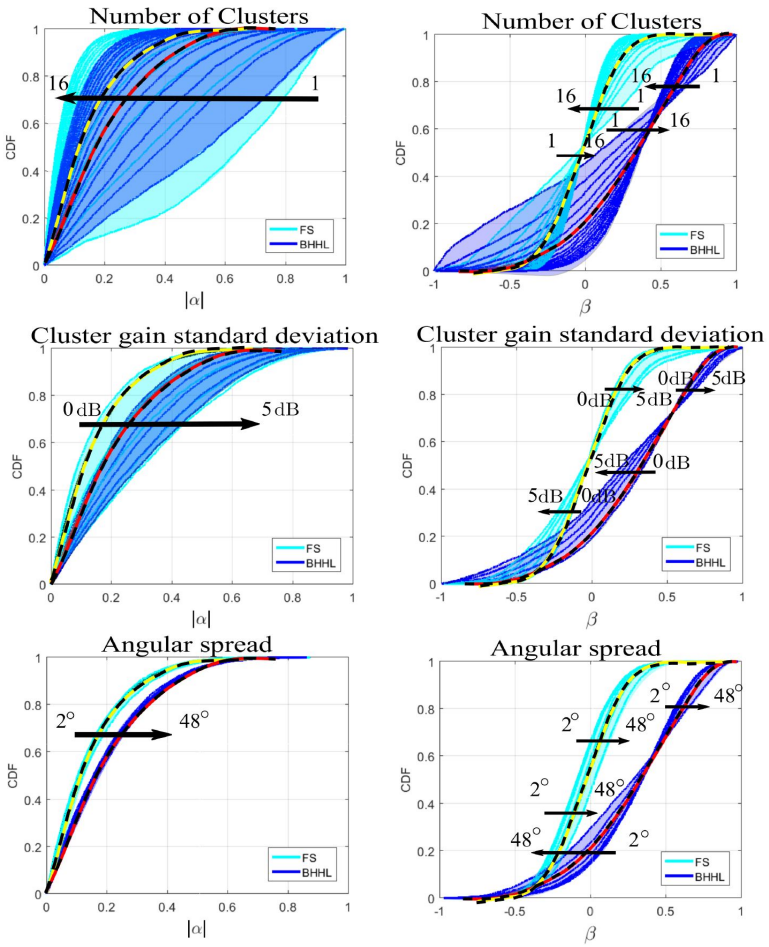

Figure 4: CDFs of the magnitude of the estimated correlation α (left column) and power imbalance β (right column). Upper row, as a function of the number of clusters, in the center as a function of cluster gain standard deviation, and bottom as a function of AS. The shaded areas highlight the region over which the curves span as a parameter is changed and the highlighted curves are the same in all figures, used as the reference.

4.1 Analysis of parameter impact on the Gramian

There are three input parameters that reflect the channel behavior used by the simulation framework, the number of clusters N, the cluster gain standard deviation, C, and the AS. The impact of the parameters is analyzed through cumulative distribution functions (CDFs) of the Gramian entries, i.e., β and the magnitude of α in (13)[3]. In Fig. 4, $|\alpha|$ and β are shown as functions of the number of clusters, cluster gain standard deviation and AS.

The leftmost plots of Fig. 4 show CDFs of $|\alpha|$ and β as the number of clusters N is changed. Changing N impacts as much on FS as it does on BHHL, as long as $N > 2$, and the CDFs can cover a wide range by adjusting N. For the case of a single cluster, the correlation in FS is increased dramatically. In this scenario the correlation is defined by the antenna cross-polarization ratio. The variation of the power imbalance decreases as N grows, while the relative difference between FS and BHHL stays about the same.

The center plots of Fig. 4 show CDFs of $|\alpha|$ and β as the cluster gain standard deviation C is altered in the range from 0 to 5 dB. When the cluster gain standard deviation is increased the effective number of clusters is reduced, thus the correlation goes up.

The right upper and lower plots of Fig. 4 show CDFs of $|\alpha|$ and β, respectively, as the AS is increased from 2°to 48°. For $|\alpha|$ the impact of changing AS is small and affects FS as much as BHHL. This may seem contradictory to the expectation that correlation between antennas decreases as the illuminated angles increases. This, however, is a result of the modeling approach, as we define a single polarization, phase, and amplitude for each cluster in (20), motivated by the fact that the BS is unable to control the signal to each individual MPC. For the power imbalance β the AS has an impact on the slope in the BHHL case while the FS curves are shifted in parallel, hence the average power imbalance is reduced. This is due to the constant value of polarization, phase, and amplitude per cluster, which impacts balanced antennas differently.

4.2 Measurement setup

Measurements have been performed in an auditorium, as shown in Fig. 5 and Fig. 6. The auditorium was chosen since earlier channel sounding campaigns have been performed in the same place, providing prior knowledge of the channel properties [24]. During all measurements, the MaMi BS was placed in the front center and the terminal in the center of the room. Both the number of clusters and the cluster-power distribution are therefore assumed constant. Additionally, we used an absorbent to block the LOS between the BS and the terminal, mainly due to limitations in the dynamic range of the BHHL measurements. Both FS and BHHL were measured using the same prototype and phantom as during antenna characterization. By only moderately altering the position and rotating the terminal while monitoring channel

[3] As we consider only two-antenna terminals, $K = 2$, the corresponding eigenvalues determining performance depend only on the magnitude of off-diagonal elements, $|\alpha|$.

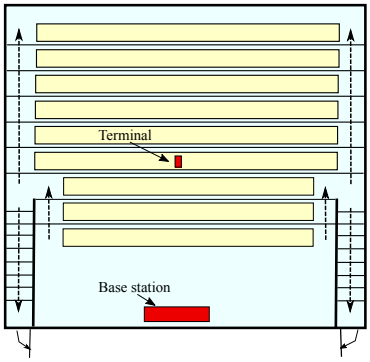

Figure 5: Overview of the measurement setup in the auditorium.

Figure 6: A photo showing the measurement setup.

properties, the variation can be assumed to be determined by the terminal antenna properties in a static propagation channel.

For both FS and BHHL, the terminal was rotated in steps of about 10° for 3 orientations, with a difference in elevation and/or azimuth by 90°. For each load case, 180 channels were measured.

4.3 Matching the channels

To compare simulation and measurement results, $|\alpha|$ and β have been computed from the measured Gramian. Then, the Gramians from the measurements and simulations have been matched according to the maximum likelihood (ML) principle, under the assumption that $|\alpha|$ and β are independent. Using empirical distributions $\mathrm{Pr}_{\mathrm{scenario}}(\alpha_s)$ and $\mathrm{Pr}_{\mathrm{scenario}}(\beta_s)$ derived from 5000 sample simulations, as described above, we proceed with the parameter estimation. For each set of environmental

Table 1: Statistics

	Median $\|\alpha\|$	**STD $\|\alpha\|$**	**Median β**	**STD β**
Sim FS	0.11	0.13	-0.02	0.21
Meas FS	0.20	0.09	-0.02	0.32
Sim BHHL	0.20	0.17	0.31	0.37
Meas BHHL	0.16	0.22	0.21	0.43

parameters the product of all probabilities,

$$\mathrm{Pr}_{\mathrm{tot}} = \prod_{s=1}^{S} \Big(\mathrm{Pr}_{\mathrm{FS}}(\alpha_s) \mathrm{Pr}_{\mathrm{FS}}(\beta_s) \Big) \prod_{v=1}^{V} \Big(\mathrm{Pr}_{\mathrm{BHHL}}(\alpha_v) \mathrm{Pr}_{\mathrm{BHHL}}(\beta_v) \Big), \tag{25}$$

is calculated, where the number of FS measurements, S, is 87 and the number of BHHL measurements, V, is 99.

The environmental parameters providing the largest probability were selected and found to be $N = 6$ clusters, AS $= 36^\circ$ and $C = 1$ dB. The cluster gain standard deviation in [24] was between 5 and 6 dB and was estimated based on a set of 14 clusters. In our measurements, we blocked the LOS component which may explain why the cluster gain standard deviation is smaller than that in [24]. It can also be noted that the most influential effect of cluster gain standard deviation is to reduce the effective number of clusters. Hence, increased number of clusters in combination with cluster gain standard deviation yield similar $\mathrm{Pr}_{\mathrm{tot}}$. Fig. 7 shows the CDFs for both measurements and simulations for the selected load cases for $|\alpha|$ and β in the upper and lower plots, respectively.

The median and standard deviations of the correlation and power imbalance are shown in Table 1. We note that the medians of the correlation for FS differ by almost a factor of 2, while both correlation and power imbalance for the loaded cases are better captured by the simulation framework.

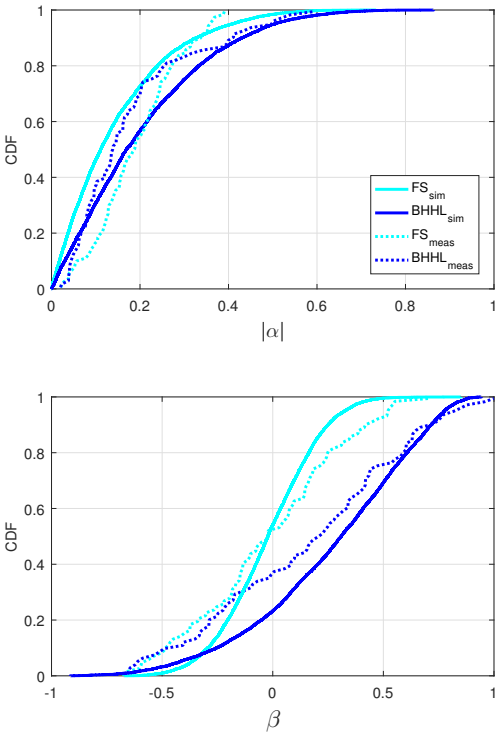

Figure 7: Estimated magnitude of the correlation $|\alpha|$ (upper) and power imbalance β (lower) for measurements and simulations.

5 Derivation of Received signal Properties at the Terminal

While the correlation and power imbalance describe the channel properties, it remains to study their impact on different transmission strategies. Therefore, received signal powers for multi-antenna terminals using the simulation framework are derived next. The three diversity schemes from [9] are implemented and the impact that different pilot transmission strategies have on the received signal will be analyzed. Also, the performance of the different schemes is related to the Gramian (21). Finally, we also introduce a second prototype with a different antenna implementation. We compare the performance of the first and second prototype, using both simulations

and measurements.

In all expressions from now on, we assume that the SNR is large so that the noise can be neglected. In section 3.2 we derived an expression for the received signal at the terminal (14) where we included the cluster based channel model from Fig. 2, still with a dependency on the BS transmit antenna elements. In equation (15) we determined the precoding needed to address each cluster individually with a feed vector with $2N$ terms. As we are only interested in the resulting E-field generated by the clusters, we simplify the notation by defining

$$\boldsymbol{\gamma} = \boldsymbol{Q}\boldsymbol{s} \tag{26}$$

from (15) with $2N$ entries $\boldsymbol{\gamma} = [\gamma_0^{\Theta}\ \gamma_0^{\Phi}\ \gamma_1^{\Theta}\ \gamma_1^{\Phi} \cdots \gamma_{N-1}^{\Phi}]^{\mathrm{T}}$. Expressing the received signal in terms of $\boldsymbol{\gamma}$-entries we get

$$\boldsymbol{y} = \sum_{n=0}^{N-1} \lambda_n \Big(\int_{4\pi} \boldsymbol{\Psi}^{\mathrm{H}}(\boldsymbol{\Omega}) \boldsymbol{U}_n(\boldsymbol{\Omega}) \mathrm{d}\boldsymbol{\Omega} \Big) \boldsymbol{\gamma}_n, \tag{27}$$

where $\boldsymbol{\gamma}_n = [\gamma_n^{\Theta}\ \gamma_n^{\Phi}]^{\mathrm{T}}$.

So far, we have assumed full knowledge of the channel at the BS side. In a real TDD MaMi system, the channel is estimated from uplink pilot signals transmitted from the terminal antennas, and the BS use the estimates to optimize $\boldsymbol{\gamma}$. The pilot signal from the terminal determines how the channel is seen by the BS. We assume that the BS blindly performs the same operations based on the received pilot and is not aware of what or which antenna(s) it has been transmitted from. In fact, the BS does not need to know how many antennas the terminal is equipped with. This means that the received signal during the downlink phase at the terminal, in turn, depends on the pilot transmission strategy and that the terminal has some freedom to select this. We define $\boldsymbol{\kappa}$ as the weight vector defining the distribution of the pilot signal to our antennas. For K antennas at the terminal the pilot vector is given by $\boldsymbol{\kappa} = [\kappa_0\, \kappa_1 \cdots \kappa_{k-1}]^{\mathrm{T}}$, with power which, without loss of generality, is set to $\|\boldsymbol{\kappa}\|^2 = 1$.

Since the assumption is single-antenna terminals, the equivalent effective antenna pattern created by pilots $\boldsymbol{\kappa}$ becomes $\boldsymbol{\Psi}_{\boldsymbol{\kappa}}(\boldsymbol{\Omega}) = \boldsymbol{\kappa}^{\mathrm{T}}\boldsymbol{\Psi}(\boldsymbol{\Omega})$. Further, with this effective antenna pattern, the exploitation of reciprocity leads to an assumed downlink

$$y_{\text{assumed}} = \sum_{n=0}^{N-1} \lambda_n \Big(\int_{4\pi} \boldsymbol{\Psi}_{\boldsymbol{\kappa}}^{\mathrm{H}}(\boldsymbol{\Omega}) \boldsymbol{U}_n(\boldsymbol{\Omega}) \mathrm{d}\boldsymbol{\Omega} \Big) \boldsymbol{\gamma}_n, \tag{28}$$

and the BS optimizes received downlink power as

$$\boldsymbol{\gamma}^{\text{opt}} = \arg \max_{\boldsymbol{\gamma}:\|\boldsymbol{\gamma}\|^2=1} |y_{\text{assumed}}|^2 . \tag{29}$$

This optimization results in $\boldsymbol{\gamma}^{\text{opt}}$ in the form of a spatially matched filter, and thus for cluster n it becomes

$$\boldsymbol{\gamma}_n^{\text{opt}} = \frac{\lambda_n}{q} \int_{4\pi} \boldsymbol{U}_n^{\mathrm{H}}(\boldsymbol{\Omega}) \boldsymbol{\Psi}_{\boldsymbol{\kappa}}(\boldsymbol{\Omega}) \mathrm{d}\boldsymbol{\Omega}, \tag{30}$$

where

$$q = \sqrt{\sum_{n=0}^{N-1} \lambda_n^2 \left\| \int_{4\pi} \boldsymbol{\Psi}_{\boldsymbol{\kappa}}^{\mathrm{H}}(\boldsymbol{\Omega}) \boldsymbol{U}_n(\boldsymbol{\Omega}) \mathrm{d}\boldsymbol{\Omega} \right\|^2} \tag{31}$$

normalizes total cluster power to unity.

Inserting $\boldsymbol{\gamma}_n^{\mathrm{opt}}$ from (30) into (27) and squaring, we express received downlink power on antenna k as

$$P_{k|\boldsymbol{\kappa}} = \frac{1}{q^2 Z_0} \left| \sum_{n=0}^{N-1} \lambda_n^2 \int_{4\pi} \int_{4\pi} \boldsymbol{\Psi}_k^{\mathrm{H}}(\boldsymbol{\Omega}_1) \boldsymbol{U}_n(\boldsymbol{\Omega}_1) \times \boldsymbol{U}_n^{\mathrm{H}}(\boldsymbol{\Omega}_2) \boldsymbol{\Psi}_{\boldsymbol{\kappa}}(\boldsymbol{\Omega}_2) \mathrm{d}\boldsymbol{\Omega}_1 \mathrm{d}\boldsymbol{\Omega}_2 \right|^2, \tag{32}$$

where Z_0 is the intrinsic impedance of vacuum (377Ω). Using Assumption 4) and notation from (20), we further simplify to

$$P_{k|\boldsymbol{\kappa}} = \frac{1}{q^2 Z_0} \left| \sum_{n=0}^{N-1} \lambda_n^2 \int_{\mathcal{A}_n} \int_{\mathcal{A}_n} \boldsymbol{\Psi}_k^{\mathrm{H}}(\boldsymbol{\Omega}_1) \boldsymbol{\Psi}_{\boldsymbol{\kappa}}(\boldsymbol{\Omega}_2) \mathrm{d}\boldsymbol{\Omega}_1 \mathrm{d}\boldsymbol{\Omega}_2 \right|^2 \tag{33}$$

$$= \frac{1}{Z_0} \frac{\left| \sum_{n=0}^{N-1} \lambda_n^2 \overline{\boldsymbol{\Psi}}_{k,n}^{\mathrm{H}} \overline{\boldsymbol{\Psi}}_{\boldsymbol{\kappa},n} \right|^2}{\sum_{n=0}^{N-1} \lambda_n^2 \left\| \overline{\boldsymbol{\Psi}}_{\boldsymbol{\kappa},n} \right\|^2}. \tag{34}$$

Like in Section 3.2 the results from now on are restricted to terminals with two antennas, antenna 0 and antenna 1.

5.1 Single antenna transmissions

Assuming that the pilot signal is transmitted from terminal antenna 0 only, using a pilot vector $\boldsymbol{\kappa}_0 = [1 \ 0]^{\mathrm{T}}$, the received downlink signal on the same antenna is given by (34) as

$$P_{0|\boldsymbol{\kappa}_0} = \frac{1}{Z_0} \sum_{n=0}^{N-1} \lambda_n^2 \left\| \overline{\boldsymbol{\Psi}}_{0,n} \right\|^2. \tag{35}$$

This corresponds to a Z_0-scaled version of the first diagonal entry of the Gramian (22), before normalization.

5.2 Passive Diversity

Passive diversity (PD) is the case when the terminal has two active receivers, while only a single transmit chain is connected to one of the antennas. This scheme achieves diversity only in the downlink where the received signals from the antennas are combined according to the maximum ratio (MRC) principle. We combine the received

signals from both antenna 0, that transmitted the pilot, given by (35), and the leaked signal to antenna 1 given by (34) to get

$$P_{\mathrm{PD}|\boldsymbol{\kappa}_0} = P_{0|\boldsymbol{\kappa}_0} + P_{1|\boldsymbol{\kappa}_0}, \tag{36}$$

where

$$P_{1|\boldsymbol{\kappa}_0} = \frac{1}{Z_0} \frac{\left| \sum_{n=0}^{N-1} \lambda_n^2 \overline{\boldsymbol{\Psi}}_{1,n}^{\mathrm{H}} \overline{\boldsymbol{\Psi}}_{0,n} \right|^2}{\sum_{n=0}^{N-1} \lambda_n^2 \left\| \overline{\boldsymbol{\Psi}}_{0,n} \right\|^2}. \tag{37}$$

As the expression indicates, the leaked signal to antenna 1 depends mainly on the off-diagonal entries of the Gramian (34).

By transmitting a pilot signal from each antenna, on different time-frequency resources, the terminal can compute the magnitude of the different entries in the Gramian from the received signals.

5.3 Switched Diversity

In switched diversity (SWD), the terminal antenna giving the highest received downlink power is always selected for all transmissions. For each cluster scenario, we need to optimize $\boldsymbol{\gamma}$ for both antennas and select the $\boldsymbol{\gamma}$ and the associated antenna that yields the highest power. This means

$$P_{\mathrm{SWD}} = \max\left(P_{0|\boldsymbol{\kappa}_0}, P_{1|\boldsymbol{\kappa}_1}\right), \tag{38}$$

where $\boldsymbol{\kappa}_1 = [0 \;\; 1]$, and from (35) we get

$$P_{0|\boldsymbol{\kappa}_0} = \frac{1}{Z_0} \sum_{n=0}^{N-1} \lambda_n^2 \left\| \overline{\boldsymbol{\Psi}}_{0,n} \right\|^2, \tag{39}$$

and

$$P_{1|\boldsymbol{\kappa}_1} = \frac{1}{Z_0} \sum_{n=0}^{N-1} \lambda_n^2 \left\| \overline{\boldsymbol{\Psi}}_{1,n} \right\|^2. \tag{40}$$

Again we see that the Gramian (21) reveals the achieved performance. This time through its largest diagonal entry.

5.4 Dominant Eigenmode

Dominant eigenmode (DEM) is when both terminal antennas are used simultaneously for all transmissions in an SNR-optimal way. Based on our framework the BS needs to determine the $\boldsymbol{\gamma}$ that maximizes received power, i.e.

$$\boldsymbol{\gamma}^{\mathrm{opt}} = \arg \max_{\boldsymbol{\gamma}:\|\boldsymbol{\gamma}\|^2=1} \left(|y_0|^2 + |y_1|^2 \right). \tag{41}$$

In an idealized noise-free case, the channel $\boldsymbol{H}$ based on (27) is given by,

$$\boldsymbol{H} = \sum_{n=0}^{N-1} \lambda_n \int_{4\pi} \boldsymbol{\Psi}^{\mathrm{H}}(\boldsymbol{\Omega}) \boldsymbol{U}_n(\boldsymbol{\Omega}) \mathrm{d}\boldsymbol{\Omega}. \tag{42}$$

With $\boldsymbol{y} = \boldsymbol{H}\boldsymbol{\gamma}$, the constrained maximization in (41) becomes,

$$\boldsymbol{\gamma}^{\mathrm{opt}} = \underset{\boldsymbol{\gamma}}{\mathrm{argmax}} \left(\frac{\boldsymbol{\gamma}\boldsymbol{H}^{\mathrm{H}}\boldsymbol{H}\boldsymbol{\gamma}}{\boldsymbol{\gamma}^{\mathrm{H}}\boldsymbol{\gamma}} \right). \tag{43}$$

To maximize (43), $\boldsymbol{\gamma}$ is selected as the eigenvector associated with the largest eigenvalue of $\boldsymbol{H}^{\mathrm{H}}\boldsymbol{H}$. This requires that the BS knows $\boldsymbol{H}$. But, the BS automatically finds $\boldsymbol{\gamma}^{\mathrm{opt}}$ if the terminal weight the pilot signals with the eigenvector associated with the strongest eigenvalue of the Gramian, defined as $\boldsymbol{\kappa}^{\mathrm{opt}} = \boldsymbol{v}_1(\boldsymbol{G})$. This follows from the fact that the inner and outer product have the same eigenvalues, $\mathrm{eig}(\boldsymbol{H}^{\mathrm{H}}\boldsymbol{H}) = \mathrm{eig}(\boldsymbol{H}\boldsymbol{H}^{\mathrm{H}})$, where the latter is $\mathrm{eig}(\boldsymbol{G})$.

We use the same weight vector for the received signals at the terminal by multiplying (27) with $\boldsymbol{\kappa}^{\mathrm{opt}}$ and

$$y_{\mathrm{DEM}} = (\boldsymbol{\kappa}^{\mathrm{opt}})^{\mathrm{T}} \boldsymbol{y}_{|\boldsymbol{\kappa}^{\mathrm{opt}}}.$$

Following (32)-(34), the received power becomes

$$P_{\mathrm{DEM}} = \frac{1}{Z_0} \sum_{n=0}^{N-1} \lambda_n^2 \left\| \overline{\boldsymbol{\Psi}}_{\boldsymbol{\kappa},n}(\boldsymbol{\Omega}) \right\|^2. \tag{44}$$

If we select the weight vector $\boldsymbol{\kappa}_0$ in (44) we get $P_{0|\boldsymbol{\kappa}_0}$ from (35) and similarly the selection of $\boldsymbol{\kappa}_1$ yields $P_{1|\boldsymbol{\kappa}_1}$.

Deriving the DEM performance from the Gramian (21) is a bit more involved than for the other schemes. The DEM performance is given by

$$P_{\mathrm{DEM}} = \frac{1}{Z_0} (\boldsymbol{v}_1 |\boldsymbol{G}|)^{\mathrm{T}} |\boldsymbol{G}| [1 \;\; 1]^{\mathrm{T}}, \tag{45}$$

where $|\cdot|$ denotes the magnitude of the matrix entries. Given the diversity schemes above, we can evaluate their performance for different terminal antenna configurations and pilot transmission strategies in the context of a MaMi by MC simulations. For this we need to select appropriate values on the AS, the number of clusters N and the cluster gain standard deviation C, matching the targeted propagation environment.

Table 2 presents a summary of pilot vectors, $\boldsymbol{\gamma}^{\mathrm{opt}}$, received powers, and how they relate to the Gramian, for the different schemes. It can be argued that a pilot needs to be transmitted from each terminal antenna in order to determine the Gramian, i.e. $\boldsymbol{\kappa}_0$ and $\boldsymbol{\kappa}_1$, before the weight vector for SWD or DEM can be computed. For this evaluation, however, we assume that they are available. This corresponds to slow-enough changes in the channel for them to be appropriately estimated.

Table 2: Terminal pilot strategies, Power and Gramian relation for a 2 antenna terminal.

Mode	Pilot vector	Received power	Gramian relation	
Single	$\boldsymbol{\kappa}_0$	$P_{0\|\boldsymbol{\kappa}_0}$	$\boldsymbol{\kappa}_0^{\mathrm{T}}\boldsymbol{G}\boldsymbol{\kappa}_0$	
Leaked	$\boldsymbol{\kappa}_0$	$P_{1\|\boldsymbol{\kappa}_0}$	$\boldsymbol{\kappa}_0^{\mathrm{T}}\boldsymbol{G}\boldsymbol{\kappa}_1$	
PD	$\boldsymbol{\kappa}_0$	$P_{0\|\boldsymbol{\kappa}_0} + P_{1\|\boldsymbol{\kappa}_0}$	$\boldsymbol{\kappa}_0^{\mathrm{T}}\|\boldsymbol{G}\|[1\ \ 1]^{\mathrm{T}}$	
SWD	$\boldsymbol{\kappa}_0$ or $\boldsymbol{\kappa}_1$	$\max(P_{0\|\boldsymbol{\kappa}_0}, P_{1\|\boldsymbol{\kappa}_1})$	$\max(\boldsymbol{\kappa}_0^{\mathrm{T}}\boldsymbol{G}\boldsymbol{\kappa}_0, \boldsymbol{\kappa}_1^{\mathrm{T}}\boldsymbol{G}\boldsymbol{\kappa}_1)$	
DEM	$\boldsymbol{\kappa}^{\mathrm{opt}}$	$P_{\boldsymbol{\kappa}^{\mathrm{opt}}\|\boldsymbol{\kappa}^{\mathrm{opt}}}$	$(\boldsymbol{\kappa}^{\mathrm{opt}})^{\mathrm{T}}\|\boldsymbol{G}\|[1\ \ 1]^{\mathrm{T}}$	

6 Prototype Terminal Simulation Results

In this section, we present results based on MC simulations where the different transmission strategies are examined. In order to evaluate the framework, we compare the SNR gains for the different transmission schemes from simulations and measurements. In the simulations, we have applied the settings described in Section 4.3. Finally, to evaluate the validity of the environmental parameters, we introduce a second prototype, simulate it with the same settings, and compare the SNR gains to measured values.

Fig. 8 shows sample means for received powers $P_{0|\boldsymbol{\kappa}_0}$, $P_{1|\boldsymbol{\kappa}_1}$, P_{SWD}, P_{DEM}, $P_{0|\boldsymbol{\kappa}_1}$, and $P_{0|\boldsymbol{\kappa}_1}$, as functions of the number of clusters at the terminal side. Power on the vertical axis is normalized to that of an isotropic radiator with gain 0 dB, P_{ISO} in Fig. 8, when a single cluster is present. For single antenna transmission (35), the expected power at $n = 1$ equals the total radiated power in an isotropic environment. In this case, the received power grows with the number of clusters n, and the slope is limited by the directive gain of the antenna and the cluster gain standard deviation.

The powers in the figure are computed for a cluster AS of 36° and a cluster-gain standard deviation C of 1 dB as we derived in Section 4.3.

The upper curves are for FS condition and the lower curves are for BHHL condition. We can clearly see that the power received by the non-pilot transmitting antennas, e.g. $P_{0|\boldsymbol{\kappa}_1}$ and $P_{1|\boldsymbol{\kappa}_0}$, do not benefit from increased number of clusters. The offset between the FS curves and the BHHL curves shows the drop in efficiency caused by loading the antennas, BHHL load degrades power by 7 dB for antenna 0 and 5 dB for antenna 1.

With DEM we observe a significant increase in the received power, about 1 dB higher average power than the average power received by the better antenna can be expected. For SWD the average received power is slightly higher than the average power of the best performing antenna. PD powers are not included in Fig. 8 for clarity. It can, however, be mentioned that the power for PD is close to the performance for the respective antenna, especially when the number of clusters increases and the ratio $P_{0|\boldsymbol{\kappa}_0}/P_{1|\boldsymbol{\kappa}_0}$ or $P_{1|\boldsymbol{\kappa}_1}/P_{0|\boldsymbol{\kappa}_1}$ becomes large. The different diversity schemes have been

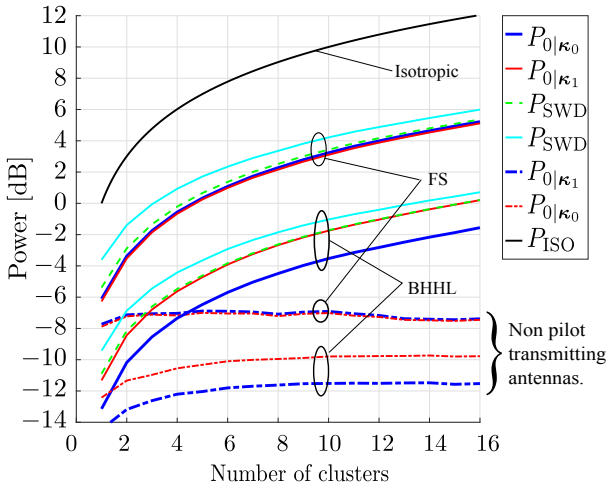

Figure 8: Simulated sample means for received powers $P_{0|\boldsymbol{\kappa}_0}$, $P_{1|\boldsymbol{\kappa}_1}$, P_{SWD}, P_{DEM}, $P_{0|\boldsymbol{\kappa}_1}$, and $P_{0|\boldsymbol{\kappa}_1}$ for FS and BHHL, as functions of the number of clusters, N, at the terminal side. Received power P_{ISO} for an isotropic radiator (top curve) is shown as reference.

implemented in the LuMaMi [10,11] testbed and measurements have been performed with the same setup as described in section 4.2. As it is not possible to sweep the number of clusters in measurements, we examine the distribution, i.e. the CDF, for $N = 6$ clusters as described in Section 4.3. By looking at the relative SNR gain obtained for the different transmission schemes compared to that of a single antenna the result become independent on the absolute power level. This enables a direct comparison to measurements.

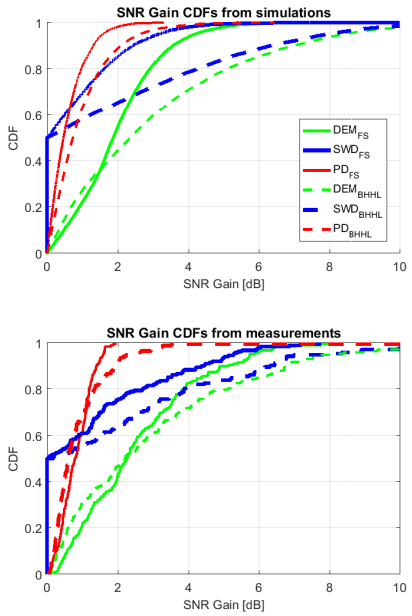

Figure 9: CDFs of SNR gains for the Xperia ZL prototype for the different diversity schemes. Simulation results above and measurement results below.

Fig. 9 shows the CDFs of simulated (top) and measured (bottom) SNR gains [9], i.e. the CDFs of the relative improvements in SNR achieved by a diversity scheme compared to that of a single antenna. Both antennas have been used as the reference in the plots and this explains why the SWD curves start at 0.5.

The plots indicate the improvement that can be expected if a second antenna is added to a MaMi terminal. SNR gain CDFs are shown for DEM, SWD, and PD, for both FS and BHHL. Channel dependent parameters in the simulations are set according to section 4.3.

We conclude that the behavior of the simulated SNR gains is similar to the measured ones, with larger values in the BHHL case for all schemes. The SNR gain is slightly underestimated in the simulations in the FS case and overestimated in the BHHL case. A possible explanation for this discrepancy is related to the fact that the BHHL loading is hard to repeat with full accuracy. A slight change in the terminal position in the hand may cause a large difference in the loading profile.

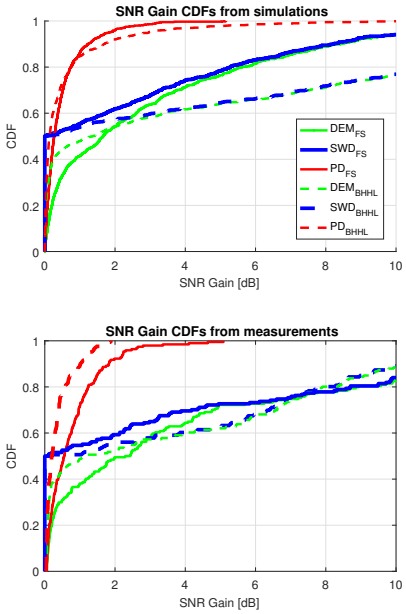

Figure 10: CDFs of the SNR gains for a second prototype, Xperia SP, for the different diversity schemes. Simulation results above and measurement results below.

To further evaluate our approach the second prototype, with a different antenna configuration based on an Xperia SP smartphone, is examined. The results are presented in Fig. 10.

Environmental settings for the simulations and the measurement environment are the same as those used with the Xperia ZL prototype. The antennas in the Xperia SP prototype are mounted in the top and bottom of the chassis. In FS condition the antennas are unbalanced by about 3 dB and the gain patterns show a directive gain in opposite directions, which is reflected in the results by larger SNR gains for the SWD and DEM schemes when compared to the results for the Xperia ZL prototype. A low correlation between antennas is indicated by the sharp slope in the beginning of the DEM curves and this is captured well both by simulations and measurements. For this reason, the DEM scheme often directs all power to only one of the antennas and DEM performance tend to be similar to that of SWD.

We conclude that the influence of different antenna properties and loading effects are well captured by the simulation framework. The behavior of the different diversity schemes and pilot transmission strategies are also nicely captured. We further

conclude that the limited number of parameters we use to model the channel yields good predictions of the antenna performance for the tested environment.

7 Summary

We have presented a simulation framework for the evaluation of the behavior of terminal antennas in a precoded MaMi system. The simulation framework randomly generates clusters with properties relevant for such MaMi channels. By ML estimation of the number of clusters, the cluster gain, and the angular spread we have shown that the proposed simulation framework can predict the behavior of different terminal antenna designs and loading effects in an indoor environment. The channel dependent parameters have been determined based on mapping of the CDFs for the antenna correlation and power imbalance to a real measured channel.

With the presented simulation framework, it is possible to evaluate terminal antenna designs, directional properties, loading effects and diversity schemes that take the pilot transmission strategies into account in a MaMi context, without performing extensive and time-consuming simulations of complicated base station processing and detailed channel models. This study is performed at 3.7 GHz. We believe that the simulation framework can be used also in a wider frequency range and in other environments, with appropriate selection of the parameters. We have, however, no results to back this up and consider it as an area for further study. At higher frequencies, above 6 GHz, some of the assumptions may need to be changed and also the transmission strategies may need to be changed accordingly.

8 Acknowledgment

The authors would like to thank Sony Mobile Communications in Lund and Stiftelsen för Strategisk Forskning (SSF) for funding. The authors also want to thank the anonymous reviewers for their valuable comments.

References

[1] T. L. Marzetta, "Noncooperative Cellular Wireless with Unlimited Numbers of Base Station Antennas OFDM," *IEEE Trans. Wireless Commun.*, vol. 9, no. 11, pp. 3590–3600, Nov. 2010, doi: http://dx.doi.org/10.1109/TWC.2010.092810.091092.

[2] E. G. Larsson, F. Tufvesson, O. Edfors, and T. L. Marzetta, "Massive MIMO for Next Generation Wireless Systems," *IEEE Communications Magazine*, vol. 52, no. 2, pp. 186–195, Feb. 2014, doi: http://dx.doi.org/10.1109/MCOM.2014.6736761.

[3] H. Q. Ngo, E. G. Larsson, and T. L. Marzetta, "Energy and Spectral Efficiency of Very Large Multiuser MIMO Systems," *IEEE Transactions on Communications*, vol. 61, no. 4, pp. 1436–1449, Apr. 2013, doi: http://dx.doi.org/10.1109/TCOMM.2013.020413.110848.

[4] A. Nordrum, "5G Researchers Set New World Record For Spectrum Efficiency," *IEEE Spectrum*, May 2016.

[5] *Study on Scenarios and Requirements for Next Generation Access Technologies*, 14th ed., ETSI, 3GPP TR 38.913, 2017.

[6] *Study on New Radio (NR) Access Technology*, 14th ed., ETSI, 3GPP TR 38.912, 2017.

[7] E. Björnson, J. Hoydis, M. Kountouris, and M. Debbah, "Massive MIMO Systems with Non-Ideal Hardware: Energy Efficiency, Estimation, and Capacity Limits," *IEEE Transactions on Information Theory*, vol. 60, no. 11, pp. 7112–7139, Nov. 2014, doi: http://dx.doi.org/10.1109/TIT.2014.2354403.

[8] E. L. Bengtsson, F. Tufvesson, and O. Edfors, "UE Antenna Properties and Their Influence on Massive MIMO Performance," in *Proceedings of the 9th European Conference on Antennas and Propagation, (EUCAP)*, Lisbon, Portugal, Apr. 2015.

[9] E. L. Bengtsson, P. C. Karlsson, F. Tufvesson, J. Vieira, S. Malkowsky, L. Liu, F. Rusek, and O. Edfors, "Transmission Schemes for Multiple Antenna Terminals in Real Massive MIMO System," in *Proceedings of GlobeCom 2016 Conference, IEEE Communications Society*, Washington DC, USA, Dec. 2016.

[10] J. Vieira, S. Malkowsky, K. Nieman, Z. Miers, N. Kundargi, L. Liu, I. Wong, V. Öwall, O. Edfors, and F. Tufvesson, "A Flexible 100-Antenna Testbed for Massive MIMO," in *Globecom Workshops (GC Wkshps)*, 2014, pp. 287–293.

[11] S. Malkowsky, J. Vieira, L. Liu, K. Nieman, N. Kundargi, I. Wong, F. Tufvesson, V. Öwall, and O. Edfors, "The Worlds First Real-Time Testbed for Massive MIMO: Design, Implementation, and Validation," *IEEE Access*, vol. 5, pp. 9073 – 9088, May. 2017, doi: http://dx.doi.org/10.1109/ACCESS.2017.2705561.

[12] B. Clerckx and C. Oestges, *MIMO Wireless Networks*, 2nd ed. Academic Press, 2013.

[13] X. Gao, O. Edfors, F. Rusek, and F. Tufvesson, "Linear Pre-Coding Performance in Measured Very-Large MIMO Channels," *Proc. of the 74th IEEE Vehicular Technology Conference*, 2011.

[14] ——, "Massive MIMO Performance Evaluation Based on Measured Propagation Data," *IEEE Transactions on Wireless Communications*, vol. 14, no. 7, pp. 3899–3911, Jul. 2015, doi: http://dx.doi.org/10.1109/TWC.2015.2414413.

[15] J. Flordelis, X. Gao, G. Dahman, F. Rusek, O. Edfors, and F. Tufvesson, "Spatial Separation of Closely-Spaced users in Measured Massive Multi-User MIMO Channels," in *Proc. IEEE International Conference on Communications (ICC)*. IEEE, Jun. 2015, pp. 1441–1446, doi: http://dx.doi.org/10.1109/ICC.2015.7248526.

[16] X. Gao, J. Flordelis, G. Dahman, F. Tufvesson, and O. Edfors, "Massive MIMO Channel Modeling - Extension of the COST 2100 Model," 2015.

[17] A. Alayon Glazunov, A. Molisch, and F. Tufvesson, "Mean Effective Gain of Antennas in a Wireless Channel," *IEEE Antennas and Propagation.*, vol. 2, pp. 214–227, Feb. 2009.

[18] K. Zhao, E. Bengtsson, Z. Ying, and S. He, "Multiplexing Efficiency of High Order MIMO in Mobile Terminal in Different Propagation Scenarios," in *Proceedings of the 10th European Conference on Antennas and Propagation (EUCAP)*, Apr. 2016, pp. 1–4.

[19] B. M. Hochwald, T. L. Marzetta, and V. Tarokh, "Multiple-Antenna Channel Hardening and its Implications for Rate Feedback and Scheduling," *IEEE Trans. Inf. Theory*, vol. 50, no. 9, pp. 1893–1909, Sep. 2004, doi: http://dx.doi.org/10.1109/TIT.2004.833345.

[20] R. Verdone and A. Zanella, *Pervasive Mobile and Ambient Wireless Communications*, final ed., COST 2100, 2012.

[21] P. Kyösti, J. Meinilä, and L. Hentilä, *WINNER II Channel Models*, final ed., 2007.

[22] X. Gao, F. Tufvesson, O. Edfors, and F. Rusek, "Measured Propagation Characteristics for Very-Large MIMO at 2.6 GHz," in *Proc. of Asilomar Conference on Signals, Systems and Computers (ASILOMAR)*, Nov. 2012, pp. 295–299, doi: http://dx.doi.org/10.1109/ACSSC.2012.6489010.

[23] *Universal Mobile Telecommunications System UMTS Spatial channel model for Multiple Input Multiple Output MIMO simulations*, 12th ed., ETSI, 3GPP TR 25.996, 2014.

[24] A. Bordoux and et al., *D1.2 MaMi Channel Characteristics: Measurement Results*, final ed., FP7 EU project 619086, MAMMOET, Jun. 2015.

Paper IV

Analysis of Transmission Schemes for Dual-Antenna Terminals in Massive MIMO Systems

The overall system performance of massive MIMO is improved by equipping user terminals with multiple antennas. In this paper, we investigate transceiver designs for the case of a single downlink stream and in particular, we study the uplink pilot design. Moreover, we study the consequences of channel estimation errors at the base-station, and to what extent a dual-antenna terminal can get access to relevant channel statistics for optimization of the pilot signal. Gain expressions for comparison of different designs are derived. We verify the analytic results based on antennas integrated into Sony-Xperia handsets measured with the Lund University massive MIMO testbed. The measurements are performed at frequencies ¡6GHz since this part of the spectrum is a candidate for NR standard according to 3GPP.

Erik L. Bengtsson, Fredrik Rusek, Peter C Karlsson, Fredrik Tufvesson, Ove Edfors, "Analysis of Transmission Schemes for Dual-Antenna Terminals in Massive MIMO Systems,"
in *Proc. of the 25:th International Conference on Telecommunications (ICT2018), Saint Malo, France, Jun. 2018.*

1 Introduction

Massive MIMO (MaMi) [1] is emerging as one of the most promising components for increasing capacity and efficiency [2]. It is an essential part of the emerging new radio (NR) standard for the fifth generation wireless communication [3]. With MaMi, both energy- and spectral-efficiency are predicted to increase by at least one order of magnitude, under reasonable assumptions on channel properties and system configurations [2]. A measured spectral efficiency of 145.6 bits/s/Hz has been reported [4], more than 20 times what can be achieved with LTE Rel-10.

The terminal perspective [5–9] has received little attention, despite a frenetic research activity in the MaMi field. One reason for this is that most new concepts only indirectly relate to terminal devices.

In practice, with integrated antennas in most hand-held terminals, users cannot avoid loading antennas with hands and other body parts. Antenna loading typically degrades the channel from a capacity perspective and is a challenge to overcome in most systems. Most of the MaMi related research assumes single-antenna terminals, where loading requires compensation by means of increased transmission power and/or modulation and coding schemes with lower throughput. Those are all spectrum inefficient methods and motivate the study of multiple-antenna terminals.

In [7] we proposed a number of transmission strategies for multi-antenna terminals in MaMi. The transmission schemes are implemented in the Lund University Massive MIMO (LuMaMi) testbed [10], [11], and a set of tests performed in a lab environment is presented.

In [7] perfect channel knowledge was assumed at both base-station (BS) and the terminal. Here we extend the work [7] to also include effects of channel estimation errors. We investigate to what extent the terminal can gain access to relevant channel statistics, needed for optimization of the different schemes and further, we analyze behavior of the different schemes. This investigation is limited to the case of two antennas as the first increment in antenna count is the one yielding the largest gain. Both single-antenna terminal performance in MaMi systems and the schemes in combination with non-MaMi systems have been widely studied. Here, we study the combination and show that the schemes behave differently in MaMi systems.

Finally, we present performance gains based on measured channels from an indoor auditorium deployment, with the ambition to conclude whether MaMi puts new requirements on the terminals compared to systems of today or not.

Main contributions of this paper are

- we show that the uplink pilot transmission strategy by means of two terminal antennas can give substantial gain on the received downlink signals, conditioned the terminal knows the receive covariance matrix.
- simulation results suggest that the hardening effect in combination with precoding enables the terminal to gain access to sufficient information to instantly estimate the the optimal pilot vector.
- we show which transmission strategies are most relevant for a precoded MaMi, by analyzing of how realistic measured channels are distributed for two different

terminals with integrated antennas.

Section 2 is divided into 3 subsections. In subection 2.1, we derive expressions revealing how uplink pilot-SNR impacts on downlink signal quality. In subsection 2.2, different transmission strategies are defined and in Section 2.3 we derive closed form expressions for further analysis of the behavior. In 3 we use simulations to investigate how different transmission schemes perform and how they relate to the channel inner product. In Section 4, we look at measured channels for two terminals and relate them to the performance of the different transmission schemes. Conclusions are provided in Section 5.

2 Method and Analysis

2.1 Expressing the SNR of the Downlink Signal with uplink Pilot Dependency

A narrow-band wireless transmission channel can be modeled by,

$$\boldsymbol{y} = \boldsymbol{H}\boldsymbol{x} + \boldsymbol{n}, \tag{1}$$

where the vector $\boldsymbol{y}$ represents the received signals at the feed of K terminal receive antennas, the vector $\boldsymbol{x}$ the signals fed to J BS transmit antennas, $\boldsymbol{H}$ is the downlink propagation channel and $\boldsymbol{n}$ the additive noise vector. An entry h_{kj} in $\boldsymbol{H}$ includes, in addition to the propagation channel, antenna gain functions at both transmit and receive side.

Following [7], we adopt the Kronecker channel model [12] and assume that the channel $\boldsymbol{H}$ can be factored as the product of the square root of a receive covariance matrix, $\boldsymbol{R}$, and a zero-mean complex Gaussian distributed matrix, $\boldsymbol{H}_W$, with unit variance, independent elements, i.e.,

$$\boldsymbol{H} = \sqrt{\boldsymbol{R}}\boldsymbol{H}_W. \tag{2}$$

As the pilot transmission strategy determines how the channel is seen by the BS, it impacts overall performance. The pilot received by the BS is used to determine the precoding for the downlink traffic and the detection of uplink traffic. In this study we focus on the downlink traffic. First, we provide expressions describing the expected uplink pilot-SNR. After that, we study impact of different uplink pilot transmission strategies on the downlink precoded MaMi signal, received by the terminal.

Since efficient means to perform reciprocity calibration [13] extist, the radio channel is assumed reciprocal and the uplink channel given by $\boldsymbol{H}^{\mathrm{T}}$, where $(\cdot)^{\mathrm{T}}$ denotes matrix transpose. The received uplink pilot signal at a BS, when a two antenna terminal transmits a pilot vector $\boldsymbol{p} = [p_0 \;\; p_1]^{\mathrm{T}}$, where p_0 and p_1 are the complex-valued pilot signals simultaneously transmitted from the two antennas, becomes

$$\boldsymbol{x}_{\boldsymbol{p}} = [x_{\boldsymbol{p},1} \;\; \ldots \;\; x_{\boldsymbol{p},J}]^{\mathrm{T}} = \boldsymbol{H}^{\mathrm{T}}\boldsymbol{p} + \boldsymbol{n}_{\mathrm{b}}. \tag{3}$$

where $\boldsymbol{n}_{\mathrm{b}} \in \mathcal{CN}(\mathbf{0}, \sigma_{\mathrm{b}}^2 \boldsymbol{I}_{J\times J})$ is the noise at the BS side, and the index $\boldsymbol{p}$ indicate the pilot vector. The expected total received pilot power at the BS antennas is given by

$$\mathbb{E}\{\|\boldsymbol{x}_{\boldsymbol{p}}\|^2\} = \mathbb{E}\{\boldsymbol{p}^{\mathrm{H}} \boldsymbol{H}^* \boldsymbol{H}^{\mathrm{T}} \boldsymbol{p}\}, \tag{4}$$

where $\mathbb{E}$ denotes expectation and $(\cdot)^{\mathrm{H}}$ Hermitian transpose. For J BS antennas the total noise power is given by $J\sigma_b^2$, and the average uplink pilot-SNR over the BS antenna elements becomes

$$\mathrm{SNR}_{\mathrm{BS}} = \frac{\mathbb{E}\{\boldsymbol{p}^{\mathrm{H}} \boldsymbol{H}^* \boldsymbol{H}^{\mathrm{T}} \boldsymbol{p}\}}{J\sigma_{\mathrm{b}}^2}. \tag{5}$$

With downlink transmission of precoded MaMi signals $\boldsymbol{x}_{\mathrm{DL}} = [x_{\mathrm{DL},1} \ \ \ldots \ \ x_{\mathrm{DL},J}]^{\mathrm{T}}$, the received downlink signal at the terminal side can be expressed

$$\boldsymbol{y} = [y_0 \ \ y_1]^{\mathrm{T}} = \boldsymbol{H}\boldsymbol{x}_{\mathrm{DL}} + \boldsymbol{n}_{\mathrm{t}}, \tag{6}$$

where $\boldsymbol{n}_{\mathrm{t}} \in \mathcal{CN}(\mathbf{0}, \sigma_{\mathrm{t}}^2 \boldsymbol{I}_{2\times 2})$ is noise at the terminal side.

We assume that the BS uses least-square channel estimation. Minimum mean square error (MMSE), as an alternative, relies on correlation between multiple pilot signals over time, frequency or antennas, which tend to be low in MaMi systems. Furthermore, for single user (SU) MaMi systems, maximum ratio transmission (MRT) and zero forcing (ZF) are equivalent. For realistic multi user (MU) MaMi systems we expect that terminals with significant interference [8] will be scheduled to orthogonal time or frequency resources by the BS. Motivated by the results from various field trials on full dimensional MIMO (FD-MIMO) [14], where this approach was used, we therefore assume that the performance of each terminal can be expected to be close to that of a SU-MaMi system also for MU-MaMi systems.

Without loss of generality we assume that $\|\boldsymbol{p}\| = 1$, the least-squares estimate of the one-dimensional channel is then directly given by the received uplink pilot signal, i.e., $\hat{\boldsymbol{h}}_{\boldsymbol{p}} = \boldsymbol{x}_{\boldsymbol{p}}$. BS side MRT is then given by

$$\boldsymbol{x}_{\mathrm{DL}} = \frac{\hat{\boldsymbol{h}}_{\boldsymbol{p}}^{\mathrm{H}}}{\|\hat{\boldsymbol{h}}_{\boldsymbol{p}}\|} s, \tag{7}$$

where s is the transmitted signal which we, without loss of generality, normalize as $\mathbb{E}\{|s|^2\} = 1$.

With the above, the received downlink signal at the terminal becomes

$$\boldsymbol{y} = \boldsymbol{H} \frac{\hat{\boldsymbol{h}}_{\boldsymbol{p}}^{\mathrm{H}}}{\|\hat{\boldsymbol{h}}_{\boldsymbol{p}}\|} s + \boldsymbol{n}_{\mathrm{t}}. \tag{8}$$

Applying maximum ratio combining (MRC) on the received antenna signals at the terminal (8), the resulting SNR becomes

$$\mathrm{SNR}_{\hat{\boldsymbol{h}}_{\boldsymbol{p}}} = \frac{\hat{\boldsymbol{h}}_{\boldsymbol{p}} \boldsymbol{H}^{\mathrm{H}} \boldsymbol{H} \hat{\boldsymbol{h}}_{\boldsymbol{p}}^{\mathrm{H}}}{\|\hat{\boldsymbol{h}}_{\boldsymbol{p}}\|^2} \frac{1}{\sigma_{\mathrm{t}}^2}, \tag{9}$$

where we, for simplicity, assume perfect knowledge of the quantity $\hat{\boldsymbol{h}}_{\boldsymbol{p}}\boldsymbol{H}^H/\|\hat{\boldsymbol{h}}_{\boldsymbol{p}}\|$ at the terminal side. This assumption, gives us an upper bound of the performance and is motivated by the fact that the downlink signals experience array gain not present at the uplink pilot signals.

For reference, we derive the expected SNR for the case of single antenna operation. The use of a single terminal antenna, for both uplink and downlink transmissions, reduces the channel to a $1 \times J$ matrix. Using pilot vector $\boldsymbol{p}_0 = [1\ 0]^{\mathrm{T}}$, we get

$$\mathrm{SNR}_{\boldsymbol{p}_0} = \frac{\|\boldsymbol{H}\hat{\boldsymbol{h}}_{\boldsymbol{p}_0}^{\mathrm{H}}\|^2}{\|\hat{\boldsymbol{h}}_{\boldsymbol{p}_0}\|^2}\frac{1}{\sigma_t^2}, \tag{10}$$

where the channel matrix, $\boldsymbol{H}$, can be replaced by $\boldsymbol{h}_{\boldsymbol{p}_0}$.

2.2 Definition of Terminal Pilot Transmission Strategies

We now define three different diversity schemes and the associated pilot transmission strategies for terminals.

Switched diversity

Switched diversity (SWD) is defined so that the terminal antenna with the largest downlink SNR is selected for both up- and downlink transmissions. By using either $\boldsymbol{p}_0$ or $\boldsymbol{p}_1 = [0\ 1]^{\mathrm{T}}$ as pilot vector, the received downlink signal yielding the largest SNR is selected for each channel realization. This gives

$$\mathrm{SNR}_{\mathrm{SWD}} = \max_{\boldsymbol{p}\in\{\boldsymbol{p}_0,\boldsymbol{p}_1\}}\left(\frac{\|\boldsymbol{h}_{\boldsymbol{p}}\hat{\boldsymbol{h}}_{\boldsymbol{p}}^{\mathrm{H}}\|^2}{\|\hat{\boldsymbol{h}}_{\boldsymbol{p}}\|^2}\frac{1}{\sigma_t^2}\right). \tag{11}$$

Passive diversity

Passive diversity (PD) is when the terminal has two active receivers and only a single transmitter, connected to one of the antennas. This scheme achieves diversity only in the downlink where MRC is applied to the received signals from the antennas. The motivation of this scheme is backward compatibility with current LTE handsets. From a MaMi context, PD is interesting as the precoding at the BS is based on the uplink pilot and do then not take the diversity antenna into account. The SNR is given by (9), where either $\boldsymbol{p}_0$ or $\boldsymbol{p}_1$ is are used as pilot.

Dominant Eigenmode Transmission

Dominant eigenmode transmission (DEM) is maximizing SNR. The DEM pilot vector is based on the Gramian $\boldsymbol{G} = \boldsymbol{H}\boldsymbol{H}^{\mathrm{H}}$, which defines the inner product space for a channel realization $\boldsymbol{H}$. It is well known that system performance is determined by $\boldsymbol{G}$ [15].

Choosing pilot vector along the dominant eigenvector of the Gramian, allows the BS to see and estimate the strongest one-dimensional subspace of the two-dimensional

Table 1: Investigated diversity schemes

Acronym	Scheme	Scheme	Pilot vector
SA	Single antenna	Antenna 0	$\boldsymbol{p}_0$
PD	Passive diversity	Antenna 0	$\boldsymbol{p}_0$
SWD	Switched Diversity	Based on the Gramian, $\boldsymbol{G}$	$\boldsymbol{p}_0$ or $\boldsymbol{p}_1$
SWD-R	Switched Diversity	Based on the covariance matrix, $\boldsymbol{R}$	$\boldsymbol{p}_0$ or $\boldsymbol{p}_1$
DEM	Dominant Eigenmode	Based on the Gramian, $\boldsymbol{G}$	$\boldsymbol{p} = v_1(\boldsymbol{G})$
DEM-R	Dominant Eigenmode	Based on the covariance matrix, $\boldsymbol{R}$	$\boldsymbol{p} = v_1(\boldsymbol{R})$

channel. This maximizes the received pilot signal power $\|\boldsymbol{x_p}\|^2$ at the BS. The terminal uses MRC in the downlink and SNR is therefore given by (9) in this case too. For DEM, MRC is obtained by also weighting the received signals with the dominant eigenvector of the Gramian. In practice the terminal will not have perfect knowledge of the instantaneous Gramian and will need to compute pilots and receive weights by other means. The results for DEM should therefore be seen an upper bound on achievable SNR for any method.

Given that we do not know the instantaneous Gramian at the terminal, an alternative approach is to use an average, or expectation. This constitutes the receive-side covariance matrix $\boldsymbol{R} = \mathbb{E}(\boldsymbol{H}\boldsymbol{H}^H)/J$, from (2), and pilots can be chosen as $\boldsymbol{p} = v_1(\boldsymbol{R})$. This strategy can be applied to both SWD and DEM, in which case we denote them SWD-R and DEM-R, respectively.

The different schemes are presented in Table 1 for easy reference. Some schemes can be combined, e.g uplink switched diversity and downlink passive diversity, but this is outside the scope of this paper.

In order to have a performance metric, which is independent of the actual level we derive an expression for the downlink SNR-gain. We define it as the ratio between the SNR of the scheme to that of single antenna operation, e.g. $\mathrm{SNR}_{\mathrm{Gain\ SWD}} = \mathrm{SNR}_{\mathrm{SWD}}/\mathrm{SNR}_{\mathrm{SA}}$. We will later plot the SNR-gains as functions of the uplink pilot-SNR (5).

2.3 Derivation of closed form expressions

It is possible to derive a closed form approximation of (9), and thus for the SNR-ratio. From the closed form, we are able to examine the behavior of the DEM scheme more in detail. As the number of BS antennas, J, grow large we can make the following

approximation of the expectation of (9),

$$\mathbb{E}\{\mathrm{SNR}|_{\hat{\boldsymbol{h}}_{\boldsymbol{p}}}\} \approx \frac{\mathbb{E}\left[\hat{\boldsymbol{h}}_{\boldsymbol{p}}\boldsymbol{H}^H\boldsymbol{H}\hat{\boldsymbol{h}}_{\boldsymbol{p}}^H\right]}{\mathbb{E}\left[\hat{\boldsymbol{h}}_{\boldsymbol{p}}\hat{\boldsymbol{h}}_{\boldsymbol{p}}^H\right]}. \tag{12}$$

From Slutsky's Theorem, (12) gets tight as $J \to \infty$.

To keep it general we define an ideal antenna with gain ρ as our reference, and we can later define any of our antennas to be the reference by setting $\rho = 1 - \beta$ or $\rho = 1 + \beta$. In section 2.2, the gain was defined as the ratio between the SNR for a scheme to the SNR of a single antenna. Based on the channel hardening, the SNR for a channel realization become the same as its expected level with increasing number of antennas.

$$\lim_{J\to\infty} \mathbb{E}\{\mathrm{SNR}_{\text{Gain DEM}}\} = \mathbb{E}\{\mathrm{SNR}_{\text{DEM}}\}/\mathbb{E}\{\mathrm{SNR}_{\rho}\}, \tag{13}$$

holds. This enable us to treat the SNRs individually. After some simplifications, and from (12) and (13), the DEM scheme SNR-gain can be expressed

$$\mathrm{SNR}_{\text{Gain DEM}} = \frac{(J+1)\left(1+\sqrt{A}\right)^2 + 1 + 2\sigma_{\mathrm{b}}^2 - A}{1+\sqrt{A}+\sigma_{\mathrm{b}}^2} \times \frac{\rho+\sigma_{\mathrm{b}}^2}{\rho^2(J+1)+\sigma_{\mathrm{b}}^2\rho}. \tag{14}$$

where the first ratio is $\mathbb{E}\{\mathrm{SNR}_{\text{DEM}}\}$, the second ratio the inverse of $\mathbb{E}\{\mathrm{SNR}_{\rho}\}$, and $A = \alpha^2 + \beta^2 - \alpha^2\beta^2$. For many BS antennas and poor BS-side SNR, we get

$$\lim_{J\to\infty,\sigma_{\mathrm{b}}^2\to\infty} \mathbb{E}\{\mathrm{SNR}_{\text{Gain DEM}}\} = \frac{2}{\rho}, \tag{15}$$

and, again for many BS antennas, but high BS-side SNR,

$$\lim_{J\to\infty,\sigma_{\mathrm{b}}^2\to 0} \mathbb{E}\{\mathrm{SNR}_{\text{Gain DEM}}\} = \frac{1+\sqrt{\alpha^2+\beta^2-\alpha^2\beta^2}}{\rho}. \tag{16}$$

Expression (14) is a bit involved and, for simplicity, we study the special case for balanced antenna signals, $\beta = 0$. This implies that both antennas have unit gain and we set $\rho = 1$. Limits (15) and (16) now become 2 and $1 + \alpha$, respectively. For the same special case, (14) simplifies to

$$\mathrm{SNR}_{\text{Gain DEM}} = \left(\frac{J(1+\alpha)^2}{1+\alpha+\sigma_{\mathrm{b}}^2} + 2\right)\frac{1+\sigma_{\mathrm{b}}^2}{1+\sigma_{\mathrm{b}}^2+J}, \tag{17}$$

whose maximum is attained at $\alpha = 1$ and a BS-side noise level depending on the number of antennas as

$$\sigma_{\mathrm{b}}^2 = \frac{\sqrt{2J}(J-1)+2}{J-2}. \tag{18}$$

The obtained DEM SNR-gain grows with the number of BS antennas and its asymptotic value is

$$\lim_{J\to\infty} \max_{\sigma_{\mathrm{b}}^2}(\mathrm{SNR}_{\text{Gain DEM}}) = 4, \tag{19}$$

which means that the largest gain we can expect from the DEM scheme is 6 dB. It can also be shown that if $\alpha > \sqrt{2}-1$, $\mathrm{SNR}_{\mathrm{Gain\ DEM}} > 2$ in some range of σ_{b}^2, and the corresponding maximum gain is $(1+\alpha)^2$.

We proceed to derive a closed form expression for the PD scheme SNR gains. Also here we use ρ as the gain from an ideal antenna to be our reference. As the number of BS antennas $J \to \infty$, from (12) and (13), after some simplification, this gives us an expression for the expectation of the $\mathrm{SNR}_{\mathrm{Gain\ PD}}$,

$$\mathrm{SNR}_{\mathrm{Gain\ PD}} = \left(\frac{J(1+\beta)(\beta - \alpha^2\beta + \alpha^2 + 1)}{1+\beta+\sigma_{\mathrm{b}}^2} + 2 \right) \times \frac{\rho + \sigma_{\mathrm{b}}^2}{\rho^2(J+1) + \sigma_{\mathrm{b}}^2\rho}, \quad (20)$$

where the first factor is $\mathbb{E}\{\mathrm{SNR}_{\mathrm{PD}}\}$ and the second ratio is the inverse of $\mathbb{E}\{\mathrm{SNR}_{\rho}\}$. For many BS antennas and low uplink pilot-SNR (20) becomes

$$\lim_{J\to\infty, \sigma_{\mathrm{b}}^2 \to \infty} \mathrm{SNR}_{\mathrm{Gain\ PD}} = \frac{2}{\rho}, \quad (21)$$

which equals the DEM SNR-gain in (15). Introducing imbalance, $\beta \neq 0$, and using the better antenna as reference, $\rho = \max(1+\beta, 1-\beta) = 1+|\beta|$, the PD SNR-gain becomes less than 2 and (20) monotonically decreases with the imbalance.

For many BS antennas and high uplink pilot-SNR we get

$$\lim_{J\to\infty, \sigma_{\mathrm{b}}^2 \to 0} \mathrm{SNR}_{\mathrm{Gain\ PD}} = \frac{\beta - \alpha^2\beta + \alpha^2 + 1}{1+|\beta|}. \quad (22)$$

For balanced antennas, $\beta = 0$, the limit in (22) becomes $1+\alpha^2$ and $\mathrm{SNR}_{\mathrm{Gain\ PD}} \leq 2$, with a square dependency on the correlation, in contrast to the DEM case where (16) converted to $1+\alpha$. This implies that the DEM scheme outperforms the PD scheme for all correlations $0 < \alpha < 1$.

3 Performance Analysis of the different diversity schemes

We now analyze achievable downlink SNR-gains for the different diversity schemes. For the special case of two terminal receive antennas, a normalized version of the Gramian matrix yields the correlation-related value α and the imbalance β between the two receive antennas for a given channel realization [16],

$$\boldsymbol{G}_{\mathrm{N}} = \begin{bmatrix} 1+\beta & \alpha \\ \alpha^* & 1-\beta \end{bmatrix}, \quad (23)$$

where $\boldsymbol{G}_{\mathrm{N}} = 2(\mathrm{tr}\{\boldsymbol{G}\})^{-1}\boldsymbol{G}$ and $\mathrm{tr}\{\cdot\}$ is the trace operator. The Gramian is, in general, a complex valued matrix. Based on the fact that eigenvalues for a complex Hermitian 2×2 matrix are the same as for the absolute of the matrix we can, without loss of generality, neglect the phase relation between the entries. As the correlation

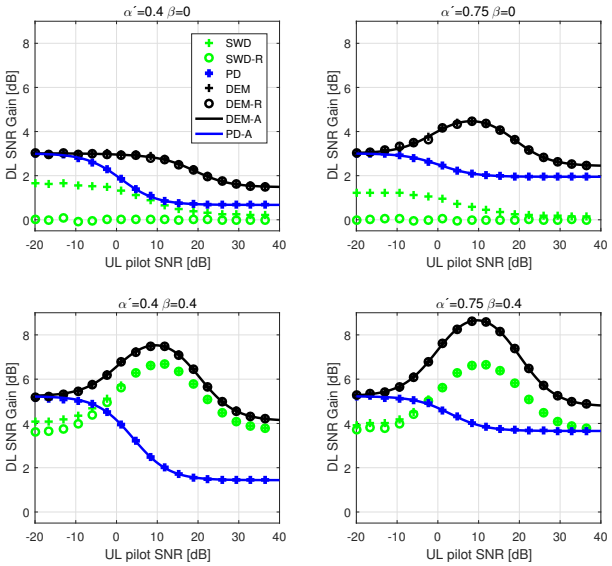

Figure 1: Downlink SNR-gain for different correlation coefficients and imbalance levels for the different diversity schemes as a function of uplink pilot-SNR. The figures includes results form MC simulations as well as analytic results.

α is limited in magnitude as $|\alpha| \leq \sqrt{1-\beta^2}$, we use the correlation coefficient $\alpha' = |\alpha|/\sqrt{1-\beta^2}$ in the figures in order to have a range $\alpha' \leq 1$ that is independent of β.

For easy comparison, both the results from Monte-Carlo (MC) simulatins where we have generated sample means for the different schemes, and results given by the closed form expressions are plotted in Fig. 1. The latter with solid lines, $\mathrm{SNR}_{\mathrm{Gain\ DEM}}$ from (14) is denoted DEM-A and $\mathrm{SNR}_{\mathrm{Gain\ PD}}$ from (20), denoted PD-A.

The figure shows downlink SNR-gain. They are plotted as functions of the uplink pilot-SNR (5), for two different correlation coefficients, $\alpha' \in (0.4, 0.75)$ and two different imbalance levels, $\beta \in (0, 0.4)$. With zero imbalance, the reference antenna does not matter in the upper plots, while in the lower plots we have used the weaker antenna as reference, which allows for gain beyond 6 dB. The SNR-gains are computed for a BS with 100 antennas.

Based on these SNR-gains, it is straightforward to convert to capacity gains, i.e. $\log(1+\mathrm{SNR})$, once a reference SNR-level is set. It shall be noted that the SNR-gains, being ratios, do not reflect the absolute received powers, which become a lot stronger as the uplink pilot-SNR increases.

At the far left in all plots, where up-link pilot-SNR is in the range of -20 dB, the

channel can be assumed too weak for communication. It is, however, still interesting to analyze the SNR-gain behavior.

At low uplink pilot-SNR, the BS has poor channel knowledge and transmitted signals on BS antennas become more random. As a result, the SNR-gain at the terminal side becomes less dependent on the pilot transmission strategy. The latter explains why DEM, DEM-R and PD converge to the same value for low uplink pilot-SNR, i.e. the difference between the schemes is in the pilot transmission strategy while all of them apply MRC on the received signals independent of the pilot signal. This is different for the SWD schemes where the same antenna as was used for the pilot transmission also is used for the reception and explains why SWD outperforms SWD-R. The effect is more pronounced when the average imbalance, caused for instance by a user loading one of the antennas, is low in comparison to the instant imbalance caused by a channel realization.

The channel estimation error is depending inversely on the uplink pilot-SNR, and as the uplink pilot-SNR increases, MaMi precoding based on channel estimates becomes more accurate. This has the effect that the received signal at the terminal side stabilizes.

It can be noted that the PD scheme shows low SNR-gain for high uplink pilot-SNR, when the the imbalance increases and the correlation is low. The BS is not aware of the diversity antenna as no pilot has been transmitted from it, and the precoding therefore do not take it into account. This means that, a receive-only antenna is of limited use in a MaMi system, which is different to the deployed systems of today.

The gain difference between DEM and DEM-R is almost negligible. As discussed in Section 2.2, the DEM schemes transmit the uplink pilot along the dominant eigenmode of the instantaneous channel. At low uplink pilot-SNR the pilot strategy becomes less important as the BS receives mostly noise. At higher uplink pilot-SNR the received downlink signal from which the terminal derive the pilot signal stabilizes. Thus, the variation between different channel realizations become small, and DEM and DEM-R perform the same.

Furthermore, the downlink SNR-gain using DEM shows an uplink noise dependency with a peak in some of the plots. This originates from improved channel estimation, as we are mapping the uplink pilot to the dominant eigenmode of the transmission channel. The SNR-gain, therefore, becomes significant only at noise levels where the channel estimation error is sufficiently small. Similarly there is a peak also in the SWD case when $\beta = 0.4$. This is when the uplink pilot-SNR is improved by a proper antenna selection and the peak therefore depend on the imbalance. To verify the above findings, we have performed further MC simulations for $J = 100$ BS antennas, imbalance $\beta = 0$, and uplink pilot-SNRs from -20 dB to +40 dB where the antenna correlations has been sweep in the interval $\alpha \in [0, 1]$. The results are shown in Fig. 2 and Fig. 3 where the simulated $\mathrm{SNR}_{\mathrm{Gain\ DEM}}$ and $\mathrm{SNR}_{\mathrm{Gain\ PD}}$, respectively are plotted. The figures are color-maps where the $\mathrm{SNR}_{\mathrm{Gain}}$ is plotted as a function of uplink pilot-SNR on the horizontal axis and correlation coefficient on the vertical axis. The results confirm the theoretical results, $\mathrm{SNR}_{\mathrm{Gain\ DEM}} \leq 4$ and $\mathrm{SNR}_{\mathrm{Gain\ PD}} \leq 2$ for all combinations of α' and uplink pilot-SNRs.

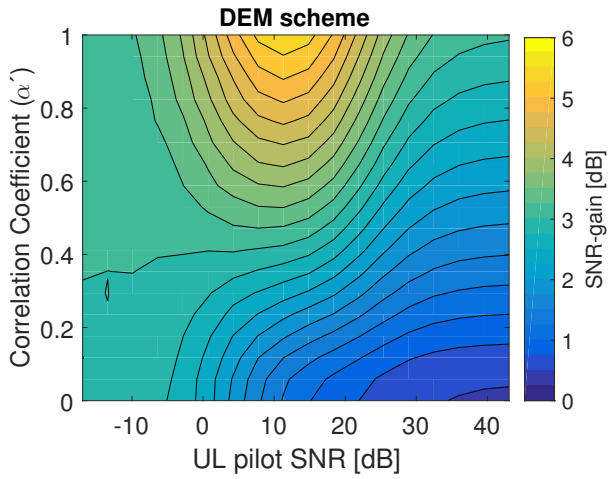

Figure 2: Mean downlink SNR-gain for the DEM scheme as a function of the uplink pilot-SNR on the horizontal axis and the correlation coefficient on the vertical axis. Simulated with 100 antennas at the BS side, $\beta = 0$.

Comparing Fig. 2 and Fig. 3 for high uplink pilot-SNR, i.e. at the right vertical edge of the plots, the linear dependency on α' in the DEM case vs. the square dependency in the PD case can be noticed, and that they yield the same gains for $\alpha' = 0$ and $\alpha' = 1$. Note, that $\alpha' = |\alpha|$ when $\beta = 0$.

As we introduce imbalance, $\beta > 0$, in (22) the gain decreases. In the case when one antenna is completely "deaf", $\beta = 1$, we get $\mathrm{SNR}_{\mathrm{Gain\ PD}} = 1/\rho$ and with $\rho = 1 + |\beta|$, we use the the stronger antenna as reference, the PD gain trivially becomes 1, or 0 dB. Finally, it can be shown that the PD scheme show gains ≤ 2 and monotonically decreases as the BS noise decrease for $\beta \geq 0$.

In Fig. 4, downlink SNR-gains for SWD, PD and DEM, from MC simulations, are shown as color-maps. The SNR-gains are plotted as functions of the imbalance on the horizontal axis, and the correlation coefficient on the vertical axis. Simulations are performed with perfect channel estimates, i.e. $\boldsymbol{n}_{\mathrm{b}} = 0$, and for the case of $J = 100$ BS antennas. For low correlation coefficients, DEM and SWD show higher gains than PD for scenarios when the imbalance is large. As the correlation coefficient increases, the schemes that combine the signals from both antennas improve (i.e. DEM and PD), and for $\beta = 0$ reach a maximum gain of 3 dB at $\alpha' = 1$. For this case, it does not matter from which antenna the pilot is transmitted and PD performance, therefore, equals the DEM performance.

In Fig. 4 the upper edge of the PD and DEM plots show that the schemes perform

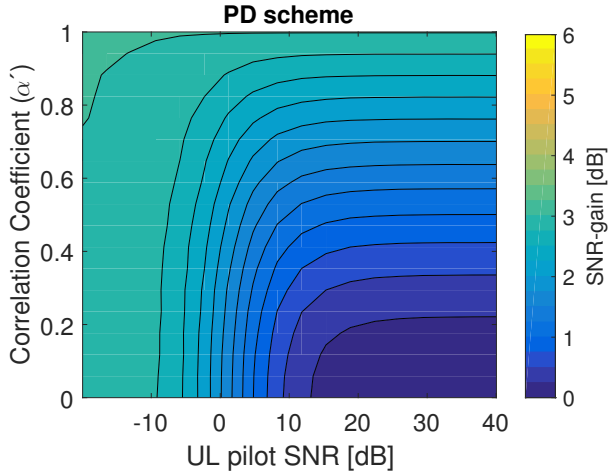

Figure 3: Mean downlink SNR-gain for the PD scheme as a function of uplink pilot-SNR on the horizontal axis and correlation coefficient on the vertical axis. Simulated with 100 antennas at the BS side, $\beta = 0$.

equally well, without β dependency.

Similarly, for low correlation SWD and DEM perform equally well and show that there is no advantage to combine the signals for fully uncorrelated antennas, this is a property which can be assigned to the MaMi precoding, as for a single BS-antenna system we would expect diversity gain in this case.

We conclude that DEM performs better than PD for any $\alpha' < 1$ and better than SWD for any $\alpha' > 0$.

It should be noted that the plots are for a downlink precoded MaMi channel. The situation is equivalent for the uplink channel, except for PD where there is only a single transmit path and thus the gain=1.

The results suggests that the expected downlink SNR-gain is the same if we compensate for the instantaneous channel realization or use the covariance matrix. This means that a terminal can get access to channel information to compute a sufficient pilot vector, which is close to what would be the case if it had instant access to the covariance matrix.

This, in turn, opens up for open loop implementations of the different diversity schemes. The terminal can estimate the Gramian from the received signals, and assuming that the channel is stable for a relatively long time such signals do not need to be transmitted very frequently. Thus, the overhead become negligible.

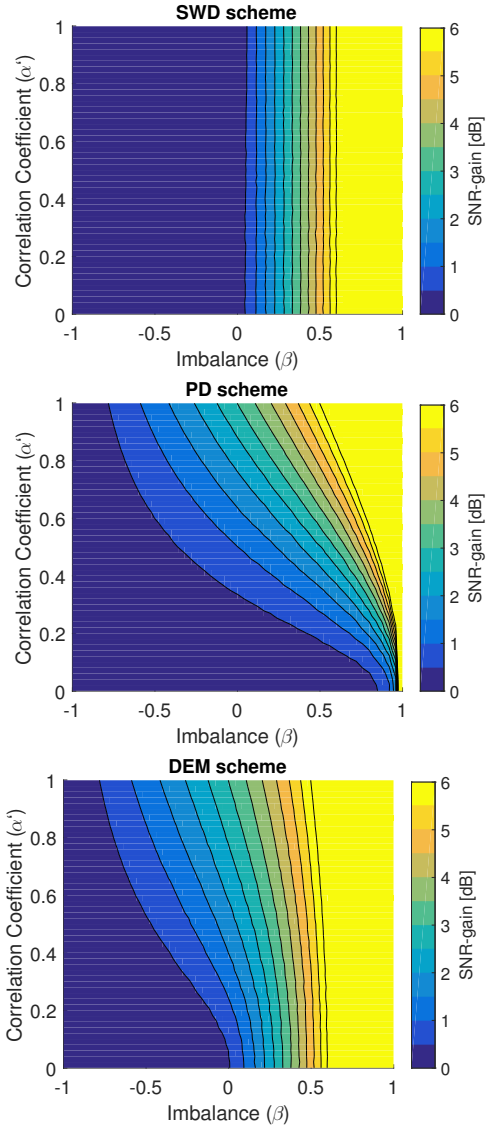

Figure 4: Mean downlink SNR-gain for the different transmission schemes as a function of the correlation coefficient and imbalance β. Simulated with 100 antennas at the BS side, $\boldsymbol{n}_b = 0$. Note that the plots have been limited to show a maximum of 6 dB gain.

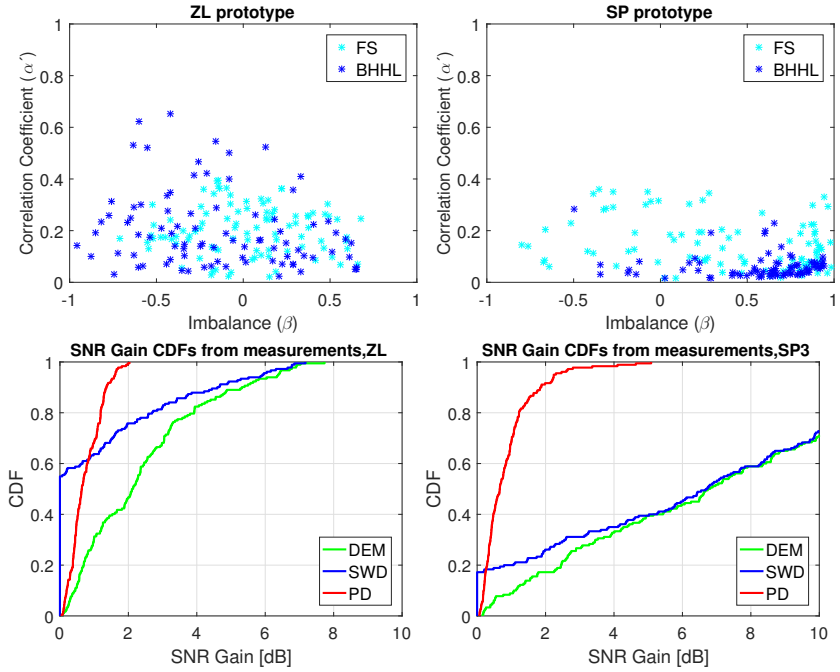

Figure 5: Above, 3D scatter plots of the imbalance on the horizontal axis and the correlation coefficient on the vertical axis, for the Xperia ZL terminal to the left and SP terminal to the right. Below, CDFs of the measured SNR gain for the different schemes and prototypes.

4 Comparison to Measured Channels

In this section, we present the correlation coefficient and imbalance for measured channels based on terminals with integrated antennas, tuned to the 3.7 GHz frequency band used by the Lund University's massive MIMO test bench LuMaMi. We examine two terminals based on Sony Xperia ZL and SP smartphones. The channels are measured in the same environment under free-space (FS), and loaded by a phantom head with the left hand (BHHL) conditions. The measurements where performed in the center of an auditorium where the terminal orientation was changed in small steps. In the Xperia ZL, both antennas are integrated at the top and the measured channels indicate that the correlation is higher compared to that of the Xperia SP, where the antennas are integrated at the top and bottom.

The upper plots in Fig. 5 shows the measured correlation coefficients α' and imbalances β as scatter plots, for both terminals. These scatter plots can be directly linked to the plots in Fig. 4, which provides understanding of how the different

schemes perform for the different antenna configurations in this environment. For both terminals, the imbalance is distributed over the full range and both SWD and DEM will therefore be effective. For the correlation coefficient, the Xperia ZL shows higher values than the Xperia SP, and the DEM scheme is, therefore, more beneficial than the SWD scheme in this case. As the correlation for both terminals, in general, is low the PD scheme provides poor performance. It can be noted that antennas by purpose are designed for low correlation as this is advantageous for multiplexed operation. This suggests that all terminal antennas needs pilot transmission capability in order to be useful in a MaMi system. The lower plots in Fig. 4 show cumulative distribution functions (CDFs) of the SNR-gains for the different schemes based on the measured channels.

This study can be extended to terminals with larger number of antennas. This will complicate the measurements as for the two antenna case only the power at the terminal side needs to be measured. Larger number of antennas require also the relative phase between the antennas to be measured.

5 Conclusions

The impact of uplink pilot-SNR on different transmission schemes has been analyzed using a Kronecker model. It is concluded that the pilot transmission strategy is an important factor in a precoded massive MIMO system.

The simulation results suggest that the hardening effect in combination with precoding gives the terminal sufficient information to instantly estimate relevant channel characteristics and to compute a close to optimal pilot vector.

Expressions have been derived that show the potential SNR-gains for different transmission schemes and how they relate to the correlation coefficient and imbalance at the terminal.

The measured correlation coefficients and imbalances, for two different antenna implementations integrated into real smart phone chassis, have been examined and clearly show that all terminal antennas needs transmit capability in order to be useful in a MaMi system.

6 Acknowledgement

The authors would like to thank Thomas Bolin for help with the prototyping, Sony Mobile Communications in Lund and Stiftelsen för Strategisk Forskning (SSF) for funding.

References

[1] T. L. Marzetta, "Noncooperative Cellular Wireless with Unlimited Numbers of Base Station Antennas OFDM," *IEEE Trans. Wireless Commun.*, vol. 9, no. 11, pp. 3590–3600, Nov. 2010, doi: http://dx.doi.org/10.1109/TWC.2010.092810.091092.

[2] H. Q. Ngo, E. G. Larsson, and T. L. Marzetta, "Energy and Spectral Efficiency of Very Large Multiuser MIMO Systems," *IEEE Transactions on Communications*, vol. 61, no. 4, pp. 1436–1449, Apr. 2013, doi: http://dx.doi.org/10.1109/TCOMM.2013.020413.110848.

[3] *Study on New Radio (NR) Access Technology*, 14th ed., ETSI, 3GPP TR 38.912, 2017.

[4] A. Nordrum, "5G Researchers Set New World Record For Spectrum Efficiency," *IEEE Spectrum*, May 2016.

[5] E. Björnson, J. Hoydis, M. Kountouris, and M. Debbah, "Massive MIMO Systems with Non-Ideal Hardware: Energy Efficiency, Estimation, and Capacity Limits," *IEEE Transactions on Information Theory*, vol. 60, no. 11, pp. 7112–7139, Nov. 2014, doi: http://dx.doi.org/10.1109/TIT.2014.2354403.

[6] E. L. Bengtsson, F. Tufvesson, and O. Edfors, "UE Antenna Properties and Their Influence on Massive MIMO Performance," in *Proceedings of the 9th European Conference on Antennas and Propagation, (EUCAP)*, Lisbon, Portugal, Apr. 2015.

[7] E. L. Bengtsson, P. C. Karlsson, F. Tufvesson, J. Vieira, S. Malkowsky, L. Liu, F. Rusek, and O. Edfors, "Transmission Schemes for Multiple Antenna Terminals in Real Massive MIMO System," in *Proceedings of GlobeCom 2016 Conference, IEEE Communications Society*, Washington DC, USA, Dec. 2016.

[8] À. O. Martínez, P. Popovski, J. Ø. Nielsen, and E. D. Carvalho, "Experimental Study of the Benefits of a Second Antenna at the User Side in a Massive MIMO System," *IEEE Access*, vol. PP, no. 99, pp. 1–1, 2017, doi: http://dx.doi.org/10.1109/ACCESS.2017.2785860.

[9] E. L. Bengtsson, F. Rusek, S. Malkowsky, F. Tufvesson, P. C. Karlsson, and O. Edfors, "A Simulation Framework for Multiple-Antenna Terminals in 5G

Massive MIMO Systems," *IEEE Access*, vol. 5, pp. 26 819–26 831, 2017, doi: http://dx.doi.org/10.1109/ACCESS.2017.2775210.

[10] J. Vieira, S. Malkowsky, K. Nieman, Z. Miers, N. Kundargi, L. Liu, I. Wong, V. Öwall, O. Edfors, and F. Tufvesson, "A Flexible 100-Antenna Testbed for Massive MIMO," in *Globecom Workshops (GC Wkshps)*, 2014, pp. 287–293.

[11] S. Malkowsky, J. Vieira, L. Liu, K. Nieman, N. Kundargi, I. Wong, F. Tufvesson, V. Öwall, and O. Edfors, "The Worlds First Real-Time Testbed for Massive MIMO: Design, Implementation, and Validation," *IEEE Access*, vol. 5, pp. 9073 – 9088, May. 2017, doi: http://dx.doi.org/10.1109/ACCESS.2017.2705561.

[12] B. Clerckx and C. Oestges, *MIMO Wireless Networks*, 2nd ed. Academic Press, 2013.

[13] J. Vieira, F. Rusek, and F. Tufvesson, "Reciprocity Calibration Methods for Massive MIMO Based on Antenna Coupling," in *2014 IEEE Global Communications Conference*, Dec. 2014, pp. 3708–3712, doi: http://dx.doi.org/10.1109/GLOCOM.2014.7037384.

[14] M. Alleven, "Samsung conducting Massive MIMO demo with Sprint at MWCA," https://www.fiercewireless.com/wireless/samsung-conducting-massive-mimo-demo-sprint-at-mwca, Sep. 2017.

[15] A. Paulraj, R. Nabar, and D. Gore, *Introduction to Space-Time Wireless Communications*, 1st ed. Cambridge University Press, 2003.

[16] X. Gao, F. Tufvesson, O. Edfors, and F. Rusek, "Measured Propagation Characteristics for Very-Large MIMO at 2.6 GHz," in *Proc. of Asilomar Conference on Signals, Systems and Computers (ASILOMAR)*, Nov. 2012, pp. 295–299, doi: http://dx.doi.org/10.1109/ACSSC.2012.6489010.

Paper V

Simulation of Multiple-Antenna Terminal Performance in Massive MIMO Systems based on Indoor Measurements

In massive MIMO systems the uplink pilot signals transmitted by a terminal define the channel seen by the base station. This gives the terminal some degree of freedom selecting the uplink pilot transmission strategy. In this paper, we investigate the benefit of different pilot transmission strategies when increasing the number of antennas in the terminal. Building on previous work on a simulation framework for Multiple-antenna terminals in 5G massive MIMO systems, this paper presents simulated performance results for various transmission schemes. The results are calibrated to reflect a communication situation in a large auditorium. Emulating the measurement set-up, we show that the framework can be tuned to generate channel distributions that matches measured data. Under generalized conditions, we perform simulations for different terminal transmission-strategies, both related to single stream and multiple streams. All evaluations are based on terminals with four antennas integrated into real Sony Xperia smartphone-chassis, tuned to 3.7 GHz. The measurements are conducted by using the Lund Massive MIMO testbed with its 100 antennas. The results clearly show the advantage of increasing the antenna-count also at the terminal side in massive MIMO systems.

Erik L. Bengtsson, Fredrik Rusek, Peter C Karlsson, Fredrik Tufvesson, Ove Edfors, "Simulation of Multiple-Antenna Terminal Performance in Massive MIMO Systems based on Indoor Measurements,"
in *Submitted to: IEEE Transactions on Vehicular Technology (TVT), 2019*

1 Introduction

The immense growth in wireless communications and applications has led both to traffic congestion in the mobile frequency bands and an increased use of energy in the networks. Thus, the costs are escalating for operators as they try to meet the ever-increasing demands of the market. This, in turn, has spurred the research community to look for solutions to improve both the spectral and energy efficiencies of the communication systems. The most propitious technology, massive MIMO (MaMi) [1], promises improvements by several orders of magnitude for power efficiency and at least an order of magnitude for spectral efficiency, compared to single antenna systems [2]. Thanks to extensive research with promising results, most of the initial skepticism has settled [3] and MaMi is now emerging as one of the most promising components in the 5G new radio (NR).

The main part of the MaMi research to date has focused on the base station (BS) with its, up to, hundreds of antennas. Noticeably, there are only a few publications that focus on the terminal perspective, and they show that terminals with multiple antennas can to a large extent influence the system performance [4–8]. In [6] we showed that besides antenna design, pilot transmission strategies will be crucial in MaMi systems.

The fundamental differences in terminal behavior are the motivation behind [8], a dedicated simulation framework with a reasonable complexity. The framework is designed for performance evaluation of multi-antenna terminals operated in a MaMi system. While it emulates the properties of a MaMi channel, as seen by a terminal, it avoids the complexity of a BS with its multitude of antennas. In the simulation framework, the environment is represented by only a few parameter settings. Random channels, distributed according to those expected form the environment of interest, are then obtained.

The channel properties within an environment not only depend on the position and orientation of a terminal but to a large portion on properties of the terminal antennas. Real integrated antennas with characteristics similar to those that can be expected in real products are therefore of essential importance in system evaluations. Multiple measurements with the same prototypes as used in [8] have shown that the distributions of the channel properties vary more than expected in seemingly similar environments. In fact, the locations of the clusters have a significant influence on the channel distribution for measurements limited to a few terminal orientations.

In this paper we conclude that, in order to achieve a good match between measured and simulated channel distributions the measurement scenario needs to be considered also in the simulation environment when estimating environmental parameters settings for the simulator.

It shall be noted that in this paper we investigate the advantage of having multiple antennas in a terminal. This is related to multiple-users (MU) sharing the same channel. The main differences are that in the MU case the signals at the different terminals can not be co-processed and that the antennas in different terminals can not be assumed to be physically static with respect to each-other. The consequences are that for the MU case the performance optimization relates to the BS side, and

that the effective channel distributions become different. The influence MU has on the channel seen by a terminal will be addressed in our further work.

In this work, we use the simulation framework from [8] to evaluate the advantage of increasing the antenna count at the terminal side, based on estimated environmental parameters. We examine received power and rate figures for different transceiver architectures and their associated pilot transmission strategies, for a quad-antenna terminal. As we consider handset terminals with the form factor of a spartphone, we do not consider it interesting with more than four antennas for the frequency band that we are investigating. This is also the number of antennas used in numerous products that can be found on the market, covering this frequency range.

The investigations are based on downlink received signals but the results are valid also for the uplink due to the reciprocity. Based on the large influence the terminal-antenna gain-patterns have on the link performance, we have used measured antenna gain-patterns from antennas integrated into a Sony Xperia ZL handset, tuned to 3.7 GHz, in all our evaluations[4]. We compare how the different antenna configurations perform in a MaMi system and investigate the advantage of having four antennas over one or two. The main contributions of this work are:

- The improved channel robustness obtained from scaling up the number of antennas at the BS side in a massive MIMO mainly relates to small scale fading. Our results clearly show an additional advantage of increasing the number of antennas also at the terminal side to address also large scale fading.
- Similar to conventional systems, asymmetric traffic, with higher downlink traffic than uplink traffic, makes it attractive to have a single transmit chain and multiple receive chains in the terminals. Our results suggest that this is feasible also for massive MIMO systems. For the single stream case, there is no need to have as many RF-chains as antennas, and switched solutions harvest most of the available capacity, also for this case.
- Contrary to conventional systems, the results confirm that opportunistic diversity approaches do not improve performance in a MaMi system.

In Section II we present the essential outcome from [8] and propose a method to derive typical channel parameter settings. We introduce the prototype based on which the simulations are performed and define different transmission schemes. In Section III we present simulation results where we compare SNR-gains for different diversity schemes and normalized-rate-gains for multiplexed schemes. Finally, in Section IV we conclude on the results.

[4] The reasons to use the 3.7 GHz band are that we have a license for this band, that this part of the spectrum is identified for the 5G new radio standard by 3GPP (i.e., the 3.5 GHz band), and is also used by the Lund University MaMi testbed, LuMaMi [9, 10].

2 Method

2.1 Framework for simulations

In this sub-section, we summarize the essential outcome of [8], a simulation framework used in this paper. The framework emulates the channel condition seen by the antennas of a terminal so that the received-signals, in a maximum-ratio-transmission (MRT) precoded MaMi system, can be computed. In the framework, it is assumed that the BS estimates channel state information based on uplink pilot-symbols transmitted from the terminal-antennas. This enables the BS to optimize the electrical field illuminating the terminal antennas in the downlink, as determined by channel properties and attributes of the pilot.

In [8] we made the following assumptions on which the framework is based:

- The multi-path-components (MPCs) are clustered.
- The BS do not have the resolution to control individual MPCs within a cluster.
- A cluster is defined by a center angle (CA), in azimuth and elevation, and an angular spread, also in azimuth and elevation, as seen from the terminal.
- The cluster gain function, and thus also the signal strength, of a cluster is constant within angles defined by the cluster.
- The center angles of clusters are uniformly distributed over the sphere, as seen by the terminal antennas.
- The cluster gain does not depend on polarization and does not favour any polarization direction.
- The BS can individually control power level, phase, and polarization of the signal to each cluster seen by the terminal.
- All clusters are in the far field as seen from the terminal antennas and they are therefore exposed to the same electrical field.

Based on above assumptions and that the framework only considers the conditions at the terminal side, the propagation-channel can be defined by only four parameters: the number of clusters, N; the angular spread, AS, of the illuminating field; and the standard deviation, C, of the cluster gain, λ. As we are not interested in the absolute channel strength we normalize the total power. Due to the normalization, the value of λ becomes indirectly defined by C, and is therefore not treated as a parameter in this work.

Fig. 1 shows the measured antenna-pattern of one antenna exposed to the electrical field built up of N clusters of multipath components. The electrical field only illuminates the terminal from the CA, indicated by red circles in the figure.

The relationship between a transmitted pilot signal and the associated received signal can be used by the terminal to gain access to the channel properties. With the antenna gain patterns defined by $\boldsymbol{\Psi}(\boldsymbol{\Omega})$, noise free conditions and the pilot set

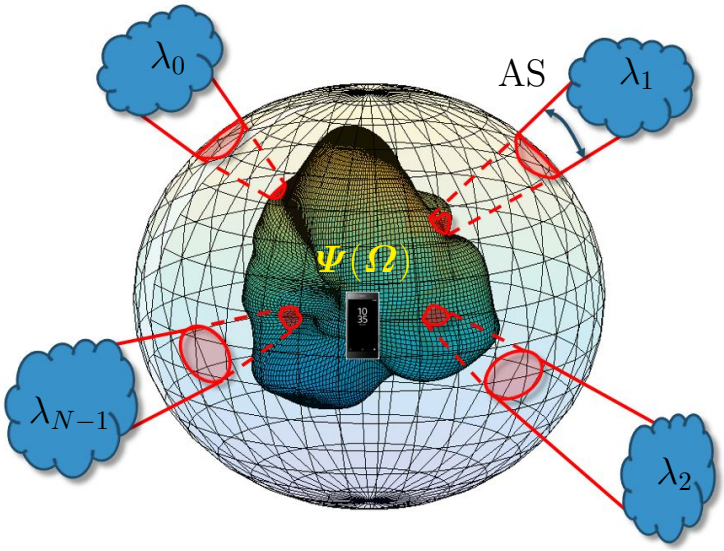

Figure 1: N clusters with normalized cluster power λ_n and angular spread, AS, illuminating terminal antennas, with a measured gain pattern $\boldsymbol{\Psi}(\boldsymbol{\Omega})$.

to unity[5] the received signal at terminal antenna k when a pilot signal has been transmitted from antenna l can be expressed as

$$y_{k|l} = \sum_{n=0}^{N-1} \lambda_n^2 \int_{\mathcal{A}_n} \int_{\mathcal{A}_n} \boldsymbol{\Psi}_k^{\mathrm{H}}(\boldsymbol{\Omega}_1)\boldsymbol{\Psi}_l(\boldsymbol{\Omega}_2)\mathrm{d}\boldsymbol{\Omega}_1\mathrm{d}\boldsymbol{\Omega}_2, \tag{1}$$

where $\boldsymbol{\Omega}$ is the directive angles and $\mathcal{A}_n$ the directive angles illuminated by cluster n. $\boldsymbol{\Psi}_l(\boldsymbol{\Omega})$ can be understood as being the illuminating E-field precoded by the BS, based on a pilot from antenna l. By complex weighing of the received signals from different antennas, exposed to the same electrical field, the received signal from the combined pattern from multiple antennas can be computed. The relative magnitudes at each of the terminal antennas, therefore, will reflect those of the channel inner products (the Gramian $\boldsymbol{G} = \boldsymbol{H}\boldsymbol{H}^{\mathrm{H}}$) which carries essential behavior of a channel [11], and from

[5] Assuming MRT precoding at the BS side, the gain λ_n from a cluster n will influence the received signal twice. First, when the pilot is transmitted to the BS, and second, when the signal is propagated back to the terminal, through the same cluster, using MRT. Here we retain the square dependency to be able to observe the channel inner product directly. With the pilot signal set to unity, the relative magnitudes at each of the terminal antennas will, therefore, reflect those of the channel inner products, which carries essential behavior of a channel [11].

which the performance can be derived. The Gramian is given by

$$\boldsymbol{G} = \begin{bmatrix} y_{0|0} & y_{0|1} & \cdots & y_{0|K-1} \\ y_{1|0} & y_{1|1} & \cdots & y_{1|K-1} \\ \vdots & \vdots & \ddots & \vdots \\ y_{K-1|0} & y_{K-1|1} & \cdots & y_{K-1|K-1} \end{bmatrix}. \tag{2}$$

Again, for a more thorough motivation we refer to our original work [8].

A large number of simulated channel realizations have been used to determine the distributions of the entries of $\boldsymbol{G}$. The simulations are defined by the following steps:

1. Measure the terminal antenna gain patterns, i.e. $\boldsymbol{\Psi}(\boldsymbol{\Omega})$, defined with a common center point.
2. Select the environmental parameters to reflect the environment of choice, i.e. N, C and AS.
3. Generate the vector $\boldsymbol{\lambda} = [\lambda_1 \ \lambda_2 \cdots \lambda_N]^{\mathrm{T}}$, where C is used as the standard deviation for the generation according to the approach in [12].
4. For each of the N clusters, define the integration area, $\mathcal{A}_n$, based on a random CA and the AS.
5. Compute the instantaneous Gramian (2).
6. Repeat steps 3) to 5) for the values defined in steps 1) and 2), to generate statistics of the Gramian.

Next we describe how to select pre-defined sets of parameters, for step two, that define a propagation environment.

2.2 Environmental settings

In this sub-section, we compare simulated channels to measured channels and motivate our choice of environmental parameters. Both simulated and measured results are generated using the same dual-antenna terminal.

The measurements were performed in an auditorium, as shown in Fig. 2. The location was chosen since earlier measurement campaigns have been performed in the same environment [13], providing prior knowledge of the channel properties. The environment is considered indoor based on the scattering properties, e.g., from walls, roof, and furnitures. While the terminal was measured in different locations in the room the MaMi BS was fixed to the front center. We used an absorbent to block the line-of-sight component between the BS and the terminal, mainly due to limitations in the dynamic range of the measurements. By only rotating the terminal, keeping it at the same location while monitoring channel properties, all channel variations can be assumed to be determined by the terminal antenna properties, as the propagation channel in that case can be assumed to be static. For the measurements, the terminal was rotated in steps of about 10°and the full channel, $\boldsymbol{H}$, captured at the BS side.

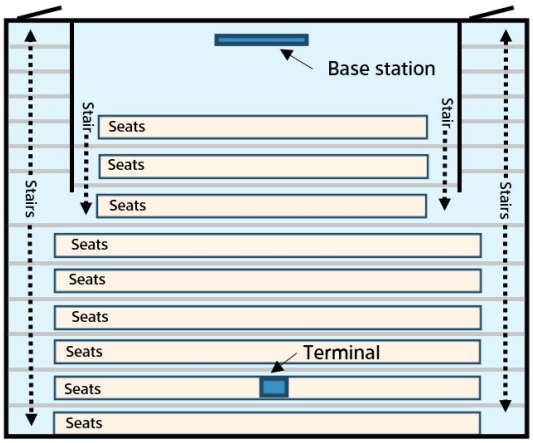

Figure 2: Drawing of the auditorium where the measurements was performed. The terminal in the center of the room and the BS at the front.

For the comparison between measured and simulated channel distributions we limit the study to the two-antenna case, while the simulation study to follow handles up to four antennas.

For the comparison, we present a channel measured in the back of the room and represent it by the power imbalance β and correlation α. From a fundamental perspective, the imbalance β is a relative measure of a channel realization that tells how strong channel the different antenna sees, while α indicates how much cross-talk there are. α and β represent a normalized channel realization and their distributions is, therefore, a measure on the channel behaviour for an environment.

For each simulated channel realization, we compute the normalized Gramian, $\boldsymbol{G}_{\text{norm}} = \frac{2}{\text{tr}\{\boldsymbol{G}\}}\boldsymbol{G}$ (where $\text{tr}\{\cdot\}$ is the trace operator). From $\boldsymbol{G}_{\text{norm}}$ we get access to the relevant channel properties, which do not depend on the precoding, and for the special case of two antennas, the power imbalance β and correlation α [14] can be identified from

$$\boldsymbol{G}_{\text{norm}} = \begin{bmatrix} 1+\beta & \alpha \\ \alpha* & 1-\beta \end{bmatrix}. \tag{3}$$

In measurements, the pilots transmitted by the terminal antennas, give direct access to the experienced channel, $\boldsymbol{H}$, from which, we can straightforwardly compute the Gramian and further identify α and β after normalization.

It can be understood from Fig. 1, that the antenna gain for integrated terminal antennas will change dramatically as a function of the illumination angle. As much as this is one of the most important motivations for doing investigations with realistic integrated antennas, it also poses challenges. As mentioned, large variations in the

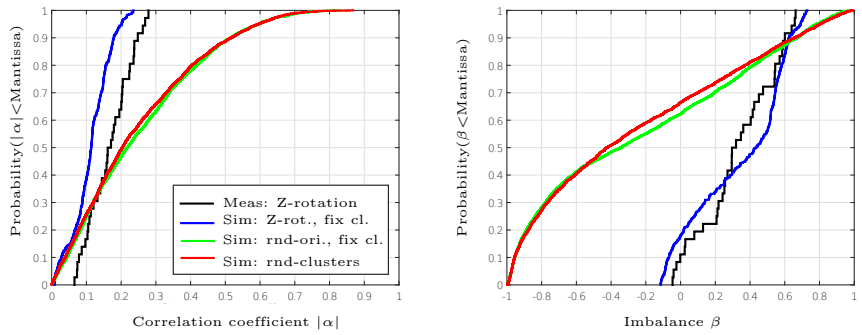

Figure 3: CDFs of correlation coefficient $|\alpha|$ and imbalance β for measurements and simulations with different settings.

received signal power as the terminal is illuminated from different angles can be expected. This will then also show up in the channel distributions, i.e. distributions of α and β, making it hard to isolate environment specific properties. Measurements performed at different locations and environments confirm this. The distributions of α and β depend as much on the environment as on the orientation of the terminal. Even if possible, extracting typical parameters for an environment is a very tedious task that involves tremendous measurement efforts for each environment.

To verify the validity of the simulation framework and keep the measurement effort reasonable, simulated α and β distributions have been matched to those measured at a single location where a terminal was rotated only around the vertical axis. We have matched the simulated results to those measured according to the maximum likelihood (ML) principle, under the assumption that the correlation coefficient, $\alpha' = |\alpha|/(\sqrt{1-\beta^2})$ and β are independent.

By restricting the simulator to rotation around the same axis as for the measurements and, with a careful selection of azimuth and elevation angles for a set of two clusters, the distributions of α and β could be significantly better matched to the measured distributions. Fig. 3 shows the distributions of α and β coloured black and blue. The distributions demonstrate that the simulation framework is capable of generating realistic distributions that reflect a specific scenario. However, they also indicate that the distributions are very sensitive to how the terminal is oriented with respect to the clusters. Indeed, by keeping the clusters' relative angles fixed in the simulator, while randomly changing the orientation of the terminal, not limited to rotation along any axis, the distributions change dramatically. This is shown as the red curves in Fig. 3. While not unexpected, an important observation is that by setting the cluster angles randomly the distribution matches the one with the fixed clusters and random orientations. This is shown as the green curves in Fig. 3. All in all, those results suggest that random selection of the illumination angles yields representative channels in most cases and therefore makes the simulated distributions

of antenna gain and correlation more generic. Hence, illumination angles will be different for different positions and the results show that random illumination angles give the same result as fixed clusters and random orientation of the terminal.

Being confident that the simulation framework generates sufficiently realistic channel realizations we continue our analysis. Initially, we set the number of clusters to $N = 2$, the AS to 12° and the cluster gain standard deviation C=0 dB, motivated by that this is what multiple measurements in different locations of the room suggested. It may be argued that expected number of clusters in this environment is larger than the two we observed [13]. A plausible explanation to the low number is that the channel behaviour is mainly determined by a few dominant clusters and the influence from weaker clusters in this setting is negligible. The effect of introducing variation to the normalized cluster power is, therefore, mainly the same as reducing the number of clusters for the single user case, and will not be further treated in this paper. In fact, we are not attempting to estimate the number of clusters but rather to find the settings that generate realistic channel distributions that match those measured. This is possible as we are limiting the investigation to the dynamic properties of the channel and do not consider the absolute level, which, is expected to vary significantly. The effect of the number of clusters on the received signals will be examined below while the physical size of the clusters has a negligible influence, for an AS within the range 6° to 18°. The influence of the AS relates to the angular variations in the antenna gain patterns, which in our case can be considered small.

2.3 Terminal antenna configurations and performance metrics

For the simulation study, we investigate an Xperia ZL smartphone with four integrated antennas, as shown in Fig. 4. This set-up enables us to evaluate six combinations of antenna pairs as well as the case of all four antennas used simultaneously. Two of the antennas in the Xperia ZL prototype are placed in the upper end, right (R) and left (L), one in the bottom (B) and one at the side (S). The prototype is equipped with switches to pair-wise select any two of the antenna pair combinations. All antenna gain-patterns have been measured in a Satimo StarGate 64 anechoic chamber for both free-space (FS) and loaded conditions. The loaded case, is a combination of; left-hand; right-hand; beside-head-with-left-hand; and beside-head-with-right-hand. The results are generated by combining the distributions generated by the different load-cases. The load-cases are selected from the perspective that they offer repeatability rather than being typical 5G use cases.

To compare the different antenna configurations on an equal basis, without the insertion loss from the switch circuitry, the received power for each antenna configuration has been normalized with the average of the median power of all four antennas under FS conditions, i.e.

$$P_{\text{ref}} = \frac{1}{4} \sum_{k \in \{L,R,S,B\}} \tilde{\text{m}} \left(y^2_{\text{FS-k—FS-k}} \right), \tag{4}$$

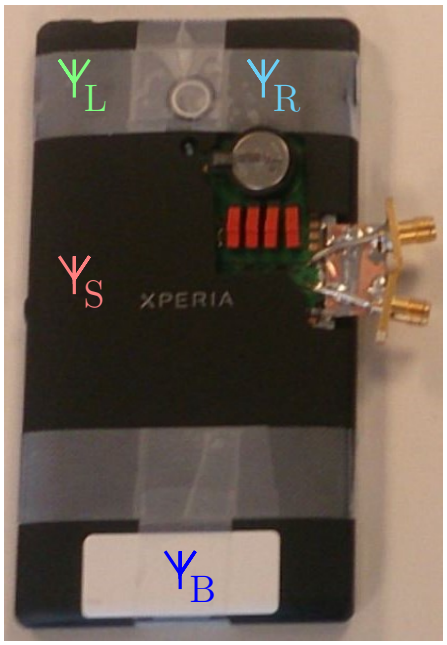

Figure 4: Xperia ZL with antenna positions indicated.

where $\tilde{\mathrm{m}}(\cdot)$ denotes the median operator and with y from (1). To simplify the notation, we relate k to the antennas rather than using an integer. The normalized power for e.g. the loaded top-right antenna is given by

$$P_{\text{Load-R}} = \frac{y^2_{\text{load-R—load-R}}}{P_{\text{ref}}}. \tag{5}$$

The simulator directly yields the Gramian (2). From the Gramian, the performance of different transmission schemes can be computed and below we put forth our selection of schemes. For the comparison of different diversity schemes, we use SNR-gain [6]. The SNR-gain shows how much the signal-to-noise-ratio (SNR) is improved by a certain scheme and is defined as the ratio between the received power achieved by a diversity scheme to that of a single antenna, for the same channel realization. Each channel realization will therefore generate as many SNR-gains as there are antennas. In the result section below we combine all those SNR-gains from a large number of realizations into a single distribution. In general, the transmission schemes below define the performance for both uplink and downlink. Passive receive diversity as described below, however, only operates in the downlink.

2.4 Single stream schemes

Passive receive diversity (PD)

The PD scheme is limited to single stream transmissions. The terminal has a single transmit antenna and multiple receive antennas. As the terminal only transmits pilots from one antenna, the BS does not get access to the full channel, and can only optimize transmissions to the same antenna. We define one transmit/receive antenna, i, and three receive-only antennas. The quality of the received signal after maximum ratio combination, without any noise enhancement is given by

$$y_{\mathrm{PD}(i)} = \|\boldsymbol{t}_i \boldsymbol{G}\|, \tag{6}$$

where the vector $\boldsymbol{t}_i$, a vector of zeros with a one at the column i, reflects which antenna transmitted the pilot signal and thus defines the channel the BS sees.

Switched diversity (SWD)

In SWD we use a switch to select one antenna among the available ones for each channel realization. The SWD scheme is limited to transmit and receive a single stream. We use only one of the antennas at the time, but we have all four antennas to switch among. The received signal is given by

$$y_{\mathrm{SWD}} = \max(y_{0|0}, y_{1|1}, y_{2|2}, y_{3|3}), \tag{7}$$

where the antenna with the strongest signal is selected.

Dominant Eigenmode (DEM) schemes, like the PD and SWD schemes, are also limited to a single stream. The DEM schemes involve all available antennas for both uplink and downlink and require as many transceiver chains as there are available antennas. We study two variants, limited by different transceiver architectures.

Dual antenna, dominant Eigenmode (DEM2)

DEM2 transmission involves two antennas (i and j). The received signal is given by

$$y_{\mathrm{DEM2}(ij)} = \max(\mathrm{eig}\{\boldsymbol{G}_{i,j}\}), \tag{8}$$

where $\mathrm{eig}\{\cdot\}$ is the operator that computes the eigenvalues of a matrix and $\boldsymbol{G}_{i,j}$ is a 2×2 sub-matrix of (2), given by

$$\boldsymbol{G}_{i,j} = \begin{bmatrix} y_{i|i} & y_{i|j} \\ y_{j|i} & y_{j|j} \end{bmatrix}, \tag{9}$$

where $y_{i|j}$ are the elements of the Gramian, $\boldsymbol{G}$ at row i and column j.

Quad-antenna dominant Eigenmode (DEM4)

This scheme involves all four antennas simultaneously. The received signal using the single most dominant eigenmode is given by

$$y_{\mathrm{DEM}} = \max(\mathrm{eig}\{\boldsymbol{G}\}). \tag{10}$$

The DEM4 scheme is the optimal scheme from a power transfer perspective and will be used as reference in comparisons later on. Note, contrary to the two antenna case, we need the complex received signals in the Gramian (2) when deriving the eigenvalues.

2.5 Multiplexed transmission (MUX)

Multiplexed transmission involves having multiple, simultaneous, and independent streams. In order to compare MUX schemes with diversity schemes on an equal basis, the received signal for each independent stream needs to be related to a rate. The reason for this is that we can sum the rates and compare to the rate of the diversity schemes. This is not possible with SNR-gains.

The capacity of a stream m is given by $\mathcal{C}_m = \log_2(1 + \mathrm{SNR}_m)$, where SNR_m is the ratio between a normalized received power, with the same normalization as in (5), P_m and an absolute noise power, N_0. We define our reference SNR to be the ratio between the average of all antenna's median power in FS, defined in (4), to the absolute noise power.

The sum rate offered by M streams with transmit-power constrained to unity is given by

$$\mathcal{C}_M = \max_{\sum_{m=1}^{M} a_m = 1} \sum_{m=1}^{M} \log_2\left(1 + \frac{a_m P_m}{N_0}\right), \tag{11}$$

where $a_m \geq 0$ and P_m are the power scaling factor and the normalized power level for stream m. The water pouring algorithm [15] is used to compute (11). We will now define three MUX schemes.

Dual antenna multiplexed transmission (MUX2)

This scheme is similar to the DEM2 scheme but uses two simultaneous independent streams by addressing both eigenmodes of the channel. The received signals for the streams, based on antennas i and j, are given by

$$y_{\mathrm{MUX2}(1,ij)} = \max(\mathrm{eig}\{\boldsymbol{G}_{i,j}\}), \tag{12}$$

and

$$y_{\mathrm{MUX2}(2,ij)} = \min(\mathrm{eig}\{\boldsymbol{G}_{i,j}\}). \tag{13}$$

The rate, $\mathcal{C}_{\mathrm{MUX2(ij)}}$, is then given by (11), where the signals are converted to powers.

Switched, dual antenna multiplexed transmission (MUX2SW)

Like the MUX2 scheme, this scheme involves two antennas simultaneously. For each realization the achieved rates for all six combinations of antenna pairs are computed and the best pair is selected. We define

$$\mathcal{C}_{\mathrm{MUX2SW}} = \max(\mathcal{C}_{\mathrm{MUX2(01)}}, \mathcal{C}_{\mathrm{MUX2(02)}}, \cdots, \mathcal{C}_{\mathrm{MUX2(23)}}). \tag{14}$$

Dual-stream, eigenmode based multiplexed transmission (MUX2DEM)

This scheme is similar to the MUX2 scheme but uses all four antennas. The received signal from each of the received streams is given by

$$y_{\mathrm{MUX}(m)} = \boldsymbol{F}_m \mathrm{eig}\{\boldsymbol{G}\}, \tag{15}$$

where $\boldsymbol{F}_m$ addresses stream $m \in \{1, 2\}$, being a row vector of zeros with a one at column m and $\mathrm{eig}\{\boldsymbol{G}\}$ is a vector of eigenvalues derived from the complex received signals. This scheme is optimal from a dual stream conditioned rate perspective. To compute the rate we use (11).

Quad-stream multiplexed transmission (MUX4)

The MUX4 scheme is a four stream scheme, similar to the MUX2DEM scheme but uses all four eigenmodes. The received signal from each of the received streams is given by (15) where $m \in \{1, 2, 3, 4\}$. This scheme is optimal from a rate perspective for each channel realization and reach capacity. To compute the rate we use (11).

Table 1: List of transmission schemes.

Acronym	**Scheme**	**Number of rx-/tx-chains**	**Streams (Rank)**
PD	4 antenna passive receive diversity	4 / 1	1
SWD	4 antenna switced diversity	1 / 1	1
DEM2	2 antenna dominant eigenmode diversity	2 / 2	1
DEM4	4 antenna dominant eigenmode diversity	4 / 4	1
MUX2	2 antenna multiplexing	2 / 2	2
MUX2SW	4 antenna SWD / 2 antenna MUX	2 / 2	2
MUX2DEM	4 antenna dual stream	4 / 4	2
MUX4	4 antenna quad stream	4 / 4	4

The different transmission schemes presented above are summarized in Table 1 for easy reference. The number of receive (Rx) and transmit (Tx) chains in the third column is of interest as they relate to power consumption and hardware complexity.

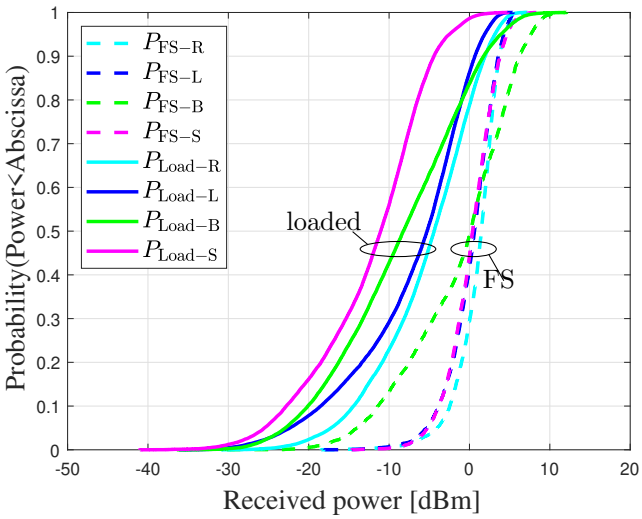

Figure 5: Simulated CDFs of the normalized received power for each of the 4 antennas, FS and loaded conditions.

3 Simulation Results

Based on the measured loaded antenna patterns and the presented simulation-framework, SNR-gains and normalized-rate-gains have been simulated. The performance of the different diversity schemes can be visualized by plotting cumulative distribution functions (CDFs) of the received power.

Fig. 5 shows the CDFs of the received power at the four antennas, both under FS and loaded condition after the power normalization. The CDFs are generated from 5000 channel realizations for each load case, with the environmental parameters set to 2 clusters, an AS of 12°and a cluster gain standard deviation of 0 dB.

Table 2: Simulated median and standard deviation of received power for the four antennas in FS and loaded.

Antenna	Median	Standard deviation
FS-L	1.5 dBm	2.8 dB
FS-R	0.6 dBm	3.0 dB
FS-B	0.1 dBm	6.7 dB
FS-S	0.4 dBm	3.0 dB
Load-L	-4.4 dBm	6.3 dB
Load-R	-5.2 dBm	7.4 dB
Load-B	-8.2 dBm	8.2 dB
Load-S	-11.1 dBm	7.1 dB

The median and standard deviations are listed in Table 2. Antenna B shows larger standard deviation than the other antennas in FS condition. This is a result of the antenna design resulting in a higher directive gain. Under the loaded condition, the standard deviation of the received powers for all antennas increase, again due to an increased directive gain. The median of the received power becomes lower in the loaded cases. The 7 dB drop is mainly caused by absorption as the matching is good for all our cases.

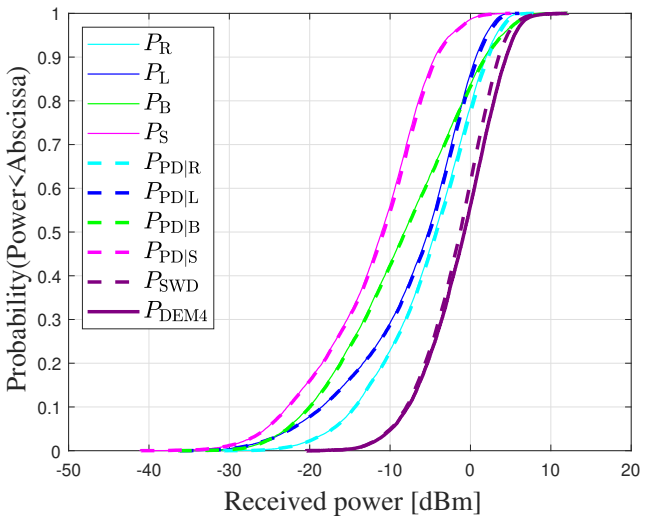

Figure 6: Simulated CDFs of the received power for the different diversity schemes under loaded conditions.

Fig. 6 shows CDFs for a selection of diversity schemes as well as CDFs of the received power at each of the antennas when no diversity is applied. The latter curves almost fully overlap the PD curves. The figure shows the performance for loaded conditions only, as we consider FS being less realistic. For the PD scheme, the performance improvement is negligible despite all four antennas being used. More interesting is that the SWD schemes perform about the same as the DEM4 scheme, the latter being optimal from a power transfer perspective. This suggests that in a majority of realizations the DEM4 scheme directs almost all power to a single antenna. This can be explained by low correlation between the antennas, as will be confirmed with the MUX schemes below.

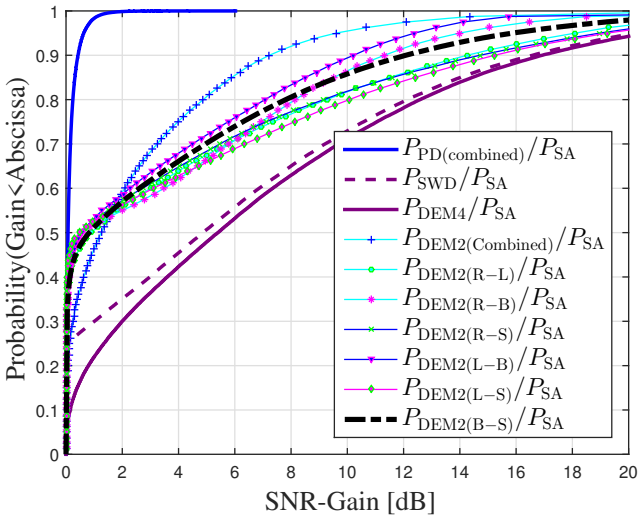

Figure 7: CDFs showing the SNR-gains for the different diversity schemes.

3.1 SNR-Gain

The SNR-gains are defined as a ratio between the received power achieved by a scheme to that with a single antenna, P_{SA}. With four antennas available, each realization therefore generates four results where each of the antennas is used as reference. Fig. 7 shows CDFs where the four distributions are combined. Consequently, as at least one antenna will always be the best and when it used as reference the gain becomes lower. This explains why the SNR-gain CDF for the SWD scheme shows 0 dB gain in 25% of the realizations.

The low correlation between the antennas in combination with the MaMi precoding has a large impact on the performance. This is the reason to the negligible SNR-gain from the PD scheme (shown as a combined CDF for all cases), which is less than 0.25 dB in the 90 percentile, and also the reason to why the SWD scheme performs close to the DEM4 scheme.

For the DEM2 schemes, we show the CDFs for all 6 antenna combinations as well as the combined CDF. When we limit the transmissions to any of the antenna pairs, the loss is significant. This, clearly show that there is an advantage to have access to all four antennas.

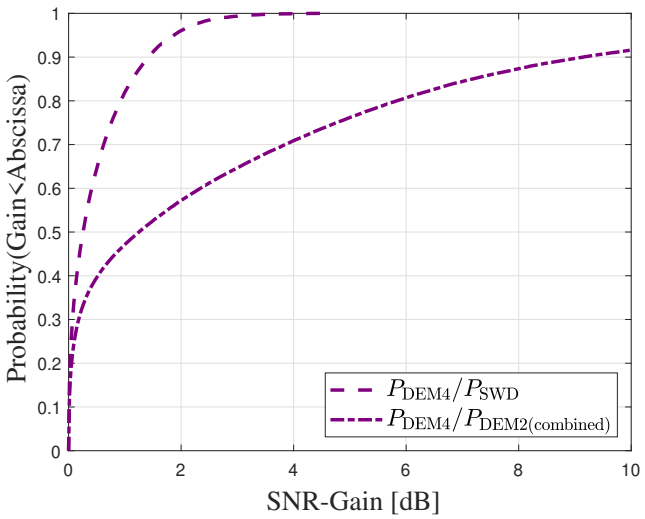

Figure 8: CDFs showing the SNR-gain ratio.

To get a more quantitative comparison between the different schemes, SNR-gain ratios have been derived. Fig. 8 shows the SNR-gain ratios between a selection of schemes to that of the DEM4 scheme (optimal). We can conclude that the SWD scheme is less than 1.5 dB from being optimal at the 90 percentile. For the DEM2 scheme, however, in 20% of the cases, it is more than 6 dB below the optimal.

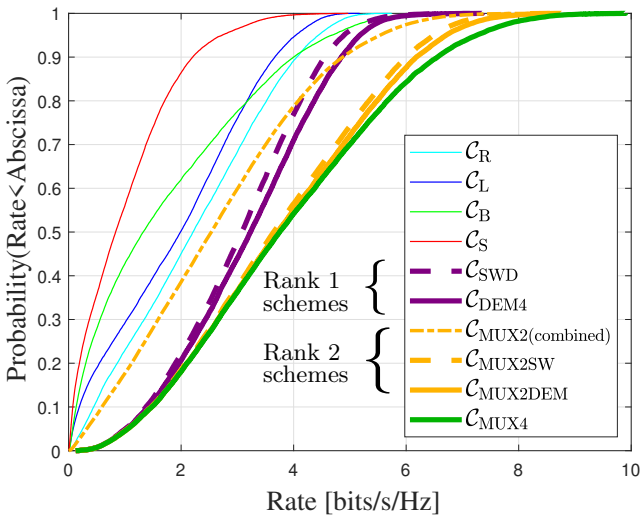

Figure 9: CDFs showing the rates at an SNR of 10 dB.

3.2 Sum rate comparison

To include the MUX schemes in this comparison, we will now plot rate CDFs. Fig. 9 shows rate CDFs for a selection of schemes, at a reference SNR of 10 dB with unity power transmitted.

In general, increasing the number of streams yields a higher rate. Interestingly, the MUX2 scheme (all 6 combinations presented in a combined CDF), where we limit the transmissions to any two of the antennas, often show lower rates than the SWD scheme. This, highlights the importance of having access to more antennas and again, is a result of the low correlation between the antennas.

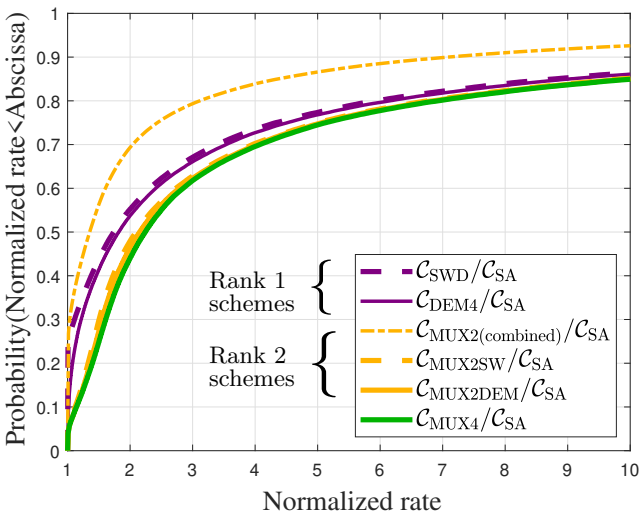

Figure 10: CDFs showing the rate, normalized to that of single antenna operation, at an SNR of 10 dB.

Similar to the SNR-gain, we express the performance as a normalized rate, where we use the capacity given by each antenna as the reference and then combine the CDFs. Fig. 10 shows CDFs of the normalized rate for a selection of schemes. The results show the same trend as for the diversity schemes, namely, increasing the antenna count is more important than having a transceiver for each antenna. The difference between the DEM4 and the MUX2DEM schemes comes from the fact that the MUX2DEM scheme addresses both eigenmodes while the DEM4 scheme selects the strongest one.

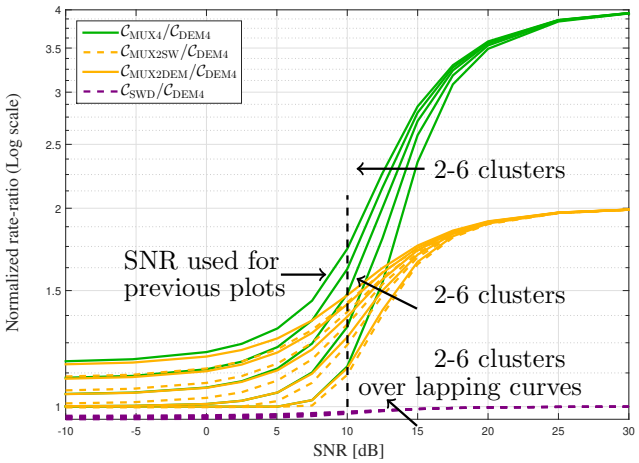

Figure 11: Normalized rate vs. the SNR and the number of clusters. The clusters are in the range 2 to 6 and a larger number yield a higher ratio.

The results, however, depend heavily on the SNR and, intrinsically when the SNR increases, the ratio between the rates for different schemes converges. The ratio of the rates from any of the dual-stream schemes (i.e. MUX2SW and MUX2DEM) converges to two and from the quad-stream scheme (i.e. MUX4) to four as they are divided by the rate of any of the single stream schemes.

The results, however, depend heavily on the SNR and, intrinsically when the SNR increases, the ratio between the rates for different schemes converges. The ratio of the rates from any of the dual-stream schemes (i.e. MUX2SW and MUX2DEM) converges to two and from the quad-stream scheme (i.e. MUX4) to four as they are divided by the rate of any of the single stream schemes.

To find the operational range where the different MUX schemes are most effective, for each channel realization, the ratio between each of the MUX schemes and the DEM4 scheme was computed and the median of the resulting ratio-distribution derived. Fig. 11 shows the median of the normalized rate-ratios for $\mathcal{C}_{\mathrm{MUX4}}/\mathcal{C}_{\mathrm{DEM4}}$, $\mathcal{C}_{\mathrm{MUX2SW}}/\mathcal{C}_{\mathrm{DEM4}}$, $\mathcal{C}_{\mathrm{MUX2DEM}}/\mathcal{C}_{\mathrm{DEM4}}$ and $\mathcal{C}_{\mathrm{SWD}}/\mathcal{C}_{\mathrm{DEM4}}$ as functions of the SNR. The dashed line at an SNR of 10 dB indicates the level at which the previous plots where generated.

It should be noted that the channel properties used in the simulations are derived from measurements based on a dual-antenna terminal and, therefore, may not be entirely representative for simulation of four multiplexed streams. Depending on

the precoder at the BS side, also weaker clusters may be heavily illuminated and the channel at the terminal side may therefore be perceived as richer. The Fig. 11 includes the impact of channel richness, in terms of number of clusters ranging from 2 to 6, where the normalized-rate-ratio increases with the number of clusters. For the sake of simplicity, we have used equally strong clusters in our simulations, which may not be entirely realistic but serves as an (upper) reference level. As the MUX4 scheme is optimal and reaches capacity, it may seem that this is the obvious choice in all cases. In a real scenario, however, a detector has an SNR limit, below which it can not operate. For the MUX schemes all streams need to have an SNR above this minimum level (which can be implemented in the water pouring algorithm). The plots in Fig. 11 are generated with the detection limit set to $-\infty$ dB, the schemes therefore show normalized rate-ratios larger than 1 also at unrealistically low SNRs.

For SNRs around 10 dB, the dual-stream schemes and the MUX4 schemes show only a small difference at lower number of clusters. In general, the MUX4 scheme shows a larger dependency on the number of clusters and has a significant advantage at SNRs beyond 10 dB. The SWD and MUX2SW schemes both are on par with their optimal counterpart the DEM4 and MUX2DEM schemes respectively. This shows the importance of having access to all antennas and that it is enough to reach close the rank conditioned capacity. A general conclusion is that, to reach a rate improvement of a factor of four, for the MUX4 scheme, the minimum SNR is about 20 dB higher than that of rate one. For the two stream schemes it is about 15 dB higher.

It can be generally stated that the switched schemes perform close to the rank conditioned capacity and this is the case also when the channel richness increases. It is naturally possible to find environments with other properties. However, we think that the environment that we selected can be considered representative for indoor propagation channels. By normalizing the propagation channels, and study dynamic properties rather than absolute levels our results show that it is mainly the number of clusters that determine the performance. As we see similar behaviour for various number of clusters we therefore assume that our conclusions are general. Furthermore, the results relies also on the antenna implementations. We believe that antennas integrated into the form-factor of a smartphone will be similar. Finally, the results are also based on how well a channel can be accurately modelled with clusters, which was evaluated in [13].

4 Discussion and Conclusion

The correlation between integrated handset-antennas tuned to the frequency range 2-6 GHz, is typically low. This, has a large influence on the rate and the SNR-gain different pilot transmission strategies return in a massive MIMO system. Our results show that switched architectures reach close to the rank-conditioned capacity of a channel and that having access to more antennas is essential.

Based on the asymmetric traffic in today's networks, a switch will not only be needed to enable uplink pilot transmission from all antennas, which is mandatory for massive MIMO systems but, the solution will be close to optimal from an uplink

power transfer perspective.

The simulations also clearly show that the passive diversity- or MIMO-receivers, mandatory for LTE, will not provide optimal performance in a massive MIMO system, e.g. emerging 5G NR radio access, due to lack of pilot transmission capability from all antennas.

The simulation results further show that, at lower SNRs the benefit of multiplexed operation is limited and similar rates can be achieved with less complex switched diversity. Even if a terminal is equipped with receive and /or transmit chains to support both the dominant eigenmode and the multiplexed schemes with two or more streams there is a lot of power that can be saved by turning the transceiver chains off and use switched diversity instead, both from a computational complexity and power consumption perspective.

We show that there is a large difference between channel distributions generated by random terminal-orientations and those limited by few spherical cuts for a terminal with integrated antennas. It is important to pay attention to this difference when estimating channel properties from measured data.

5 Acknowledgment

The authors would like to thank Sony Mobile Communications in Lund, Sweden and Stiftelsen för Strategisk Forskning (SSF) for funding the project. The authors would also like to thank unnamed reviewers for their valuable contributions.

References

[1] T. L. Marzetta, "Noncooperative Cellular Wireless with Unlimited Numbers of Base Station Antennas OFDM," *IEEE Trans. Wireless Commun.*, vol. 9, no. 11, pp. 3590–3600, Nov. 2010, doi: http://dx.doi.org/10.1109/TWC.2010.092810.091092.

[2] H. Q. Ngo, E. G. Larsson, and T. L. Marzetta, "Energy and Spectral Efficiency of Very Large Multiuser MIMO Systems," *IEEE Transactions on Communications*, vol. 61, no. 4, pp. 1436–1449, Apr. 2013, doi: http://dx.doi.org/10.1109/TCOMM.2013.020413.110848.

[3] E. Björnson, E. G. Larsson, and T. L. Marzetta, "Massive MIMO: 10 Myths and One Critical Question," *IEEE Communications Magazine*, pp. 114–123, Feb. 2016, doi: http://10.1109/MCOM.2016.7402270.

[4] E. Björnson, J. Hoydis, M. Kountouris, and M. Debbah, "Massive MIMO Systems with Non-Ideal Hardware: Energy Efficiency, Estimation, and Capacity Limits," *IEEE Transactions on Information Theory*, vol. 60, no. 11, pp. 7112–7139, Nov. 2014, doi: http://dx.doi.org/10.1109/TIT.2014.2354403.

[5] E. L. Bengtsson, F. Tufvesson, and O. Edfors, "UE Antenna Properties and Their Influence on Massive MIMO Performance," in *Proceedings of the 9th European Conference on Antennas and Propagation, (EUCAP)*, Lisbon, Portugal, Apr. 2015.

[6] E. L. Bengtsson, P. C. Karlsson, F. Tufvesson, J. Vieira, S. Malkowsky, L. Liu, F. Rusek, and O. Edfors, "Transmission Schemes for Multiple Antenna Terminals in Real Massive MIMO System," in *Proceedings of GlobeCom 2016 Conference, IEEE Communications Society*, Washington DC, USA, Dec. 2016.

[7] À. O. Martínez, P. Popovski, J. Ø. Nielsen, and E. D. Carvalho, "Experimental Study of the Benefits of a Second Antenna at the User Side in a Massive MIMO System," *IEEE Access*, vol. PP, no. 99, pp. 1–1, 2017, doi: http://dx.doi.org/10.1109/ACCESS.2017.2785860.

[8] E. L. Bengtsson, F. Rusek, S. Malkowsky, F. Tufvesson, P. C. Karlsson, and O. Edfors, "A Simulation Framework for Multiple-Antenna Terminals in 5G Massive MIMO Systems," *IEEE Access*, vol. 5, pp. 26 819–26 831, 2017, doi: http://dx.doi.org/10.1109/ACCESS.2017.2775210.

[9] J. Vieira, S. Malkowsky, K. Nieman, Z. Miers, N. Kundargi, L. Liu, I. Wong, V. Öwall, O. Edfors, and F. Tufvesson, "A Flexible 100-Antenna Testbed for Massive MIMO," in *Globecom Workshops (GC Wkshps)*, 2014, pp. 287–293.

[10] S. Malkowsky, J. Vieira, L. Liu, K. Nieman, N. Kundargi, I. Wong, F. Tufvesson, V. Öwall, and O. Edfors, "The Worlds First Real-Time Testbed for Massive MIMO: Design, Implementation, and Validation," *IEEE Access*, vol. 5, pp. 9073 – 9088, May. 2017, doi: http://dx.doi.org/10.1109/ACCESS.2017.2705561.

[11] A. Paulraj, R. Nabar, and D. Gore, *Introduction to Space-Time Wireless Communications*, 1st ed. Cambridge University Press, 2003.

[12] *Universal Mobile Telecommunications System UMTS Spatial channel model for Multiple Input Multiple Output MIMO simulations*, 12th ed., ETSI, 3GPP TR 25.996, 2014.

[13] X. Gao, J. Flordelis, G. Dahman, F. Tufvesson, and O. Edfors, "Massive MIMO Channel Modeling - Extension of the COST 2100 Model," 2015.

[14] X. Gao, F. Tufvesson, O. Edfors, and F. Rusek, "Measured Propagation Characteristics for Very-Large MIMO at 2.6 GHz," in *Proc. of Asilomar Conference on Signals, Systems and Computers (ASILOMAR)*, Nov. 2012, pp. 295–299, doi: http://dx.doi.org/10.1109/ACSSC.2012.6489010.

[15] T. Cover and J. Thomas, *Elements of Information Theory*, 2nd ed. Wiley-Interscience, 2006.

Paper VI

A Case Study on the Influence of Multiple Users on the Effective Channel in a Massive MIMO System

We investigate the importance of weak clusters when modeling a wireless massive MIMO channel. We do this by studying the influence of densely spaced terminals and the number of base-station antennas for a zero-forcing precoded massive MIMO system. In particular, we focus on the influence on the correlation and imbalance between the signals at the terminal antennas, the effective channel-gain, the eigenvalue distributions and the number of clusters. The study is based on measured radio-channels from terminal prototypes with integrated antennas, connected to a massive MIMO testbed. We further evaluate the advantage of using block-diagonalized zero-forcing compared to conventional zero-forcing in a massive MIMO system. Unexpectedly, terminals with low antenna envelope correlation coefficient may benefit significantly from block-diagonal zero-forcing in a massive MIMO system. The main conclusion is that weaker clusters are important when modeling multi-user scenarios.

1 Introduction

Massive MIMO (MaMi) [1] is an essential part of the emerging new radio (NR) standard for the fifth-generation (5G) wireless communication [2]. MaMi has received a lot of attention in the wireless communication community [3–8] and suggests that capacity can be increased by an order of magnitude and energy-efficiency by two orders of magnitude. Except for of a few papers [9–13], the terminal side of the MaMi system has not received much attention in the literature and relates mostly to idealized isotropically radiating single antenna terminals.

In [13] we proposed a cluster[6] based, link-level, MaMi simulation model that uses measured terminal-antenna characteristics. However, the scope of [13] was limited to a single terminal, although with multiple antennas, at a static physical location in space. It is, therefore, our ambition to extend the simulator, and this paper presents investigations of underlying channel properties that need to be accounted for. More specifically, in [20] the number of clusters is estimated using a channel sounder, but simplifications are made in [13] to include only clusters of significant power. This builds on the understanding that in the single-user (SU) case a zero-forcing (ZF) precoder allocates power according to the maximum ratio principle. This means that mainly dominant clusters are illuminated while weaker clusters become insignificant. If the number of terminals in a limited area increase, and thus a higher rank needs to be utilized, the importance of the weaker clusters seen by each terminal grows. To separate terminals, also weaker clusters become significant in the effective channel and therefore needs to be present in a model. From a mathematical perspective this is a plausible mechanism behind a better conditioned channel matrix, but with weaker eigenvalues. Furthermore, it is often unclear how many clusters that are exclusive to a single terminal, and how many that are common. Ultimately, our goal is to establish a multi-terminal simulator that assigns non-shared clusters to each terminal, seen only by that terminal and shared clusters to a group of terminals, seen by all terminals in the group. Furthermore, we aim to include dependencies on: the distance between terminals, the distance to the basestation (BS), and the environment type. This is an important aspect in the multilink case of the COST 2100 channel model [18], and we apply it in a MaMi context.

We identify properties that must be accounted for in simulations when multi-users (MU) are present, and analyze those in detail. We investigate two channel-properties. Firstly, we investigate how other users influence the effective channel of an individual terminal. Secondly, we perform an investigation of the relation between inter-terminal distance and the number of shared clusters.

Concerning the impact of other users on a single terminal, we aim to verify a working hypothesis, based on the following facts and assumptions: For a SU MaMi case, the strongest effective channels for a dual-antenna terminal are given by the dominant eigenmodes of the channel. In a cluster/geometry-based channel model,

[6] Based on observations of wireless channels, e.g. [14–16], contributions of signals propagating along various paths, a.k.a. multipath components (MPCs), tend to be clustered. This can be explained by the reflections caused by various objects in the environment. Numerous cluster-based simulation models for MIMO systems exist, e.g. [17–19].

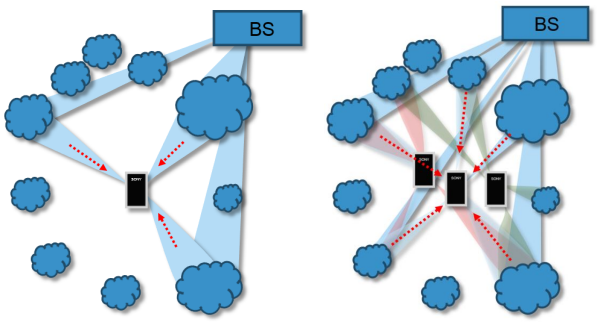

Figure 1: Geometry-based cluster-model, where a few dominant clusters determine the effective channel at the terminal side (left), and an MU scenario where more clusters are used to separate the terminals (right).

this can be modeled as transmissions via a few dominant clusters (left of Fig. 1). In an MU MaMi system using zero-forcing (ZF) precoder, the eigenmodes of the effective channel between the terminal and the BS change. The channel typically becomes weaker when the rank is increased by the introduction of more terminals. The change of the eigenmodes is consistent with that when also weaker clusters are illuminated in the cluster-based model (right of Fig. 1).

We aim to validate the following hypothesis: *When multiple terminals are introduced in a limited space, a ZF precoder causes a larger set of clusters to be illuminated.* We aim to verify this by studying the effective correlation between the signals at the antennas of a terminal, which can then be expected to decrease and approach the envelope correlation coefficient [21] of the antennas.

The main contributions of this paper are:

- The measured radio channels do not show any sign of being limited to a few clusters, and the channel matrix, $\boldsymbol{H}$, seen from the BS side can be expected to have a high rank.
- We demonstrate that, in our measured scenario, two terminals at a distance of only 5 m share essentially no clusters, which means that the channel matrix, $\boldsymbol{H}$, seen from the BS side is well conditioned.
- We study empirically the advantage block-diagonal ZF (BDZF) [22] has over classical ZF (CZF) in MaMi systems and relate it to the terminal antenna correlation.

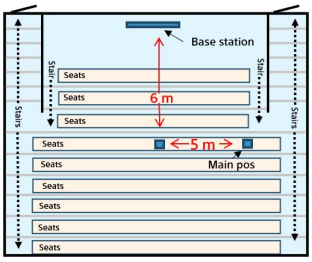

Figure 2: Drawing of the auditorium where the measurements was performed.

2 Set-Up and Evaluation Model

Since we deal with multiple terminals, we need some form of BS precoding. BDZF separate terminals, without separating antennas within a terminal. BDZF, therefore, allows for evaluation of the influence terminals sharing the same channel have on the correlation and power imbalance between the antennas of a terminal. Loosely speaking, the performance of CZF is often assumed to approach the channel capacity as the number of BS antennas grows large [6] and, BDZF may therefore not be significantly better in MaMi systems.

2.1 Measurement Set-up

All measurements were conducted in an auditorium as shown in Fig. 2. Four measurement conditions were defined based on two terminals, each measured both stand-alone and loaded by a phantom head with a left hand (HHL). The terminal prototypes are based on Sony Xperia handsets with integrated antennas, tuned to the 3.7 GHz band used by the Lund massive MIMO testbed [23]. It can be noted that the envelope correlation coefficients between the antennas in both prototypes are close to zero. The terminals were transmitting pilot signals from both antennas to the testbed, and estimated transfer functions between all antennas, representing snapshots of the channel, were stored. Each snapshot corresponds to a unique terminal orientation, rotation angle, and location in the room. For the stand-alone captures, two different orientations were used, each measured at about 30 different rotation angles, giving $C_s \approx 60$ channel snapshots. For the HHL captures three different orientations were used, resulting in $C_s \approx 90$ channel snapshots. In all, about 300 different channel snapshots, each with two terminal-antennas, were logged for the four terminal-conditions. A snapshot contains 20 sampled sub-carriers, each sub-carrier with a bandwidth of 15 kHz, equally spaced over 20 MHz.

2.2 Experimental Evaluation

In the evaluations, one of the four measured terminal-conditions is considered being the reference. As the SNR of the measured channels was about 20 dB or more in all cases we ignore measurement noise and assume the measured channels to be the true ones. In each evaluation, the number of terminals, K, is increased from 1 to 10. With each terminal sharing the channel having two antennas, the total number of streams, therefore, increases from 2 to 20. For each realization, a randomly selected snapshot from the reference condition is combined with those of the $K-1$ terminals. For each of the terminals, a random snapshot is selected, and all of the added terminals are different from the reference terminal. For each set of K terminals, 1000 realizations are generated and we record the medians of the correlation, power imbalance, and channel-gain (i.e., the trace of the inner product of the channel) between the antennas of the reference terminal.

The channels from terminal k are represented by an $M \times 2$ matrix, $\boldsymbol{H}_k$, where M is the number of BS antennas. For SU-MaMi, the channel properties are given by the inner product, $\boldsymbol{G}_k = \boldsymbol{H}_k^{\mathrm{H}} \boldsymbol{H}_k$, which is a 2×2 matrix. Using the normalized version of the inner product, the terminal antenna correlation, α, and power imbalance, β can be identified [24]

$$\boldsymbol{G}_{\mathrm{norm}} = \frac{2}{\mathrm{tr}(\boldsymbol{G}_k)} \boldsymbol{G}_k = \begin{bmatrix} 1+\beta & \alpha \\ \alpha^* & 1-\beta \end{bmatrix}, \tag{1}$$

where $\mathrm{tr}(\cdot)$ is the trace operator.

For the MU-MaMi case, we adjoin the channel matrices from all terminals, each with two antennas, into a full channel matrix $\boldsymbol{H} = [\boldsymbol{H}_1 \boldsymbol{H}_2 \cdots \boldsymbol{H}_K]$. To find the space where the BS can perform transmissions to terminal k without causing interference to the other $K-1$ terminals, we define $\boldsymbol{H}_{\mathrm{I}|k} = [\boldsymbol{H}_1 \cdots \boldsymbol{H}_{k-1} \ \boldsymbol{H}_{k+1} \cdots \boldsymbol{H}_K]$, and compute its null-space, $\mathcal{N}_{\mathrm{space}|k}$. Assuming that $\boldsymbol{H}_{\mathrm{I}|k}$ has full rank, $\mathcal{N}_{\mathrm{space}|k}$ can be represented by an $M \times (M - 2(K-1))$ matrix $\boldsymbol{N}_{\mathrm{space}|k}$ with orthogonal columns. By multiplying the channel of terminal k, $\boldsymbol{H}_k$, with the null-space of the other terminals, $N_{\mathrm{space}\,|k}$, we obtain the effective channel matrix for terminal k, $\boldsymbol{H}_{\mathrm{BD}k} = \boldsymbol{H}_k^{\mathrm{H}} \boldsymbol{N}_{\mathrm{space}|k}$, which is a $2 \times (M - 2(K-1))$ matrix. We can now compute the BD-based inner product $\boldsymbol{G}_{\mathrm{BDk}} = \boldsymbol{H}_{\mathrm{BDk}} \boldsymbol{H}_{\mathrm{BDk}}^{\mathrm{H}}$, which is a 2×2 matrix that represents the interference free subspace for terminal k, for the BD precoder case. Normalizing $\boldsymbol{G}_{\mathrm{BDk}}$, the same way as in (1), the effective correlation, α_{BDk}, and power imbalance, β_{BDk} can be identified analogously to the SU-MaMi case. The term $\mathrm{tr}(\boldsymbol{G}_{\mathrm{BDk}})$ reflects the effective channel-gain seen by the terminal antennas, which we refer to as γ.

Similarly, to compute the effective channel in the CZF case, for a given terminal antenna l, $1 \leq l \leq 2K$, we define the matrix, $\boldsymbol{H}_{\mathrm{I}|l} = [\boldsymbol{H}_1 \cdots \boldsymbol{H}_{l-1} \ \boldsymbol{H}_{l+1} \cdots \boldsymbol{H}_{2K}]$. We follow the same steps as above but use the null-space of $\boldsymbol{H}_{\mathrm{I}|l}$ as our precoder. For terminal antenna l, $\boldsymbol{H}_{\mathrm{ZF}l} = \boldsymbol{H}_l^{\mathrm{H}} \boldsymbol{N}_{\mathrm{space}|l}$, and we arrive at $\boldsymbol{G}_{\mathrm{ZF}l} = \boldsymbol{H}_{\mathrm{ZF}l} \boldsymbol{H}_{\mathrm{ZFl}}^{\mathrm{H}}$, a scalar that defines the effective channel-gain for antenna l. For terminal k, we can compare the sum effective channel-gain from both of its antennas to γ from the BDZF case.

Furthermore, the eigenvalues of the measured channels' outer product can be used for dimensionality evaluations. Based on the channel matrix $\boldsymbol{H}$ ($\boldsymbol{H}_{\mathrm{ZF}l}$ in the

CZF case), the outer product for a single antenna l, seeing the channel $\boldsymbol{h}_l$ is given by $\boldsymbol{O}_l = \boldsymbol{h}_l \boldsymbol{h}_l^{\mathrm{H}}$, an $M \times M$ matrix. The outer product for a single snapshot has a unit rank. A matrix with the size of the outer product can have a rank of at most M. By averaging the outer products over the C_s orientations and rotation angles for a measured condition, $\widetilde{\boldsymbol{O}}_l = \frac{1}{C} \sum_{c=1}^{C} \boldsymbol{h}_l(c) \boldsymbol{h}_l(c)^{\mathrm{H}}$, all available dimensions become included. The energy distribution of the eigenvalues of $\widetilde{\boldsymbol{O}}_l$ indicates how many dimensions are needed to represent all the channels included in C_s. The approach is similar to a sample covariance matrix. If we normalize the trace of $\widetilde{\boldsymbol{O}}_l$ to unity, $\widetilde{\boldsymbol{O}}'_l = \frac{1}{\mathrm{tr}(\widetilde{\boldsymbol{O}}_l)} \widetilde{\boldsymbol{O}}_l$, the magnitude of each eigenvalue will directly reflect the fraction of energy said eigenmode carries.

The number of dimensions carrying the essential part of the energy relates to the number of clusters and indicates the richness of the environment. With $\widetilde{\boldsymbol{O}}'_l$ being Hermitian, an eigen-decomposition (ED) yields both the eigenvalues and the eigenvectors, $\mathrm{ED}(\widetilde{\boldsymbol{O}}'_l) = \boldsymbol{U}_l \boldsymbol{\Lambda}_l \boldsymbol{U}_l^{\mathrm{H}}$, where $\boldsymbol{U}_l$ is a unitary matrix containing the eigenvectors and $\boldsymbol{\Lambda}_l$ is a diagonal matrix with the eigenvalues along the diagonal. The energy projected from the i^{th} eigenvector of antenna l, (i.e., $\boldsymbol{U}_{l,\mathrm{col}:i}$) on the normalized matrix $\widetilde{\boldsymbol{O}}'_j$ of antenna j is

$$P_{l \to j,i} = \boldsymbol{U}_{l,\mathrm{col}:i}^{\mathrm{H}} \widetilde{\boldsymbol{O}}'_j \boldsymbol{U}_{l,\mathrm{col}:i}. \tag{2}$$

We are aware that the estimation of dimensions from sampled measured data is a complex matter [14]. We assume that there is a direct relation between eigenmodes and clusters and that the SNRs are large enough to make relevant conclusions. The results are then used for relative comparisons rather than manifesting any absolute numbers.

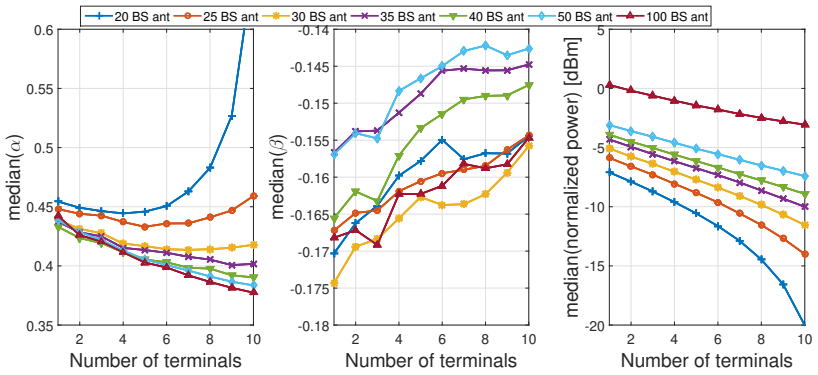

Figure 3: From the left, median of the correlation α, the power imbalance β and the normalized channel-gain, as functions of the number of terminals (with BDZF) for a various number of BS antennas. The figures correspond to condition 2. The antenna selection is randomized from the array when $M < 100$.

3 Evaluation Results

3.1 The Influence of Multiple Users to the Channel

In Fig. 3, we show the medians of the terminal antenna correlation α, power imbalance β, and the normalized effective channel gain. The plots are drawn as functions of the total number of terminals, K, using BDZF for a various number of BS antennas, M.

When the number of BS antennas is at least twice that of the streams present, a decrease in correlation as a function of the number of terminals can be observed. A lower number of antennas at the BS can not easily resolve the streams, and the correlation increases, as more streams, are introduced. For $M > 40$, the plots seem to converge to one curve, and therefore adding more antennas at the BS side will not significantly change the terminal antenna correlation α.

The power imbalance of the terminal antennas is not significantly influenced by the number of terminals or BS antennas. On the other hand, the gain drops as more terminals are introduced. Its dependence on the number of BS antennas for $M > 40$ relates to array gain and the more BS antennas the stronger the gain. It is also possible to determine when MaMi properties apply from the gain plots. When the curvature (2nd order derivative) increases so-called favorable propagation cannot be assumed, which also here suggests $M > 40$.

The results are consistent with our hypothesis, that the BDZF and plausibly also for CZF algorithms allocate power to weaker clusters when the number of streams is increased, in a limited environment. For different terminal antenna designs or

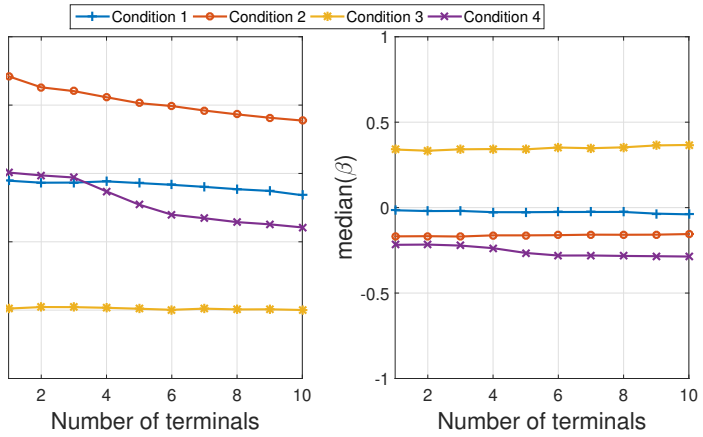

Figure 4: The median of the correlation α to the left and the median of the power imbalance β to the right, both as functions of terminals introduced in the same location, for 100 BS antennas, and the 4 alternative conditions. Note that the curves corresponding to condition 2 are the same as those in Figure 2 for M=100.

loading scenarios, however, the correlation may behave differently. From our results shown in Fig. 4, where each of the four conditions is used as reference terminal, the correlation is either unaffected by the number of terminals or drops, while the power imbalance only shows a minor dependency. It shall be noted, that even if the decrease in correlation improves the capacity of the effective channel, the reduction in channel strength reduces it by a much larger extent and the net capacity typically decreases.

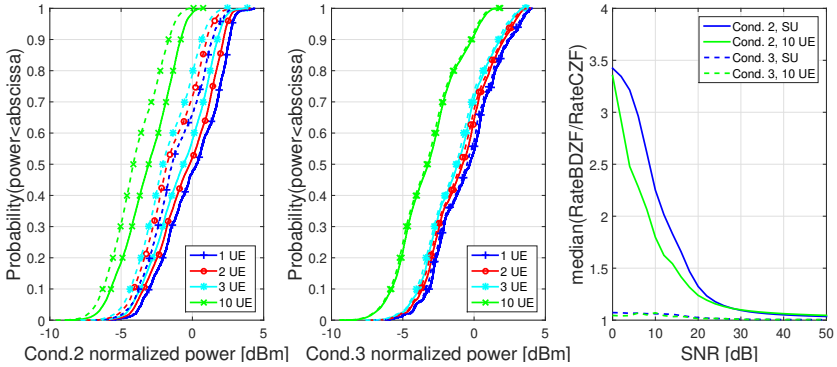

Figure 5: CDFs of the normalized effective channel-gain for the CZF (dashed) and the BDZF (solid) case. To the left for condition 2, high correlation, and at the center condition 3, low correlation. To the right, the ratio of the median rates for the BDZF/CZF as a function of the SNR.

The channel strength for CZF without the BD is also interesting as it relaxes the processing burden on the terminal. The terminal will then receive an independent stream at each antenna. If there is BD the UE need to co-process the signals fed to its antennas but can address the eigenmodes of the effective channel and with optimal power-allocation can reach the capacity of the effective channel. The two plots to the left in Fig. 5 shows CDFs of the normalized effective channel-gain, for both the CZF case (dashed lines) and the BDZF case (solid lines), for $K \in 1, 2, 3, 10$ terminals. The left plot represents condition 2, for which the terminal antenna correlation is in the range 0.35 to 0.45 and the center plot represents condition 3, for which the correlation is about 0.1.

As the correlation decreases from 0.45 to 0.35 in the left figure, corresponding to the SU case and the 10-terminal case, the difference in the effective channel-gain for the CZF and BDZF cases also decreases. The difference in the median for the SU case is about 2 dB, while, in the 10 terminal case only about 1 dB. The figures indicate that when the correlation is larger it is advantageous to address the eigenmodes rather than using CZF. Indeed, for terminal condition-2 the rate can be improved by more than a factor of three, depending on the signal-to-noise-ratio (SNR). This is shown in the right plot of Fig. 5, where the ratio between the median of the rates of the BDZF and CZF cases is plotted for condition-2 and condition-3, as a function of the SNR.

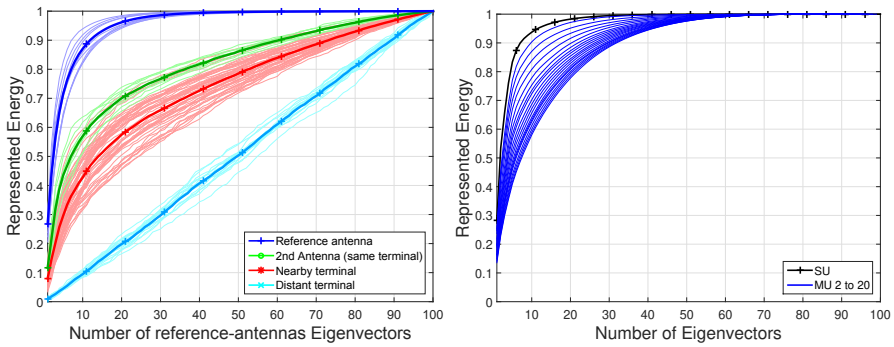

Figure 6: The number of eigenvectors from an antenna condition that are needed to represent the energy in other antennas (left). The energy become distributed among the eigenvectors as the number of terminals increase (right). With CZF precoder at the BS side for both cases.

3.2 Common Clusters as a Function of Inter-Terminal Distance

The dimensionality of the signal subspace, in terms of the number of effective clusters or eigenvectors (assumed strongly related), is hard to estimate from inner product-based measures, since it influences the distributions of α, β, and γ through second-order phenomena, e.g. slope or curvature. Therefore, we look directly at the energy represented by the eigenvectors of the averaged outer products, based on (2). The plot to the left in Fig. 6 shows how many eigenvectors, sorted according to the strength of the eigenvalues computed from one of the terminal antennas, that are needed to represent the energy seen by any other antenna. It can be noted that in this case there is no precoder involved and hence we are studying the physical channels. There are four populations of curves in the plot together with the average for the respective population.

The first category, the blue curves, shows the accumulated energy for a selection of antennas as the sorted eigenvectors derived from their channels increases. The 10 strongest eigenvectors represent in average 87% of the energy. The small variation among the curves suggests that the number of dominating/effective clusters present is similar in all cases.

The green curves represent how well the sorted eigenvectors of one antenna can represent the energy of a second antenna, measured at the same time and located in the same terminal. In average 57% of the energy is represented by the 10 strongest eigenvectors. Also, in this case, we see a small variation, suggesting that the number of dominant physical clusters, seen by all antenna pairs, is about the same.

The red curves represent how well the sorted eigenvectors of one antenna can represent the energy of a second antenna, which is located in a different terminal, measured at the same location (and therefore not measured simultaneously). In average 43% of the energy is represented by the 10 strongest eigenvectors. Again, the slope is steep at the beginning for all curves, suggesting that there are a few dominant common physical clusters. The fact that the antennas are not in the same terminal and that the measurements not made simultaneously are likely contributions to the larger variation among the curves. In average, the correlation between the antennas of different users at the same location is also expected to be smaller than when in the same terminal, which, will lower the number of shared physical clusters. For both the green and red curves, the initial steep slope suggests that channels share the most dominant clusters.

The cyan curves, represent how well the sorted eigenvectors of one antenna can represent the energy of a second antenna at a different location, measured in the same room about 5 meters apart. In this case, the curves become straight lines, which, suggests that different clusters are dominant, or at least independent, in the different positions and no correlation between the channels can be observed. Thus, our results indicate that in a large auditorium, terminals spaced 5 meters apart may very well not share any clusters. There is a clear trend that co-located terminals seems to share more clusters.

The right plot in Fig 6 shows the accumulated energy for one of the antennas as the sorted eigenvectors derived from the channel increases. The curves represent the different number of interfering streams, with CZF precoder at the BS. As, the number of streams increases, ranging from 1 to 20, more eigenvectors are needed to represent the same amount of energy. The figure is generated as an average, where the antennas are randomly selected from a set of measurements performed at a limited space. The result is in line with those based on the inner product and is consistent with our hypothesis that the energy becomes more evenly distributed among the effective eigenvectors as the number of streams increases also in the CZF. Based on the relation between eigenvectors and clusters, this result suggests that the number of effective clusters increases with the number of simultaneous streams in a CZF precoded system.

4 Conclusions

The results from the measurement-based analysis are consistent with the hypothesis: With a single terminal, the effective channel properties (i.e., correlation, power imbalance, and channel-gain) are consistent with the results from a cluster model when only a few dominant clusters are present. In multi-user situations, the results correspond to the case when also weaker clusters contribute to the effective channel.

The results explain the large discrepancy in the estimated number of clusters [13] between a precoded channel with a single terminal and that reported in [20] performed in the same environment. While the number of clusters in the physical channel may be large, precoded channels rely on a few strong clusters and the number of active

clusters depends on the number of active streams. It is therefore important that realistic channel models for multiplexed operation include both dominant and weaker clusters in a given environment.

The results show that 40 BS antennas are sufficient in our environment and beyond that only the array-gain increases. We also showed that 20 streams can be resolved with only the array-gain penalty and no reduction in channel dimensionality. We found that block-diagonalized-zero-forcing can give a significant advantage compared to conventional zero-forcing even when the antennas within a terminal have a very low envelope correlation coefficient. Finally, a study of the outer products of the effective channel matrix support that terminals close to each other share more clusters.

5 Acknowledgement

The authors would like to thank Sony Mobile Communications in Lund and Stiftelsen för Strategisk Forskning (SSF) for funding of the project.

References

[1] T. L. Marzetta, "Noncooperative Cellular Wireless with Unlimited Numbers of Base Station Antennas OFDM," *IEEE Trans. Wireless Commun.*, vol. 9, no. 11, pp. 3590–3600, Nov. 2010, doi: http://dx.doi.org/10.1109/TWC.2010.092810.091092.

[2] *Study on New Radio (NR) Access Technology*, 14th ed., ETSI, 3GPP TR 38.912, 2017.

[3] E. G. Larsson, F. Tufvesson, O. Edfors, and T. L. Marzetta, "Massive MIMO for Next Generation Wireless Systems," *IEEE Communications Magazine*, vol. 52, no. 2, pp. 186–195, Feb. 2014, doi: http://dx.doi.org/10.1109/MCOM.2014.6736761.

[4] H. Q. Ngo, E. G. Larsson, and T. L. Marzetta, "Energy and Spectral Efficiency of Very Large Multiuser MIMO Systems," *IEEE Transactions on Communications*, vol. 61, no. 4, pp. 1436–1449, Apr. 2013, doi: http://dx.doi.org/10.1109/TCOMM.2013.020413.110848.

[5] F. Rusek, D. Persson, B. K. Lau, E. G. Larsson, T. L. Marzetta, O. Edfors, and F. Tufvesson, "Scaling Up MIMO: Opportunities and Challenges with Very Large Arrays," *IEEE Signal Processing Magazine*, vol. 30, no. 1, pp. 40–60, Dec. 2012, doi: http://dx.doi.org/10.1109/MSP.2011.2178495.

[6] E. Björnson, E. G. Larsson, and T. L. Marzetta, "Massive MIMO: 10 Myths and One Critical Question," *IEEE Communications Magazine*, pp. 114–123, Feb. 2016, doi: http://10.1109/MCOM.2016.7402270.

[7] E. G. Larsson, T. L. Marzetta, H. Yang, and H. Q. Ngo, *Fundamentals of Massive MIMO*, 1st ed. CAMBRIDGE UNIVERSITY PRESS, 2016.

[8] E. Björnson, J. Hoydis, and L. Sanguinetti, *Massive MIMO Networks: Spectral, Energy, and Hardware Efficiency*, 1st ed. now Publishers Inc., 2017.

[9] E. Björnson, J. Hoydis, M. Kountouris, and M. Debbah, "Massive MIMO Systems with Non-Ideal Hardware: Energy Efficiency, Estimation, and Capacity Limits," *IEEE Transactions on Information Theory*, vol. 60, no. 11, pp. 7112–7139, Nov. 2014, doi: http://dx.doi.org/10.1109/TIT.2014.2354403.

[10] E. L. Bengtsson, F. Tufvesson, and O. Edfors, "UE Antenna Properties and Their Influence on Massive MIMO Performance," in *Proceedings of the 9th European Conference on Antennas and Propagation, (EUCAP)*, Lisbon, Portugal, Apr. 2015.

[11] E. L. Bengtsson, P. C. Karlsson, F. Tufvesson, J. Vieira, S. Malkowsky, L. Liu, F. Rusek, and O. Edfors, "Transmission Schemes for Multiple Antenna Terminals in Real Massive MIMO System," in *Proceedings of GlobeCom 2016 Conference, IEEE Communications Society*, Washington DC, USA, Dec. 2016.

[12] À. O. Martínez, P. Popovski, J. Ø. Nielsen, and E. D. Carvalho, "Experimental Study of the Benefits of a Second Antenna at the User Side in a Massive MIMO System," *IEEE Access*, vol. PP, no. 99, pp. 1–1, 2017, doi: http://dx.doi.org/10.1109/ACCESS.2017.2785860.

[13] E. L. Bengtsson, F. Rusek, S. Malkowsky, F. Tufvesson, P. C. Karlsson, and O. Edfors, "A Simulation Framework for Multiple-Antenna Terminals in 5G Massive MIMO Systems," *IEEE Access*, vol. 5, pp. 26 819–26 831, 2017, doi: http://dx.doi.org/10.1109/ACCESS.2017.2775210.

[14] Q. H. Spencer, B. D. Jeffs, M. A. Jensen, and A. L. Swindlehurst, "Modeling the statistical time and angle of arrival characteristics of an indoor multipath channel," *IEEE Journal on Selected Areas in Communications*, vol. 18, no. 3, pp. 347–360, March 2000, doi: http://10.1109/49.840194.

[15] Y. Li, J. Zhang, and Z. Ma, "Clustering in Wireless Propagation Channel With a Statistics-Based Framework," in *2018 IEEE Wireless Communications and Networking Conference (WCNC)*, April 2018, pp. 1–6, doi: http://10.1109/WCNC.2018.8377218.

[16] K. Yu, Q. Li, D. Cheung, and C. Pretie, "On the Tap and Cluster Angular Spreads of Indoor WLAN Channels," *Proceedings IEEE Vehicular Technology Conference*, 2004.

[17] *Universal Mobile Telecommunications System UMTS Spatial channel model for Multiple Input Multiple Output MIMO simulations*, 12th ed., ETSI, 3GPP TR 25.996, 2014.

[18] J. Poutanen, J. Salmi, K. Haneda, V. Kolmonen, F. Tufvesson, and P. Vainikainen, "Propagation Characteristics of Dense Multipath Components," *IEEE Antennas and Wireless Propagation Letters*, vol. 9, pp. 791–794, 2010, doi: http://10.1109/LAWP.2010.2064751.

[19] A. F. Molisch, "A Generic Model for MIMO Wireless Propagation Channels in Macro- and Microcells," *IEEE Transactions on Signal Processing*, vol. 52, no. 1, pp. 61–71, Jan 2004, doi: http://dx.doi.org/10.1109/TSP.2003.820144.

[20] A. Bordoux and et al., *D1.2 MaMi Channel Characteristics: Measurement Results*, final ed., FP7 EU project 619086, MAMMOET, Jun. 2015.

[21] R. G. Vaughan and J. B. Andersen, "Antenna Diversity in Mobile Communications," *IEEE Transactions on Vehicular Technology*, vol. 36, no. 4, pp. 149–172, Nov. 1987, doi: http://dx.doi.org/10.1109/T-VT.1987.24115.

[22] Q. H. Spencer, A. L. Swindlehurst, and M. Haardt, "Zero-Forcing Methods for Downlink Spatial Multiplexing in Multiuser MIMO Channels," *IEEE Transactions on Signal Processing*, vol. 52, no. 2, pp. 461–471, Feb. 2004.

[23] J. Vieira, S. Malkowsky, K. Nieman, Z. Miers, N. Kundargi, L. Liu, I. Wong, V. Öwall, O. Edfors, and F. Tufvesson, "A Flexible 100-Antenna Testbed for Massive MIMO," in *Globecom Workshops (GC Wkshps)*, 2014, pp. 287–293.

[24] X. Gao, "Doctoral Thesis: Massive MIMO in Real Propagation Environments," *Series of Licentiate and Doctoral Theses*, 2016.

Paper VII

A 28 GHz Channel Sounder for Dynamic Propagation Measurements

A pre-requisite for the design of future wireless systems is the understanding of the involved propagation processes, and derivation of insightful models. In this paper, we present a 28 GHz massive multiple-input multiple-output (MIMO) channel sounder intended for measuring dynamic propagation behavior. Based on the switched array principle, our design is capable of characterizing 256×128 dual-polarized channels with a switching duration of approximately 10 μs. Unlike previous systems, this extraordinary angular resolution is complemented with a 1 GHz measurement bandwidth enabling nanosecond delay resolution. To this end, a complete MIMO snapshot can be acquired in real time with 380 ms, in sharp contrast to tens of minutes (or more) with rotating horn antenna sounders. The short measurement time combined with the high phase stability of the 28 GHz radio frequency up/down-conversion chains facilitates phase-coherent measurements. This allows for tracking of multipath behavior over time to investigate the temporal dependencies of channel parameters. Overall, the paper presents the design and implementation aspects of sounder, and discusses a plan for future work in order to measure the dynamic angular, delay, Doppler and polarization parameters.

Erik L Bengtsson, Harsh Tataria, Peter C Karlsson, Ove Edfors, Fredrik Tufvesson
"A 28 GHz Channel Sounder for Dynamic Propagation Measurements"
Published in *TBD*

Table 1: A comprehensive summary of mmWave channel sounders.

Specification	Lund Univ./ Sony Research	USC/ Samsung [32]	NIST Labs [34,35]	New York Univ. [2,28,31]	Durham Univ. [36,37]	Aalto Univ. Nokia [39]	Keysight [38]	BUPT [40]
Sounder type	Switched array	Switched beam	Switched horn	Rotating horn	Switched array	Switched beam	TX:Switched array RX:Parallel array	Switched/virtual array
Carrier frequency	28 GHz	27.85 GHz	28.5, 60 GHz	28, 38, 73 GHz	30, 60, 90 GHz	71-76, 81-86 GHz	¡ 44 GHz	3.5, 6 GHz
Bandwidth	1 GHz	400 MHz	2 GHz	1 GHz	3, 6, 9 GHz	2 GHz	2 GHz	100/200 MHz
TX EIRP	53 dBm	57.1 dBm	51.5 dBm	54.6 dBm	36.7 dBm	28 dBm	23 dBm + TX gain	-
Antenna array sizes	128 x 256	16 x 16	16 x 8	-	8 x 8	64 x 1	8 x 8	(8*32)×16
Polarization	Dual (H and V)	Single	Single	Single	Single	Single	Single	Single
RX antenna gain	27.07 dBi	19.5 dBi	18.5 dBi	24.5 dBi	20.7 dBi	6 dBi	-	-
Switch rate	10 μs	2 μs	4 μs	10 s to minutes	-	200ns	-	-
MIMO snapshot rate	380 ms	0.512 ms	0.512 ms	-	-	0.0128 ms	-	10 s to minutes
TX-RX Synchronization	Rubidium ref.	GPS-Rubidium ref.	GPS-Rubidium ref.	Rubidium ref.	Rubidium ref.	GPS-Rubidium ref.	GPS-Rubidium ref.	Rubidium ref.

1 Introduction

The explosive growth of mobile data rates and the number of connected devices is motivating the use of previously unused spectrum for cellular communications. As a result, higher frequency bands have received considerable attention where larger quantities of vacant spectrum is available. Particularly, the so-called *millimeter-wave* (mmWave) bands ranging from 30-300 GHz have been intensely studied during the last five years [1–4]. Spectrum in the 24-28 GHz band has been recently auctioned in the United States by the Federal Communications Commission, triggering further research and developments [5]. Other countries in North America, Europe, Asia and Oceania are en-route to follow the same path. To this end, standardization bodies such as the Third Generation Partnership Project (3GPP) have accelerated plans to integrate mmWave frequencies into Release 15 (and beyond) specifications, the global standard for fifth-generation (5G) cellular systems [6, 7]. For efficient design, performance assessment and deployment planning of mmWave systems, understanding of the propagation channel by means of real-time measurements is essential. This would allow us to design suitable channel models which capture the physical behavior of involved propagation processes, to characterize their impact on the resulting system performance. Since mmWave systems suffer from high omnidirectional free-space attenuation, a large amount of antenna gain is required at the transmit side of the link end to effectively penetrate the signal [4]. Under a common environment, mmWave channels behave relatively differently to cannonical frequencies below 6 GHz. In particular, the *directional characteristics* of mmWave propagation utilizing *beamforming* over both spatial and temporal domains needs to be accurately measured and modeled.

In order to measure the channel impulse response, a *channel sounder* needs to be designed. The basic operating principle of a channel sounder is to inject a known waveform into the propagation channel, so that suitable signal processing can deconvolve the transmitted signal from the received signal, in turn acquiring the channel impulse response. The sounding waveforms are usually designed in accordance with the sounder type (described later in the paper). They range from standard pulse trains [8,9], PN-sequences [10,13], chirp signals [14,15], or multitone sequences [16,18]. Steady progress is seen in the literature on channel sounder design at mmWave frequencies. Nevertheless, majority of the existing directional sounding setups for indoor mmWave systems are based on vector network analyzers, which use slow chirp or fre-

quency scanning, combined with virtual arrays (mechanical movement of a single antenna along a track). Such sounders are unable to operate in *dynamic environments* and need a cabled connection between the transmit and receive link ends limiting their separation distance [18–23]. For outdoor scenarios, the prevalent method for directionally resolved measurements is based on mechanically rotating horn antennas and measuring the channel impulse response for a fixed pair of transmit and receive horn orientations [2, 24–29]. There are three limitations of such an approach: First is the *non-coherent* nature of the measurements, such that the obtained *angular* resolution is limited by narrow half-power beamwidth (HPBW) of the horn element. As a result, many multipath components (MPCs) may fall into the antenna beamwidth, but appear as a single MPC. To this end, it has been difficult to predict the precise number of contributing MPCs in a given propagation environment and the fundamental question on mmWave channels being *sparse* (in the sense of having small number of MPCs) remains unanswered. Secondly, mechanically rotating horn elements requires measurement run times on the order of multiple hours to complete a single measurement at a given location (cycling through all horn orientations). An exception from this is the sounder presented in [29], which is able to perform 360° scans across the azimuth plane, albeit only at the transmit side in 200 ms. Thirdly, due to the long measurement times, such setups can not characterize dynamic channels for more than one transmit-receive horn combination.

Keeping the above in mind, majority of the measurements reported at mmWave bands either investigate the angular characteristics without considering the temporal behavior of parameters, or have focused on the temporal dynamics without considering the angular characteristics [30, 31]. To the best of our knowledge, the sounder design presented in [32] is the most complete in terms of characterizing both the temporal and angular properties of the mmWave channel in dynamic outdoor scenarios. However, the design in [32] is restricted to measure over 90° sectors in the azimuth and zenith domains, limiting the sounding field-of-view. Unlike all previous studies, in this paper, we present a channel sounder capable of measuring links between 128 transmit and 256 receive dual-polarized antennas. Our ultimate aim is to extract the directionally resolved channels within 180° at the transmitter and 360° at the receiver. To this end, our design facilitates measurements of an order-of-magnitude more channels and higher spatial resolution in comparison with other sounders in [28, 29, 31, 32, 34–40]. Although the presented design operates at 28 GHz over a bandwidth of 1 GHz, its principles could be applied to other mmWave bands as well. Our design is based on the *switched array* principle, circumventing most of the mechanical limitations and allows for accurate measurements across elevation, azimuth, and polarization domains. A bank of high speed electronic switches (exact structure discussed later on) are connected to both transmit and receive antenna elements followed by single 28 GHz up/down-conversion radio frequency (RF) chains. The measurement sequence facilitates each channel combination (transmit-receive antenna pair) to be measured. With the transmit and receive control interface implemented in field programmable gate arrays (FPGAs), our design is capable of switching from one antenna to another in 10 μs. Hence, the same overall effect as in rotating horn antennas can be

achieved in much shorter time. To this end, the developed sounder allows for several order-of-magnitudes reduction of the measurement run time for a single location. In particular, a complete multiple-input multiple-output (MIMO) snapshot (32768 channel combinations) can be measured in 380 ms (further details presented later in the paper).

In addition to the above, our sounding setup has four important distinguishing features: (1) Since a MIMO snapshot can be measured in a time shorter than the channel coherence time (for moderate velocity of scatterers and/or receiver), double-directional characterization of dynamic environments is possible. This allows us to evaluate the impact of mobility on the temporal evolution of the angular spectrum, which is critical for accurate beamforming control [33]. (2) We consider both horizontal and vertical polarizations per-element at the transmit and receive sides. This enables a more complete description of the propagation channel, as we are able to characterize all properties of MPCs. To the best our knowledge, all of the sounders reported above do not consider polarization aspects. (3) Via careful RF design, low phase drift is seen between the local oscillators (LOs) at both link ends even in the absence of a cabled connection for clock synchronization. The accumulated phase drift within the measurement duration of one snapshot is low, which enables averaging of multiple complex waveforms to improve the measurement signal-to-noise-ratio (SNR). This is particularly valuable for measurements with high geometric attenuation. It also helps in eliminating any delay uncertainty for measurement with a large number of channel combinations. Even more importantly, it enables the use of high resolution parameter extraction (HRPE) algorithms such as SAGE and RiMAX [41, 42] to obtain post-processing gain, bringing the results well within the Fourier resolution limits.

Table 1 presents the state-of-the-art mmWave sounder characteristics known in the public domain. Rather interestingly, architectures based on switched arrays can be further divided into *switched beam architectures* (SBA), *switched horn antenna arrays* (SHA), and *switched patch arrays* (SPA), respectively. The corresponding references are as listed in the table. The major difference between the various approaches relates to sensitivity (achievable dynamic range) and scaliability. The SBA achieves high gain by coherently combining signals from multiple elements, while the SHA achieves array gain via the horn antenna directivity. In contrast to these, the SPA digitizes the channel impulse response measured at each antenna to achieve array gain in the digital domain via further processing. For the SBA, a critical part of the circuit design is the phase shifting network. Using standard complementary metal oxide semiconductor (CMOS) or Gallium Arsenide (GaAs) technology, an insertion loss on the order of 10 dB is expected at moderate switch rate of 1 μs [43]. Thus, to fully exploit the array gain and overcome the insertion loss of the network, an amplifier (low-noise at the receiver or high power at the transmitter) between the element and the phase shifter is needed. Nevertheless, this will have a significant impact on the cost and power consumption when the number of elements are increased. Moreover, they also set a fundamental practical limit to the beam switching rate, which should be smaller than the overall channel acquisition time. The main limitation of SHA relates to cost,

mechanical complexity and size, since each well designed horn element is expensive and needs to be arranged mechanically to cover a unique angle (see e.g., the array known as "Porcupine" used in [44], which is about 0.5 m in diameter). Different to SBA and SHA, the SPA design has the ability to utilize the recent advances in RF switching technology, significantly reducing the net insertion to 2-3 dB with a switching rate on the order of 100s of nanoseconds at mmWave frequencies [45]. This has opened up the prospects for massive SPA designs, offering the best trade-off solution in terms of implementation complexity, cost and performance with scaling up the number of elements.

The key contributions of the paper are: (1) We present a switched channel sounder operating at 28 GHz over 1 GHz bandwidth which is capable of measuring 128×256 dual-polarized channels in 382 ms. To the best of our knowledge, the design provides an order-of-magnitude superior angular resolution and is complimented with a nanosecond delay resolution relative to current setups. To this end, the design presents an opportunity to jointly characterize the delay, angles, Doppler and polarization parameters, respectively. Though not done in this paper, with the above information, an accurate double-directional model can be derived after high-resolution post processing. (2) With the short measurement run times and highly stable RF design, the sounder is tailored for characterizing dynamic propagation scenarios and allows us to track the evolution of the channel properties in both the spatial and temporal domains. This is in stark contrast to previous setups. (3) Via efficient FPGA implementation at both link ends, we can utilize complex real-time averaging of the received waveform to gain higher measurement SNR. As such, approximately 1 Gigabyte of data can be efficiently processed and downloaded each second.

2 Channel Sounder Design

As for any given channel sounder, a known waveform is generated at baseband and up-converted to carrier frequency of interest, followed by power amplification and transmission. On the receiving end, the waveform is down-converted, sampled and stored for post-processing. The channel impulse response is extracted from the received signal envelope relative to what was transmitted. In order to extract the directional characteristics of the channel, *multiple repetitions* of the sounding waveform are sent into (and thus received from) different directions, where different transmit and receive antenna combinations. The subsequent section explains this process in further detail.

2.1 Sounding Waveform

The baseband sounding waveform implemented in the transmit side of the sounder is a multi-tone *Zadoff-Chu (ZC) sequence*. ZC sequences contain ideal correlation properties in both time and frequency domains, and are thus well suited to channel sounding. Several other mmWave sounders reported in the literature use such sequences or other multi-tone waveforms [16, 17, 32]. The ZC sounding waveform can

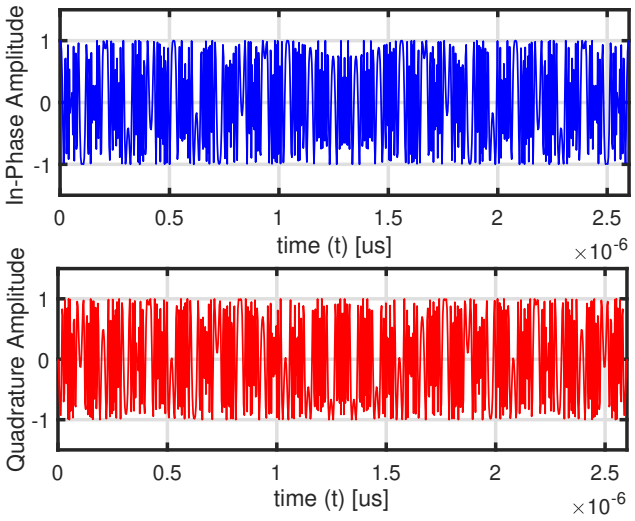

Figure 1: In-phase and quadrature components of $x(t)$, the ZC signal over 2.6 μs sampled with a rate of 1.4 Gigasamples/second.

be represented as

$$x(t) = \sum_{n=-N}^{N} e^{j(2\pi n \delta f t + \theta_n)}, \tag{1}$$

where δf denotes the tone spacing, $2N+1$ is the total number of tones governed by N, and θ_n is the complex phase of the n-th tone. Figure 1 depicts the in-phase (top sub-figure) and quadrature (bottom sub-figure) components of $x(t)$. A total of 2002 tones spaced by 500 kHz were selected to cover the instantaneous measurement bandwidth of 1 GHz. It can be readily observed that the resulting frequency spectrum of the ZC signal will be *flat* across the desired band of interest, providing SNR uniformity at all frequency tones. As derived in [46] and mentioned in [32], the values of θ_n can be modified to achieve a low peak-to-average-power ratio. Figure 2 shows the normalized amplitude of the waveform, which has a PAPR within 1.5 dB, enabling us to transmit with power as close as possible to the 1 dB compression point of the power amplifier without driving it into saturation mode. Furthermore, the ZC sequences are easily scalable across both time and frequency domains. Wider bandwidth of the signal helps to increase the delay resolution, while the duration of the signal needs to be on the order of the furthest resolvable MPC. In order to accurately acquire the received waveform, multiple ZC signals need to be transmitted in order to correlate the transmitted waveform with the one received. To avoid discontinuities between sequential ZC sequences, each waveform is effectively built up from two ZC sequences,

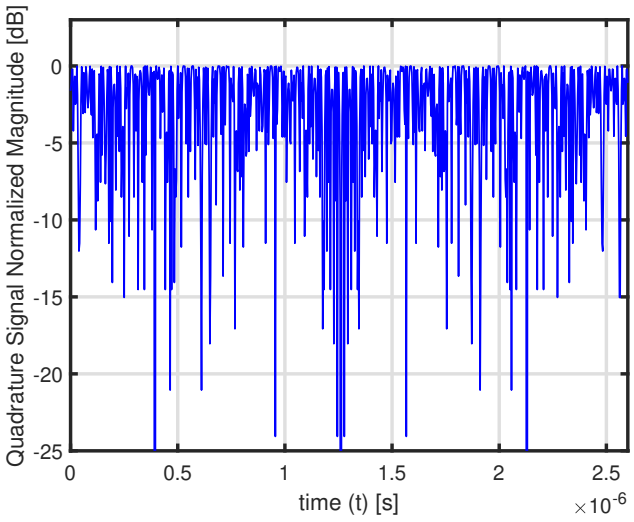

Figure 2: Normalized magnitude of the quadrature component over time.

Table 2: Baseband waveform and frame structure specifications.

Parameter	Value
Type	ZC (2× over-sampled)
Length	2048 samples
Waveform duration	2.6 μs
Phase drift margin	2 ZC durations
Switching duration and guard	(2.6 μs × 4) + 0.1 μs = 10.5 μs
Total # of antenna pairs	32768

where one is time reversed, i.e., over sampled by a factor of two. This approach has the advantage that repeated transmissions yield a time continuous signal used for averaging. Table 2 reports the exact ZC properties employed and implemented in the sounder.

2.2 Frame Structure and Sounding Sequence

The sounder frame structure is built up from a multiplicity of ZC sequences repeated after one another, followed by a so called *guard time* for switching (settling time for

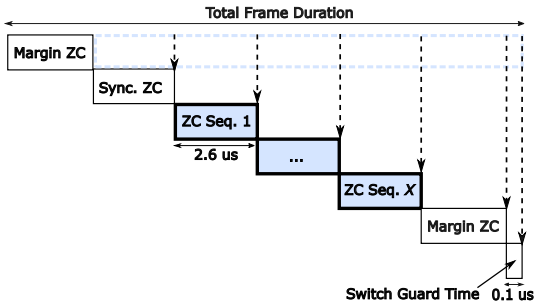

Figure 3: Overall frame structure for each transmit-receive antenna pair.

switches after activation). The *minimum* number of ZC sequences in each frame is four. In particular, the first and last ZC sequences are added as *margins* in case there are random phase drifts in a given direction, causing the switching to be unsynchronized. To this end, the second ZC sequence is used by the receiver to detect and synchronize the received signal, while the remaining arbitrary number of ZC sequences are used for *real-time averaging* to improve the SNR of the estimated channel impulse responses. This increases the measured dynamic range of the sounder. Since a single ZC sequence is of duration 2.6 μs, a switch guard time of 100 ns gives a minimum frame duration time of 10.5 μs. To this end, with 32768 channel combinations, a MIMO snapshot duration of 380 ms is obtained. The key properties of the frame structure are listed in Tab. 2. The overall frame structure for any given transmit and receive antenna combination, with the number of acquisitions set to X, is depicted in Fig. 3.

Since our ultimate aim is to accurately extract the propagation parameters in dynamic scenarios using HRPE algorithms, we need to ensure that the *duration of one MIMO snapshot is shorter than the channel coherence time.* Followed by this, the *MIMO cycle rate*, inverse of the duration between two adjacent snapshots should be *greater than or equal to half of the maximum absolute Doppler shift, in order to avoid ambiguities in estimating the Doppler shifts of MPCs.* Since in a switched sounder, the MIMO snapshot duration increases with the number of elements, there is an inherent conflict between the desired accuracy of the direction-of-arrival and direction-of-departure estimates (which implicitly demand a larger number of antennas) and the admissible maximum Doppler frequency. The authors in [47] were first to realize that it was the choice of *sequential* antenna switching pattern which causes this limitation in time-division multiplexed sounders. Instead, a *non-sequential* switching sequence has the potential to greatly extend the Doppler estimation range and nullify the aforementioned ambiguities. This principle relies on the fact that the signal phase can be inversely derived from the Doppler spread as long as its second-order statistics are time invariant, and that aliasing from systematic spatial switching can be avoided. In a similar line, with directional antennas, authors in [48, 49] proposed

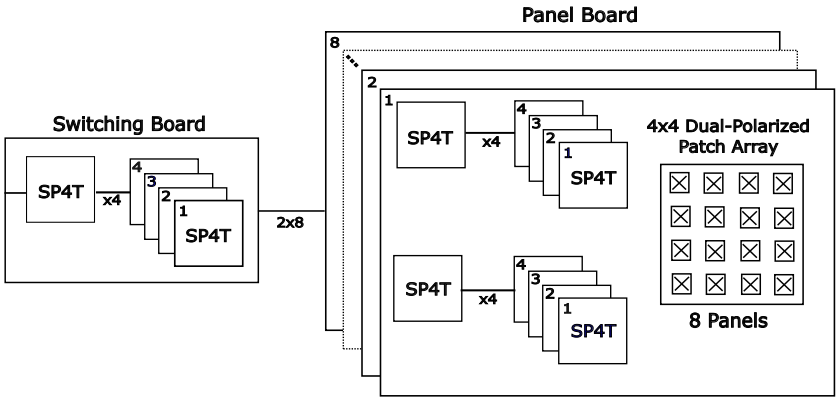

Figure 4: The cascaded switching topology divided into a switch board feeding up to 8 antenna panels with 16 dual-polarized (32 effective).

the use of the normalized sidelobe levels as the objective function to derived the necessary conditions of array switching sequence which leads to ambiguities. Henceforth, similar to [50], we employ the use of *pseudo-random switching at both link ends* of our sounder.[7] In the implementation context, both the transmit and receive sides locally use the same codebook the switching sequences prior to the sounding process. We highlight the fact that codebook implementation in software (discussed later in Section 3.4) offers unique flexibility to change the total number of actively switched antenna elements. This gives our design the flexibility to trade, angular resolution, coverage, and polarization with a more rapid MIMO snapshot duration. This naturally facilitates dynamic characterization of the channel with even higher receiver/scatterer velocities. One key difference between previous mmWave setups and the current sounder is the measurement of polarization properties, especially in dynamic environments. For sequential measurements in a dynamic environment, both the time offset between the measurements and the estimated Doppler spread needs to be considered in the estimation of the polarization properties. This may put very stringent requirements on the Doppler spread to be invariant, i.e., the measured trajectories may need to be along a straight line with constant speed. The approach will not jeopardize the random switching based relaxation as it relates to temporal de-correlation of spatially separated antenna elements. The opposite polarized elements are orthogonal and have a common center point, hence they are uncorrelated.

[7] For clarification, we note that the authors in [50] considered random switching only at a single (either transmit or receive) link end.

3 Sounder Architecture

This section presents details on the antenna array and switching architectures, transmit and receive sounder hardware, as well as software implementation aspects.

3.1 Antenna Array and Switching Architecture

The antenna architecture at both the transmit and receive link ends are based on dual-polarized patch elements, complemented by a quadruple cascaded switching circuit. The switch circuitry needed to support the transmit/receive arrays is based on 28 GHz absorptive single-pole-four-throw (SP4T) switches developed by Sony Inc. The utilized switches have superior power handling capabilities (on the order of +27 dBm) and have a net insertion loss on the order of 1.5 dB, well below the switches available in the public domain. The switching architecture enables up to 256 elements to be activated according to the pseudo-random switching sequence, and its design is divided in *two* parts: The first half of the circuit is located on a dedicated *switch board* that carriers two levels of cascade and distribute an input signal to 16 coaxial connectors. The second half is located at the *backplane of the antenna element panels*, where each panel has two coaxial inputs that are switched out to 32 antenna feeds compiled in a 4×4 fashion with two polarizations. Naturally, for the 256 element receive array, there are eight such panels, while for the 128 element transmit array, there are four panels. The overall cascaded switching topology complimenting panels of 4×4 dual-polarized antennas is demonstrated in Fig. 4. All boards are designed in six-layer printed-circuit-board (PCB) technology based on Rogers RO4450B substrate with favorable loss tangent and absolute permittivity. The process supports stacked vias through all layers.[8] This enabled a more compact layout with low insertion loss and facilitated half of the switch circuitry at the back of the panels next to the feed of the patch elements. Each antenna is assembled from the panels, shown in top and bottom sub-figures of Fig. 5, as discussed earlier. It can be seen from the bottom sub-figure that a corrugation structure (i.e., the horizontal stripes on the panels in Fig. 5) was introduced to prevent surface currents from distorting the antenna gain patterns. Due to processing limitations, the required grounding of the corrugation structure could not be supported, and a layer of an absorbing material was later added instead.

Each patch antenna is designed as a coupled parasitic resonator where the feed element is connected through stacked vias to the switch outputs at the antenna backplane. The elements are designed in a three-layered structure. The lowest layer is the ground plane; the second layer elevated to 100 μm is a dual feed coupling element; and the top layer at 300 μm, is the radiator. The coupling element in combination with the radiator generates two closely spaced resonances that are tuned to achieve a bandwidth that covers the desired frequencies. The simulated radiation patterns for both the vertical and horizontal modes from a patch element is shown in Fig. 6. The HPBW is approximately 85° in azimuth and 50° in elevation for both modes. The

[8] Stacked vias enable signal-paths to go through arbitrary layers of a PCB without introducing sidewise offsets.

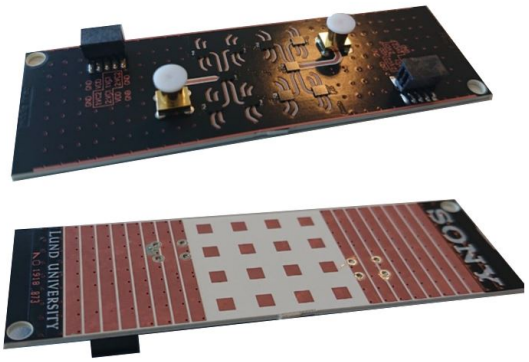

Figure 5: 28 GHz 4×4 patch antenna array front and back views.

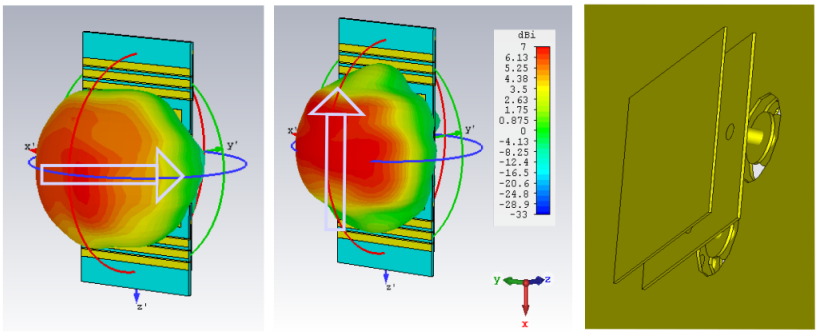

Figure 6: To the left, simulated gain patterns for horizontal and vertical polarization. To the right, the structure of a dual-polarized patch antenna element.

simulated total -10 dB return-loss bandwidth is about 4 GHz, and this matches the measured radiation bandwidth. The simulated isolation between antenna elements is about 20 dB. The peak radiated power from the antenna panel including the switch circuitry was measured and compared to that of a reference patch antenna. The IL from the switch circuitry was then estimated to about 5 dB, which, is close to the expectation. The total IL from cabling and switch circuitry, including the switchboard, is about 15 dB for an antenna. Each switchboard includes the first two layers of the switch cascade and is equipped with a coaxial connector for the feeding and 16 coaxial connectors that distribute the signal to the panels. The switchboard is shown in Fig. 7. The panels are further assembled into an eight-faced octagon

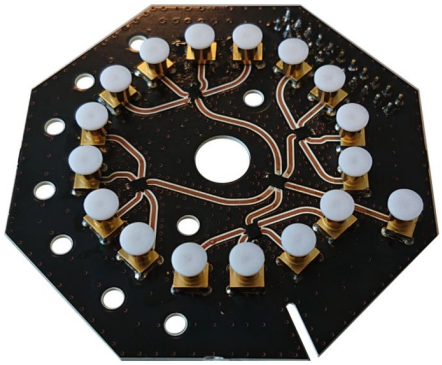

Figure 7: Switchboard with two layers of cascaded SP4T switches, coaxial connectors for input and 16 outputs and a control interface.

Figure 8: Left: 256 element receiver array. Right: 128 element transmit array.

shown to the left in Fig. 8 and the rectangular array shown to the right in Fig. 8. The octagonal array will be used at the receiver, while the rectangular array will be used at the transmit end for propagation measurements. Both arrays are shielded to prevent leakage from the switch circuitry and the inter-board connections to distort the radiation patterns. Amplifiers are attached to the feeds at both the receive and transmit antennas. This ensures that we can maximize the link budget by having an as high power as the switches can tolerate at the transmit side, despite a long feed cable. Similar at the receive side, an LNA is used to minimize degradation of the SNR from cable-related loss.

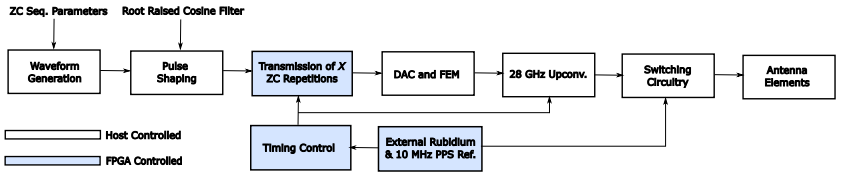

Figure 9: Overall implementation of the transmitter architecture for switched array channel sounding at 28 GHz.

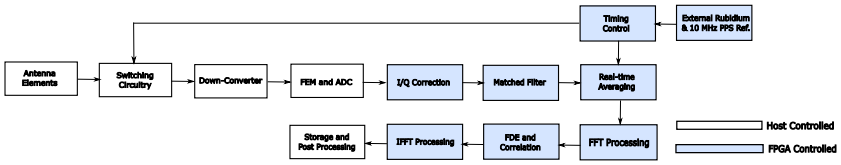

Figure 10: Overall implementation of the receiver architecture for switched array channel sounding at 28 GHz.

3.2 Antenna Array Calibration

The calibration of both antenna arrays involves three-dimensional measurements of the antenna gain pattern in an anechoic chamber suitable for 28 GHz. Each element needs to be individually measured with high accuracy in phase, amplitude, and polarization domains for maximum sensitivity in resolving the angular parameters. With the standard setup, one such full sphere (azimuth and zenith directions) measurement consumes on the order of 3 hours or more. Fortunately, the major part of this time relates to the physical movement of the antenna arrays in the chamber. By switching through all antenna elements at each physical orientation, the total time could be kept within reasonable limits. For rectangular transmit array, only half sphere measurement centered at boresight are considered, unlike the octagonal receive array where full sphere measurements will be conducted. The antenna calibration process is work which is currently under progress.

3.3 Transmitter and Receiver Architectures

Figure 9 shows the overall implementation of the transmitter architecture. Parts of the transmitter operation are controlled locally by the host computer, while others require integration with a FPGA. The sounding waveform is generated at the host with the required parameters, and is shaped with root raised cosine filtering before going into the FPGA for sequential transmission of X ZC sequences. The transmission process triggers the timing control governed by the FPGA, which receives an external 10 MHz clock reference. The clock used for the sounding setup is based on

a rubidium reference and is extremely stable. A 12-bit Digital-to-analog converter (DAC) and a front-end module (FEM) are used before upconversion of the baseband signal. The clock also triggers the switch timing and is used as a reference for the up-conversion process. Finally, the gain is set, activating a particular switch state, forwarding the signal to the antenna port for transmission over-the-air. The corresponding architecture at the receiver is shown in Fig. 10. The receive switch circuitry is controlled by the rubidium reference signal which triggers the capturing of the received waveform. This is followed by a down-converter to baseband and corresponding 12-bit analog-to-digital conversion (ADC). The receiver FPGA is then able to trigger in-phase and quadrature sample correction followed by a power maximization stage introduced by the matched filter. The FPGA performs real-time averaging of the many acquired replicas of ZC sequences and transforms the averaged waveform to the frequency domain for equalization and further processing. The resulting average is correlated with the transmitted ZC sequence and converted back to time domain to extract the influence of the propagation channel. The channel impulse response is then extracted and is sent for storage (with a streaming rate of 1 Gigabyte per-second) and further post-processing to extract the delay, Doppler, angular and polarization parameters.[9] Figure 11 demonstrates the complete sounding system with antenna arrays and transmitter/receiver architectures integrated. The different units are indicated with references to Table 3 where they are listed for ease of reference. At the transmit side, we use a power amplifier to compensate for cable loss and to ensure that the signal level is as large and as constant as possible. This is naturally within the power handling capabilities of the RF switches. Similarly at the receiver side, we use a low-noise amplifier directly at the feed of the switch board. The RF heads at each side, perform up and down conversion. The remaining hardware modules are all assembled in the National Instrument PXI-e 1085 chassis, and are directly controlled by the National Instrument LabVIEW host code via a backplane communication interfaces.

3.4 Software Implementation

The software used to control the channel sounder is entirely programmed in LabView. Both the receive side and transmit side have a similar set-up, which is shown in Fig. 12. The code is divided in three parts, the host code, the signal processing FPGA code, and the switch control FPGA code.

The host code is the controller and main user interface at both sides. It mainly controls the operational state and defines: the waveform, the number of repetitions, and the number of switch states. At the receive side, it additionally receives the raw CIRs, perform calibration, and add meta-data before saving them. The host code is not a real-time code, this enable the system to run in a standard Windows environment. The signal processing FPGA code operates in real-time, clocked by a rubidium source. The transmit side transmit the waveform with the predefined number of repetitions, adds switch guard time and generate a switch triggering signal between each

[9] The post-processing also involves calibration and addition of meta data, e.g., absolute time and antenna pair identification.

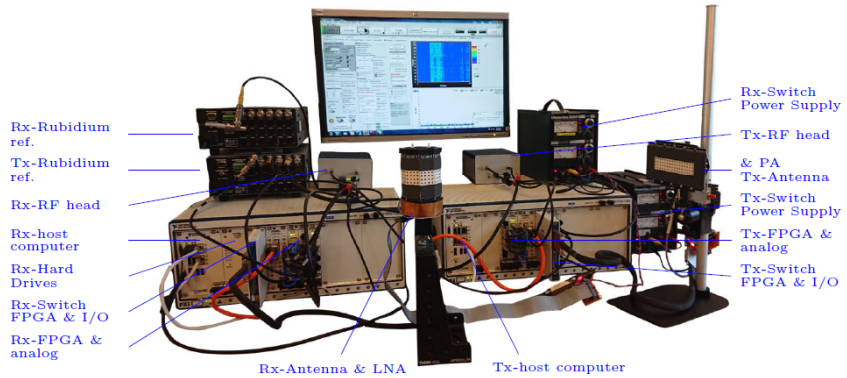

Figure 11: The overall channel Sounder measurement system with sub-units indicated with references to Table 3.

Table 3: Sounder transmit and receive hardware units.

Ref	Unit	Model
1	Power amplifier	Sage, SBP-2633332228-KFKF-S1
2	Low noise amplifier	Pasternack, PE15A3300
3	Transmit radio head	NI 3642
4	Receive radio head	NI 3652
5	LO/IF Module	NI PXIe 3620
6	DAC Module	NI PXIe 3610
7	ADC Module	NI PXIe 3630
8	FPGA Module	NI PXIe 7976R
9	Switch control module	NI 6581B
10	Timing and Sync Module	NI PXIe 6674T
11	Host computer	NI PXIe 8880
12	Chassis	NI PXIe 1085
13	Fast Array Hard drive	NI PXIe HDD 8261
14	Rubidium Source	FS725 Rubidium Frequency Standard

frame. A pulse-per-second (PPS) signal generated by the rubidium source triggers the code to transmit a predefined number of frames. The receive side, similarly, process each frame, generate a switch triggering signal and sends the resulting CIR with a timing identifier to the host. The processing involves synchronization, averaging and correlation to the known waveform. The switch FPGA code is the least complex and is the same at both sides. It change the switch state based on a code-book each time

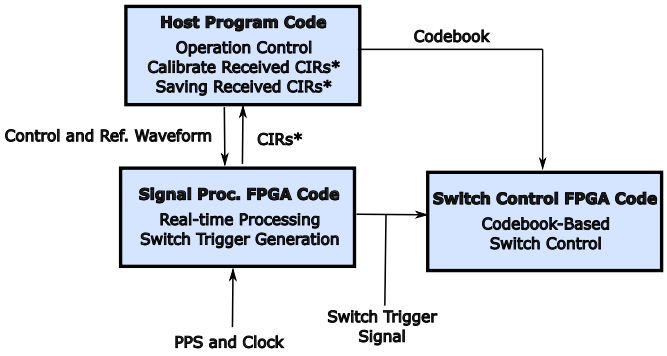

Figure 12: Overall channel sounder software architecture, where *indicate functions that only are present at the receive side.

it receives a trigger signal from the real-time signal processing FPGA.

4 Summary and Future Work

This paper presents the design and implementation aspects of a 28 GHz channel sounder intended for characterizing dynamic propagation environments. Based on the switched array principle, our design is capable of measuring 256×128 dual polarized channels with a switch rate of approximately 10 μs. Based on this, the sounder has the ability to obtain magnificent spatial resolution and is complimented with a large bandwidth resulting in nanoseond delay resolution. The 32768 channel combinations can be measured within 380 ms, within which the phase of the up/down-converters remain constant. This facilitates tracking of the MPCs to observe their temporal dependencies. To the best of our knowledge, our design is the first to have the capability to characterize amplitude, delays, angles, Doppler, and polarization parameters at 28 GHz for non-stationary scenarios. With a complete system at hand, we are currently working towards the calibration of both the transmit and receive antenna arrays, Followed by this, we will conduct our first indoor and outdoor dynamic propagation measurements in quest to build the most complete model of 28 GHz propagation. Along with pseudo-random switching sequences, the HRPE algorithms will ensure the highest accuracy in characterizing the aforementioned parameters. With resolution close to the Fourier limits, we aim to answer the fundamental question of channel sparsity at mmWave frequencies and aim to study the effects of blockages which feature prominently in mmWave channels.

5 Acknowledgement

The authors would firstly like to thank Sony Research Center Lund, Sony Semiconductor Solutions, Ericsson Research, National Instruments Inc., and Stiftelsen för Strategisk Forskning (SSF) for funding the project. The authors would also like to thank Prof. Andreas F. Molisch for the insightful discussions on various aspects of the work.

References

[1] J. G. Andrews, *et al.*, "What will 5G be?," *IEEE J. Sel. Areas Commun.*, vol. 32, no. 6, pp. 1065-1082, Jun. 2014.

[2] T. S. Rappaport, *et al.*, "Wideband millimeter-wave propagation measurements and channel models for future wireless communication system design," *IEEE Trans. Commun.*, vol. 63, no. 9, pp. 3029-3056, Sep. 2015.

[3] M. Shafi, *et al.*, "5G: A tutorial overview of standards, trials, challenges, deployment, and practice," *IEEE J. Sel. Areas Commun.*, vol. 35, no. 6, pp. 1201-1221, Jun. 2017.

[4] M. Shafi, *et al.*, "Microwave vs. millimeter-wave propagation channels: Key differences and impact on 5G cellular systems," *IEEE Commun. Mag.*, vol. 56, no. 12, pp. 14-20, Dec. 2018.

[5] FCC, "Technical Report on Auction 102 for Spectrum Frontiers - 24 GHz," May 2019.

[6] ITU-R M.2083-0, "IMT-2020 Vision - Framework and overall objectives of the future development of IMT for 2020 and beyond," ITU-R, Sep. 2015.

[7] 3GPP TR 21.95 v1.1.0, "Technical Specification Group Services and System Aspects for Release 15," Mar. 2019.

[8] N. Deparis, *et al.*, "Transposition of a baseband UWB signal at 60 GHz for high data rate indoor WLAN," *IEEE Microwave and Wireless Components Lett.*, vol. 15, no. 10, pp. 609-611, Oct. 2005.

[9] U. Demir and S. C. Ergen, "ARIMA-based time variation model for beneath the chassis UWB channel," *EURASIP J. Wireless Commun. and Networking*, vol. 2016, no. 1, pp. 1-18, Aug. 2016.

[10] D. Cassioli, "60 GHz UWB channel measurement and model," in *Proc. IEEE Int. Conf. Ultra-Wideband (UWB)*, Sept. 2012, pp. 145-149.

[11] S. Ranvier, *et al.*, "Millimeter-wave MIMO radio channel sounder," *IEEE Trans. Instrumentation and Measurement*, vol. 56, no. 3, pp. 1018-1024, June 2007.

[12] S. Piersanti, *et al.*, "Millimeter waves channel measurements and path loss models," in *Proc. IEEE ICC*, Jun. 2012, pp. 4552-4556.

[13] T. Zwick, *et al.*, "Wideband channel sounder with measurements and model for the 60 GHz indoor radio channel," *IEEE Trans. Veh. Technol.*, vol. 54, no. 4, pp. 1266-1277, Jul. 2005.

[14] J. E. Hakegard, *et al.*, "mm-Wave channel sounding using a fully programmable SoC," in *Proc. IEEE PIMRC*, Sept. 2016.

[15] A. Prokes, *et al.*, "Time-domain nonstationary intra-car channel measurement in 60 GHz band," *IEEE ATC*, Oct. 2016.

[16] J. M. Conrat, *et al.*, "A multibands wideband propagation channel sounder from 2 to 60 GHz," in *Proc. IEEE Instrumentation and Measurement Technology*, Apr. 2006, pp. 590-595.

[17] M. Peter, *et al.*, "Measurement and ray-tracing simulation of the 60 GHz indoor broadband channel: Model accuracy and parameterization," in *Proc. EuCAP*, Nov. 2007, pp. 1-8.

[18] P. F. M. Smulders and A. G. Wagemans, "Wide-band measurements of mm-wave indoor radio channels," in *Proc. IEEE PIMRC*, Oct. 1992, pp. 329-333.

[19] C. Gustafson, *et al.*, "Directional analysis of measured 60 GHz indoor radio channels using SAGE," in *Proc. IEEE VTC-Spring*, May 2011, pp. 1-5.

[20] C. Gustafson and F. Tufvesson, "Characterization of 60 GHz shadowing by human bodies and simple phantoms," in Proc. EuCAP, Mar. 2012, pp. 473-477.

[21] W. Fu, *et al.*, "Frequency-domain measurement of 60 GHz indoor channels: A measurement setup, literature data, and analysis," *IEEE Instrumentation Measurement Mag.*, vol. 16, no. 2, pp. 34-40, Apr. 2013.

[22] J. Blumenstein, *et al.*, "In-vehicle channel measurement, characterization, and spatial consistency Comparison of 30-11 GHz and 55-65 GHz frequency bands," *IEEE Trans. Veh. Technol.*, vol. 66, no. 5, pp. 3526-3537, May 2017.

[23] J. Medbo, *et al.*, "60 GHz channel directional characterization using extreme size virtual antenna array," in *Proc. IEEE PIMRC*, Aug. 2015, pp. 176-180.

[24] T. S. Rappaport, *et al.*, "Broadband millimeter-wave propagation measurements and models using adaptive-beam antennas for outdoor urban cellular communications," *IEEE Trans. Antennas and Propag.*, vol. 61, no. 4, pp. 1850-1859, April 2013.

[25] S. Hur, *et al.*, "Synchronous channel sounder using horn antenna and indoor measurements on 28 GHz," in *Proc. IEEE BlackSeaCom*, May 2014, pp. 83-87.

[26] M. D. Kim, *et al.*, "28 GHz path loss measurements in urban environments using wideband channel sounder," in *Proc. IEEE APS*, July 2015, pp. 1798-1799.

[27] J. Ko, *et al.*, "Millimeter-wave channel measurements and analysis for statistical spatial channel model in in-building and urban environments at 28 GHz," *IEEE Trans. Wireless Commun.*, vol. 16, no. 9, pp. 5853-5868, Sept. 2017.

[28] G. R. MacCartney and T. S. Rappaport, "A flexible millimeter-wave channel sounder with absolute timing," *IEEE J. Sel. Areas in Commun.*, vol. 35, no. 6, pp. 1402-1418, June 2017.

[29] J. Du, *et al.*, "Suburban residential building penetration loss at 28 GHz for fixed wireless access," *IEEE Wireless Commun. Lett.*, vol. 7, no. 6, pp. 890-893, Dec. 2018.

[30] D. He, *et al.*, "Influence analysis of typical objects in rural railway environments at 28 GHz," *IEEE Trans. Veh. Technol.*, vol. 68, no. 3, pp. 2066-2076, Mar. 2019.

[31] G. R. MacCartney, *et al.*, "Rapid fading due to human blockage in pedestrian crowds at 5G millimeter-wave frequencies," in *Proc. IEEE GLOBECOM*, Dec. 2017.

[32] C. U. Bas, *et al.*, "Real-time millimeter-wave MIMO channel sounder for dynamic directional measurements," *IEEE Trans. Veh. Technol.*, Jul. 2019.

[33] A. F. Molisch *et al.*, "Millimeter-wave channels in urban environments," in *Proc. EuCAP*, Oct. 2016.

[34] R. Sun, *et al.*, "Millimeter-wave radio channels vs. synthetic beamwidth," *IEEE Commun. Mag.*, vol. 56, no. 12, pp. 53-59, Dec. 2018.

[35] C. Gentile, *et al.*, "Millimeter-wave channel measurement and modeling: A NIST perspective," *IEEE Commun. Mag.*, vol. 56, no. 12, pp. 30-37, Dec. 2018.

[36] S. Salous, "Multi-band multi-antenna chirp channel sounder for frequencies above 6 GHz," in *Proc. EuCAP*, Apr. 2016.

[37] S. Salous, *et al.*, "Wideband MIMO channel sounder for radio measurements in the 60 GHz band," *IEEE Trans. Wireless Commun.*, vol. 15, no. 4, pp. 2825-2832, Apr. 2016.

[38] Z. Wen, *et al.*, "mmWave channel sounder based on COTS instruments for 5G and indoor channel measurement," in Proc. IEEE WCNC, Apr. 2016.

[39] J. Ala-Laurinaho, *et al.*, "2-D beam-steerable integrated lens antenna system for 5G E-Band access and backhaul," *IEEE Trans. Microwave Theory and Techn.*, vol. 64, no. 7, pp. 2244-2255, Jul. 2016.

[40] J. Zhang, *et al.*, "3D MIMO for 5G NR: Several observations from 32 to massive 256 antennas based on channel measurement," *IEEE Commun. Mag.*, vol. 56, no. 3, pp. 62-70, Mar. 2018.

[41] A. Richter, *Estimation of radio channel parameters: Models and algorithms*, Ph.D. dissertation, Technische Universität Ilmenau, Germany, 2005, Available online: www.db-thueringen.de.

[42] H. Tataria, *et al.*, "Channel correlation diversity in MU-MIMO systems - Analysis and measurements," in *Proc. IEEE PIMRC*, Sep. 2019.

[43] G.-S. Shin, *et al.*, "Low insertion loss, compact 4-bit phase shifter in 65 nm CMOS for 5G applications," *IEEE Microwave and Wireless Components Lett.*, Vol. 26, no. 1, pp. 37-39, Jan. 2016.

[44] AT&T, "AT&T debuts 5G channel sounder "porcupinea" with NI," [online]. accessible from http://www.fiercewireless.com/wireless/at-t-debuts-5g-channel-sounder-porcupine-ni, Aug. 2019.

[45] Peregrine Semiconductors. Portfolio of RF Switches, accessed on Feb. 11, 2018. [Online]. Available: http://www.psemi.com/products/rf-switches.

[46] M. Friese, "Multitone signals with low crest factor," *IEEE Trans. Commun.*, vol. 45, no. 10, pp. 1338-1344, Oct. 1997.

[47] X. Yin, *et al.*, "Doppler frequency estimation for channel sounding using switched multiple-element transmit and receive antennas," in *Proc. IEEE GLOBECOM*, Dec. 2003, pp. 2177-2181.

[48] T. Pedersen, *et al.*, "Joint estimation of Doppler frequency and directions in channel sounding using switched Tx and Rx arrays," in Proc. IEEE GLOBECOM, Dec. 2004, pp. 2354-2360.

[49] T. Pedersen, *et al.*, "Optimization of spatio-temporal apertures in channel sounding," *IEEE Trans. Signal Process.*, vol. 56, no. 10, pp. 4810-4824, Oct. 2008.

[50] R. Wang, *et al.*, "Antenna switching sequence design for channel sounding in a fast time-varying channel," in *Proc. IEEE ICC*, May 2018.